Development of Intelligent Low Field Nuclear Magnetic Resonance Tools for the Field of Biodiesel

**Thesis submitted in partial fulfillment
of the requirements for the degree of
"DOCTOR OF PHILOSOPHY"**

by

Paula Berman

**Submitted to the Senate of Ben-Gurion University
of the Negev**

January 2015

Beer-Sheva

Development of Intelligent Low Field Nuclear Magnetic Resonance Tools for the Field of Biodiesel

**Thesis submitted in partial fulfillment
of the requirements for the degree of
"DOCTOR OF PHILOSOPHY"**

by

Paula Berman

**Submitted to the Senate of Ben-Gurion University
of the Negev**

Approved by the advisors:

Prof. Zeev Wiesman: _____

Prof. Yael Edan: _____

Approved by the Dean of the Kreitman School of Advanced Graduate Studies

_____

January 2015

Beer-Sheva

This work was carried out under the supervision of

Prof. Zeev Wiesman

From the Department of Biotechnology Engineering
Faculty of Engineering

and

Prof. Yael Edan

From the Department of Industrial Engineering and Management
Faculty of Engineering

In the Environmental Engineering Unit
Faculty of Engineering

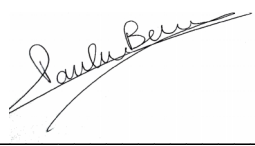# Research-Student's Affidavit when Submitting the Doctoral Thesis for Judgment

I <u>Paula Berman</u>, whose signature appears below, hereby declare that
(Please mark the appropriate statements):

X I have written this Thesis by myself, except for the help and guidance offered by my Thesis Advisors.

X The scientific materials included in this Thesis are products of my own research, culled <u>from the period during which I was a research student</u>.

__ This Thesis incorporates research materials produced in cooperation with others, excluding the technical help commonly received during experimental work. Therefore, I am attaching another affidavit stating the contributions made by myself and the other participants in this research, which has been approved by them and submitted with their approval.

Date: <u>27.1.2015</u>   Student's name: <u>Paula Berman</u>

Signature:_____

Acknowledgements

Abstract

Biodiesel offers a viable alternative to petroleum-based diesel fuels. Its production has increased dramatically over the last decade; however, several technical challenges still remain for improving its sustainability as a biofuel, including (a) researching for advanced, high prospect, second generation biodiesel feedstocks; (b) development of alternative transesterification conversion routes for transformation of complex, poor quality feedstocks; (c) coping with diverse biodiesel physical properties owing to an assortment in feedstocks quality and fatty acid compositions; and more. These challenges have raised the need for new rapid and non-destructive analytical tools and technologies. Most current conventional analytical methods cannot analyze composite materials in their pure state, and require prior extraction and purification of the desired fraction, using environmentally unfriendly solvents and complex analyses. [1]H Low Field Nuclear Magnetic Resonance (LF-NMR) relaxometry has been suggested as a tool to distinguish between molecular populations in complex systems with differential mobilities and/or microscopic compartmentalization. Still, development of appropriate tools and methodologies for data acquisition and interpretation is required to specifically address the technical challenges facing the biodiesel field.

In this dissertation we first describe the development of an improved data analysis tool for Laplace inversion of ^{1}H LF-NMR data using advanced sparse representation methods. This new formulation yielded better resolved relaxation time distributions and more accurate solutions, compared to the commercially available tool. Using the newly developed algorithm and advanced chemometric data analysis tools, several ^{1}H LF-NMR applications were designed, dealing with various technical challenges facing the whole process of biodiesel production: from feedstock to the end biodiesel product. These included ^{1}H LF-NMR applications for the characterization of new alternative biodiesel resources in their whole conformation, monitoring of the biodiesel transesterification reaction, and quality evaluation of the final product. As a final step, a comprehensive assignment of the peaks in relaxation time distributions of fatty acid methyl esters in the liquid phase was suggested, by exploring their molecular details and aggregation versus segmental and translational movements.

The potential for future applications using the developed tools is significant for the field of biodiesel, but also to other research and applied disciplines. The new inverse Laplace transform algorithm for data analysis of ^{1}H LF-NMR, is a powerful new tool that can shed light on new constituents and increase resolution of analyses for the numerous applications and researches published in the literature. Using the methodologies presented in this dissertation, we suggest the possibility of further studying dynamic processes, melting mechanisms, and structural organizations of alkyl chains, with important applications in the development of biodiesel fuels.

Table of Contents

List of Figures

Abbreviations

1D	One Dimensional
2D	Two Dimensional
FA	Fatty Acid
FFA	Free Fatty Acid
FID	Free Induction Decay
HF	High Field
ILT	Inverse Laplace Transform
LF	Low Field
MO	Methyl Oleate
NMR	Nuclear Magnetic Resonance
OA	Oleic Acid
P90	90° Pulse
P180	180° Pulse
PC	Principal Component
PCA	Principal Component Analysis
PDCO	Primal-Dual interior method for Convex Optimization
PLS	Partial Least Squares
RF	Radio Frequency
SNR	Signal to Noise Ratio
TAG	Triacylglycerol
TE	Transesterification

CHAPTER 1

Introduction

1.1. General introduction

1.1.1. Lipids

Classes of lipids

Lipids are substances that are (a) insoluble in water, (b) soluble in organic solvents, (c) contain long chain hydrocarbon groups, and (d) are present in or derived from living organisms [1]. Based on their structure, lipids can be classified as derived, simple, or complex.

Derived lipids are the building blocks for simple and complex lipids. They include Fatty Acids (FAs) and their derivatives. The majority of the FAs found in nature consist of saturated or unsaturated alkyl chains with an even number of carbon atoms (commonly C_{12} to C_{22}) [2]. Unusual FAs with different position or configuration of the double bonds or additional functional groups can also be found, having added value for their unique properties [3]. Some of the usual and unusual FAs available in plants are listed in Figure 1.1.
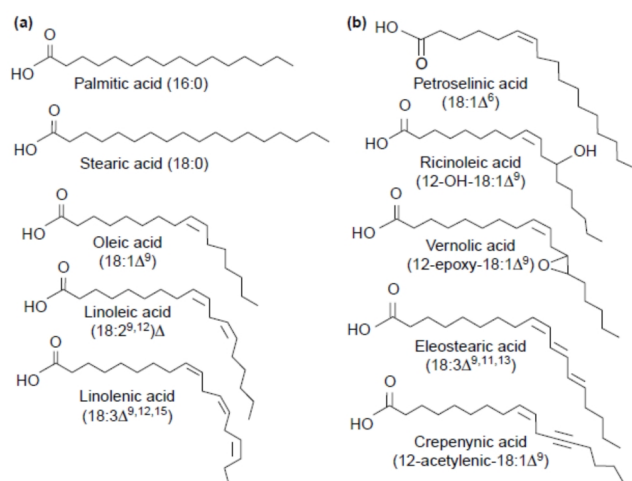
Figure 1.1. Comparison of the chemical structures of (a) FAs that occur widely in seeds and (b) unusual FAs that occur in seeds of a limited number of plants [3].

Simple lipids are molecules that can be hydrolyzed into two different components, usually an alcohol and an acid. These include acylglycerols, wax esters, and sterols. Acylglycerols are the predominant constituents in commercial oils and fats. They consist of a glycerol backbone with one, two, or three esterified FAs, thus respectively termed mono-, di-, or Triacylglycerols (TAGs). Waxes are esters of FAs and long chain alcohols. They are found in animal, microbial, and plant tissues and act as energy stores, protective coatings, and lubricants. Sterols consist of a steroid ring structure and a hydroxyl group, usually attached to carbon number 3. The hydroxyl group can be esterified with a FA to form a sterol ester.

Complex lipids are polar molecules that can be hydrolyzed into three or more components, one of which is phospholipids, which consist of a diacylglycerol molecule linked to a phosphorous moiety. These are a major part of membranes.

1.1.2. Biodiesel

Biodiesel is defined as mono-alkyl esters of long chain FAs, offering a viable alternative to petroleum-based diesel fuel. It has recently become more attractive due to diminishing petroleum reserves and the environmental consequences of exhaust gases. It is biodegradable, nontoxic and essentially free of sulfur and aromatics. Generally speaking, biodiesel has low oxidative stability, higher cetane number, higher viscosity, and higher cloud and pour points compared to conventional diesel [4]. Additionally, it has high boiling point, flash point, and extremely low vapor pressure. These indicate of a high level of safety for handling biodiesel [5]. Biodiesel can be used in its neat form (B100) or blended at any level with petrodiesel to create a blend. Blends are denoted as "BXX", where "XX" represents the biodiesel fraction (i.e,. B20 is 20% biodiesel and 80% petrodiesel).

Biodiesel can be derived from a wide range of lipid-containing materials, although more than 95% is currently produced from edible-grade oils [6]. This intensive production and commercialization of biodiesel have raised some critical environmental concerns. Its large-scale production can lead to imbalance in the global food market by drastically increasing consumption oil prices, which mainly affect developing countries. Land availability, and in particular competition for acreage with food crops, is also considered a core limitation [6].

To successfully market a new biodiesel feedstock, the biodiesel overall production process should be cost-effective to compete with petrodiesel prices. Zhang et al. [7] reported that 70–95% of the biodiesel production cost is the price of the feedstock itself. Therefore, high oil content sources are favored. In addition, biodiesel must meet international quality standards, several of which are related to the FA composition of the parent oil, thus determined by choice of feedstock. Hence, oil content and physical properties related to FA composition are important parameters in the successful commercialization of a new feedstock. To address this demand, alternative high yield and quality feedstocks are continuously researched. These include non-edible oilseeds such as castor [8,9] and jatropha [10]; algae [11]; and waste materials such as recycled oils [12], municipal [13,14] and winery [15] wastes. All the aforementioned materials consist of composite lipid mixtures including additional non-lipid components such as water, proteins, carbohydrates, and small amounts of vitamins.

Biodiesel is commonly produced by a chemical reaction named Transesterification (TE), where a lipid is reacted with an alcohol in the presence of a catalyst to form esters and glycerol (Figure 1.2). TAGs are the most common biodiesel source, although any lipid that can be converted into monoalkyl esters can be used as a primary source [13,16]. The conditions and materials of the TE reaction may vary significantly according to the type of lipid. Thus, even though these can be transformed into mono-alkyl esters, the different conditions required for each one makes the reaction of composite lipids difficult and at times impossible [12,17-19].

$$
\begin{array}{cccccc}
CH_2-OOC-R_1 & & & R_1-COO-R' & & CH_2-OH \\
| & & Catalyst & & & | \\
CH-OOC-R_2 & + & 3R'OH & \rightleftharpoons & R_2-COO-R' & + & CH-OH \\
| & & & & & | \\
CH_2-OOC-R_3 & & & R_3-COO-R' & & CH_2-OH \\
\text{Glyceride} & & \text{Alcohol} & & \text{Esters} & \text{Glycerol}
\end{array}
$$
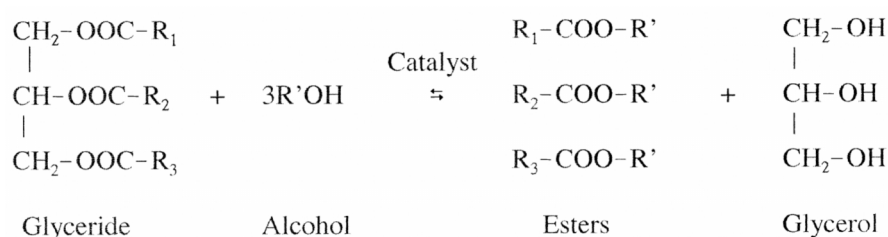
Figure 1.2. TE of TAGs with alcohol [20].

TE reaction can be catalyzed by homogeneous (alkali and acid), heterogeneous catalysts and enzymatic catalysts. Among other methods mentioned are supercritical and subcritical alcohol TE, microwave assisted TE and ultrasound assisted TE [21]. The most common TE reaction is performed under alkaline conditions by reacting oil with methanol, because of its lower price compared to other alcohols. The alkali

catalyst leads to a relatively fast conversion, while requiring only a moderate temperature. However, high yields are only achieved on low acid value (Free Fatty Acid, FFA< 3%) substrates, that are substantially anhydrous. In cases of poor oil quality alkali catalysts become inefficient due to soap formation, which makes the biodiesel separation very difficult. Alternatively, low grade substrates and/or non-acylglycerol lipids can be reacted using Brönsted acids. Yet, the reaction is usually carried out at higher temperatures and for longer periods [17].

The nature of the starting material, the production process, and subsequent handling can influence the biodiesel quality. Residues of unreacted lipids such as sterols, acylglycerols, phospholipids, and FFAs, or residues such as glycerol, alcohols, and water in the biodiesel can lead to severe operational problems including engine deposits, filter clogging, and fuel deterioration [22]. The biodiesel performance in a compression-ignition engine is determined by the physical properties of the fuel attributed by the biodiesel composition, which corresponds to the FA profile of the parent lipid [23,24].

Physical properties of FAMEs

The physical properties of FAs and their derivatives are largely determined by the length of the hydrocarbon chain and the degree of unsaturation, due to different degrees of packing of the molecules. In the fully saturated compounds, free rotation around each carbon–carbon bond gives the hydrocarbon chain great flexibility; the most stable conformation is the fully extended form, in which the steric hindrance of neighboring atoms is minimized. These molecules can pack together tightly in nearly crystalline arrays, with atoms all along their lengths in van der Waals contact with the atoms of neighboring molecules. In unsaturated FAs, a cis double bond forces a kink in the hydrocarbon chain. FAs with several such kinks cannot pack together as tightly as one kink or fully saturated FAs, and their intermolecular interactions are therefore weaker. FAs of the same chain length have lower melting points as the degree of unsaturation is increased, since it takes less thermal energy to disorder them [25].

Matsuzawa et al. [26], studied different molecular packing densities, and suggested that the existence of aggregate clusters most likely determines liquid properties of FAs such as density and fluidity. It is probable to assume that this is similar for

FAMEs, although very little research has been performed on the liquid phase molecular organization of FAMEs. Hence the liquid morphological structure of these materials will affect the physicochemical properties of the biodiesel including viscosity, density, fluid dynamics and low temperature operability. In addition, it has been well established in the past that the biodiesel composition determines several physical properties of the fuel, including ignition quality, heat of combustion, cold flow, oxidative stability, viscosity, and lubricity [4]. Therefore, to maintain proper vehicle performance, official standards were established that require analyses consisting of chromatographic, spectroscopic, physical properties-based, and wet chemical methods [22]. These methods are destructive, time consuming, laborious and environmentally unfriendly.

1.1.3. Nuclear Magnetic Resonance (NMR)

NMR is a form of spectroscopy that depends on the absorption and emission of energy arising from changes in the spin states of the nucleus of an atom. High Field (HF)-NMR spectroscopy provides insight into mixtures of various components belonging to the same or different chemical classes without previous separation of the individual components. It has been extensively applied for lipid identification and quantification. However, HF-NMR has two major disadvantages: (a) the extremely complicated analysis of the acquired spectra applied to composite materials, and (b) the overwhelming price of the HF instruments. Low Field (LF)-NMR instruments, on the other hand, use smaller, thus cheaper, magnets on the expanse of magnetic field homogeneity. Nevertheless, for applications that involve identifying certain populations according to their chemical and physical arrangement, these magnets are sufficient.

Basics of NMR

The principles of NMR have been discussed thoroughly in numerous books. The book by Abragam [27] is considered one of the seminal treatises. In this chapter, only the basic concepts will be defined. Charged unpaired protons, as in the case of hydrogen, spin around their axis creating a magnetic moment which acts like a small magnet. In the absence of an externally applied magnetic field, the magnetic moments are distributed randomly. As an externally applied magnetic field (B_0) is imposed, the

magnetic moments align parallel or anti-parallel to it and precess. When a second magnetic field in the form of Radio Frequency (RF) electromagnetic radiation at right angles to B_0 and at the same frequency as the precession of the nuclei is applied, the spins resonate and absorb energy. By absorbing energy they increase their angle of precession, depending on the intensity of the RF field and the time length applied to the sample. A pulse which is switched on long enough to cause a 90° rotation of the precession angle is a "90° pulse" (P90) and a pulse causing 180° rotation is called a "180° pulse" (P180). These are the two kinds of pulses most commonly used in pulse sequences.

As the precession angles of the spins increase from zero, the rotating magnetic vectors have two components - one in the direction of B_0 (determined as the Z direction) and the other in the same plane as the RF coil (the X-Y plane). The X-Y component, rotating at the precession frequency, cuts across the RF coil and induces a voltage at the precession frequency. Following a 90° pulse, the RF coil immediately detects a signal from the rotating X-Y component, which gradually decays as the spins lose energy, the precession angle decreases and the spins return to the equilibrium position. This signal is referred to as a Free Induction Decay (FID). The FID can be further processed to produce an NMR spectrum. In LF-NMR instruments the relaxation signal is analyzed.

^{1}H LF-NMR

The field of ^{1}H LF-NMR relaxometry is a powerful tool for identifying molecular species and to study their dynamics even in complex materials. The advantage of ^{1}H LF-NMR technology for the biodiesel field is the possibility of measuring composite materials in their whole conformation. This relates to the measurement of relaxation constants as a consequence of interactions among nuclear spins and between them and their surroundings. The FID shape and decay time are characteristic of the sample's physical state. Typically, the spin-spin relaxation time of solids is rapid and that of liquids is slow. Relaxation of the excited nuclei is characterized by two time constants known as T_1 and T_2. T_1 describes the time constant for the longitudinal magnetization to return to equilibrium following application of an RF field due to energy transferred to the lattice. It is referred to as the spin-lattice or longitudinal relaxation time (Figure 1.3).
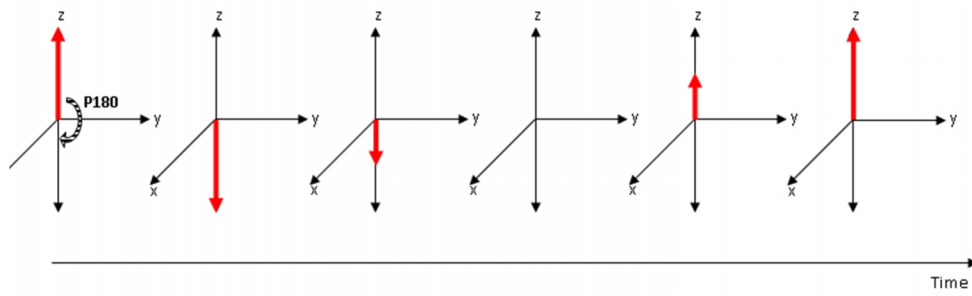
Figure 1.3. Longitudinal magnetization relaxation following RF excitation.

T_2 describes the time constant of transverse magnetization following a 90° pulse thus named spin–spin or transverse relaxation time. This time constant dissipates by field inhomogeneities and spin-spin interactions (Figure 1.4).
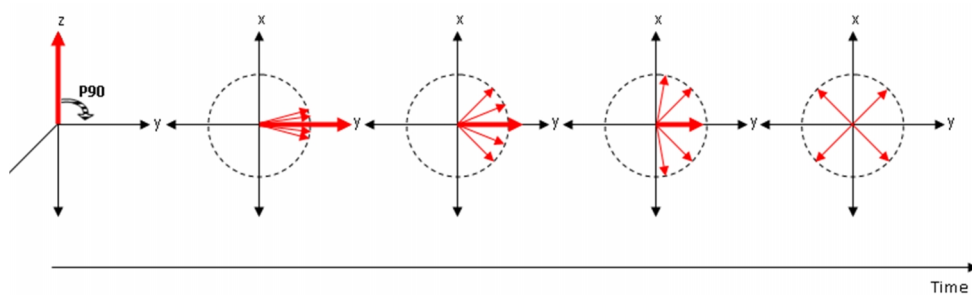
Figure 1.4. Transverse magnetization relaxation following RF excitation.

Relaxation time distribution experiments range from simple and rapid one dimensional (1D) tests to more complicated multidimensional ones. 1D tests use constant intervals between pulses, allowing for either longitudinal or transverse relaxation to be evaluated, whereas in multidimensional experiments, the signal is measured as a function of two or more independent variables, allowing the spin system to evolve under different relaxation mechanisms [28]. In biological samples, spins exist in a variety of different environments, giving rise to a distribution of relaxation times in which the measured relaxation decay is a sum of contributions from all spins [29].

Most commonly applied 1D tools are based on either acquisition of the FID signal following a 90° pulse, or pulse sequences such as the spin echo [30], pulsed field gradient spin echo [31], CPMG [32,33] or inversion/saturation recovery [27]. Only few of the applications found in the literature, mainly for the food industry, include measuring oil content in low moisture oilseeds [34-36], algae [37], and meat [38]; for

solid fat content measurement [39]; water holding capacity in meat and fish, [40-42]; characterization of water in agrofood products [43]; molecular mobility in wheat starch [44]; study of the denaturation of proteins in eggs and whey [45]; effect of formulation on liquid and solid fat ice cream [46]; prediction of viscosity, cetane number, and iodine value of oilseeds [47]; drug delivery [48]; and many others.

More recently, new two-dimensional (2D) relaxation time distribution pulse sequences have been suggested, including T_1-T_2 [28], T_2-store-T_2 [49] and T_2-D [50]. Several of the applications published in the last decade include 2D relaxation/diffusion correlations in porous media [50-52]; determination of avocado maturity [53]; monitoring the effect of high pressure and microwave processing on the microscopic water distribution and starch chain dynamics in potato and starch [54]; investigation of the physiological changes associated with ripening and mealiness in apples [55]; peak assignment to cell components, including compartmentalized water, pectins, starch, protein, and hemicelluloses in carrots [56]; and peak assignment for exploratory purposes in other foodstuffs including eggs, fish, dairy products, salad cream, and cake [57].

Data analysis of ^{1}H LF-NMR signals

The speed with which data is obtained and the complexity of the signal acquired can become overwhelming unless suitable methods for interpretation are used. Data analysis of relaxation experiments is traditionally performed in one of several ways:

a. By projecting the data into new coordinates that maximize the original variance. This can be applied only on a group of observations, as the model looks for commonalities in the original data. The main advantage is that the method imposes no mathematical constraints. This field is termed chemometrics and it comprises the application of multivariate statistics, mathematics, and computational methods to chemical measurements to enhance the productivity of chemical experimentation [58]. Chemometric methods include clustering techniques (to spot differences between samples, detection of outliers, and grouping) and regression models (for correlating NMR measurements to reference data) [59].

Principal Component Analysis (PCA) and Partial Least Squares (PLS) [60] are two commonly used chemometric methods in ^{1}H LF-NMR. Both methods extract

principal components and loadings to maximize the original variance and reduce dimensionality; hence they describe the data in a more condensed form. PCA is used for unsupervised exploration of the acquired data and dimensionality reduction; and PLS is a multicomponent regression method. The Principal Components (PCs) are mutually orthogonal and their extraction is such that the first PC holds the maximum variance, the second holds the second-maximum variance, and so on.

b. By assuming discrete multi-exponential behavior of the data, a fixed number (i) of pre-exponential weighting factors and relaxation decay constants are extracted. Time constants have been found to characterize and distinguish between populations (such as water and oil), and the pre-exponential weighting factors represent a quantitative measurement of each T_1/T_2 population [35]. Coefficients are extracted using nonlinear fitting models according to Eq. (1) and (2) for T_1 and T_2 respectively,

Eq. (1) $$s(t) = \sum_{i=0}^{N} w_i (1 - 2e^{-t/T_{1i}}).$$

Eq. (2) $$s(t) = \sum_{i=0}^{N} w_i e^{-t/T_{2i}}.$$

where s(t) is the acquired signal at t times, w_i are the pre-exponential weighting factors, and T_{1i} and T_{2i} are the relaxation time constants for longitudinal and transverse relaxations respectively. The calculated coefficients can then be used in prediction models [61-64].

c. By assuming a continuous distribution of exponentials. Here a relaxation time distribution of exponential coefficients is achieved with components appearing as peaks [28,29,65-67]. For the 1D case, conversion of the relaxation signal into a continuous distribution of relaxation components is performed using Eq. (3), where the probability density $f(T_2)$ is calculated applying Inverse Laplace Transform (ILT), s(t) is the relaxation signal acquired with ^{1}H LF-NMR at time t, T_2 are the time constants, and E(t) is the measurements error:

Eq. (3) $$s(t) = \int e^{-t/T_2} f(T_2) dT_2 + E(t).$$

The most common numerical method implemented today for dealing with ill-posed problems of this kind is based on L_2-norm regularization [29], where Eq. (4) is approximated by a discretized matrix form, and minimized according to the L_2-norm expression:

Eq. (4)
$$f = arg\,min\|s - Kf\|_2^{\,2} + \lambda\|f\|_2^{\,2},$$
$$f \geq 0$$

where K is the discrete Laplace transform, and λ is the L_2 weight. This type of regularization, however, can significantly distort the solution by contributing to the broadening of peaks, making it difficult to resolve close adjacent peaks.

^{1}H LF-NMR T2 distribution of lipids

The peaks in the analyzed T_2 distributions of lipids have not been hitherto assigned to the appropriate molecular population arrangements with certainty. Marigheto et al. [53] speculated that the analyzed bimodal T_2 distribution of an avocado oil sample arises from molecules of differing mobility, such as the oleic and palmitic constituents, or from nonequivalent proton pools of different mobility, such as those on methyl and olefinic groups. Adam-Berret et al. [68] found a similar two-peak distribution for tricaprin in the melt state, and suggested that this may be due to inhomogeneous relaxation rates for the protons along the side chains, or inhomogeneous organization of the TAGs in the liquid with intermolecular interactions. Of course these hypotheses are interrelated, since different mobilities along the side chains of the TAGs in the liquid phase are characteristic of different organizations and vice versa. Callaghan [69] studied the molecular motion of tristearin in the melt and found different T_2s along the chains, which in turn were used to explain the tuning fork molecular configuration.

1.2. Research objectives

The primary objective of this research was to explore the potential of ^{1}H LF-NMR technology, to address several of the technical challenges facing the biodiesel field. The specific objectives were to:

a. Develop an improved data analysis tool for Laplace inversion of ^{1}H LF-NMR relaxation signals using advanced sparse representation methods.

b. Design novel ^{1}H LF-NMR applications for the characterization of new alternative biodiesel resources in their whole conformation, monitoring of the biodiesel TE reaction, and quality evaluation of the final product, using advanced data analysis tools.

c. Assign the peaks of lipid standard materials analyzed by the new ILT algorithm to the appropriate molecular population arrangements.

1.3. List of publications

The order of the publications that comprise the presented dissertation is:

I. **Berman P**, Levi O, Parmet Y, Saunders M, Wiesman Z: Laplace inversion of LR-NMR relaxometry data using sparse representation methods. Concept Magn Reson A 2013, **42:**72–88.

II. **Berman P**, Nizri S, Parmet Y, Wiesman Z: Large-scale screening of intact castor seeds by viscosity using time-domain NMR and chemometrics. J Am Oil Chem Soc 2010, **87:**1247–1254.

III. **Berman P**, Leshem A, Etziony O, Levi O, Parmet Y, Saunders M, Wiesman Z: Novel ^{1}H low field (LF)-NMR applications for the field of biodiesel. Biotechnol Biofuels 2013, **6:**55.

IV. **Berman P**, Meiri N, Colnago LA, Moraes TB, Linder C, Levi O, Parmet Y, Saunders M, Wiesman Z: Study of liquid phase molecular packing interactions and morphology of fatty acid methyl esters (biodiesel) by ^{1}H low field nuclear magnetic resonance relaxometry. Biotechnol Biofuels 2015, in press.

Supplementary results in the form of a recently submitted manuscript to Biotechnology for Biofuels journal will be additionally presented.

V. Meiri N, **Berman P**, Colnago LA, Moraes TB, Linder C and Wiesman Z: Liquid phase characterization of molecular interactions in polyunsaturated and n-fatty acid methyl esters by ^{1}H Low field nuclear magnetic resonance, submitted to *Biotechnol Biofuels* journal.

1.4. Publications' logic and their contribution and order in the dissertation

The main component in dried oilseeds is the oil constituent; therefore the acquired ^{1}H LF-NMR signal can be directly related to oil quantity and quality. For these relatively simple materials, application of multi-exponential fitting and/or chemometric tools on the acquired signals is well suited; the latter being especially advantageous when dealing with large ^{1}H LF-NMR datasets. More advanced 2nd generation biodiesel feedstocks, which comprise composite materials, including fibers compartmentalized water and others, require a more comprehensive analysis of the relaxation signals using ILT analysis. The commercially available WinDXP ILT software package (Distributed ExPonential Analysis, Oxford Instruments, UK) for analyzing ^{1}H LF-NMR relaxation data, provides very broad relaxation time distributions, leading to overlapping of peaks and reduced resolution. Therefore, in order to differentiate between close peaks in relaxation time distributions, like in the case of oil residues in biodiesel, we developed as a first step of this doctoral research, a novel ILT algorithm using a relatively new approach for effective analysis and processing of digital images and signals.

In the first publication [I], therefore, we describe our novel numerical optimization method for analyzing LF-NMR relaxometry data by applying a Primal-Dual interior method for Convex Optimization (PDCO) solver. In this work, we used an integrated approach that included validation of analyses by simulations, testing repeatability of experiments, and validation of the model and its statistical assumptions. The proposed integrated approach has led to the development of an improved tool for analyzing LF-NMR relaxometry data by (1) introducing an L_1 regularization term to the mathematical formulation, (2) adjusting and applying the accurate and numerically stable PDCO solver, and (3) choosing universal coefficients for the calibration based on extensive simulations with different types of signal and Signal-to-Noise Ratio (SNR) values.

The second and third publications [II,III] consist of several of the ^{1}H LF-NMR applications designed throughout this research, dealing with various technical challenges facing the biodiesel field. In these two works we provide analytical tools that relate to the whole process of biodiesel production: from feedstock to the end biodiesel product.

The second publication [II] summarizes a rapid and non-destructive method for large-scale screening of intact castor seeds according to their viscosity by ^{1}H LF-NMR and chemometrics. Castor is one of the most promising non-edible oil crops, due to its high oil content and since it can be grown on marginal lands and in a semi-arid climate. However, its high content of ricinoleic acid results in an extremely high viscosity of castor-based biodiesel. In this work, a qualitative PCA model was constructed, where each castor sample was assigned to a different viscosity group. The model suggested was found superior to conventional analytical methods when screening thousands of seeds, since unique outliers showing reduced viscosity can be detected straightforwardly. This work's methodology can also be applied for screening within other types of oilseeds that differ in their FA profiles.

The third publication [III] is a broad publication that details additional novel applications for the characterization of new alternative biodiesel resources in their whole conformation and also monitoring of the biodiesel TE reaction, and quality evaluation of the final product. In this work 1D and 2D ^{1}H LF-NMR pulse sequences were used, and different data analysis strategies were applied, including the newly developed ILT algorithm. Supervised and unsupervised chemometric tools were suggested for screening new alternative biodiesel feedstocks according to oil content and viscosity. The tools allowed assignment into viscosity groups of biodiesel-petrodiesel samples whose viscosity is unknown, and revealed biodiesel samples that have residues of unreacted acylglycerol and/or methanol, and poorly separated and cleaned glycerol and water. In the case of composite materials, relaxation time distribution, and cross-correlation methods were successfully applied to differentiate components. Continuous distributed methods were also applied to calculate the yield of the TE reaction, and thus monitor the progress of the common and *in situ* TE reactions, offering a tool for optimization of reaction parameters.

In the third publication [III], the new ILT algorithm revealed a larger number of resolved peaks in the analyzed T_2 distributions of oil and biodiesel samples, compared to existing tools. Owing to the novelty of the tools used in this study, these had not yet been assigned to the appropriate molecular population arrangements with certainty. Following the suggested possible assignment of the peaks in T_2 distributions of oil [53,68], the fourth and fifth publications [IV,V] aimed at suggesting a comprehensive

explanation for the peaks by exploring the molecular details and aggregation versus segmental and translational movements of FAMEs in the liquid phase.

In the fourth publication [IV], we showed that pure Oleic Acid (OA) and Methyl Oleate (MO) standards exhibited both similarities and differences in the ^{1}H LF-NMR relaxation times (T_2s) and peak areas, for a range of temperatures. Based on X-ray measurements, both molecules were found to possess a liquid crystal-like order, although a larger fluidity was found for MO because as the temperature is increased, MO molecules separate both longitudinally and transversely from one another. In addition, both molecules exhibited a preferred direction of diffusion based on the apparent hydrodynamic radius. The close molecular packing arrangement and interactions were found to affect the translational and segmental motions of the molecules, as a result of dimerization of the head group in OA as opposed to weaker polar interactions in MO. As a result of this research, a comprehensive model for the liquid crystal-like arrangement of FAMEs in the liquid phase was suggested. The differences in translational and segmental motions of the molecules were rationalized by the differences in the ^{1}H LF-NMR T_2 distributions of OA and MO, which was further supported by ^{13}C HF-NMR spectra and ^{1}H HF-NMR relaxation.

The peaks assignments and the model for the liquid crystal-like morphology in the liquid phase of FAMEs presented in the fourth publication [IV], were further supported using different alkyl chain lengths (10 to 20 carbons) and degrees of unsaturation (0, 1, 2, and 3 double bonds) of FAMEs in their pure liquid phase. These complementary results were summarized in the fifth manuscript [V], recently submitted to Biotechnology for Biofuels journal presented in this dissertation as additional unpublished results. In this work, based on density values and X-ray measurements, it was proposed that FAMEs possess a liquid crystal-like order above their melting point, consisting of randomly aggregated liquid clusters with void spaces, whose morphological properties depend on chain length and degree of unsaturation. FAMEs were also found to exhibit different degrees of rotational and translational motions, which were rationalized by chain organization within the clusters, and the degree and type of molecular interactions and temperature effects. At equivalent fixed temperature differences from melting point, saturated FAMEs molecules were found to have similar translational motion regardless of chain length,

expressed by viscosity, self-diffusion coefficients, and T_2 measurements. T_2 distributions suggest increased alkyl chain rigidity and a reduced temperature response of the peaks' relative contribution with increasing unsaturation, which are a direct outcome of the alkyl chain morphological packing and molecular interactions.

CHAPTER 2

Publications

2.1. **<u>Berman P</u>**, Levi O, Parmet Y, Saunders M, Wiesman Z: Laplace inversion of LR-NMR relaxometry data using sparse representation methods. *Concept Magn Reson A* 2013, **42:**72–88.

Laplace Inversion of Low-Resolution NMR Relaxometry Data Using Sparse Representation Methods

PAULA BERMAN,[1] OFER LEVI,[2] YISRAEL PARMET,[2] MICHAEL SAUNDERS,[3] ZEEV WIESMAN[1]

[1]*The Phyto-Lipid Biotechnology Laboratory, Departments of Biotechnology and Environmental Engineering, The Institutes for Applied Research, Ben-Gurion University of the Negev, Beer-Sheva, Israel*
[2]*Department of Industrial Engineering and Management, Ben-Gurion University of the Negev, Beer-Sheva, Israel*
[3]*Department of Management Science and Engineering, Stanford University, Stanford, CA*

ABSTRACT: Low-resolution nuclear magnetic resonance (LR-NMR) relaxometry is a powerful tool that can be harnessed for characterizing constituents in complex materials. Conversion of the relaxation signal into a continuous distribution of relaxation components is an ill-posed inverse Laplace transform problem. The most common numerical method implemented today for dealing with this kind of problem is based on L_2-norm regularization. However, sparse representation methods via L_1 regularization and convex optimization are a relatively new approach for effective analysis and processing of digital images and signals. In this article, a numerical optimization method for analyzing LR-NMR data by including non-negativity constraints and L_1 regularization and by applying a convex optimization solver PDCO, a primal-dual interior method for convex objectives, that allows general linear constraints to be treated as linear operators is presented. The integrated approach includes validation of analyses by simulations, testing repeatability of experiments, and validation of the model and its statistical assumptions. The proposed method provides better resolved and more accurate solutions when compared with those suggested by existing tools. © 2013 Wiley Periodicals, Inc. Concepts Magn Reson Part A 42A: 72–88, 2013.

KEY WORDS: low-resolution NMR; sparse reconstruction; L_1 regularization; convex optimization

I.   INTRODUCTION

Low-resolution nuclear magnetic resonance (LR-NMR) relaxometry has emerged as a powerful new tool for identifying molecular species and to study their dynamics even in complex materials. This technology is widely used in industrial quality control for the determination of solid-to-liquid and oil-to-water ratios in materials as diverse as oil-bearing rock, food emulsions, and plant seeds (*1*). It offers great potential for characterization and ultimately quantification of components in different materials in their whole conformation. Many recent developments are reviewed by Blümich et al. (*2*). Note that the term LR-NMR is used in other contexts such as time-domain NMR, ex situ NMR, and portable NMR.

The process of relaxation occurs as a consequence of interactions among nuclear spins and between them and their surroundings. In biological samples, spins exist in a variety of different environments, giving rise to a spectrum of relaxation times, where the measured relaxation decay is a sum of contributions from all spins (*3*). Spin–spin interactions are the main relaxation mechanism in a CPMG (Carr, Purcell, Meiboom and Gill) pulse sequence (*4,5*).

Conversion of the relaxation signal into a continuous distribution of relaxation components is an ill-posed inverse Laplace transform (ILT) problem. The probability density $f(T_2)$ is calculated as follows:

$$s(t) = \int_0^\infty e^{-t/T_2} f(T_2) dT_2 + E(t), \qquad (1)$$

where $s(t)$ is the relaxation signal acquired with LR-NMR at time t; T_2 denotes the time constants; and $E(t)$ is the measurements error.

Istratov and Vyvenko (*6*) reviewed the fundamentals and limitations of the ILT. The most common numerical method implemented today for dealing with ill-posed problems of this kind is based on L_2-norm regularization (*3,7–9*), where Eq. [1] is approximated by a discretized matrix form and optimized according to the following equation:

$$\mathbf{f} = \arg\min_{\mathbf{f} \geq 0} \|\mathbf{s} - K\mathbf{f}\|_2^2 + \lambda \|\mathbf{f}\|_2^2, \qquad (2)$$

where K is the discrete Laplace transform and λ is the L_2 weight. This type of regularization, however, can significantly distort the solution by contributing to the broadening of peaks.

It should be noted that the non-negativity constraint in Eq. [2] makes the problem much harder to solve.

Without the constraint, a standard least-squares (LS) solver can be applied. The solution $\mathbf{f}$ obtained will satisfy the related normal equation:

$$(K^T K + \lambda I)f = K^T \mathbf{s}, \qquad (3)$$

However, there is no guarantee that $\mathbf{f}$ will be non-negative even if negative components are not physically feasible, as in the LR-NMR case. In practice, it is not acceptable to set negative values to zero. To solve Eq. [2], optimally, we need more sophisticated optimization tools such as interior-point methods (*10*).

Sparse representation methods are a relatively new approach for analysis and processing of digital images and signals (*11*). State-of-the-art optimization tools are used to handle efficiently even highly underdetermined systems. The main feature of these methods lies in using L_1 regularization in addition to the common L_2 regularization. It has been shown in theory and in practice that the L_1 norm is closely related to the sparsity of signals (*12*). The L_1 norm of the solution is the sum of absolute values of its components. Absolute value terms in the objective function are harder to handle than quadratic terms. However, it is possible to state the L_1-regularized problem as a convex optimization problem and then use an appropriate convex optimization solver. Typically, such solvers can handle the non-negativity constraint.

In this work, we apply advanced sparse representation tools to the problem of LR-NMR relaxometry. We use PDCO, a primal-dual interior method for convex objectives (*13*). PDCO can be adjusted to solve the LR-NMR relaxometry inverse problem with non-negativity constraints and an L_1 regularization term that stabilizes the solution process without introducing the typical L_2 peak broadening. Our new suggested method makes it possible to resolve close adjacent peaks, whereas existing tools typically fail, as we demonstrate below.

The underlying principle is that all structured signals have sparse representation in an appropriate coordinate system, and using such a system/dictionary typically results in better solutions when the noise level is relatively low. Evidently, one of the most important elements of this approach is choosing an appropriate dictionary.

## II.   THE LR-NMR DISCRETE INVERSE PROBLEM

Inverse problems and their solutions are of great importance in many disciplines. Application fields include medical and biological imaging, radar, seismic imaging, nondestructive testing, and more. An inverse problem is typically related to a physical system that can

take indirect measurements *s* of some unknown function *f*. The relationship between *s* and *f* is determined by the characteristics of the measurement system and relevant physical principles.

The general setting of an inverse problem in the continuous time domain is as follows:

$$s(t) = K(f(t)) + \varepsilon(t), \tag{4}$$

where *K* is an operator that models the action of the measurement system. The source of the error ε might be machine noise, incorrect or simplified modeling of the system, additional factors or variables that were not included in the model, or varying conditions during different measurements. A schematic description of the system is as follows:
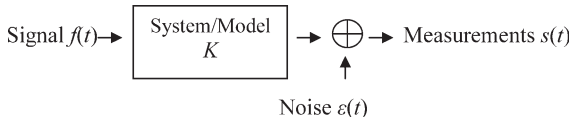
Equation [4] can be used to compute directly the expected measurement function of a known signal *f*. This computation is referred as the forward problem. It does not provide a direct method to estimate the signal *f* given a measurement function *s*. The latter problem is referred to as the inverse problem and requires appropriate optimization tools.

In many cases, as well as for NMR, the relationship between *f* and *s* can be accurately expressed by a linear transformation. For NMR, it is a direct result of the fact that the noiseless model is a Fredholm equation of the first kind—an integral model of the form:

$$s(t) = \int K(t, T) f(T) dT. \tag{5}$$

In this context, $K(t,T)$ is termed as the transformation kernel. One of the main characteristics of such integral transformations is that they are ill posed. An ill-posed problem is one that has one or more of the following properties: a) it does not have a solution; b) the solution is not unique; and c) a small perturbation of the problem may cause a large change in the solution.

Thus, even a low noise might lead to a completely wrong solution.

In practice, the inverse problem at hand is a discrete inverse problem defined as $\mathbf{s} = K\mathbf{f} + \mathbf{e}$, where *s* and *e* are *m* vectors and *K* is an $m \times n$ matrix. It is typically advised to choose $n < m$ and find a LS solution to a tall rectangular system:

$$\min_{\mathbf{f}} \|\mathbf{s} - K\mathbf{f}\|_2^2. \tag{6}$$

The exact choice of *n* depends on the nature and conditioning of the matrix *K*. As can be expected, the discrete problem is also ill-posed, and one must be very careful when trying to solve it. Standard methods can lead to very erroneous results because very different functions **f** could correspond to almost the same measurement function **s**.

A common approach is to use regularization methods, which force the solution **f** to possess certain properties. Often one searches for solutions of low magnitude using the L_2 norm; see Eqs. [2] and [3]. This method is known as Tikhonov regularization and typically results in smooth, noise-free solutions. The main drawback is its tendency to oversmooth the solution, and thus inability to detect low-intensity peaks or to resolve between two or more neighboring peaks (which tend to be merged into a single smooth wide peak).

The relationship between the spectrum function *f(T)* and the NMR measurements function *s(t)* is given by the Laplace transform (Eq. [1]). As can be seen, this is a special case of the Fredholm equation of the first kind (Eq. [5]) with the kernel defined as $K(t,T) = \exp(-t/T)$.

The discrete version of the Laplace transform is defined as $s_1 = s(t_1), \ldots, s_m = s(t_m)$, where $t_1, \ldots, t_m$ are the NMR signal acquisition times. The discrete values of **f** are $f_1 = f(T_1), \ldots, f_n = f(T_n)$, where $T_1, \ldots, T_n$ are the relaxation times, and the elements of *K* are $K_{l,j} = \exp(-l\Delta t/j\Delta T)$.

With $m > n$, the singular value decomposition (SVD) $K = U\Sigma V^T$ solves the LS problem (Eq. [6]) according to the following equation:

$$\mathbf{f} = V\Sigma^+ U^T \mathbf{s} = \sum_{j=1}^{n} \frac{\mathbf{u}_j^T \mathbf{s}}{\sigma_j} \mathbf{v}_j, \tag{7}$$

where *U* and *V* are orthogonal matrices of size *m* and *n*, respectively, and Σ has a lower block of zeros and an upper diagonal block $\Sigma_n = \mathrm{diag}(\sigma_1, \sigma_2, \ldots, \sigma_n)$ with the singular values of *K* on its diagonal (*14*). The singular values are ordered according to $\sigma_1 \geq \sigma_2 \ldots \geq \sigma_n \geq 0$, and the system is ill conditioned when σ_1/σ_n is large. It can be shown that the error in the solution is as follows:

$$\varepsilon_{\mathbf{f}} = K\varepsilon = \sum_{j=1}^{n} \frac{\mathbf{v}_j^T \varepsilon}{\sigma_j} \mathbf{u}_j, \tag{8}$$

where ε is the vector of measurement errors. Evidently, when *K* has small singular values, small errors in the measurements can result in large errors in the resolved values of **f** because the error is proportional to the reciprocals of the σ_j. Hence, it is a common practice to compress the linear operator *K* by truncating its smallest singular values, making the solution process more stable and less sensitive to measurement errors. This approach was suggested by Song (*15*) to enable two-dimensional inversions by compressing two

one-dimensional inversion matrices before constructing the larger two-dimensional matrix. (Tikhonov regularization is still typically necessary.) The best rank-r approximation to K is the partial sum of the first r SVD components: $\sum_{j=1}^{r} \sigma_j \mathbf{u}_j \mathbf{v}_j^T$. This compression stabilizes the solution while making a relatively small perturbation to the original problem defined by K.

Apparently, both L_2 regularization and SVD compression could be applied to improve the condition and stability of the inverse problem as well as to reduce the level of noise in the solution. There is an interesting relationship between the two methods: the L_2 regularization in Eq. [2] is equivalent to applying multiplicative weights to the singular values of K, where the weights are given by $w(\sigma) = \sigma^2/(\sigma^2 + \lambda)$ (16), and therefore, the larger singular values become more dominant. Thus, L_2 regularization is equivalent to smooth damping of the small singular values, whereas the SVD compression applies sharp truncation to the singular value series.

Other approaches for the NMR spectrum reconstruction include Monte Carlo simulation inversion (17), where an entire family of probable solutions are for a given measurements set. In addition, in Ref. (18), a phase analysis is applied to the measurements function using the Fourier transform to evaluate the exponential decay rates.

Herrholz and Teschke (19) considered sparse approximate solutions to ill-posed inversion problems, using compressed sensing methods, Tikhonov regularization, and possibly infinite-dimensional reconstruction spaces. Their results may be relevant for future work.

III.   THE PROPOSED SOLUTION

The mathematical formulation of our proposed method is the linearly constrained convex optimization problem:

$$\min_{\mathbf{f},\mathbf{c},\mathbf{r}} \; \lambda_1 \|\mathbf{c}\|_1 + \frac{1}{2} \lambda_2 \|\mathbf{c}\|_2^2 + \frac{1}{2}\|\mathbf{r}\|_2^2$$
$$s.t. \quad K\mathbf{f} + \mathbf{r} = \mathbf{s}, \tag{9}$$
$$-\mathbf{f} + B\mathbf{c} = 0, \qquad \mathbf{f} \geq 0,$$

where K is the discrete Laplace transform, $\mathbf{f}$ is the unknown spectrum vector, s is the measurements vector, $\mathbf{r}$ is the residual vector, and B is a sparsifying dictionary.

This model is a generalization of the LS model with non-negativity constraints. The objective function includes both L_1 and L_2 penalties on the vector $\mathbf{c}$, which is a representation of the solution in a given dictionary B. If $B = I$ (the identity matrix), then $\mathbf{c} = \mathbf{f}$ and the

sparsity property is imposed on $\mathbf{f}$ itself. This is most appropriate when the spectrum peaks are expected to be sharp and well localized. The basis pursuit denoising formulation as described in Ref. (11) allows high flexibility in the actual shape of the spectrum peaks. What allows this flexibility is the dictionary B. For example, B can be chosen to be a wavelet basis and then because of the multiscale property of wavelets, a sparse solution in the wavelet domain can correspond to both thin and thick spectrum peaks, and the optimal solution is expected to represent the actual sample properties. Another efficient choice for B might be a dictionary of Gaussians at different locations and with different widths.

Model [9] includes two regularization parameters λ_1 and λ_2 as weights on the L_1 and L_2 terms, where λ_1 controls the solution sparsity in the chosen dictionary B, and λ_2 affects the smoothness of the solution: it can be increased to smooth the solution and to remove noise. In our experiments, $\|K\| = O(1)$ and $\|B\| = O(1)$; however, the choice of λ_1 and λ_2 must allow for $\|s\|$ and $\|\mathbf{r}\|$. In general, λ_1 and λ_2 should be proportional to $\|\mathbf{s}\|$ and to the level of noise in the measurements: the higher the noise, the larger the regularization parameters.

IV.   METHODS

The PDCO Solver

PDCO (13,20) is a convex optimization solver implemented in Matlab. It applies a primal-dual interior method to linearly constrained optimization problems with a convex objective function. The problems are assumed to be of the following form:

$$\min_{\mathbf{x},\mathbf{r}} \varphi(\mathbf{x}) + \frac{1}{2}\|D_1\mathbf{x}\|_2^2 + \frac{1}{2}\|\mathbf{r}\|_2^2$$
$$s.t. \quad A\mathbf{x} + D_2\mathbf{r} = \mathbf{b} \tag{10}$$
$$\mathbf{l} \leq \mathbf{x} \leq \mathbf{u},$$

where $\mathbf{x}$ and $\mathbf{r}$ are variables, and D_1 and D_2 are positive-definite diagonal matrices. A feature of PDCO is that A may be a dense or sparse matrix or a linear operator for which a procedure is available to compute products $A\mathbf{v}$ or $A^T\mathbf{w}$ on request for given vectors $\mathbf{v}$ and $\mathbf{w}$. The gradient and Hessian of the convex function $\varphi(\mathbf{x})$ are provided by another procedure for any vector x satisfying the bounds $l \leq x \leq \mathbf{u}$. Greater efficiency is achieved if the Hessian is diagonal [i.e., $\varphi(\mathbf{x})$ is separable].

Typically, 25–50 PDCO iterations are required, each generating search directions $\Delta\mathbf{x}$ and $\Delta\mathbf{y}$ for the primal variables $\mathbf{x}$ and the dual variables $\mathbf{y}$ associated

with $A\mathbf{x} + D_2\mathbf{r} = \mathbf{b}$. The main work per iteration lies in solving a positive-definite system

$$\left(AD^2A^T + D_2^2\right)\Delta\mathbf{y} = AD^2\mathbf{w} + \mathbf{t}, \qquad (11)$$

and then $\Delta\mathbf{x} = D^2(A^T\Delta\mathbf{y} - \mathbf{w})$, where D is diagonal if $\varphi(\mathbf{x})$ is separable. As $\mathbf{x}$ and $\mathbf{y}$ converge, D becomes increasingly ill conditioned. When A is an operator, an iterative (conjugate-gradient type) solver is applied to

Eq. [11], and the total time depends greatly on the increasing number of iterations required by that solver (and the cost of a product $A\mathbf{v}$ and a product $A^T\mathbf{w}$ at each iteration).

To solve problem [9] with a general dictionary B, we would work with $\mathbf{c} = \mathbf{c}_1 - \mathbf{c}_2$ (where $\mathbf{c}_1, \mathbf{c}_2 \geq 0$) and apply PDCO to Eq. [10] with the following input and output:

$$\varphi(x) = \lambda_1\|\mathbf{c}\|_1 = \lambda_1\Sigma_j\left\{(c_1)_j + (c_2)_j\right\},$$

$$A = \begin{pmatrix} K & 0 & 0 \\ -I & B & -B \end{pmatrix}, \qquad D_1 = \begin{pmatrix} \delta_1 I & & \\ & \sqrt{\lambda_2}I & \\ & & \sqrt{\lambda_2}I \end{pmatrix}, \qquad D_2 = \begin{pmatrix} I & & \\ & \delta_2 I & \\ & & \delta_2 I \end{pmatrix},$$

$$l = \begin{pmatrix} 0 \\ 0 \\ 0 \end{pmatrix}, \qquad u = \begin{pmatrix} \infty \\ \infty \\ \infty \end{pmatrix}, \qquad x = \begin{pmatrix} f \\ c_1 \\ c_2 \end{pmatrix}, \qquad r = \begin{pmatrix} r_1 \\ r_2 \end{pmatrix}, \qquad b = \begin{pmatrix} s \\ 0 \end{pmatrix},$$

where δ_1 and δ_2 are small positive scalars (typically 10^{-3} or 10^{-4}), r_1 represents r in Eq. [9], and r_2 will be of order δ_2. For certain dictionaries, we might constrain $c \geq 0$, in which case, $c = c_1$ above and $c_2 = 0$.

LR-NMR Measurements

LR-NMR experiments were performed on a Maran Ultra bench-top pulsed NMR analyzer (Oxford Instruments, Witney, UK), equipped with a permanent magnet and an 18-mm probe head, operating at 23.4 MHz. Samples were measured four times to test the repeatability of the analysis. Prior to measurement, samples were heated to 40°C for 1 h and then allowed to equilibrate inside the instrument for 5 min. In between measurements, the instrument was allowed to stabilize for an additional 5 min.

The CPMG sequence was used with a 90° pulse with 4.9 ms, echo time (τ) of 100 ms, recycle delay of 2 s, and 4, 16, 32, or 64 scans. For each sample, 16,384 echoes were acquired. Following data acquisition, the signal was phase rotated and only the main channel was used for the analyses.

RI-WinDXP

Distributed exponential fitting of simulations and real LR-NMR data were performed with the WinDXP ILT

toolbox (21). Data were logarithmically pruned to 256 points prior to analysis, the weight was determined using the noise estimation algorithm, and logarithmically spaced constants were used in the solution.

SNR Calculations

SNR consisted of taking the ratio of the calculated signal and noise. The signal was calculated as the maximum of a moving average of eight points. For the noise calculation, the last 1,024 echoes were chosen and corrected using the slope and intercept of the noise (χ_i) versus the number of echoes, and the noise was calculated from the following equation:

$$\text{Noise} = \sqrt{\left(\sum_{i=1}^{1024}\chi_i^2\right)/1024}. \qquad (12)$$

Stability

Signal stability was determined using the coefficient of variation (cv) calculated as follows:

$$cv_i = 100\times\text{Standard Deviation}_i/\text{Mean}_i \qquad (13)$$

where the mean and standard deviation were calculated from four repeated measurements, and $i = 1:256$ is the distribution value. To get a measurement of the

Table I   Intrinsic T_2 Values of the Simulated Narrow-Peak Signal (ms)

	Intrinsic T_2 of Peak 1	Intrinsic T_2 of Peak 2	Intrinsic T_2 of Peak 3
Signal 1	1.44	21.54	323.45
Signal 2	2.25	21.54	205.93
Signal 3	3.54	21.54	131.11
Signal 4	5.56	21.54	83.48
Signal 5	8.73	21.54	53.15

signal stability and disregard the noise, mean cv calculations were performed on the data that were higher than 25% and 10% of the maximum signal. Maximum cv values of around 15% were considered to give acceptable stability.

V.   RESULTS AND DISCUSSION

The new algorithm was extensively tested and calibrated using simulated data computed with an in-house Matlab function library. The objective of the simulations was to determine the accuracy and resolution of the analyzed spectra when compared with the noise-free simulated signal. In addition, simulations were used to determine universal, robust regularization coefficients that provide accurate and stable solutions for a broad range of signal types and SNR levels.

Two types of signals were simulated: i) a broad-peak signal and ii) a signal with narrow peaks that progressively become closer. The broad-peak signal was chosen as a typical L_2 solution of an oil sample, with varying noise levels. The narrow-peak signal consisted of three peaks, artificially constructed according to a Gaussian distribution, with varying widths, signal strengths, and noise levels. Five types of narrow signals were used with the intrinsic T_2 values described in Table 1.

An additional narrow two-peak simulation, with peaks of varying widths that progressively become closer, was used to evaluate the resolution of the PDCO algorithm. In the simulations, a peak with an intrinsic T_2 value of 81.54 ms was kept constant and another peak was gradually brought closer (27.53, 30.03, 32.75, 35.73, 38.97, 42.51, 46.36, 50.57, 55.16, 60.16, 65.62, and 71.58 ms). Similar peak widths were used in the two narrow-peak simulations, using four Gaussian functions with standard deviations 2, 3, 4, and 5.

Calibration

As previously mentioned, it has been well established in the literature that the ILT is a notorious and common ill-conditioned inversion problem, whose direct inversion is unstable in the presence of noise or artifacts. Choosing an appropriate regularization method is therefore crucial for the establishment of an accurate and stable solution. In the experiments below, we used the simplest dictionary $B = I$ and applied PDCO to the problem

$$\min_{\mathbf{f},\mathbf{r}} \; \lambda_1 \|\mathbf{f}\|_1 + \frac{1}{2}\,\lambda_2\|\mathbf{f}\|_2^2 + \frac{1}{2}\|\mathbf{r}\|_2^2 \tag{14}$$
$$s.t. \quad K\mathbf{f}+\mathbf{r}=\mathbf{s}, \qquad \mathbf{f} \geq 0,$$

with $\lambda_1 = \alpha_1\beta/\text{SNR}$ and $\lambda_2 = \alpha_2/\text{SNR}$, where $K_{ij} \geq 0$, max $K_{ij} = 1$, and $\beta = \|\mathbf{s}\|\infty$. Dividing the regularization coefficients by SNR provides calibration with respect to the signal strength, as less regularization is needed for larger SNR. Making λ_1 proportional to β gives robustness with respect to scaling or normalization of the signals. These two kinds of robustness were tested and validated with a high level of certainty throughout the simulations, by ensuring that a single set of chosen values for α_1 and α_2 provides stable and high-quality solutions for different levels of noise or signal strengths. The method's robustness was validated for a minimum SNR value of 150. For much lower SNR values, larger α_2 is recommended to prevent peak-splitting artifacts.

We believe that a tailored overcomplete dictionary B with a variety of peak widths and locations can significantly improve the results, as suggested by preliminary experiments. This remains for future study.

Calibration of α_1 and α_2 was performed using the simulated narrow-peak signals. For each simulated signal, a grid search was performed for the α_1 and α_2 values that gave the smallest error relative to the known solutions (min $\|\mathbf{f} - \mathbf{x}\|_2$, where $\mathbf{x}$ is the noise-free signal and f is the reconstructed signal). It was verified that the optimal results based on the residual L_2 norm criteria were consistent with the decision of an expert using visual inspection.

Figures 1(a,b) show histograms of the $\log_{10}(\alpha_1)$ and $\log_{10}(\alpha_2)$ values. As can be seen, optimal values of both αs were found in a relatively small range (the x-axis shows the entire range that was used for screening). Based on the histograms, the most common values chosen were $\alpha_1 = 3$ and $\alpha_2 = 0.5$, and this would be the natural choice for the calibration. The larger values (especially for α_2) were mostly chosen for the widest peaks and low SNR values. Therefore, to establish a conservative calibration that also gives a stable solution for wide peaks and very low SNR values, 10 and 5 were ultimately chosen as the optimal α_1 and α_2 (marked in red on the histograms). As shown in the following examples, this choice of universal coefficients
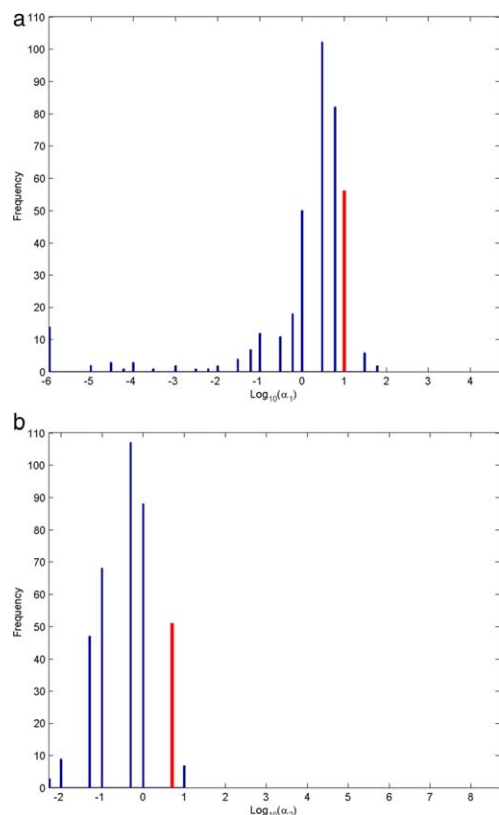
Figure 1 Histograms of the optimal (a) $\log_{10}(\alpha_1)$ and (b) $\log_{10}(\alpha_2)$ values that were obtained in the regularization parameters calibration simulation study. The universal $\log_{10}(\alpha_1)$ and $\log_{10}(\alpha_2)$ values chosen for the calibration are marked in red.

provides accurate and stable results for a wide range of signals and scenarios.

The effect of under-regularizing the noisy signal was mostly stressed for the broad-peak simulations and the widest-well-separated peak simulations. These are more challenging factors to reconstruct an accurate and stable manner when compared with narrow peaks. Figures 2 and 3 compare representative PDCO analyses of the broad-peak simulations and Signal 1 simulations using wide peaks, respectively. The analyses were performed using the universal regularization values for α_1 and α_2 (PDCO) and two less conservative choices for these parameters. As shown, the relatively conservative choice of the proposed universal regularization parameters provides very good reconstruction of the broad peaks, even for low SNR levels. It is also important to note that decreasing the regularization parameters below the recommended universal values, especially α_2, leads to the formation of spurious peaks that result in very different and unstable solutions when the SNR value is low. On the other hand, when the SNR value is high (according to these results approximately above 1,000), a slight decrease of α_1

and α_2 values does not degrade the solution. This, however, can lead to a dramatic change in resolving narrow adjacent peaks, which are more affected by the broadening effect of choosing a conservative choice for λ_2 (data not shown).

Resolution Analysis

To determine the resolution limit of the proposed method, we applied the narrow two-peak signal simulation with peaks of varying widths that progressively become closer. This procedure was carried out for four different SNR levels. The T_{22}/T_{21} results (ratio of intrinsic T_2 values of the two peaks) are summarized in Table 2.

For each peak width and SNR level, the resolution limit was determined by marking the smallest separation in between the peaks for which the PDCO algorithm succeeded in separating the two peaks (separation was determined based on identification of peaks maxima). This procedure was repeated twice, one time using the conservative universal values for the regularization coefficients and another time using a lower α_2 value.

It is important to note that both the peak width and SNR value have a major effect on the determination of resolution. The wider the peaks or the lower the SNR, the higher is the ratio of T_{22}/T_{21} values that can be resolved. It has been shown that a Tikhonov regularization algorithm for a double exponential with $T_{22}/T_{21} > 2$ can be reliably resolved if $SNR > 1,000$ (6). These results are in excellent agreement with those achieved using PDCO and the universal set of α_1 and α_2 values. As expected, with the less conservative regularization, the resolution limits were markedly improved, especially for narrow peaks.

Comparison Between WinDXP and PDCO Results for Simulated Data

Distributed exponential settings of simulations were performed with the WinDXP ILT toolbox (21). To compare PDCO with the WinDXP solutions on the same simulated data, an in-house Matlab script was used to transform the simulated signals into the proper file format to be read by the WinDXP program. In addition, to remove uncertainties in the choice of regularization of WinDXP is unknown, and to demonstrate the influence of the L_1 regularization component, relaxation time distributions were compared for PDCO with $\alpha_1 = 0$ and the universal value for α_2, as determined by calibration.

Figures 4(a–p) compare representative simulation analyses using the PDCO-established universal
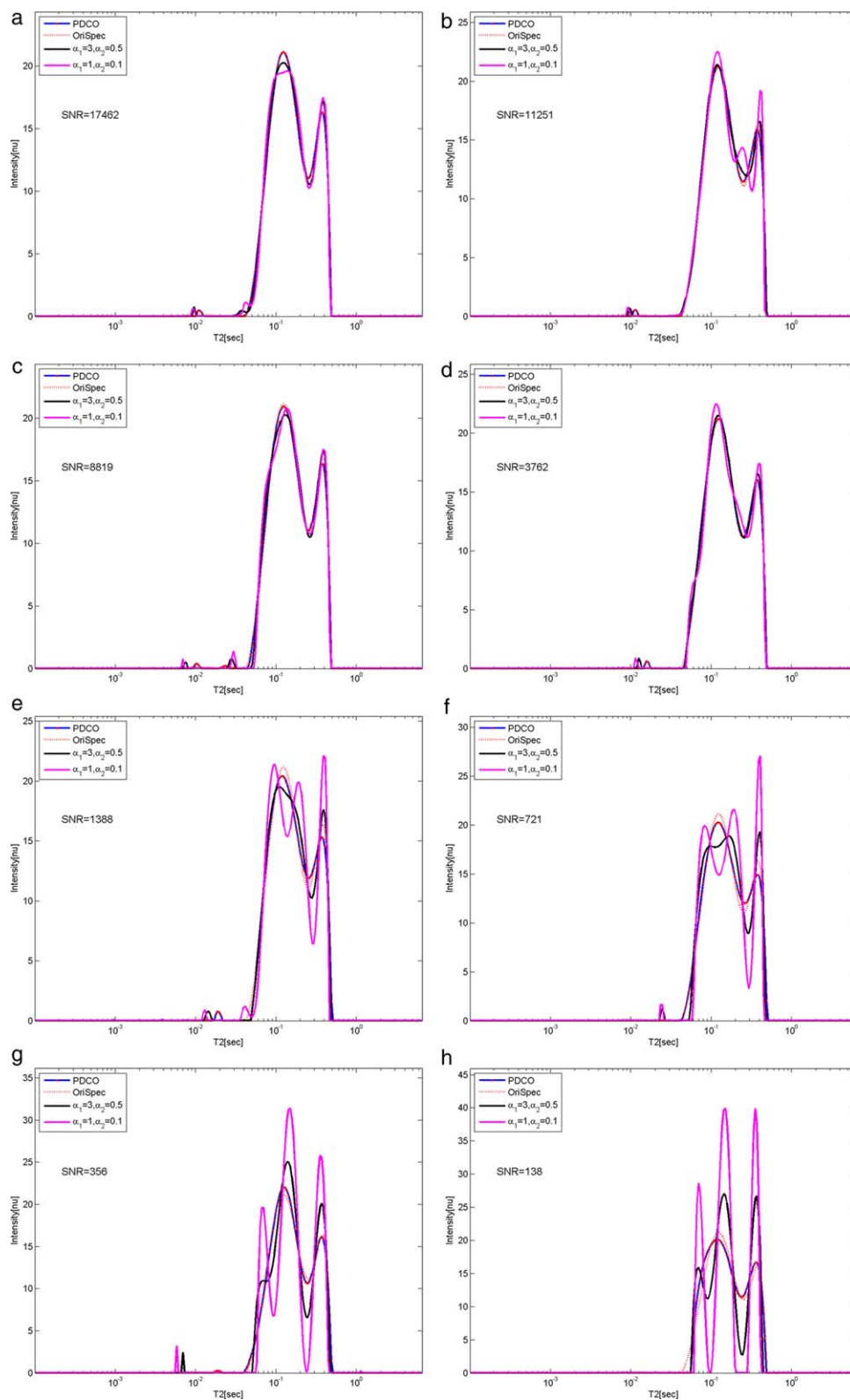
Figure 2 Comparison of representative PDCO analyses of the broad-peak signal simulations, using the universal regularization values for α_1 and α_2 (PDCO), the original simulated signal (OriSpec), and two less conservative choices for these parameters. The results are ordered by descending SNR values (a)–(h). The original noise-free simulated spectrum is shown for reference.

Figure 3 Comparison of representative PDCO analyses of Signal 1 simulations with wide peaks, using the universal regularization values for α_1 and α_2 (PDCO), the original simulated signal (OriSpec), and two less conservative choices for these parameters. The results are ordered by descending SNR values (a)–(h). The original noise-free spectrum is shown for reference.
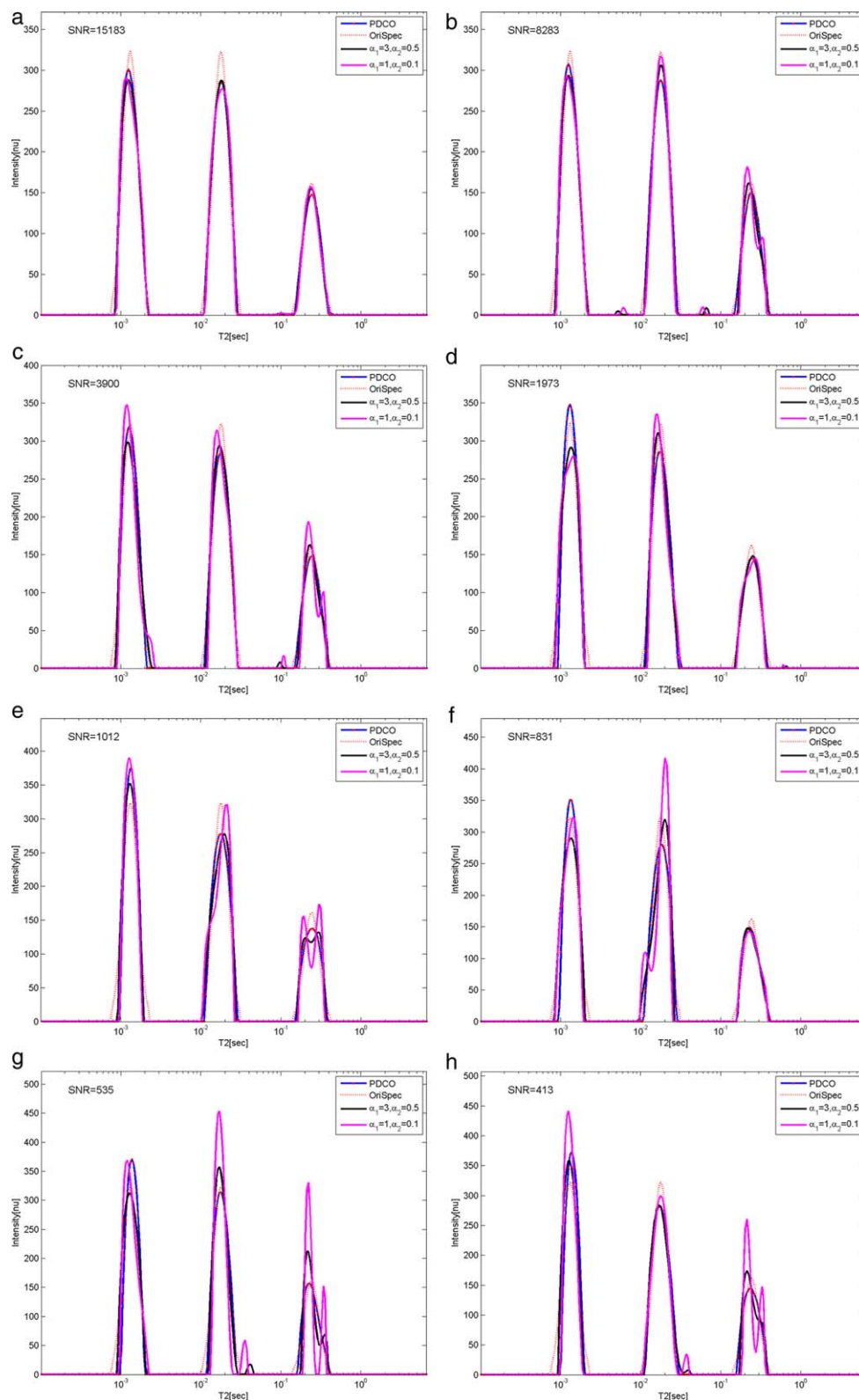
Table 2 Resolution Analysis of a Two-Peak Signal Simulation with Four Widths Depending on SNR

		Peak 1		Peak 2		Peak 3		Peak 4	
α_2		5	0.5	5	0.5	5	0.5	5	0.5
SNR									
10,000		1.61	1.48	1.61	1.61	1.76	1.76	1.92	1.92
1,000		1.92	1.61	1.92	1.61	1.92	1.76	1.92	1.92
100		2.28	1.76	2.28	1.76	2.28	1.76	2.49	1.92
50		2.71	1.76	2.28	1.92	2.28	2.28	2.28	1.92

regularization values for α_1 and α_2 (PDCO), PDCO with $\alpha_1 = 0$ and universal α_2 (PDCO-L2), and the WinDXP (WinDXP) solutions for four types of simulations and SNR values. Combined logarithmic plots of representative time-domain signals at different SNR values used for the comparison are shown in Figs. 5(a,b).

In the case of the wide-peak simulations, WinDXP and PDCO both solve relatively well [Figs. 4(m–p)]. The superiority of the PDCO solution over WinDXP is clearly demonstrated, especially for close and noisy signals. Based on the intrinsic T_2 values of the narrow simulated peaks, a noted decrease in resolution is to be expected only for SNR < 1,000 of the closest peaks simulation ($T_{22}/T_{21} = T_{23}/T_{22} = 2.47$). This is in excellent agreement with the resolution analysis. Interestingly, even for a high SNR signal of 18,829, WinDXP cannot resolve any of the close peaks, and instead results in a very wide distribution [Fig. 4(i)].

In addition, with the L_1 regularization term eliminated by setting $\lambda_1 = 0$, the PDCO results are significantly better than for WinDXP. This may be due to a more conservative choice of calibration of the WinDXP, but perhaps more to the superior accuracy and numerical stability of the PDCO solver. In the latter case, PDCO would be a preferred solver even for traditional L_2 regularization. It is also evident that the L_1 regularization term improves the quality of the reconstruction results especially for low SNR. On the other hand, it has no apparent additional contribution to the solution of broad-peak signal simulations beyond the L_2 term [Figs. 4(m–p)].

Despite introduction of the L_1 term, the conservative calibration of PDCO leads to peak broadening, even at high SNR values [e.g., Fig. 4(i)]. This can lead to inaccurate conclusions regarding the physical and/or chemical microstructure organization. Based on extensive simulations of different types of signals and noise realizations, we feel confident in suggesting that the calibration can be moderated when SNR is high to search for a more general truth. This is shown in the next section using an oil sample whose true distribution is unknown.

Comparison and Repeatability Analysis of WinDXP and PDCO Relaxation Time Distributions of a Real Rapeseed Oil Sample

Preliminary analysis of biological relaxation data acquired using LR-NMR is presented in Figs. 6(a–d and e–h) for WinDXP and PDCO, respectively. Here, a rapeseed oil sample was chosen as the model for comparison. The solutions are ordered by descending SNR values, based on the number of scans acquired (NS = 64, 32, 16, and 4, respectively). To test repeatability of results, measurements were separately acquired four times for each NS value. Combined logarithmic plots of representative time-domain signals at different SNR values used for the comparison are shown in Fig. 7.

Two other authors have presented broad-peak distributions, like the ones presented here for the WinDXP solutions [Figs. 6(a–d)] on pure avocado (22) and palm (23) oil samples. These were also analyzed using WinDXP. In contrast, the PDCO solutions have four distinct, moderately resolved peaks. As for this data, the original solution is unknown, these results raise the question of improved resolution versus the risk of introducing false peaks. To increase confidence in these results, we would like to point out several facts:

1. As previously shown, with the universal regularization values for α_1 and α_2 in PDCO on different types of simulations, no spurious peaks were introduced into the solution. More precisely, in Figs. 2(a–d), we presented the PDCO solutions of a broad-peak signal simulation whose SNR values closely meet those presented here. Based on these results, provided the broad-peak signal is the true signal, no peak splitting is to be expected in the solution.
2. In the case of under-regularizing, unstable solutions are to be expected in the form of spurious peaks that are due to random noise (as shown in Figs. 2 and 3). As can be seen, all four repetitions of the PDCO solutions, per and between NS values, are highly repeatable and stable.
3. From a physical point of view and in accordance with the resolution analysis, the minimum separation between peaks in the oil sample can in theory be accurately resolved for SNR > 1,000 (intrinsic T_2 values at 46, 114, 277, and 542 ms).

Based on these arguments, it is our belief that the PDCO formulation provides better resolved relaxation time distributions and more accurate solutions. Moreover, as it was shown that the universal calibration

27
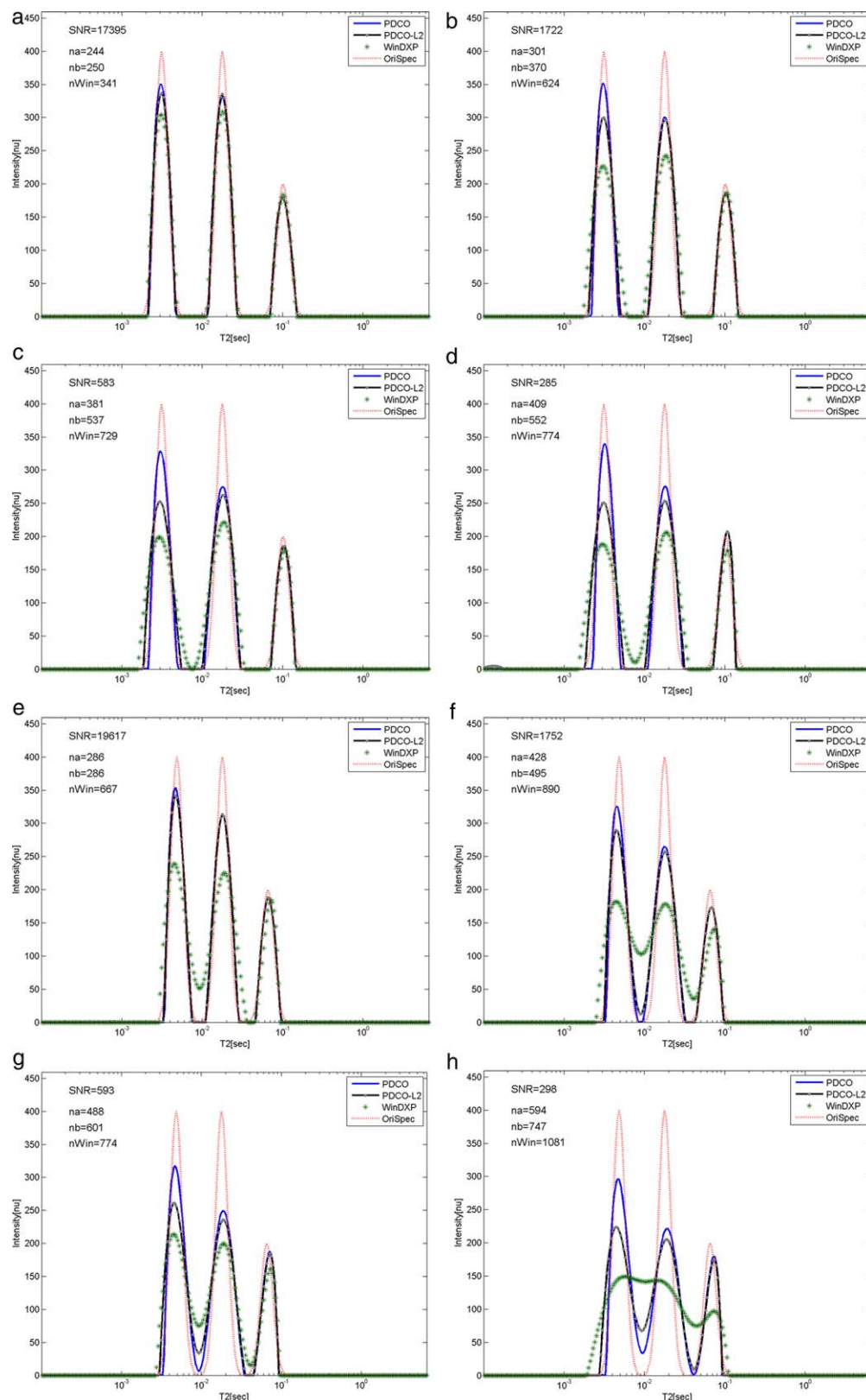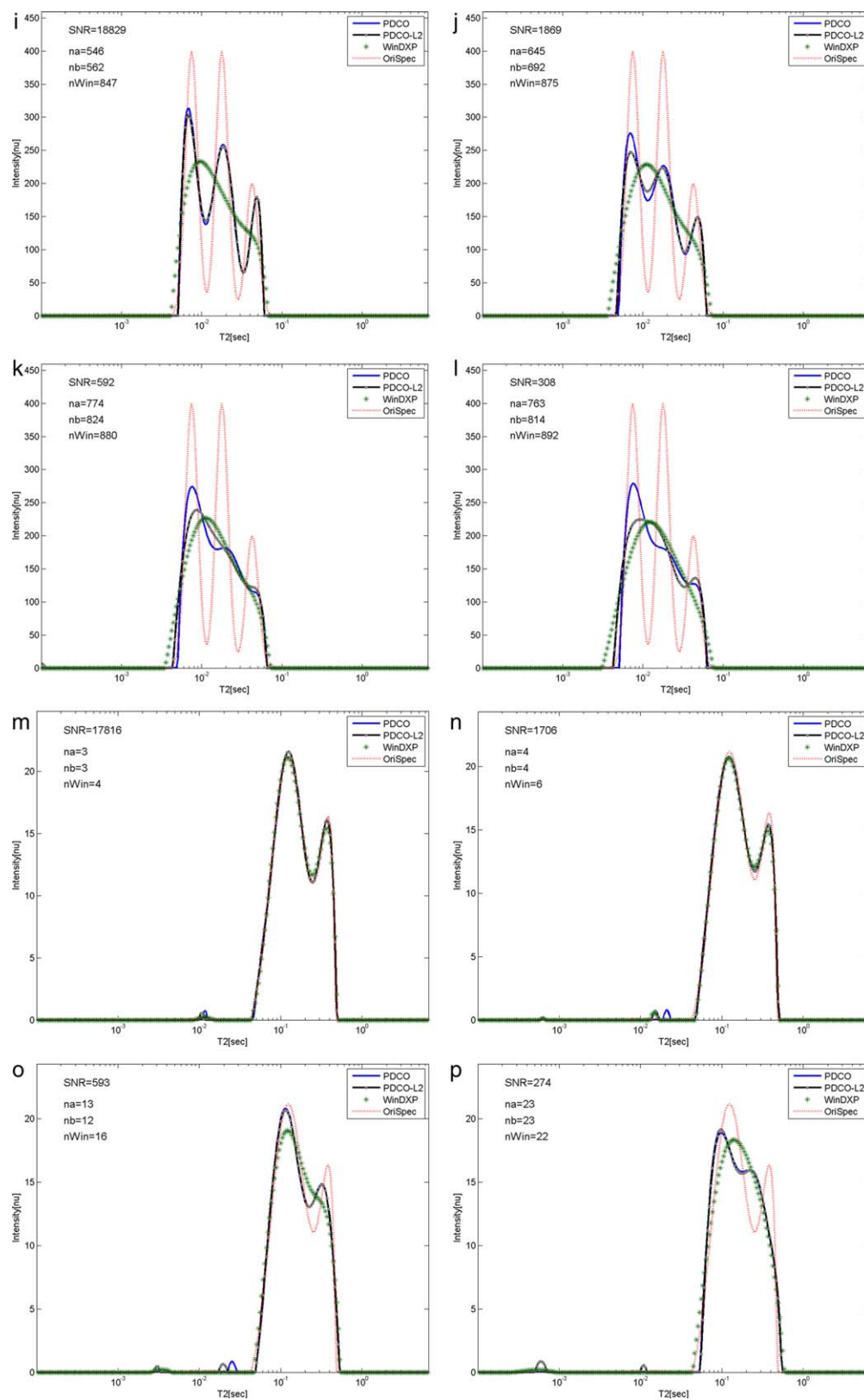
Figure 4   (Continued)

28

values of α_1 and α_2 introduce a broadening effect to originally narrow peaks, we wanted to explore the effect of using a more moderate value for α_2 (0.5) on the solution [Figs. 8(a–d) for decreasing SNR values]. We feel confident that the relatively high SNR values of the oil samples still allow us to remain in the safe zone in light of the risk of under-regularizing. As shown, the results are highly repeatable, even for the different SNR values, and look very similar to those analyzed using the more conservative α_2 value, in that no splitting or spurious peaks appear in the distribution.

Assuming that the PDCO solution for the rapeseed oil sample is more accurate than the accepted WinDXP one, an explanation for the different peaks is still needed. Their assignment is not an obvious task, as several authors struggled with this question even for the bimodal distribution, and did not provide a conclusive answer. Marigheto et al. (*24*) speculated that it arises from molecules of differing mobility, such as the oleic and palmitic constituents, or from nonequivalent proton pools of different mobility, such as those on methyl and olefinic groups. Adam-Berret et al. (*25*) suggested that this may be due to inhomogenous relaxation rates for the protons along the side chains or inhomogenous organization of the triacylglycerols in the liquid with intermolecular interactions. We intend to address this question and already initiated a thorough research plan in this area using the new PDCO algorithm. However, it is not in the scope of the current work and will be explored in a separate publication.

Stability Analysis

A stability comparison of the relaxation time distributions calculated by the PDCO algorithm according to the coefficients determined by calibration ($\alpha_1 = 10$; $\alpha_2 = 5$), less conservative PDCO algorithm ($\alpha_2 = 0.5$), and WinDXP on the oil sample is shown. Data were analyzed using the four repetitions acquired using 4, 16, 32, and 64 scans. The comparison of the numerical
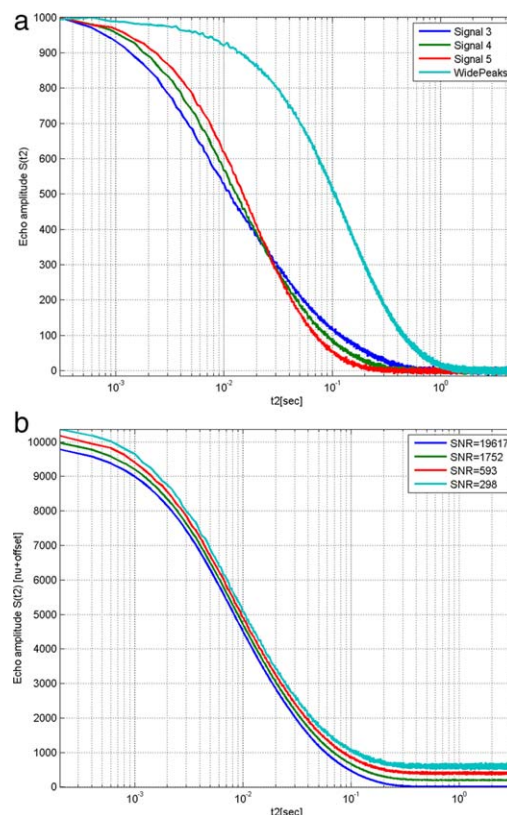
Figure 5 Logarithmic plots of the combined time-domain signals shown in Fig. 4 for (a) an SNR value of ~300 (the echo amplitude of each signal was normalized to its highest value for simplicity of comparison) and (b) four different SNR values for Signal 4 (an offset was added to each relaxation curve for simplicity of comparison).

stability of the two algorithms based on these results is shown in Table 3.

As can be seen, both algorithms are highly stable for all cases except one where the mean cv exceeds the 15% maximum threshold determined for acceptable stability. Furthermore, mean cv lower than 10% was found for the two cutoff values and all NS for PDCO

Figure 4 A: Comparison of representative simulation analyses using the PDCO universal regularization values for α_1 and α_2 (PDCO), PDCO with $\alpha_1 = 0$ and universal α_2 (PDCO-L2), and the WinDXP (WinDXP) solutions. Relaxation time distributions for the narrow-peak simulations Signal 3 and Signal 4 are ordered by descending SNR values (a)–(d) and (e)–(h), respectively. The original noise-free simulated spectrum is shown for reference. na, nb, and nWin are the norm of the error relative to the known solutions for the PDCO, PDCO-L2, and WinDXP analyses, respectively. B: Comparison of representative simulation analyses using the PDCO universal regularization values for α_1 and α_2 (PDCO), PDCO with $\alpha_1 = 0$ and universal α_2 (PDCO-L2), and the WinDXP (WinDXP) solutions. Relaxation time distributions for the narrow-peak simulations Signal 5 and the broad-peak signal are ordered by descending SNR values (i)–(l) and (m)–(p), respectively. The original noise-free simulated spectrum is shown for reference. na, nb, and nWin are the norm of the error relative to the known solutions for the PDCO, PDCO-L2, and WinDXP analyses, respectively.
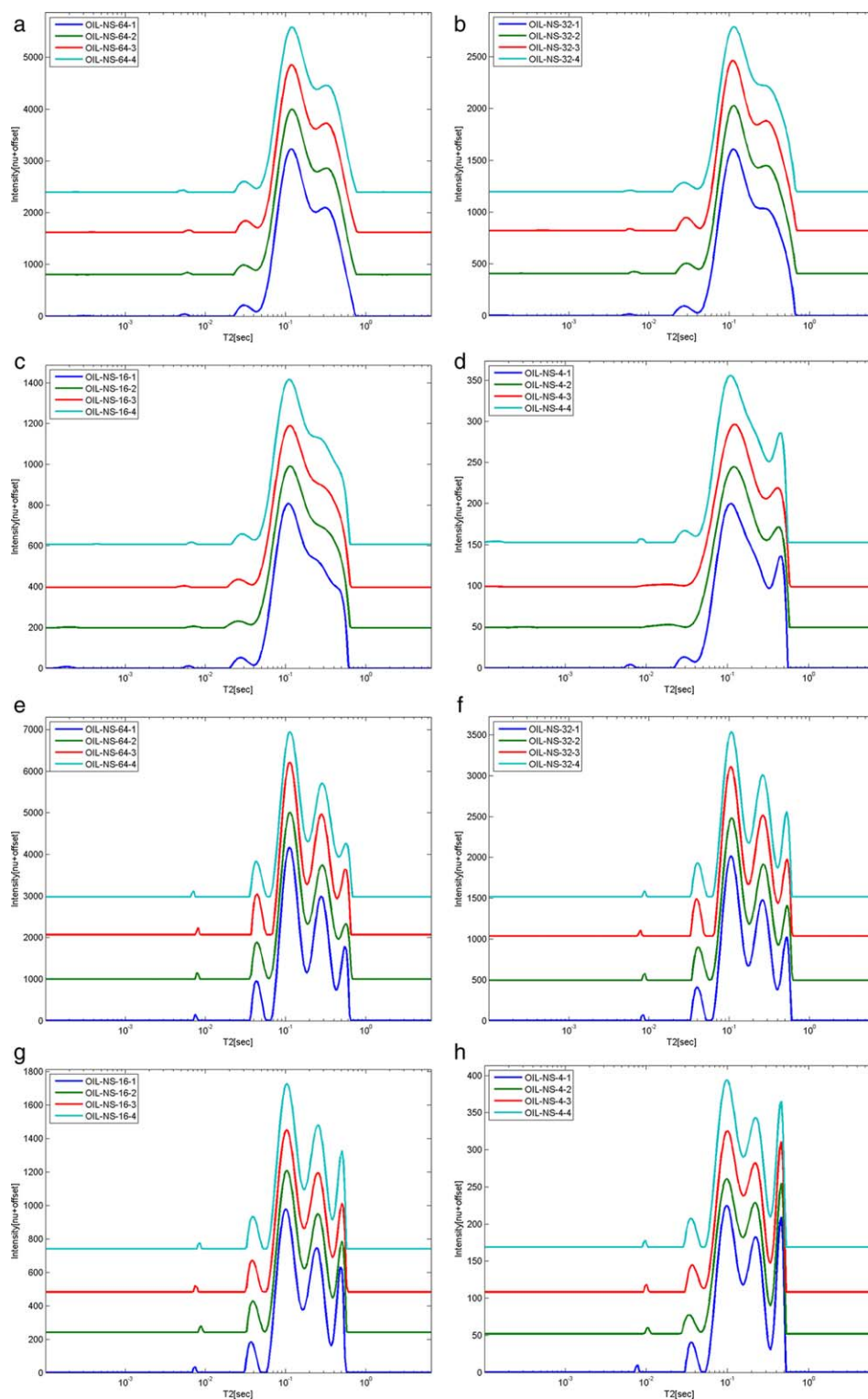
Figure 6 Comparison of WinDXP (a)–(d) and PDCO using the universal regularization values for α_1 and α_2 (e)–(h) solutions on a real LR-NMR dataset acquired from an oil sample. The results are ordered by descending number of scans (descending SNR).
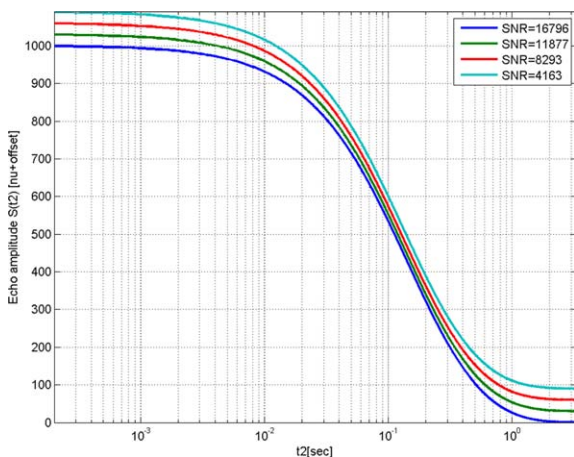
Figure 7 Logarithmic plot of the combined time-domain signals of a rapeseed oil sample acquired using 64, 32, 16, and 4 scans. For each NS value, only one representative signal and its SNR value are shown. The echo amplitude of each signal was normalized to its highest value, and an offset was added to each relaxation curve for simplicity of comparison.

Table 3 Comparison of the Stability of WinDXP and PDCO Using the Universal Regularization Values for α_1 and α_2 and PDCO with a Less Conservative Choice of α_2 Based on the Data Acquired on an Oil Sample

	Mean Coefficient of Variation That Exceeded the 25% Threshold			Mean Coefficient of Variation That Exceeded the 10% Threshold		
	WinDXP	PDCO	PDCO	WinDXP	PDCO	PDCO
α_2		5	0.5		5	0.5
NS						
4	3.8	3.6	5.0	7.2	6.7	10.9
16	2.4	6.6	13.3	2.9	8.0	20.0
32	1.7	4.1	7.5	2.2	5.6	13.7
64	1.4	5.7	5.8	1.7	7.2	10.5

The tabulated numbers are means of the cv_i that exceeded the 25% and 10% thresholds.
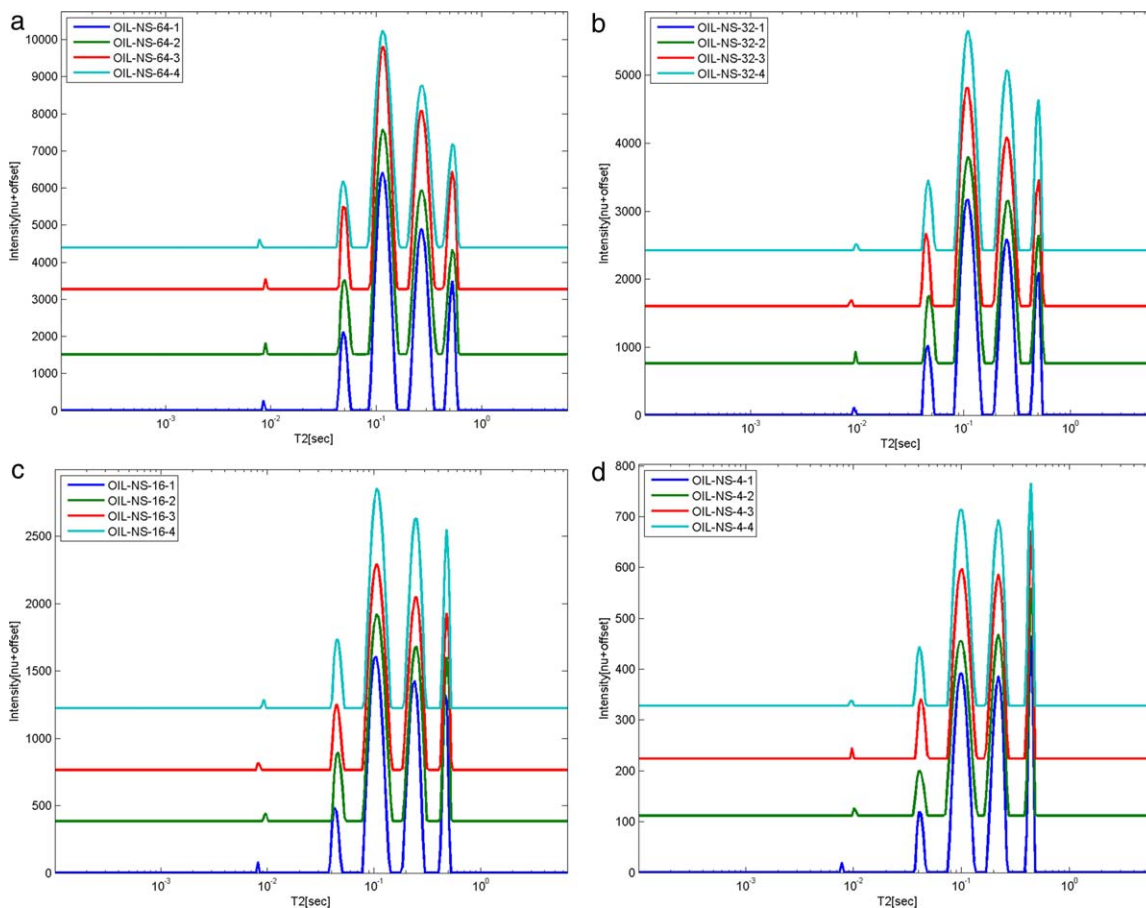
Figure 8 Relaxation time distributions analyzed using less conservative PDCO ($\alpha_2 = 0.5$) on the same real LR-NMR dataset acquired from a rapeseed oil sample. The results are ordered (a)–(d) by descending number of scans (descending SNR).

with universal α_1 and α_2. It is also shown that WinDXP has a slight advantage. This is probably due to the broad smooth distributions of the WinDXP when compared with the more resolved distributions of the PDCO, where small changes in the solutions are notably more pronounced in the cv parameter. As WinDXP smoothes the solution, it is substantially less prone to random changes that arise from noise in repetitions of the same signal. This same smoothing, however, leads to a large bias in the solution, as shown before for the reconstructed simulated signals.

It is worth noting that variability in the solutions may originate from instabilities in the acquired signals. From a preliminary experiment of signal acquisition using LR-NMR, we found that the PDCO algorithm is more sensitive to measurement imperfections than WinDXP. We concluded that in order to achieve high-quality repeatable results using PDCO, the offset frequency (O1) should be calibrated prior to each measurement, and the instrument should be allowed to stabilize between data acquisitions.

VI.   CONCLUSIONS

Effective solution of the inverse LR-NMR problem requires an integrated multidisciplinary methodology. Our proposed integrated approach, including validation of analyses by simulations, testing repeatability of experiments, and validation of the model and its statistical assumptions, has led to the development of an improved tool for analyzing LR-NMR relaxometry data. Improvement was achieved by 1) introducing an L_1 regularization term to the mathematical formulation, 2) adjusting and applying the accurate and numerically stable PDCO solver, and 3) choosing universal coefficients for the calibration based on extensive simulations with different types of signal and SNR values. We believe that this new methodology could be applied to the two-dimensional cross-correlation problem (*26,27*) to improve the peaks distortion problem mentioned by Venturi et al. (*28*).

ACKNOWLEDGMENTS

REFERENCES

1. Hills B, Benamira S, Marigheto N, Wright K. 2004. T_1–T_2 correlation analysis of complex foods. Appl Magn Reson 26:543–560.

2. Blümich B, Perlo J, Casanova F. 2008. Mobile single-sided NMR. Prog Nucl Magn Reson Spectrosc 52:197–269.

3. Kroeker RM, Henkelman RM. 1986. Analysis of biological NMR relaxation data with continuous distributions of relaxation times. J Magn Reson 69:218–235.

4. Carr HY, Purcell EM. 1954. Effects of diffusion on free precession in nuclear magnetic resonance experiments. Phys Rev 94:630–638.

5. Meiboom S, Gill D. 1958. Modified spin-echo method for measuring nuclear relaxation times. Rev Sci Instrum 29:688–691.

6. Istratov AA, Vyvenko OF. 1999. Exponential analysis in physical phenomena. Rev Sci Instrum 70:1233–1257.

7. Whittall KP, MacKay AL. 1989. Quantitative interpretation of NMR relaxation data. J Magn Reson 84:134–152.

8. Graham SJ, Stanchev PL, Bronskill MJ. 1996. Criteria for analysis of multicomponent tissue T_2 relaxation data. Magnet Reson Med 35:370–378.

9. Moody JB, Xia Y. 2004. Analysis of multi-exponential relaxation data with very short components using linear regularization. J Magn Reson 167:36–41.

10. Nocedal J, Wright SJ. 2006. Numerical Optimization, 2nd edition. New York: Springer.

11. Chen SS, Donoho DL, Saunders MA. 2001. Atomic decomposition by basis pursuit. SIAM Rev 43:129–159.

12. Elad M. 2010. Sparse and Redundant Representations: From Theory to Applications in Signal and Image Processing. Heidelberg: Springer.

13. Saunders MA, Bunggyoo K, Chris M, Santiago A. PDCO: primal-dual interior method for convex objectives. Available at: http://www.stanford.edu/group/SOL/software/pdco.html. [Website accessed April 2012].

14. Golub GH, Van Loan CF. 1996. Matrix Computations, 3rd edition. Baltimore, MD: The Johns Hopkins University Press.

15. Song YQ. 2007. Resolution and uncertainty of Laplace inversion spectrum. Magn Reson Imaging 25:445–448.

16. Hastie T, Tibshirani R, Friedman JH. 2001. The Elements of Statistical Learning. New York: Springer.

17. Prange M, Song YQ. 2009. Identifying uncertainty in NMR T_2 spectra using Monte Carlo inversion. J Magn Reson 196:54–60.

18. Zhou Y, Zhuang X. 2006. Robust reconstruction of the rate constant distribution using the phase function method. Biophys J 91:4045–4053.

19. Herrholz E, Teschke G. 2010. Compressive sensing principles and iterative sparse recovery for inverse and ill-posed problems. Inverse Probl 26:125012.

20. Saunders MA. 2011. PDCO: primal-dual interior methods, Notes 7. Available at: http://www.stanford.edu/class/msande318/notes.html. [Website accessed February 2013].

21. WinDXP Toolbox. Software release version 1.8, 2006. Distributed EXPonential Analysis. Witney, UK: Oxford Instruments.

22. Marigheto N, Duarte S, Hills B. 2005. NMR relaxation study of avocado quality. Appl Magn Reson 29:687–701.

23. Assifaoui A, Champion D, Chiotelli E, Verel A. 2006. Characterization of water mobility in biscuit dough using a low-field ^{1}H NMR technique. Carbohydr Polym 64:197–204.

24. Marigheto N, Duarte S, Hills B. 2005. NMR relaxation study of avocado quality. Appl Magn Reson 29:687–701.

25. Adam-Berret M, Boulard M, Riaublanc M, Mariette F. 2011. Evolution of fat crystal network microstructure followed by NMR. J Agric Food Chem 59:1767–1773.

26. Song YQ, Venkataramanan L, Hürlimann M, Flaum M, Frulla P, Straley C. 2002. T_1–T_2 correlation spectra obtained using a fast two-dimensional Laplace inversion. J Magn Reson 154:261–268.

27. Mitchell J, Chandrasekera T, Gladden L. 2012. Numerical estimation of relaxation and diffusion distributions in two dimensions. Prog Nucl Magn Reson Spectrosc 62:34–50.

28. Venturi L, Woodward N, Hibberd D, Marigheto N, Gravelle A, Ferrante G, et al. 2008. Multidimensional cross-correlation relaxometry of aqueous protein systems. Appl Magn Reson 33:213–234.

BIOGRAPHIES

Paula Berman obtained her B.Sc. in Biotechnology Engineering in 2008 at Ben Gurion University of the Negev, Beer Sheva, Israel, and is currently a doctoral student at the Department of Environmental Engineering at the same institute. Paula's research is conducted under the supervision of Prof. Zeev Wiesman and involves development of new low-resolution NMR tools and their application to the field of biodiesel.

Ofer Levi received his PhD in Scientific Computing and Computational Mathematics from the Stanford University in 2004. Levi has been a lecturer in the Department of Industrial Engineering Management of Ben-Gurion University since 2004. Levi's main interests include mathematical and statistical modeling of physical systems, inverse problems, compressed sensing, signal and image processing, parallel and distributed computing, biologically inspired analysis methods, and physiological signal processing.

Yisrael Parmet is a senior lecturer at the Department of Industrial Engineering and Management of Ben-Gurion University. He holds a B.A. in Economics and Statistics and M.Sc. and Ph.D. degrees in statistics from the Tel-Aviv University. He specializes in area design of experiments and statistical modeling. During his studies for a master and doctorate degrees, he served as research assistant at the statistical laboratory at the Department of Statistics and OR, Tel Aviv University, which granted him knowledgeableness in practical data analysis. In 2007–2008, Parmet was a visiting professor at Department of Dermatology and Cutaneous Surgery in the UM Miller School of Medicine.

Michael Saunders specializes in numerical optimization and matrix computation. He is known worldwide for his contributions to mathematical software, including the large-scale optimization packages MINOS, SNOPT, SQOPT, PDCO, and the sparse linear equation solvers SYMMLQ, MINRES, MINRES-QLP, LUSOL, LSQR, and LSMR. He is a research professor at Stanford University in the Department of Management Science and Engineering (MS&E) and a core member of the Systems Optimization Laboratory (SOL) and the Institute for Computational and Mathematical Engineering (ICME). In 2007, he was elected Honorary Fellow of the Royal Society of New Zealand, and in 2012, he was inducted into the Stanford University Invention Hall of Fame.

Zeev Wiesman is an expert in plant lipid biotechnology. His research group studies are focused on advanced multispectral technologies development including low-resolution NMR and mass spectrometry for monitoring, evaluation, and prediction modeling of biomass feedstocks and processes most relevant for biofuels industry. In the past 20 years, he has published about 100 manuscripts, chapters in books, a book, and patents. He is heading an Interdisciplinary Energy Engineering program of research students at Faculty of Engineering Sciences at Ben Gurion University of the Negev, Beer Sheva, Israel.

2.2. **Berman P**, Nizri S, Parmet Y, Wiesman Z: Large-scale screening of intact castor seeds by viscosity using time-domain NMR and chemometrics. J Am Oil Chem Soc 2010, **87:**1247–1254.

ORIGINAL PAPER

Large-Scale Screening of Intact Castor Seeds by Viscosity Using Time-Domain NMR and Chemometrics

Paula Berman · Shahar Nizri · Yisrael Parmet · Zeev Wiesman

Abstract Castor is one of the most promising non-edible oil crops, due to its high oil content and since it can be grown on marginal lands and in a semi-arid climate. However, the high content of ricinoleic acid results in an extremely high viscosity of castor-based biodiesel. In this study, we report on the development of a rapid and non-destructive method for large-scale screening of intact castor seeds according to their viscosity by time domain NMR and chemometrics. A qualitative principal component analysis model was constructed, where each observation was assigned to a different viscosity group. This model straightforwardly detects desirable outliers, and can also be applied for detection of other transgenic oilseeds, especially those containing small levels of hydroxylated fatty acid.

Keywords Time-domain NMR · Castor oil · Biodiesel · PCA · Chemometrics

Introduction

Biodiesel offers a viable alternative to petroleum-based diesel fuel. However, large-scale production of biodiesel

P. Berman · S. Nizri · Z. Wiesman (✉)
The Phyto-Lipid Biotechnology Lab,
Department of Biotechnology Engineering,
The Institutes for Applied Research,
Ben-Gurion University of the Negev, P.O. Box 653,
84105 Beersheba, Israel
e-mail: wiesman@bgu.ac.il

Y. Parmet
Department of Industrial Engineering and Management,
Ben-Gurion University of the Negev, P.O. Box 653,
84105 Beersheba, Israel

from edible-grade oils (>95%) can lead to imbalance in the global food market [1]. Land availability is another core limitation. Therefore, other oilseeds are currently being researched as alternative feedstocks.

Castor (*Ricinus communis* L.) is one of the most promising non-edible oil crops, with an annual seed production of 1.14 Mt and an average seed yield of 902 kg/ha [2]. Compared to other conventional oil crops, castor plants can grow on marginal lands and in a semi-arid climate. Castor oil consists mainly of ricinoleic acid (12-hydroxy-*cis*-9-octadecenoic acid). The high content of this hydroxylated fatty acid (FA) gives castor-based biodiesel unique physical properties such as a favorably high calorific value and cetane number and a low iodine number of less than 90. On the other hand, castor oil is adversely characterized by high hygroscopicity [3]. Nevertheless, extremely high viscosity remains the main barrier for its use as a fuel. Neat castor biodiesel viscosity was found to reach 13.75 mm^2/s, much larger than the ASTM limit of 6 mm^2/s [3].

Genetic breeding programs have introduced new alternatives for the biodiesel industry. These programs aim at increasing the oil content of the seeds and modifying their FA composition to gain high quality and profitable yields [4]. In the case of castor oil, reduced levels of ricinoleic acid will lead to reduced biodiesel viscosity [5], possibly meeting the ASTM limits. Rojas-Barros et al. [6] were able to identify a natural castor mutant with very high oleic acid (18.9%) and low ricinoleic acid content (71.4%). This exceptional mutant, showing reduced viscosity, might be more suitable as a biodiesel feedstock than conventional castor seeds. Screening of oilseeds, as in the Rojas-Barros study, was conducted by standard analytical methods, which are considered exhaustive and environmentally unfriendly. Screening thousands of samples as required for genetic

breeding programs with these methods is not realistic. An alternative rapid method is therefore required.

TD-NMR is a rapid and non-destructive technology that can be implemented for large-scale screening of intact oilseeds. TD-NMR experiments involve excitation of hydrogen protons in the presence of a constant magnetic field, and acquisition of signal intensities as these relax back to equilibrium. One typical pulse sequence, called CPMG [7, 8], consists of a single 90° pulse followed by multiple consecutive 180° pulses, which allows transverse relaxation to take place. This test can be applied for measuring some qualitative aspects of a sample, since the shape of the signal acquired through time is characteristic of its physical state. The CPMG sequence involves acquisition of thousands of data points per sample. Analysis of these huge datasets requires advanced statistical tools, known as chemometrics. Chemometrics include the application of multivariate statistics, mathematics, and computational methods to chemical measurements to enhance the productivity of chemical experimentation.

Recently, Prestes et al. [9] predicted the viscosity of different oilseeds using TD-NMR and partial least square analysis (a common chemometric tool). Yet castor was excluded from this model due to its unique FA composition. Quantitative prediction of viscosity, however, fails in portraying relations between observations. Pedersen et al. [10] constructed a 2D scatter plot using principle component analysis (PCA), which distinguished between rape and mustard seeds and between dried and fresh seeds from each family. This graphical representation can offer insights otherwise overlooked, especially for large-scale screening, including detection of outliers and groupings [11]. PCA provides a map-like representation, where all observations are scaled according to one (line plot) or two (scatter plot) axes. Classification with this method, however, can only be determined intuitively according to one's judgment. K-means, a clustering algorithm [12], complements this method to achieve impartial sorting.

In this study, a qualitative chemometric model is suggested for rapid large-scale screening of castor seeds according to viscosity. Viscosity was calculated from the FA composition using GC, assuming varieties showing reduced levels of ricinoleic acid will also show reduced castor-based biodiesel viscosity. Lower viscosity will lead to a measurable change in decay rates relative to the position of a sample in a PCA plot. Classification of observations into three viscosity clusters was performed using k-means. The model was first developed for mustard seeds, which show high natural FA variability, and was later applied to the screening of castor seeds.

Experimental Procedure

Materials

Chemicals

All chemicals and reagents used in this study were analytical grade. GC standard rapeseed oil was purchased from Supelco (Bellefonte, PA, USA).

Plant Material

Twenty varieties of mustard seed (M1–M20) were purchased from local suppliers in Israel. Castor seeds were obtained from the international seed bank (US) in 2009, and included 175 varieties from all over the world. Thirty seeds were randomly chosen for building the screening model (C1–C30).

Methods

TD-NMR Measurements

Prior to measurement, the seeds were oven dried at 70 °C for 72 h to remove excess moisture. TD-NMR experiments were performed on a Maran bench-top pulsed NMR analyzer (Resonance Instruments, Witney, United Kingdom), equipped with a permanent magnet and a 18-mm probe head, operating at 23.4 MHz. The seeds were equilibrated at 40 °C for 30 min before measurement. The CPMG sequence was performed using a 90° pulse width of 6.2 μs, echo time (τ) of 0.1 ms, recycle delay of 1 s, and 4 scans. For each sample, 8,000 echoes were acquired.

Oil Extraction

About 3 g of seeds were crushed manually in a mortar and incubated overnight with 100 mL of hexane in an orbital shaker at 25 °C. The oil and hexane solution was then evaporated under a mild vacuum with a rotary evaporator. In cases where larger volumes of oil were required (>10 mL), a cold-pressed extruder was used (Komet CA 59G, Mönchengladbach, Germany).

Viscosity Calculations

The FA composition of the seeds was determined by GC on a Varian 3400 apparatus (Palo Alto, CA, USA), equipped with a flame ionization detector and a capillary column (RESTEK, Bellefonte, PA, USA; Dimensions: 15 m × 0.32 mm × 0.25 μm). Results were normalized to 100% with less than 3% unidentified FAs. The composition was then used to calculate the kinematic viscosity, as described

Table 1 Kinematic viscosities of neat FA methyl esters [14]

Structure	Systematic name	Kinematic viscosity (mm^2/s)	Structure (cont.)	Systematic name	Kinematic viscosity (mm^2/s)
14:0	Myristic acid	3.23	20:0	Arachidic acid	5.85[a]
16:0	Palmitic acid	4.38	20:1	Eicosenoic acid	5.77
16:1	Palmitoleic acid	3.67	22:0	Behenic acid	5.85[a]
18:0	Stearic acid	5.85	22:1	Erucic acid	7.33
18:1	Oleic acid	4.51	24:0	Lignoceric acid	5.85[a]
18:2	Linoleic acid	3.65	24:1	Nervonic acid	8.8[b]
18:3	Linolenic acid	3.14	18:1-OH	Ricinoleic acid	15.44

[a] Allen et al. (1999) [13]

[b] Through personal correspondence with Dr. G. Knothe; data not published

by Allen et al. [13] using Eq. 1. μ_i and μ_0 are the kinematic viscosities at 40 °C of each FA and biodiesel, respectively; y_i is the mass fraction of each FA. Neat FA viscosities, given as fatty acid methyl esters (FAMEs), were taken from [14], and are listed in Table 1.

$$\ln \mu_0 = \sum_{i=1}^{n} y_i \ln \mu_i. \tag{1}$$

Mustard and castor oil contain minor levels of arachidic (20:0), behenic (22:0), and lignoceric (24:0) FAs, which are solid at 40 °C. Their neat viscosities were assumed to have values similar to those of stearic acid (18:0), as suggested by Allen et al. [13]. Nervonic (24:1) acid viscosity could not be found in the literature, thus was extrapolated (8.8 mm^2/s; see Table 1 remarks). The accuracy of the method, following these assumptions, was validated using the ASTM D445 standard method (performed at ICT laboratories, Israel) by comparing measured and calculated viscosities. A 20-mL specimen of the oil were transesterified as described by Dorado et al. [15] for mustard oil and Meneghetti et al. [16] for castor oil. Measured and calculated viscosities were identical for mustard oil (5.53 mm^2/s) and accurate for castor oil (12.68 and 12.78 mm^2/s, respectively), confirming the use of the FAME profile to calculate viscosity. Calculated viscosities are given as triplicates in Table 2 for mustard seeds and Table 3 for castor (STD was less than 0.1 and 0.3, respectively).

Chemometrics

All chemometric calculations were performed using STATISTICA (version 8.0, StatSoft). PCA is a common chemometric tool, mainly used to reduce data dimensionality [17]. The algorithm maximizes the original variance using a minimal number of principal components (PCs). The PCs are mutually orthogonal and their extraction is such that the first PC holds the maximum variance, the

Table 2 Average T_2, w_0 and viscosity of 20 mustard seeds

Sample	T_2 (ms)	M_0	Viscosity (mm^2/s)	Cluster[a]
M1	155.46	826.14	4.59	L
M2	131.77	803.86	5.53	H
M3	146.02	796.50	4.82	L
M4	133.97	821.18	5.48	H
M5	135.93	850.46	5.39	H
M6	134.93	824.24	5.54	H
M7	137.69	831.14	5.44	H
M8	137.45	853.90	5.37	H
M9	153.17	804.85	4.59	L
M10	146.09	808.86	5.15	M
M11	147.29	829.37	5.18	M
M12	138.79	846.72	5.30	M
M13	134.90	837.37	5.50	H
M14	135.71	851.52	5.45	H
M15	135.70	825.76	5.47	H
M16	138.35	830.14	5.48	H
M17	153.03	824.18	4.83	L
M18	134.36	836.70	5.55	H
M19	137.07	828.08	5.41	H
M20	133.47	856.19	5.64	H

[a] The three categories were defined by k-means as: $5.08 > L$; $5.08 \leq M \geq 5.32$; $H > 5.32$ mm^2/s

second holds the second-maximum variance, and so on. The general mathematical model can be described by Eq. 2, where **X** is the transverse TD-NMR relaxation data ($I \times J$), **P** contains the underlying profiles ($J \times N$; called loadings), and **T** is the contributing amplitude ($I \times N$; called scores).

$$\mathbf{X} = \mathbf{T} \cdot \mathbf{P}^{T} + \mathbf{E}. \tag{2}$$

The scalar N is the number of PCs resolved and **E** ($I \times J$) holds the residual unexplained variation. PCA was

Table 3 Average viscosity of 21 castor seeds used for building the screening model and 9 seeds used for validation

Sample	Viscosity (mm²/s)	Cluster[a]	Sample (cont.)	Viscosity (mm²/s)	Cluster[a]	Sample (cont.)	Viscosity (mm²/s)	Cluster[a]
C1	12.39	H	C11	12.06	M	C21[b]	12.56	H
C2	12.12	M	C12[b]	12.08	M	C22	11.96	M
C3	12.00	M	C13	12.43	H	C23[b]	11.87	L
C4	12.26	H	C14[b]	12.36	H	C24	11.72	L
C5	11.85	L	C15	11.85	L	C25	11.90	L
C6	11.71	L	C16	12.23	H	C26	11.80	L
C7[b]	12.05	M	C17	12.33	H	C27	11.97	M
C8	12.34	H	C18[b]	12.38	H	C28[b]	11.83	L
C9	12.06	M	C19[b]	11.87	L	C29	11.67	L
C10	12.30	H	C20	12.37	H	C30[b]	12.13	M

[a] The three categories were defined by k-means as: $11.96 > L$; $11.96 \leq M \leq 12.20$; $H > 12.20$ mm²/s

[b] Used for validation

applied on the normalized CPMG data using the NIPALS algorithm. Normalization was performed by dividing the spectrum of each sample by its first (and highest) intensity and mean-centering it (covariance matrix). Only the scores of the first two PCs were extracted.

K-means is a fast iterative algorithm that has been extensively used for classification [12]. Defining three clusters yielded high, medium, and low viscosity clusters (H, M, and L, respectively). Clustering was applied to the calculated viscosities (Tables 2 and 3 for mustard and castor seeds, respectively) and the scores of PC$_1$ and/or PC$_2$. Observation assignment according to the calculated viscosity was considered the proper grouping.

T_2 Measurements

Assuming an exponential decay of the acquired CPMG data, a fixed number of pre-exponential weighting factors (w_i) and relaxation decay constants (T_{2i}) are extracted. T_{2i}s have been found to characterize and distinguish between populations (such as water and oil), and the pre-exponential weighting factors represent a quantitative measurement of each T_2 population [18].

The CPMG raw data were exponentially fitted using SPSS software (version 15.0, SPSS Inc.) and Eq. 3. w_i is the amplitude of the ith exponential, indicating the concentration of the ith component, and T_{2i} is the characteristic relaxation time constant.

$$W = \sum_{i=0}^{N} w_i \exp(-t/T_{2,i}) \tag{3}$$

The viscosity of oils is one order of magnitude greater than that of biodiesel [5], as can be realized from exploring their decay rates. T_2 of castor oil was approx. 40 ms, whereas for the corresponding biodiesel this was 230 ms.

Typically, the transverse relaxation time of solids is rapid and that of liquids is slow [18]. Triacylglycerols have lower mobility due to their more rigid structure, whereas biodiesels, which consist of individual FAMEs, have greater freedom of movement. Previously published findings about the inverse relation of T_2 and viscosity strengthen this result [9].

The oil in oil-containing materials usually follows a bi-exponential behavior, possibly due to the presence of saturated and unsaturated oil phases [19]. Given that viscosity is a property that stems from all of the oil components, only a single exponential was used in this study. T_2 and w_0 of mustard seeds are shown in Table 2 as triplicates. The broader range of T_2s compared to castor (133–156 and 43–46 ms, respectively; data not shown for castor) emphasizes the initial assumption on the broad FA profile natural diversity in mustard.

Results and Discussion

Screening of Mustard Seeds

The score scatter plot of PC$_1$ (score of PC$_1$) and PC$_2$, holding 100% of the original variance, is shown in Fig. 1. Clusters were drawn according to the groupings assigned by k-means, using both scores. Ascription of observations to the appropriate cluster was not in good agreement with the real viscosity categories listed in Table 2. For example, M10 and M20 were clustered together though they were assigned to different calculated viscosity categories (M and H, respectively). Repeating k-means calculations using only PC$_2$ as the active input yielded similar groupings as the reference data (Fig. 2), with only two misclassifications (M3 and M13). This indicates PC$_2$ holds information about
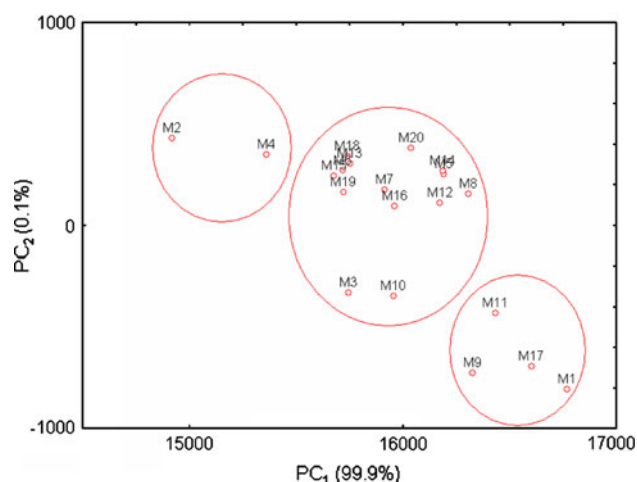
Fig. 1 PCA score scatter plot of 20 mustard seeds, clustered to three groups by 2D k-means. The clusters were not correlated to viscosity
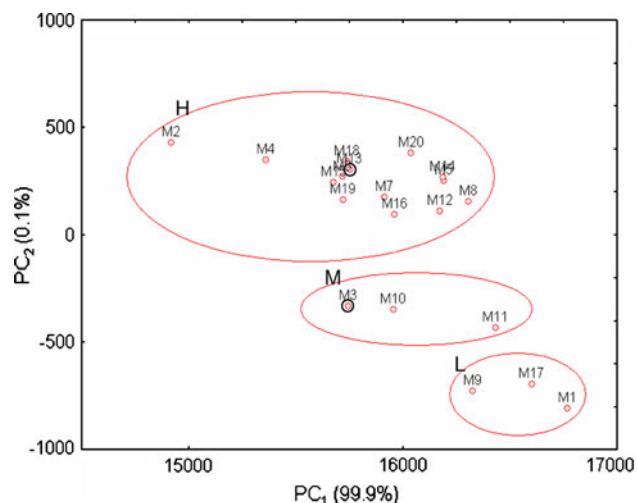
Fig. 2 PCA score scatter plot of 20 mustard seeds, clustered to three groups by 1D k-means with PC_2 as a single input. The new clusters were highly correlated to viscosity, with only two misclassifications (*circled* cases M3 and M13)

viscosity, meaning high score represents high viscosity and vice versa; whereas PC_1, though holding most of the variance (99.9%), was immaterial for screening by viscosity.
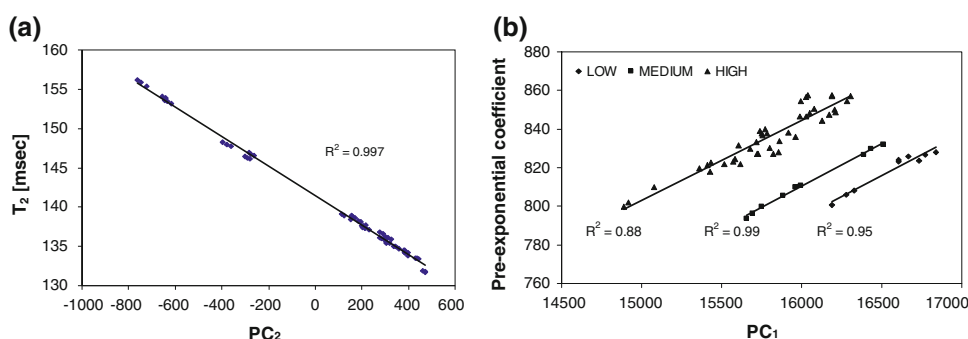
A possible explanation for the two misclassifications may be their greater water content relative to the other seeds, which has been shown to lead to longer decay rates [10, 19].

Despite the fact that T_2 is extracted using exponential fitting while PC_2 is strictly a linear transformation of the data with no model constrains, they were found to be closely linked ($R^2 = 0.99$; Fig. 3a). Another interesting finding was the correlation of PC_1 to the pre-exponential coefficient w_0 according to each viscosity group, as shown in Fig. 3b ($R^2 = 0.88$, 0.99, and 0.95 for H, M, and L categories, respectively). w_0 was previously found to correlate to quantitative aspects such as oil content [20], when divided by the weight. This interpretation was true only when scaling the raw NMR data of each observation by its first value. Therefore, it is our assumption that by scaling the NMR data by the first value, PC_2 can be used as a viscosity marker.

Since PC_1 was found to only interfere with data interpretation, as previously suggested, observations were plotted against PC_2 in a 1D line plot (Fig. 4). This is a different representation of the same scores, leading to identical viscosity clusters as in Fig. 3. The same three clusters are now separated by linear thresholds as defined by k-means (L ≤ -520; $-520 < $ M ≤ -148; and H > -148). Mapping of observations using a line plot coupled with k-means was chosen as the preferred screening model. The same methodology was then applied on castor seeds.

Screening of Castor Seeds

The thirty castor seeds that were chosen to represent high, medium, and low viscosity in order to develop a similar screening model are shown in Table 3. This batch was further divided into 21 and 9 samples for constructing and validating the model, respectively. The three viscosity regions ($-40 > $ L; $-40 \leq$ M ≤ 60; and H > 60) as defined by k-means with PC_2 as classification criteria are shown in Fig. 5. Only one misclassification was detected (C22; 11.96 mm²/s), probably since it lies on the border between clusters L and M in Table 3. The performance of

Fig. 3 A strong linear correlation was found between **a** PC_2 and T_2, and **b** PC_1 and M_0, for each viscosity cluster. Results are presented for each measurement and not as triplicates
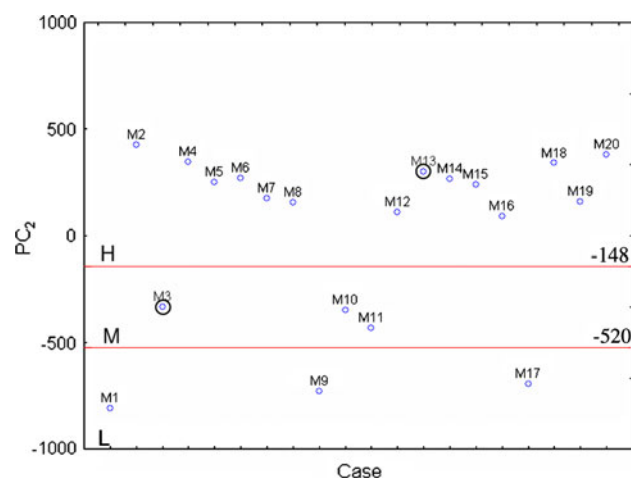
Fig. 4 Line plot of mustard seeds divided into three viscosity regions (L, M, H) by PC_2. Only two misclassifications were found (*circled* cases M3 and M13)
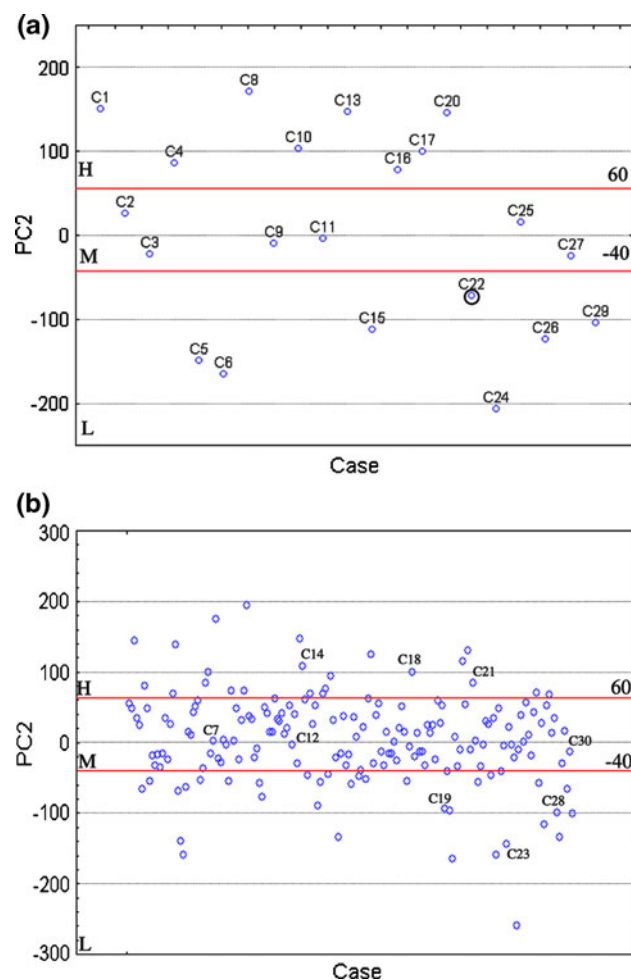
Fig. 5 Line plot of **a** 21 castor seeds divided into three viscosity regions (L, M, H) by PC_2. Only a single misclassification was detected (*circled* case C22); **b** 175 seeds used in this study, with nine samples used for validation, without misclassifications

the model was validated using the remaining nine samples without any misclassifications (marked in Fig. 5b, which shows all of the seeds), emphasizing its accuracy. As in the case of mustard, T_2 and PC_2 were highly correlated ($R^2 = 0.99$; data not shown), indicating that the interaction between these parameters is not limited to a specific family of oilseeds.

According to the screening model proposed here, unique castor seeds with low viscosity will be easily observed at the lowest end of this line plot—the lower its PC_2 score, the lower its viscosity. Unfortunately, among the 175 types of castor seeds from all over the world, no samples were found to comply with the standard viscosity specification.

Mustard and Castor Mixed Model

The FA composition and calculated viscosity of three characteristic seeds, one for each viscosity cluster, from each variety, along with a mixture of these seeds (CM2, CM4, and CM6) are shown in Table 4. CM samples consist of 2 g mustard seeds with varying quantities of castor seeds, i.e. CM4 consists of four castor seeds and 2 g of mustard seeds. Since we were not able to obtain low viscosity castor seeds, measuring this type of mixture provided a simple simulation of reduced ricinoleic acid content. The relation between the level of the dominant FA content and viscosity is also pointed out in Table 4. The main FAs in castor and mustard seeds are ricinoleic and erucic acids, respectively. The greater their relative content the greater the viscosity. This is due to their increased viscosities in relation to all other FAs (Table 1). When exploring each type of seed it can be observed that a decrease of 6.7% in ricinoleic acid content in castor seeds reduces viscosity by 7% (C24 and C21, respectively), while the same 7% reduction of viscosity in mustard seeds (M10 and M18, respectively) is achieved only by decreasing the erucic acid levels by 35%. This can be explained by examining the neat FA viscosities of ricinoleic and erucic acids (15.44 and 7.33 mm^2/s, respectively; Table 1). Therefore, a moderate decrease in ricinoleic acid will lead to a sharp decrease in viscosity, which will be easily detected by the model.

A PCA line plot of all mustard, castor, and mixture samples is shown in Fig. 6. Here CM samples were positioned far below the neat castor seed array, confirming the feasibility of this method in easily detecting outliers with reduced viscosity. Furthermore, neat castor and mustard seed clustering remained unchanged compared to Figs. 5a and 6. These results emphasize the need for genetically modified castor seeds, since their FA composition's natural variability is quite low compared to that of mustard.

The model suggested here can also be used for screening transgenic seeds from established crops, containing elevated

Table 4 Characteristic FA composition of C, M, and CM from each viscosity category

Sample	Category[b]	FA composition[a] (%)								Average viscosity (mm²/s)
		16:0	18:0	18:1	18:1-OH	18:2	18:3	20:1	22:1	
M1	L	3.48	0.87	23.52	–	29.69	12.58	9.23	18.34	4.59
M10	M	3.15	1.24	11.00	–	19.59	15.19	7.07	37.77	5.15
M18	H	2.26	0.75	8.57	–	16.66	10.74	5.92	50.89	5.55
C24	L	2.12	2.04	8.10	78.86	7.37	0.72	0.78	–	11.72
C11	M	1.97	2.03	5.97	80.97	7.85	0.63	0.58	–	12.06
C21	H	1.64	1.51	2.99	84.13	7.60	1.07	0.53	–	12.56
CM2		2.79	1.53	10.34	11.81	12.55	9.16	6.27	42.78	6.28
CM4		2.29	1.34	8.29	26.32	10.34	7.00	5.14	35.97	7.34
CM6		2.26	1.58	7.93	40.08	9.68	5.94	3.99	26.18	8.22

[a] Only major FAs are shown

[b] According to the corresponding line plots
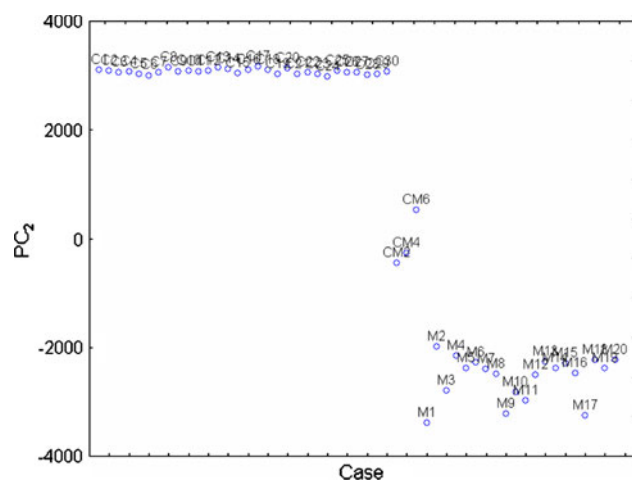
Fig. 6 Castor and mustard seeds from the previous models are plotted in a line plot along with CM mixed samples, simulating seeds with reduced ricinoleic acid content. Outliers with reduced viscosity are easily detected for a large batch of seeds

levels of hydroxylated FAs. Due to strict environmental regulations, sulfur content in petrodiesel has been significantly reduced. This has led to reduced fuel lubricity, which can cause severe damage to an engine [5]. Recent studies have shown that a blend of high oleic vegetable oil and castor oil (with 10–15% ricinoleic acid content) is an excellent feedstock for a variety of lubricant applications [21]. Developing transgenic oilseeds with moderate levels of hydroxylated FAs may answer this industry's need. Detection of transgenic seeds with elevated levels of hydroxylated FAs (and thus increased viscosity) can be easily achieved with the model proposed herein.

The main drawback of the suggested large-scale screening procedure is the extended pre-drying phase (72 h), given the contribution of water components to the acquired relaxation signal [9, 19]. One possible solution would be to employ a pulse sequence consisting of a combination of pulsed field gradient (PFG) and CPMG [22], thus eliminating contributions from water protons without the need for drying.

Conclusions

Rapid large-scale screening of intact castor seeds can be easily achieved using a combined TD-NMR and chemometrics approach. The model suggested in this work is superior to conventional analytical methods when screening thousands of seeds, since unique outliers showing reduced viscosity can be detected straightforwardly. The same approach can also be applied to screening within other types of oilseeds which differ in their FA profiles.

References

1. Gui MM, Lee KT, Bhatia S (2008) Feasibility of edible oil vs. non-edible oil vs. waste edible oil as biodiesel feedstock. Energy 33:1646–1653
2. Sailaja M, Tarakeswari M, Sujatha M (2008) Stable genetic transformation of castor (*Ricinus communis* L.) via particle gun-mediated gene transfer using embryo axes from mature seeds. Plant Cell Rep 27:1509–1519
3. Scholz V, da Silva JN (2008) Prospects and risks of the use of castor oil as a fuel. Biomass Bioenergy 32:95–100
4. Kinney AJ, Clemente TE (2005) Modifying soybean oil for enhanced performance in biodiesel blends. Fuel Process Technol 86:1137–1147
5. Knothe G, Steidley KR (2005) Kinematic viscosity of biodiesel fuel components and related compounds. Influence of compound structure and comparison to petrodiesel fuel components. Fuel 84:1059–1065

6. Rojas-Barros P, De Haro A, Muñoz J, Fernández-Martínez JM (2004) Isolation of a natural mutant in castor (*Ricinus communis* L.) with high oleic/low ricinoleic acid content in the oil. Crop Sci 44:76–80

7. Carr HY, Purcell EM (1954) Effects of diffusion on free precession in nuclear magnetic resonance experiments. Phys Rev 94:630–638

8. Meiboom S, Gill D (1958) Modified spin-echo method for measuring nuclear relaxation times. Rev Sci Instrum 29:688–691

9. Prestes RA, Colnago LA, Forato LA, Vizzotto L, Novotny EH, Carrilho E (2007) A rapid and automated low resolution NMR method to analyze oil quality in intact oilseeds. Anal Chim Acta 596:325–329

10. Pedersen HT, Munck L, Engelsen SB (2000) Low-field 1H nuclear magnetic resonance and chemometrics combined for simultaneous determination of water, oil, and protein contents in oilseeds. J Am Oil Chem Soc 77:1069–1077

11. Wold S, Berglund A, Kettaneh N (2002) New and old trends in chemometrics. How to deal with the increasing data volumes in R&D&P (research, development and production): with examples from pharmaceutical research and process modeling. J Chemometrics 16:377–386

12. Likas A, Vlassis N, Verbeek J (2003) The global k-means clustering algorithm. Pattern Recogn 36:451–461

13. Allen CAW, Watts KC, Ackman RG, Pegg MJ (1999) Predicting the viscosity of biodiesel fuels from their fatty acid ester composition. Fuel 78:1319–1326

14. Knothe G (2005) Dependence of biodiesel fuel properties on the structure of fatty acid alkyl esters. Fuel Process Technol 86:1059–1070

15. Dorado MP, Ballesteros E, López FJ, Mittelbach M (2004) Optimization of alkali-catalyzed transesterification of *Brassica Carinata* oil for biodiesel production. Energy Fuels 18:77–83

16. Meneghetti SMP, Meneghetti MR, Wolf CR, Silva EC, Lima GES, Silva LL, Serra TM, Cauduro F, Oliveira LG (2006) Biodiesel from castor oil: a comparison of ethanolysis versus methanolysis. Energy Fuels 20:2262–2265

17. Bechmann IE, Pedersen HT, Nørgaard L, Engelsen SB (1999) Comparative chemometric analysis of transverse low-field 1H NMR relaxation data. In: Belton PS, Hills BP, Webb G (eds) Advances in magnetic resonance in food science. Royal Society of Chemistry, London

18. Rubel G (1994) Simultaneous determination of oil and water contents in different oilseeds by pulsed nuclear magnetic resonance. J Am Oil Chem Soc 71:1057–1062

19. Hickey H, MacMillan B, Newling B, Ramesh M, Eijck PV, Balcom B (2006) Magnetic resonance relaxation measurements to determine oil and water content in fried foods. Food Res Int 39:612–618

20. Povlsen VT, Rinnan A, van den Berg F, Andersen HJ, Thybo AK (2003) Direct decomposition of NMR relaxation profiles and prediction of sensory attributes of potato samples. Lebensmittel-Wissenschaft und-Technologie 36:423–432

21. Grushcow J, Smith M (2006) Engineering high-performance biolubricants in crop plants. Ind Biotechnol 2:48–50

22. Seland JG, Sørland GH, Anthonsen HW, Krane J (2003) Combining PFG and CPMG NMR measurements for separate characterization of oil and water simultaneously present in heterogeneous system. Appl Magn Reson 24:41–53

2.3. **<u>Berman P</u>**, Leshem A, Etziony O, Levi O, Parmet Y, Saunders M, Wiesman Z: Novel ^{1}H low field (LF)-NMR applications for the field of biodiesel. *Biotechnol Biofuels* 2013, **6:**55.

Biotechnology for Biofuels

Novel ^{1}H low field nuclear magnetic resonance applications for the field of biodiesel

Paula Berman[1], Adi Leshem[1], Oren Etziony[1], Ofer Levi[2], Yisrael Parmet[2], Michael Saunders[3] and Zeev Wiesman[1*]

Abstract

Background: Biodiesel production has increased dramatically over the last decade, raising the need for new rapid and non-destructive analytical tools and technologies. [1]H Low Field Nuclear Magnetic Resonance (LF-NMR) applications, which offer great potential to the field of biodiesel, have been developed by the Phyto Lipid Biotechnology Lab research team in the last few years.

Results: Supervised and un-supervised chemometric tools are suggested for screening new alternative biodiesel feedstocks according to oil content and viscosity. The tools allowed assignment into viscosity groups of biodiesel-petrodiesel samples whose viscosity is unknown, and uncovered biodiesel samples that have residues of unreacted acylglycerol and/or methanol, and poorly separated and cleaned glycerol and water. In the case of composite materials, relaxation time distribution, and cross-correlation methods were successfully applied to differentiate components. Continuous distributed methods were also applied to calculate the yield of the transesterification reaction, and thus monitor the progress of the common and in-situ transesterification reactions, offering a tool for optimization of reaction parameters.

Conclusions: Comprehensive applied tools are detailed for the characterization of new alternative biodiesel resources in their whole conformation, monitoring of the biodiesel transesterification reaction, and quality evaluation of the final product, using a non-invasive and non-destructive technology that is new to the biodiesel research area. A new integrated computational-experimental approach for analysis of ^{1}H LF-NMR relaxometry data is also presented, suggesting improved solution stability and peak resolution.

Keywords: [1]H low field nuclear magnetic resonance, Biodiesel, Biodiesel physical properties, Chemometrics, Laplace inversion, Transesterification

Background

Biodiesel is defined as mono-alkyl esters of long chain Fatty Acids (FAs), offering a viable alternative to petroleum-based diesel fuel. Biodiesel has become more attractive recently because of diminishing petroleum reserves and the environmental consequences of exhaust gases from petroleum-fueled engines. It is simple to use, biodegradable, nontoxic and essentially free of sulfur and aromatics. Since it can be manufactured using existing industrial production capacity, and used with conventional equipment, it provides substantial opportunity for immediately addressing energy security issues [1]. As a consequence, biodiesel production grew in the last decade from 0.8 to 14.7×10^9 l [2].

Biodiesel is commonly produced by a chemical reaction named transesterification (TE), where a lipid is reacted with an alcohol in the presence of a catalyst. It can be derived from a wide range of lipid-containing materials, although more than 95% is currently produced from edible-grade oils [3]. Large-scale production of biodiesel from edible resources can lead to imbalance in the global food market. Thus, alternative high yield and high quality feedstocks are continuously researched. These include non-edible oilseeds such as castor [4,5] and jatropha [6]; algae [7]; and waste materials such as recycled oils [8], municipal [9,10] and winery [11] wastes.

The quality of the biodiesel produced is of paramount importance to its successful commercialization [12]. Its performance in a compression-ignition engine is determined

* Correspondence: wiesman@bgu.ac.il
[1]The Phyto-Lipid Biotechnology Lab, Departments of Biotechnology, Energy and Environmental Engineering, Ben-Gurion University of the Negev, P.O. Box 653, Beer-Sheva 84105, Israel
Full list of author information is available at the end of the article

by the physical properties of the fuel attributed by the bio-diesel composition, which corresponds to the FA profile of the parent lipid [13,14]. Severe operational problems including engine deposits, filter clogging, and fuel deterioration can be caused by residues of unreacted lipids such as sterols, acylglycerols, phospholipids, and Free Fatty Acids (FFAs), or residues such as glycerol, alcohols, and water in the biodiesel [12]. Therefore, to maintain proper vehicle performance, official international standards were established that require analyses consisting of chromatographic, spectroscopic, physical properties-based, and wet chemical methods. These methods are destructive, time consuming, laborious and environmentally unfriendly.

^{1}H Low Field Nuclear Magnetic Resonance (LF-NMR) is a rapid non-destructive technology extensively used in the food, polymer, petroleum and pharmaceutical industries. It is widely used in industrial quality control for the determination of solid-to-liquid and oil-to-water ratios in materials as diverse as oil-bearing rock, food emulsions and plant seeds [15].

The field of ^{1}H LF-NMR relaxometry is a powerful tool for identifying molecular species and to study their dynamics even in complex materials. This relates to the measurement of relaxation constants as a consequence of interactions among nuclear spins and between them and their surroundings. Longitudinal magnetization returns to equilibrium following application of a radio frequency field because of energy transferred to the lattice, and transverse relaxation arises from spin-spin interactions following a 90° pulse. The time constants for longitudinal and transverse relaxations are T_1 and T_2 respectively.

Relaxation time distribution experiments range from simple and rapid one dimensional (1D) tests to more complicated multidimensional ones. 1D tests use constant intervals between pulses, allowing for either longitudinal or transverse relaxation to be evaluated, whereas in multi-dimensional experiments, the signal is measured as a function of two or more independent variables, allowing the spin system to evolve under different relaxation mechanisms [16]. In biological samples, spins exist in a variety of different environments, giving rise to a distribution of relaxation times in which the measured relaxation decay is a sum of contributions from all spins [17].

Most commonly applied 1D tools are based on either acquisition of the free induction decay signal following a 90° pulse, or pulse sequences such as the spin echo [18], pulsed field gradient spin echo [19], CPMG [20,21] or inversion/saturation recovery [22]. Only few of the applications found in the literature, mainly for the food industry, include measuring oil content in low moisture oilseeds [23-25], algae [26], and meat [27]; for solid fat content measurement [28]; water holding capacity in meat and fish, [29-31]; characterization of water in agro-food products [32]; molecular mobility in wheat starch

[33]; study of the denaturation of proteins in eggs and whey [34]; effect of formulation on liquid and solid fat ice cream [35]; prediction of viscosity, cetane number, and iodine value of oilseeds [36]; drug delivery [37]; and many others.

More recently, new two-dimensional (2D) relaxation time distribution pulse sequences have been suggested, including T_1-T_2 [16], T_2-store-T_2 [38] and T_2-D [39]. Several of the applications published in the last decade include 2D relaxation/diffusion correlations in porous media [39-41]; determination of avocado maturity [42]; monitoring the effect of high pressure and microwave processing on the microscopic water distribution and starch chain dynamics in potato and starch [43]; investigation of the physiological changes associated with ripening and mealiness in apples [44]; peak assignment to cell components, including compartmentalized water, pectins, starch, protein, and hemicelluloses in carrots [45]; and peak assignment for exploratory purposes in other foodstuffs including eggs, fish, dairy products, salad cream, and cake [46].

The speed with which data is obtained and the complexity of the signal acquired can become overwhelming unless suitable methods for interpretation are used. Data analysis of relaxation time distribution experiments is traditionally performed in one of several ways:

a. By projecting the data into new coordinates that maximize the original variance. This can be applied only on a group of observations, as the model looks for commonalities in the original data. The main advantage is that the method imposes no mathematical constraints. This field is termed chemometrics and it comprises the application of multivariate statistics, mathematics, and computational methods to chemical measurements to enhance the productivity of chemical experimentation [47]. Chemometric methods include clustering techniques (to spot differences between samples, detection of outliers, and grouping) and regression models (for correlating NMR measurements to reference data) [48].

b. By assuming discrete multi-exponential behavior of the data. Coefficients are extracted using nonlinear fitting models, and the coefficients can be used in prediction models [49-52].

c. By assuming a continuous distribution of exponentials. Here a relaxation time distribution of exponential coefficients is achieved with components appearing as peaks. This is an ill-posed Inverse Laplace Transform (ILT) problem. The common mathematical solution implemented today, for both 1D and 2D data, is based on L_2-norm regularization [16,17,53-55].

The goal of this summary is to show the potential of applying ^{1}H LF-NMR technology to the field of biodiesel. We detail novel applications based on 1D (CPMG) and 2D (T_1-T_2) pulse sequences for (a) screening new alternative biodiesel resources in their whole conformation, (b) monitoring the biodiesel TE reaction, and (c) evaluating the quality of the final product. A new algorithm for the 1D ILT problem, suggested by our research team, is also presented. This new approach applies L_1-norm regularization to find sparse solutions, using a formulation suitable for the PDCO solver (Primal-Dual interior method for Convex Objectives) [56]. In comparison, the common L_2-norm (least squares) result has been found to contribute to the broadening of peaks.

Results and discussion

The methodology for performing the research presented hereby is detailed in Figure 1. This multidisciplinary research consists of applying different data analysis methods to correlate the information acquired with ^{1}H LF-NMR on different materials to standard chromatographic and spectroscopic methods.

Selection of alternative biodiesel feedstocks

To successfully market a new biodiesel feedstock, the biodiesel overall production process should be cost-effective to compete with petrodiesel prices. Zhang et al. [57] reported that 70–95% of the biodiesel production cost is the price of the feedstock itself. Therefore, high oil content sources are favored. In addition, biodiesel must meet international quality standards, several of which are related to the FA composition of the parent oil, thus determined by choice of feedstock. Hence, oil content and physical properties related to FA composition are important parameters in the successful commercialization of a new feedstock.

Oil content has long been measured using ^{1}H LF-NMR. In addition, biodiesel quality parameters were successfully predicted from oilseeds relaxation signals [36]. The main

component in dried oilseeds is the oil constituent; therefore the acquired ^{1}H LF-NMR signal can be directly related to oil quantity and quality. Different composite materials consisting of additional components such as fibers, compartmentalized water and others require a more comprehensive analysis of the relaxation signals using ILT analysis.

In the following section, we present two ^{1}H LF-NMR tools that can be applied for finding new alternative biodiesel feedstocks. The first involves simultaneous screening of oilseeds by viscosity and oil content using chemometric tools. The second involves assigning peaks to the different components in olives using 1D and 2D tools, and thus relates only to the desired components.

Simultaneous screening of oilseeds by viscosity and oil content using chemometrics

The standard relaxation time distribution method, for oil content measurement in oilseeds, consists of acquisition of a single intensity signal and its correlation to oil content, to construct a calibration curve according to the international standard [58]. Each type of oilseed requires a specific calibration curve, since different types of oilseed hold unique FA profiles and therefore result in unique slopes and intercepts. This procedure is relatively simple but has several weaknesses, including (a) loss of qualitative information, (b) lack of robustness, since univariate models cannot properly handle outliers that result from abnormal signals or varied quality of oilseeds, and (c) applicability only to oilseeds whose calibration curve has already been established.

Screening of suitable biodiesel feedstocks often involves sampling extremely large batches of samples. Here a new protocol is suggested for qualitative and quantitative large-scale screening of oilseeds. A fast application that provides comprehensive information on observations will simplify the characterization and quantification of new and existing alternative biodiesel resources. This is very important to this field.
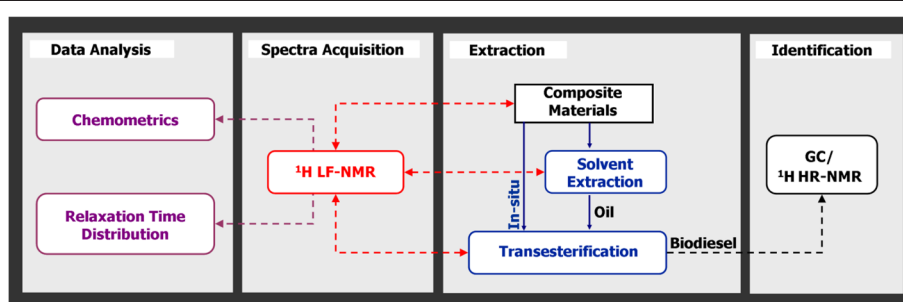

Figure 1 Schematic representation of work methodology. Work methodology consisted of four steps: Extraction of material, signal acquisition using ^{1}H LF-NMR, identification of constituents using standard chromatographic and spectroscopic methods, and finally applying different data analysis methods to correlate the acquired information.

The protocol was demonstrated using the acquired 1D transverse relaxation data of nine oils, each approximately 1, 2, 3, and 4 ml, that were correlated against oil content. The different oil volumes were used to represent varying oil contents. Oils were chosen for the application because of the possibility of controlling oil content with constant FA content of each sample from the same oil source. Unsupervised data exploration was initially conducted using Principal Component Analysis (PCA). The oils used in this analysis are almond (ALM), canola (CAN), castor (CAS), linseed (LIN), mustard1 (MUS-A), mustard2 (MUS-B), olive (OLI), soy (SOY) and sunflower (SUN).

PCA score scatter plots of the first two Principal Components (PC_1 and PC_2) extracted using the covariance matrice pre-processed by the first value or without pre-processing, are described in Figure 2A and 2B. Figure 2A shows no information related to oil content, given that almost no differentiation was observable between the different volumes from the same type of oil. Since all the samples per type of oil were very closely clustered, the name of only one of the oil samples for each of the oils is shown on the plot, to facilitate its interpretation. Still, PC_2 revealed qualitative information, meaning high or low values of PC_2 correlated to high or low viscosities, as shown in a previous study [59]. In that study, a PCA model was suggested for rapid large-scale screening of castor seeds according to viscosity. An excellent correlation was found there between viscosity and PC_2 calculated from the 1D transverse relaxation data, acquired on castor genotypes.

In Figure 2B on the other hand, both PC_1 and PC_2 held significant information regarding oil content. Fitting of the calculated PC_1 and PC_2 for each of the individual oils separately yielded an excellent linear regression (without intercept). The slope extracted from each of these curves was found to linearly correlate with the $\ln(T_2)$ of the oils (y = $-0.49\ln(T_2) + 2.54$, R^2=0.99; the Figure was added in an additional file [see Additional file 1]). T_2 was the average value for each of the 4 samples per oil, calculated using monoexponential fitting.

Based on the unsupervised results shown, it was assumed that construction of an oil content (according to the oil weight) calibration including various types of oils would be possible using multivariate regression. Partial Least Squares (PLS) was then applied on the unprocessed covariance matrice. Training of the model was performed using three samples per oil, and the fourth was used for validation. The established model showed excellent prediction capability, as calculated on the validation set (R_p^2=0.99, Root Mean Squared Error of Prediction (RMSEP) = 0.075 g, the Figure was added in an additional file [see Additional file 2]). This suggests that the PLS model considers the decay rate of the specific oil, and generates an oil content reading accordingly. This model met the initial goal of eliminating the need for constructing specific calibration curves for each oil quality composition. These are important findings, suggesting that both quantitative and qualitative information can be extracted using PCA for data exploration and PLS for prediction.

Selection of alternative biodiesel feedstocks according to chemical composition

As a first step in characterizing lipid components in composite materials using ^{1}H LF-NMR, for ultimately screening new feedstocks, we chose olives as a test case. This work was performed in collaboration with Dr. Brian Hills from the Institute of Food Research (Norwich, UK).

A major opportunity within the olive oil production industry is the exploitation of certain by-products obtained
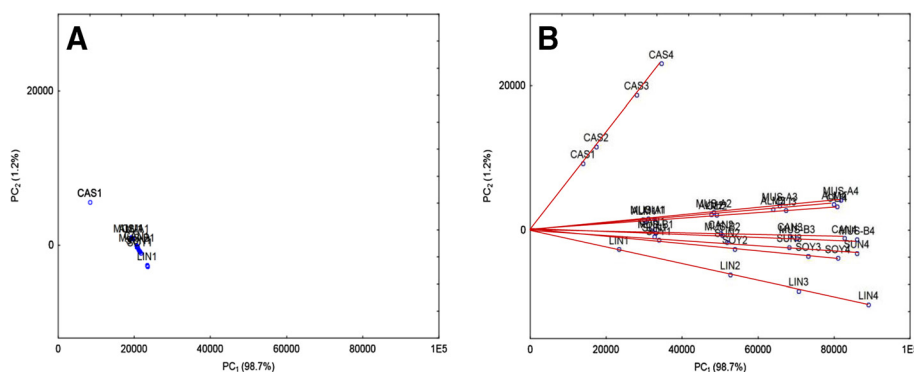
Figure 2 Simultaneous screening of oils by viscosity and oil content using chemometrics. Oils were chosen for the application because of the possibility of controlling oil content with constant FA content of each sample from the same oil source. PCA score scatter plots of PC_1 and PC_2 are shown for: (**A**) The covariance matrice pre-processed by the 1st intensity value. Since all the samples per type of oil were very closely clustered, the name of only one of the oil samples, for each of the oils, is shown. (**B**) The covariance matrice without pre-processing. Fitting of the calculated PC_1 and PC_2 for each of the individual oils separately yielded a perfect linear regression (the curves for each of the separate oils are illustrated on the plot).

during the processing of olives for oil, such as pomace and olive pits, which can be used as biofuels [60]. Olive fruits have been studied for many years from an analytical point of view. The olive fruit is an ovoidal drupe consisting of an epicarp (1.5-3.5% of the fruit weight), mesocarp (or pulp, 65-83%), and kernel (or stone, 13-30% of fruit weight). Its average chemical composition is water 50%, oil 22%, proteins 1.6%, sugar 19.1%, cellulose 5.8% and ash 1.5% [61].

In this study, 1D and 2D pulse sequences were used for signal acquisition of olive oil, a whole fresh olive fruit, olive stone, and dry whole olive fruit samples. 1D relaxation time distribution using the WinDXP ILT software package, and 2D cross-correlation ILT software, were used for data analysis. Peaks were provisionally assigned to olive components by collating information from the different

samples, and according to published peak assignment on avocado, apples, and xylem and phloem of carrots, as described below. Real peaks were marked A-H and cross peaks were marked according to the two exchanging components (e.g. BF stands for proton exchange of peaks B and F).

1D relaxation time distribution The olive oil 1D peak distribution consists of peaks B and C (Figure 3A). Olive oil contains mostly triacylglycerols (98-99%); therefore, peaks B and C were assigned as oil peaks. These two oil peaks agree with the bi-exponential behavior of oil in oil-containing materials as previously suggested [25,50]. This result also coincided with previous peak assignment in avocado [42].

Figure 3 Peaks assignment of the 1D relaxation time distributions of olive constituents. Continuous distribution of exponentials of (**A**) olive oil, (**B**) whole fresh olive, (**C**) whole dry olive, and (**D**) olive stone were calculated using the WinDXP ILT software package. Peaks in each Figure were assigned (A-F) to olive components by collating information from the different samples, and according to published peak assignment on avocado, apples, and xylem and phloem of carrots.

The 1D olive fruit sample contains four peaks in addition to the two oil peaks (Figure 3B). Interestingly, in the oil sample, peak C has a higher relative intensity than peak B, whereas in the fruit this ratio is flipped. As noted before, fresh olives consist of approximately 50% water. Since these components are the major peaks in the fruit sample, and based on previous peak assignment [44], it was assumed that they arise also from cytoplasmic and extracellular water. This was validated using the dry whole olive sample (Figure 3C).

Peak A in Figure 3B was assigned as vacuolar water because of the high fluidity of water molecules in this organelle as suggested for apples [44]. Indeed, in a dissected olive sample, peak A changed into one of the major peaks (data not shown), probably because of free water released as a consequence of dissecting the olive flesh. Peak E did not appear in the dissected olive flesh sample. Its relative intensity in a dry olive sample was significantly reduced compared to the fresh sample, suggesting that water had been evaporated, though not entirely. Peak E was therefore assigned as a water component in the olive stone. The chemical composition of olive stones (% dry weight) according to Heredia et al. [62] consists almost entirely of fibers (80%), around 10% moisture, 5% oil and some other minor components. Based on this information, it is reasonable to assume that the peaks in the olive stone sample, with the lowest relative importance, are the oil components B and C, whereas peak D probably arises from a water component (Figure 3D).

Peak F in apples was assigned as water associated with the rigid components of the cell wall [44]. This however did not coincide with the relative intensity of this peak in the stone sample (Figure 3D), where it is the principal component. As previously stated, the major constituent compatible with this peak, is the lignocellulosic material, which frameworks the cell wall, with hemicellulose, cellulose and lignin as the main components. MacKay et al. [63] suggested that the primary cell wall molecules (not including water) can be divided into a practically rigid fraction consisting of all the cellulose and some of the hemicellulose molecules; and a higher mobility fraction consisting of pectic polysaccharide and some hemicellulosic molecules. At this point, it is difficult to determine whether peak F arises from these very fast relaxing molecules, or from water attached to them, and will be further discussed using 2D cross-correlation measurements.

2D cross-correlation Figures 4A-4D show the 2D cross-correlation relaxation time distributions analyses for the olive oil, whole fresh and dry olive fruit, and olive stone samples respectively. The previously assigned peaks A-F appear here on the diagonal where $T_1 \approx T_2$. Here two new peaks (marked G and H) appear off-diagonal in the area where $T_2 < T_1$. These were assigned as the higher mobility hemicellulosic fraction (Peak G) and the more rigid cellulosic constituent, as they are the major peaks in the stone sample (Figure 4D). This coincided with previous peak assignment in xylem and phloem of carrots [45]. A summary of the relaxation contribution assignment is presented in Table 1.

The advantage of using multidimensional cross-correlation methods is apparent from comparing Figures 3B and 4B. Components G and H have similar transverse relaxation times as peaks E and F, and therefore cannot be distinguished in a 1D representation. This is most emphasized for the stone sample as discussed before in the assignment of Peak F. In addition, cross-correlation methods can be used to study proton exchange, which is not discussed in this work.

Relaxation time distribution analysis and cross-correlation methods allow the identification of components in composite materials. These can be used to identify separately oil, fibers, compartmentalized water and more, to search for new biodiesel feedstocks. The application of these methods in combination with simple linear and/or multivariate regression methods, can lead to the construction of intelligent and robust calibration curves and prediction models. The construction of an oil content calibration curve of olive mill pomace, using relaxation time distribution analysis, was recently shown by our research team [64]. In this study only eight olive mill pomace samples were used. Full leave one out cross validation yielded $R^2 = 0.83$.

Monitoring of the biodiesel TE reaction

The conditions and materials of the TE reaction may vary significantly according to the type of lipid substrate. The most common TE reaction is performed under alkaline conditions by reacting oil with methanol, because of its lower price compared to other alcohols. The alkali catalyst leads to a relatively fast conversion, while requiring only a moderate temperature. However, high yields are only achieved when the starting material is essentially free of moisture and consists of a low FFA content (<3%). Alternatively, low grade substrates and/or non-acylglycerol lipids can be reacted using Brönsted acids. Yet, the reaction is usually carried out at higher temperatures and for longer periods [65].

Another common biodiesel production process is an in situ TE reaction, which differs from the conventional reaction in that the oil-bearing material contacts with acidified or alkalized alcohol directly, instead of reacting alcohol with the pre-extracted oil. That is, extraction and TE proceed in one step, the alcohol acting both as an extraction solvent and as an esterification reagent [66]. This is a complicated process with several reactions and procedures, where the outcome of each one can

Figure 4 Peaks assignment of the 2D cross correlation time distributions of olive constituents. T_1-T_2 correlation time distribution of (**A**) olive oil, (**B**) whole fresh olive, (**C**) whole dry olive, and (**D**) olive stone were calculated using an in-house 2D-ILT tool [15]. Peaks A-F on the diagonal consist of the high mobility molecules as previously assigned. The two new off-diagonal peaks (marked G and H) in the area where $T_2 < T_1$ were assigned as the higher mobility hemicellulosic fraction (Peak G) and the more rigid cellulosic constituent, as they are the major peaks in the stone sample.

potentially influence the quality of the following one, and of the final product.

The reactants in the TE reaction include the lipid substrate and alcohol, which is usually added in excess to drive the process forward. The desired product consists of high purity Fatty Acid Methyl Esters (FAMEs). However, residual glycerol, acylglycerol constituents (tri-, di- and mono-glycerides), alcohol, catalyst, water and others can often be found at diverse concentrations in the product, according to the reaction process. Therefore, assessment of the conversion of oil to biodiesel is required for monitoring and control of the production process in order to meet international biodiesel standards.

Monitoring of the TE reaction and biodiesel product using relaxation time distribution experiments, requires as a first step assigning peaks in the analyzed relaxation time

distribution signals. Several of the components that participate in this reaction including soy oil, soy biodiesel, glycerol, water and methanol were sampled separately using ^{1}H LF-NMR. Data was analyzed using the WinDXP ILT software package, and the combined relaxation time distributions are shown in Figure 5. Each solution was normalized to its highest value for simplicity of comparison. Here, the position of every component on the relaxation time distribution can be explained by its chemical structure. Water and methanol are polar, very mobile liquids, and thus have the largest T_2 values. The biodiesel and oil samples consist of the same FA composition (biodiesel was produced from the analyzed oil). However, biodiesel consists of individual FAMEs (that have high freedom of movement and thus large T_2) and oil, which consists mainly of triacylglycerols (three FAs esterified to a glycerol

Table 1 Peaks assignment of olives according to relaxation time distribution and cross correlation experiments

Description	Peak
Vacuolar/free water	A
Oil 1 and cytoplasmic water	B
Oil 2 and extracellular water	C
Pectin and extracellular water	D
Water in fibers	E
Cell wall water	F
Hemicellulose (stone)	G
Cellulose (stone)	H

backbone) that have lower mobility and T_2 because of this more rigid structure. Glycerol is a three-carbon molecule with three hydroxyl groups. As a result it has the lowest mobility and T_2 because of hydrogen bonding.

Figures 6A-6D show the analyzed relaxation time distributions acquired from mixtures (1:1 v/v) of biodiesel and oil, glycerol, water and methanol respectively (the relaxation time distributions of the pure materials presented above are shown for reference). As expected from their chemical composition, the biodiesel-water and biodiesel-glycerol mixtures formed two immiscible and separated phases inside the test tube, while the biodiesel-oil and biodiesel-methanol consisted of a single phase. As can be seen, the position of the different peaks in Figures 6A-6C is constant also for composite samples, though the peaks in the oil-biodiesel mixture are difficult to resolve because
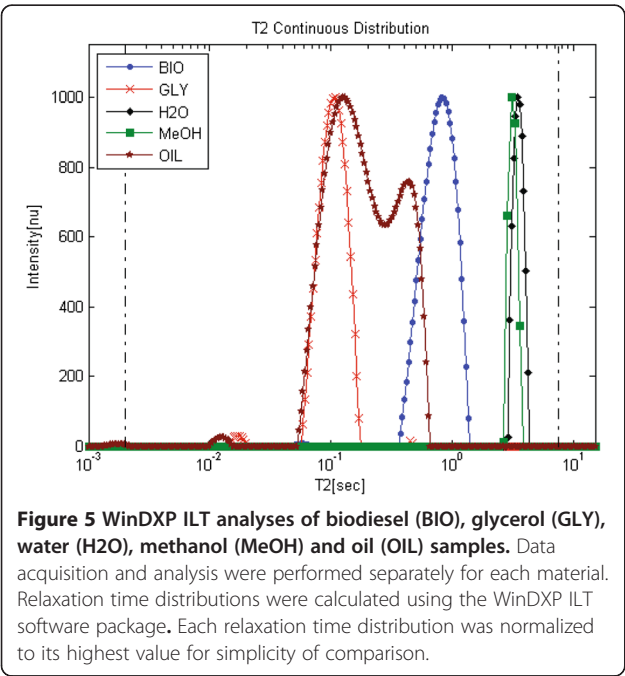
of overlapping of components and widening of peaks imposed partly by the WinDXP ILT algorithm. In the biodiesel-methanol mixture (Figure 6D), the position of the biodiesel peak is shifted toward the methanol component probably because of solubility interactions between the two components. This suggests that if methanol (or other alcohol) residues exist in the biodiesel; a shift is to be expected for the biodiesel peak in relation to its content.
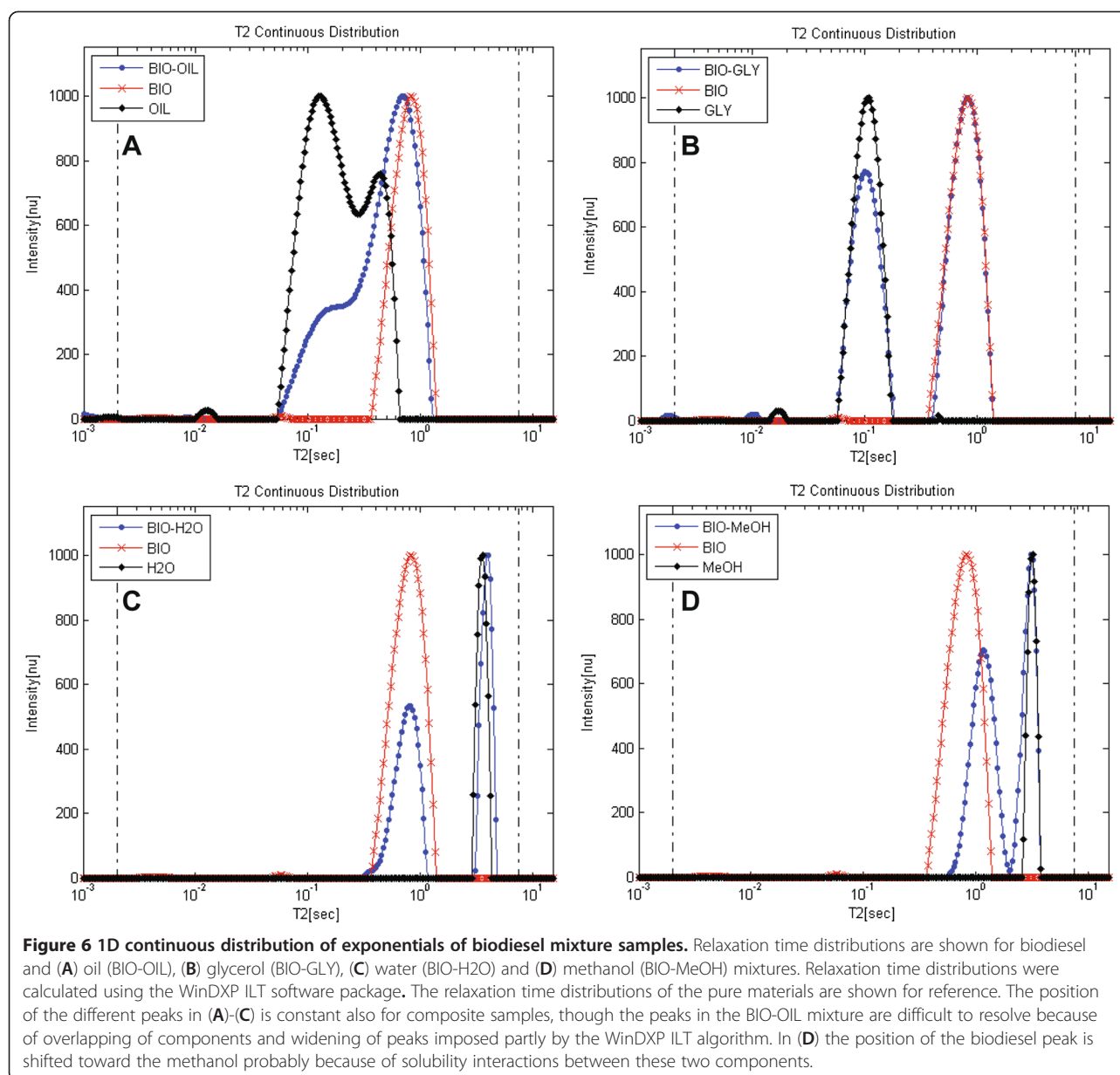
Application of the new L_1-norm regularization based PDCO algorithm [56] to find sparse solutions (recently submitted article by our research group to Concepts in Magnetic Resonance A Journal) on the same biodiesel, glycerol, water, oil and methanol samples (Figure 7) showed better resolved relaxation time distributions and more accurate solutions. The PDCO analyzed relaxation time distributions of the oil and biodiesel samples reveal a larger number of peaks compared with the conventional results analyzed by the WinDXP ILT toolbox (Figure 5). As previously mentioned and as shown here, WinDXP analysis of oil reveals two overlapping peaks. Marigheto et al. [42] suggested that the peaks arise from molecules of differing mobility, such as the oleic and palmitic constituents, or from nonequivalent proton pools of different mobility, such as those on methyl and olefinic groups. In the current study, the PDCO algorithm reveals four resolved peaks instead of only two, suggesting promising unpublished information regarding identification of lipids constituents using relaxation time distribution experiments, and its supremacy as an analytical tool. Assignment of peaks to the appropriate components will be performed in the near future using standard materials.

To monitor the conversion reaction of oils to biodiesel, samples were acquired at different times during TE of rapeseed oil, and measured using relaxation time distribution experiments to track the progression of this reaction until completion. To calculate the yield of TE from the relaxation time distributions, a correlation with the data acquired by ^{1}H High Resolution (HR)-NMR following the procedure of Meher et al. [65] was established. In situ TE process of olive mill waste was also monitored using relaxation time distribution experiments by measuring the relaxation signal of the pomace and biodiesel products following acid esterification, alkali TE and n-hexane extraction. Monitoring of this process led to successful optimization of reaction parameters.

Monitoring of the TE process and calculation of yield using ^{1}H LF-NMR

As previously shown, oil and biodiesel mixtures can be evaluated using relaxation time distribution experiments. This can also be applied to monitor the progression of the TE reaction and to calculate its yield. Accurate measurement of the biodiesel yield, and analysis of the

Figure 5 WinDXP ILT analyses of biodiesel (BIO), glycerol (GLY), water (H2O), methanol (MeOH) and oil (OIL) samples. Data acquisition and analysis were performed separately for each material. Relaxation time distributions were calculated using the WinDXP ILT software package. Each relaxation time distribution was normalized to its highest value for simplicity of comparison.

51

Figure 6 **1D continuous distribution of exponentials of biodiesel mixture samples.** Relaxation time distributions are shown for biodiesel and (**A**) oil (BIO-OIL), (**B**) glycerol (BIO-GLY), (**C**) water (BIO-H2O) and (**D**) methanol (BIO-MeOH) mixtures. Relaxation time distributions were calculated using the WinDXP ILT software package**.** The relaxation time distributions of the pure materials are shown for reference. The position of the different peaks in (**A**)-(**C**) is constant also for composite samples, though the peaks in the BIO-OIL mixture are difficult to resolve because of overlapping of components and widening of peaks imposed partly by the WinDXP ILT algorithm. In (**D**) the position of the biodiesel peak is shifted toward the methanol probably because of solubility interactions between these two components.
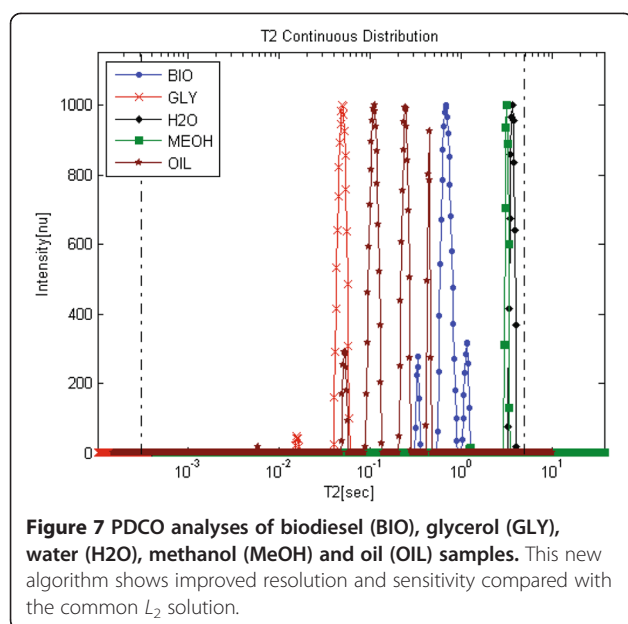
final FAME product for the presence of acylglycerol, is of paramount importance for establishing its quality.

As a first step, two rapeseed oil biodiesels were prepared, each using 0.05% and 0.5% (w/w) KOH catalyst (samples A and B respectively). Yield of TE was calculated using ^{1}H HR-NMR. Figures 8A and 8B show the 500 MHz ^{1}H HR-NMR spectra acquired for samples A and B. The integrals of the peaks used for the yield calculations, as well as glyceryl peaks are listed in Table 2. Peak numbers are according to the numbers shown on the Figures. As expected from the low catalyst concentration, the integral of the glycerol peaks in sample A is larger, suggesting of high acylglycerol residues in the biodiesel. Consequently, samples A and B achieved yields of 54.7% and 93.3%

respectively. Still, the last did not meet international standards (0.96% w/w total bound glycerol content, as measured from the same sample using Gas Chromatograph (GC), by an accredited European biodiesel laboratory, ASG Analytik-Service Gesellschaft mbH, Germany).

Figures 8C and 8D show the ^{1}H LF-NMR relaxation time distributions analyzed for samples A and B respectively, using the WinDXP ILT software package and PDCO. According to the WinDXP ILT relaxation time distributions, sample B consists of mainly a single biodiesel peak, whereas sample A exhibits two overlapping peaks consistent with an oil-biodiesel mixture previously shown in Figure 6A. A possible solution to increase the resolution and sensitivity of the method may be the application of L_1

52

Figure 7 PDCO analyses of biodiesel (BIO), glycerol (GLY), water (H2O), methanol (MeOH) and oil (OIL) samples. This new algorithm shows improved resolution and sensitivity compared with the common L_2 solution.

regularization via PDCO. As Figure 8C shows for the PDCO solution, one of the oil peaks can now be distinguished (intrinsic T_2 at approximately 220 ms).

This suggests that ^{1}H LF-NMR is a simple and rapid tool for estimating acylglycerol content in biodiesel. It should be stated, however, that based on Figure 8D, it is not yet clear whether the limit of detection of the proposed method will allow detecting low acylglycerol residues in biodiesels that don't meet international standards.
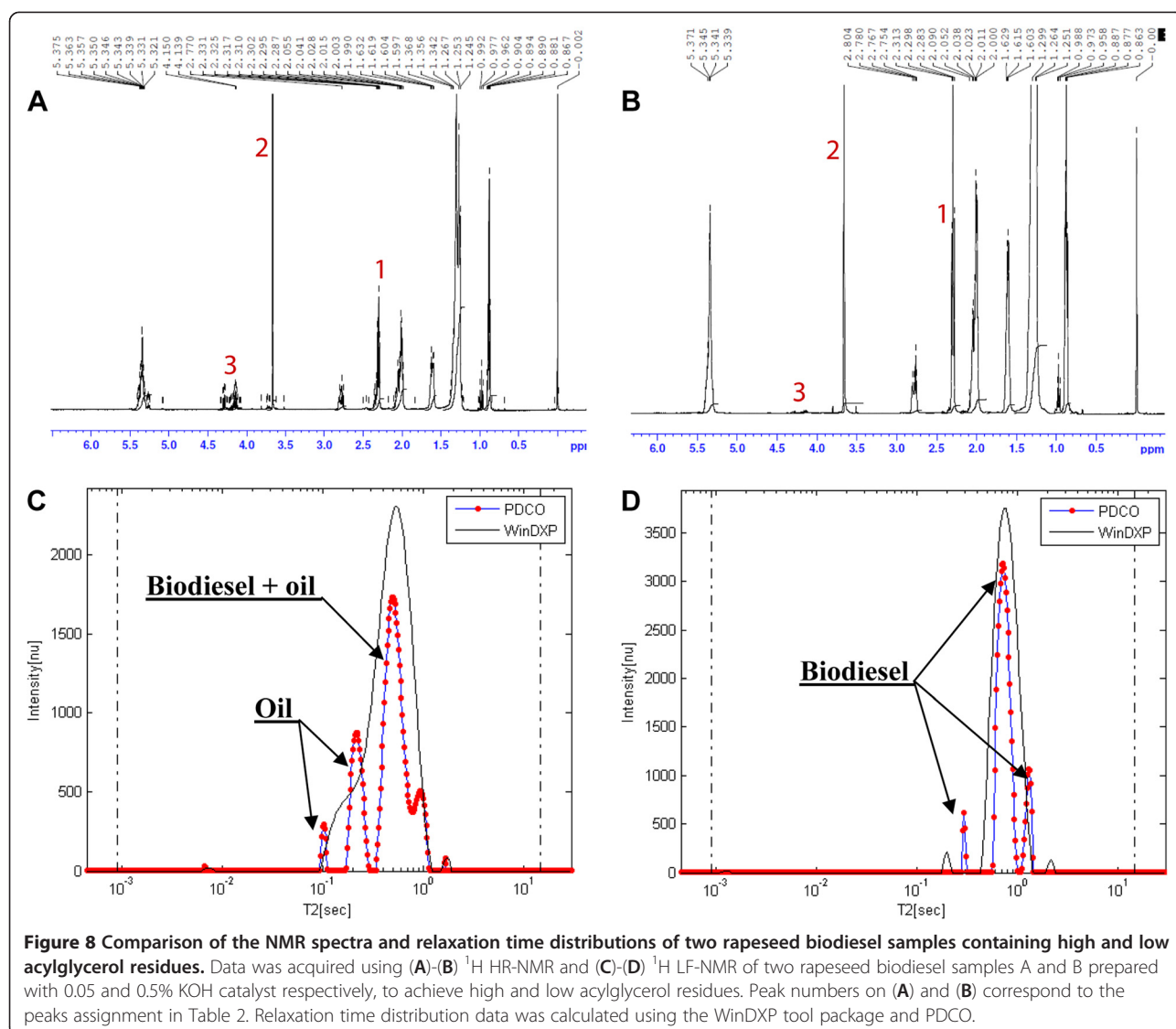
Several process and reaction monitoring applications, using ^{1}H LF-NMR either spectroscopically or using relaxation analysis, have been described in the literature ([68-71] and references therein). More recently, Linck et al. [72] have shown the potential of applying a mobile LF ^{1}H NMR spectrometer for the analysis and monitoring of biodiesel production. Cabeça et al. [73] suggested a method for off-line monitoring the biodiesel TE reaction using monoexponential fitting. In that study, monoexponential T_2 measurements were used to track the progression of the reaction until completion. In the case, however, where residues of methanol remained in the sample, an increase in T_2 value was observed. This is consistent with the previous result shown for a biodiesel-methanol mixture (Figure 6D). Likewise, glycerol residues would lead to a decrease in the calculated T_2 value, even though the reaction may have been completed. Since monoexponential fitting does not provide information regarding individual constituents, rather an average estimation of all T_2s in regards to their content in the sample, the application of relaxation time distribution analysis using PDCO is hereby described. Using this approach, both at-line and off-line process monitoring can be performed, by tracking the disappearance of the oil peak in relation to the biodiesel peaks.

At-line monitoring of the TE process of rapeseed oil was performed by collecting aliquots from the reaction flask, and immediately measuring them using relaxation time distribution, without further cleaning or tempering. Figure 9 shows the combined relaxation time distributions of five of the samples collected throughout the reaction, according to the order of collection, along with a rapeseed oil sample as reference. Since the TE reaction is performed at 50℃, and the ^{1}H LF-NMR instrument operates at 40℃, there was a small influence to the relaxation time distributions, that can be observed from the shifts in the position of the peaks. Despite of this change, four peaks are clearly resolved for each sample.

According to previous peak assignment, peak 3 was the main biodiesel component and peak 4 was attributed to methanol. Peaks 1 and 2 were previously related to oil components. As can be seen, their relative intensities reach equilibrium but are not reduced to zero intensity as would have been expected. In order to assign these peaks, the sample collected following 110 min from the beginning of the reaction, was allowed to separate into two phases for twenty minutes, and then an aliquot from the upper layer was measured using relaxation time distribution. The analyzed distribution showed a result consistent with a biodiesel sample (without oil residues), as previously shown in Figure 7. It was therefore assumed that peak 2 belong both to glycerol and residues of oil components. The shift in the position of the glycerol component, to a higher T_2 value is caused due to its solubility in methanol (relaxation time distribution of different methanol-glycerol mixtures is shown in Additional file 3). Peak 1 is more difficult to assign with certainty. At short reaction times it most probably originates from the oil component. However at longer periods this is not probable, especially since it disappears when measuring the upper layer alone. This remains for further study.

The kinetics of the reaction according to the oil to biodiesel peaks area ((peak2/peak2+peak 3)*100%) is shown in Figure 10. As expected, the reaction progresses logarithmically, and a plateau is achieved at approximately 100 min. This trend is consistent with the results presented by Rashid and Anwar [74] for the kinetics of a rapeseed oil TE reaction at the same conditions. However, since the oil and glycerol peaks cannot be distinguished, the maximum calculated yield achieved is about 90%. This suggests that using the methodology described, the actual yield of the reaction cannot be accurately determined. Assessment of actual yields requires at least one separation step. This takes time, and therefore cannot be performed at-line.

To examine the possibility of calculating yields using relaxation time distribution, correlation of the yield calculated according to the relaxation time distribution (predictor) to the yield of TE calculated using ^{1}H HR-NMR (predicted) was performed. For this purpose, six

Figure 8 Comparison of the NMR spectra and relaxation time distributions of two rapeseed biodiesel samples containing high and low acylglycerol residues. Data was acquired using (**A**)-(**B**) ^{1}H HR-NMR and (**C**)-(**D**) ^{1}H LF-NMR of two rapeseed biodiesel samples A and B prepared with 0.05 and 0.5% KOH catalyst respectively, to achieve high and low acylglycerol residues. Peak numbers on (**A**) and (**B**) correspond to the peaks assignment in Table 2. Relaxation time distribution data was calculated using the WinDXP tool package and PDCO.

samples were collected while TE reaction of rapeseed oil was proceeding, and immediately placed on ice. Following phase separation, glycerol was drained and the biodiesel was cleaned. Three additional samples prepared using low catalyst concentration (0.05%, 0.1% and 0.15% w/w KOH) were also used in the correlation, in order to broaden the range of yields. Since the prepared samples were cleaned, no glycerol or methanol residues were shown in the relaxation time distributions. The yield based on relaxation

time distribution was therefore calculated from the oil to biodiesel peaks area.

This correlation yielded an excellent linear fit ($y = 0.78x + 20.50$, $R^2 = 0.99$; the Figure was added in an additional file [see Additional file 4]). This suggests that the proposed method is a good tool for monitoring and calculating the yield of the TE reaction. Its disadvantage, however, is the time consuming cleaning process which makes this an off-line tool.

Table 2 Peaks assignment and corresponding integrals of the ^{1}H HR-NMR spectra of samples A and B

Peak number	Functional group[a]	Chemical shift[a] [ppm]	Sample A[b] integral [nu]	Sample B[b] integral [nu]
1	-OCO-C**H**$_2$- (Acyl group)	2.23-2.36	0.78	0.80
2	R-OCO-C**H**$_3$ (Methyl ester group)	3.7	0.64	1.12
3	-C**H**$_2$OCOR (Glycerol group)	4.1-4.32	0.25	0.01

[a] Peaks were assigned according to Meher et al. [65] and Guillén and Ruiz [67].
[b] Rapeseed biodiesels A and B were prepared using 0.05% and 0.5% (w/w) KOH catalyst respectively.
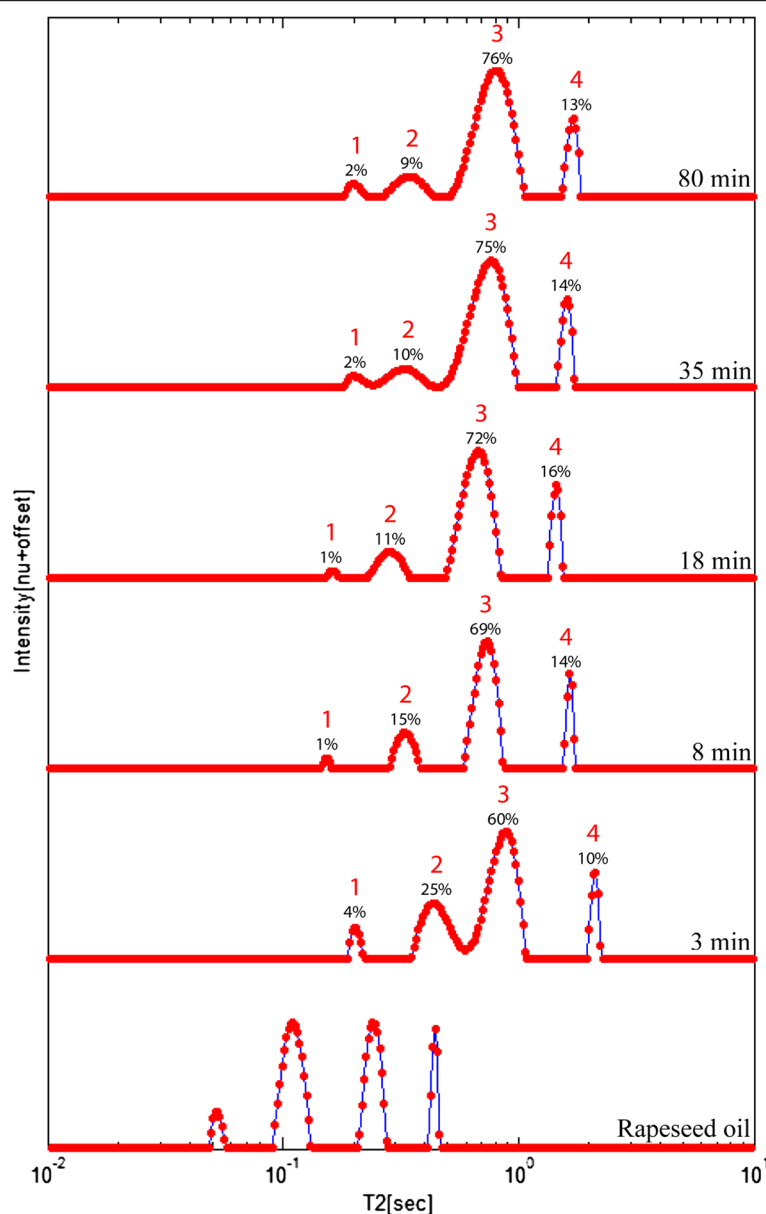
Figure 9 At-line monitoring of the TE reaction using relaxation time distribution experiments. Monitoring is shown using the combined 1D continuous distribution of exponentials of five samples acquired at different times in the course of the TE reaction of rapeseed oil into biodiesel. Samples were analyzed using PDCO. The content of each component, in relation to other components in the mixture, is shown on each relaxation time distribution.
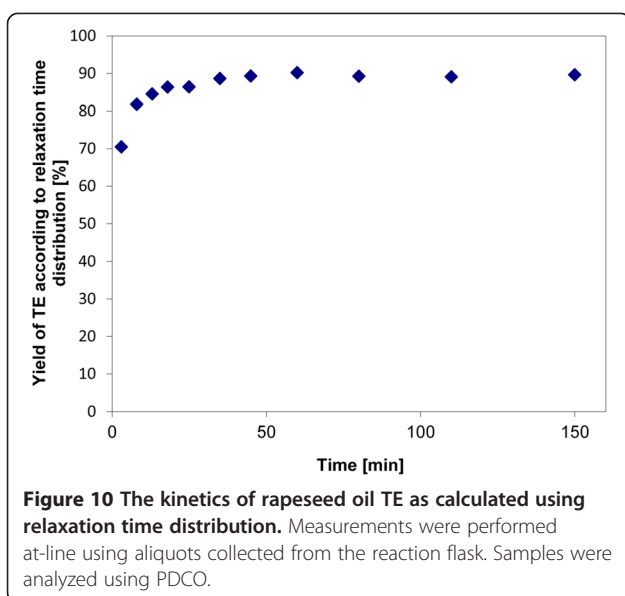
A combined tool is therefore suggested, were monitoring of the TE reaction is qualitatively performed at-line, until reaching equilibrium, and yield quantification is carried out off-line, following phase separation and cleaning of the upper layer.

Monitoring of the in situ TE process of pomace
Reutilization of bio-wastes as alternative energy holds the possibility of reducing their impact on the environment, along with the potential to expand the currently limited biodiesel industry [10]. Solid olive mill waste is a promising composite feedstock for the biofuel industry because of its high content of both lipids and cellulosic materials. In this study, relaxation time distribution experiments were performed to monitor the TE reaction of the in situ conversion of oil in olive pomace to biodiesel.

Olive mill pomace contains low grade oil with high content of FFAs (>3%). This leads to the formation of soaps in a base catalyzed reaction, which causes an increase in viscosity or formation of gels that interfere in

Figure 10 The kinetics of rapeseed oil TE as calculated using relaxation time distribution. Measurements were performed at-line using aliquots collected from the reaction flask. Samples were analyzed using PDCO.

the reaction as well as with the separation of glycerol [65]. In order to carry out the in situ TE reaction, a preliminary acidic esterification step is required in which FFAs are transformed into FAMEs. If carried out for long periods, oil is additionally transesterified into biodiesel. This is energy consuming because it is performed at a relatively high temperature (100°C), and thus not desirable. In the current study, the in situ process consisted of an acidic esterification step, followed by alkali TE. As a final step, the solid pomace with methoxide sludge was washed with n-hexane to remove oil and FAME residues in order to achieve low oil content pomace.

Monitoring of this process is shown in Figures 11A-11D and 11E-11G for the analyzed relaxation time distributions of the solid pomace and biodiesel products respectively, using the WinDXP ILT toolbox. Data was acquired at each step of the reaction. 1, 2, and 3 mark each of the reaction steps: acid esterification, alkali TE and n-hexane extraction.

Based on the previous peaks assignment in olives, the main constituents in the initial dry solid pomace sample consisted of oil (intrinsic peak at approximately 90 ms) and fibers (intrinsic peak at approximately 0.1 ms) components, as shown on Figure 11A. Following the esterification step, the area of these two types of components was changed, meaning the oil component was reduced while the fibers increased (Figure 11B). This suggested that not only FFAs were reacted following this step, but also oil was transesterified into FAMEs. This was assessed by analyzing the liquid product following this step (Figure 11E). Here a biodiesel peak was observed. In addition, another major component was detected, which was attributed to suspended solids in the sample because the liquid fraction was opaque in color. The increase in

the fibers peak area was attributed to the formation of more mobile constituents, following breaking down of fibers which could not be detected before because of their fast relaxation. As expected, an additional reduction in the relative content of the oil fraction was accomplished following the alkali TE step (Figure 11C). Still additional optimization of these process parameters is required because the reacted pomace contained substantial amounts of oil. The residual oil was successfully extracted using n-hexane as shown on Figure 11D. Monitoring of the liquid fraction following each step confirmed the successful production of biodiesel, and showed the presence of impurities in the product (Figures 11E-11G).

The achieved low oil content pomace, which is very rich in fibrous material, can be further used for production of bioethanol. In a collaborative work with Dr. Ely Morag (Designers Energy Ltd, Israel) and Prof. Edward A. Bayer (Weizmann Institute of Science, Israel), it was found that reducing the oil content in olive pomace, prior to cellulase enzymatic hydrolysis, showed significant increase of sugar release from the pomace cellulosic fraction. In addition, the acidic and alkali treatments described above for the in situ biodiesel production significantly supported the enzymatic pre-treating procedure. This suggests that relaxation time distribution experiments can be applied for monitoring the production of other biofuels, including bioethanol. Such a study is currently being carried out.

In this work, monitoring of the in situ biodiesel TE process was performed qualitatively. However, development of calibration curves or the use of internal standards can reveal important quantitative information, including oil content, conversion yield, quantity of biodiesel produced, and more. These applications are currently being developed by our team for optimization of the in situ TE process of olive pomace.

Quality assessment of the biodiesel product

As previously shown, relaxation time distribution experiments can be applied to calculate the yield of the TE reaction. This gives an approximation of residual acylglycerol content in the biodiesel, which is a qualitative indication of whether it meets international standards. Another qualitative aspect is the biodiesel FA composition, which affects several physical properties of the fuel. Several of the parameters specified in international biodiesel standards are determined directly by choice of feedstock, according to their FA profile. Prestes et al. [36] showed that it is possible to predict several of these parameters by measuring transverse relaxation data of oilseeds, even without extracting and transesterifying the oil. However, evaluation of physical properties of the biodiesel product is also of paramount importance, especially for biodiesel and/or petrodiesel blends.
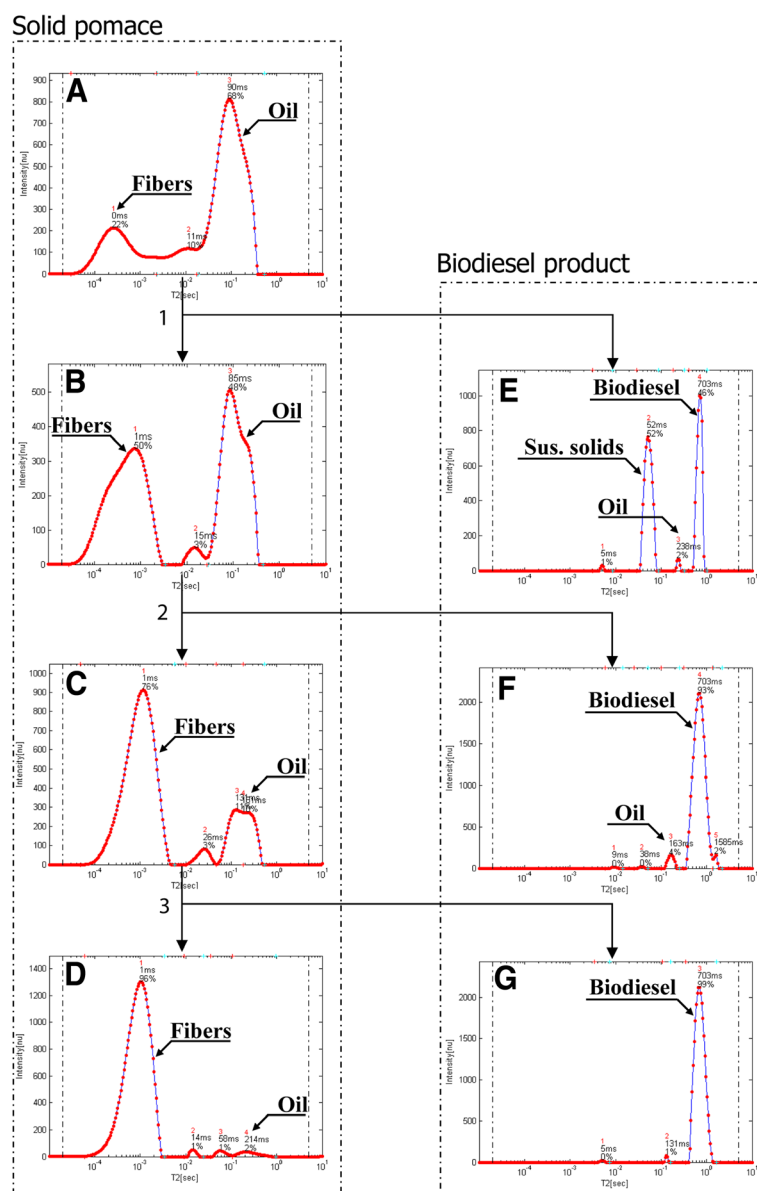
Figure 11 Monitoring of the in-situ TE process of pomace. Samples were collected following (1) acid esterification (2) alkali TE, and (3) n-hexane extraction using relaxation time distributions. Figures are ordered according to the appropriate step in the reaction process. (**A**)-(**D**) show the results for the solid pomace, and (**E**)-(**G**) for the biodiesel product.

In this study, transverse relaxation data of six different types of biodiesels and nine petrodiesel-biodiesel mixture samples (BXX, where XX stands for the amount of castor biodiesel in the mixture) was acquired using LF-NMR. Hierarchical Cluster Analysis (HCA) was applied to explore the relative distance and grouping of samples according to the pre-processed relaxation data. Biodiesel viscosities were calculated from their FA composition, as suggested by Allen et al. [13].

Biodiesel consists of a mixture of FAMEs in which each constituent contributes to the overall viscosity. Viscosity increases with chain length and with increasing degree of saturation [75]. The main FAMEs and calculated viscosities are shown on Table 3 (observations are ordered by ascending calculated viscosities). Even though the viscosity of the BXX samples cannot be determined by GC, samples were assigned to viscosity groups based on the HCA dendrogram mixture.

Figure 12 shows the HCA dendrogram. Using a linkage distance threshold of 4000, four distinct groups (marked 1–4) were observed, that can be related to the viscosity of the samples. Linseed and soy biodiesels, rich in the polyunsaturated, linoleic and linolenic acids, showed the lowest viscosities (3.60 and 3.99 mm^2/s respectively) and were

Table 3 FAME profiles according to GC and calculated viscosities of the six biodiesels produced

Sample[a]	FAME composition[b] [%]									Calculated viscosities [mm^2/s]
	C$_{16:0}$	C$_{18:0}$	C$_{18:1}$	C$_{18:2}$	C$_{18:3}$	C$_{20:0}$	C$_{20:1}$	C$_{22:1}$	C$_{18:1-OH}$	
Linseed	5.6	4.6	18.2	15.4	56.1	-	-	-	-	3.60
Soy	10.8	3.6	25.6	53.4	5.5	0.4	0.4	0.4	-	3.99
Canola	4.8	1.6	63.7	20.3	7.2	0.6	1.3	-	-	4.25
Olive	10.6	2.8	77.3	7.4	0.6	0.4	-	-	-	4.45
Mustard	1.7	1.0	9.8	13.8	12.9	0.8	6.2	51.4	-	5.52
Castor	1.0	1.1	3.0	3.9	-	-	-	-	91.1	13.76

[a] Samples are ordered by ascending calculated viscosities.
[b] Only major FAMEs are shown.

thus assigned to group 1. Group 2 was subdivided into two groups. The first included the olive and canola samples (rich in the monounsaturated oleic acid, 4.25 and 4.45 mm^2/s respectively) and B0-B10 mixtures. The second included the mustard sample (rich in erucic acid, 5.52 mm^2/s) and B15-B30 mixtures. Erucic acid increases viscosity because of its larger chain length compared to the more common 18 carbon components. Group 3 comprised of only mixture samples (B50-B80). Even though their exact viscosity values are unknown, based on the mixing ratio they should have higher viscosity than B30 and lower than B100 (pure castor biodiesel). Therefore, the highest viscosity group 4 was assigned to castor biodiesel, having very high viscosity (13.76 mm^2/s) imparted by intermolecular hydrogen bonds caused by ricinoleic acid.

The proposed methodology allows the assignment into viscosity groups of samples whose viscosity is unknown, simply by acquiring their transverse ^{1}H LF-NMR signals

Figure 12 Viscosity assessment of the biodiesel product using chemometrics. HCA dendrogram of six biodiesels (LIN: linseed, SOY: soy, CAN: canola, OLI: olive, MUS: mustard and CAS: castor) and nine petrodiesel-biodiesel mixture samples (BXX, where XX stands for the amount of castor biodiesel in the mixture) was calculated using the acquired transverse relaxation signals. A linkage distance threshold of 4000 yielded four groups which were assigned to different viscosities.

and analyzing them using chemometric tools like HCA and PCA. These methods can also be applied to find biodiesel samples that have residues of unreacted acylglycerol and/or methanol, and poorly separated and cleaned glycerol and water, provided a high quality biodiesel of the same source is used for comparison. All the aforementioned residues influence the viscosity of the sample, and accordingly affect the acquired transverse relaxation signal.

An example is shown on the PC_2 score line plot calculated using PCA on the pre-processed transverse relaxation signals (Figure 13). In order to show the effect of residues on the position of samples in the score line plot, the following samples were used along with all the biodiesels described before: (a) four of the samples collected and used to calculate the yield of TE reaction (3, 6, 12 and 30 min), to demonstrate acylglycerol residues; (b) two biodiesel samples with low water content (BIO+H2O1 and BIO+H2O2 consist of 3.33% and 6.66% v/v water in rapeseed biodiesel respectively); and (c) two biodiesel samples with low methanol content (BIO+MeOH1 and BIO+MeOH2 consist of 3.33% and 6.66% v/v methanol in rapeseed biodiesel respectively). The PC_2 scale of the plot was enlarged, in order to focus on the area of interest, therefore the castor biodiesel sample is not shown. Following the established correlation of PC_2 and viscosity [59], it is clearly demonstrated, that residues of water and/or methanol lead to lower than expected biodiesel viscosities, whereas high acylglycerol content lead to the opposite effect.

This tool allows to rapidly identify lower or higher viscosity samples than the one expected. More precisely, when using additionally samples whose viscosity is known (or estimated by their FAME profiles); it is possible to also approximate the viscosity value of the unknown samples, rather than simply assign them as higher or lower viscosities than the reference.

Conclusions
The novel ^{1}H LF-NMR applications presented offer great potential to the biodiesel industry for characterizing new alternative biodiesel resources in their whole conformation, monitoring the biodiesel TE reaction and evaluating
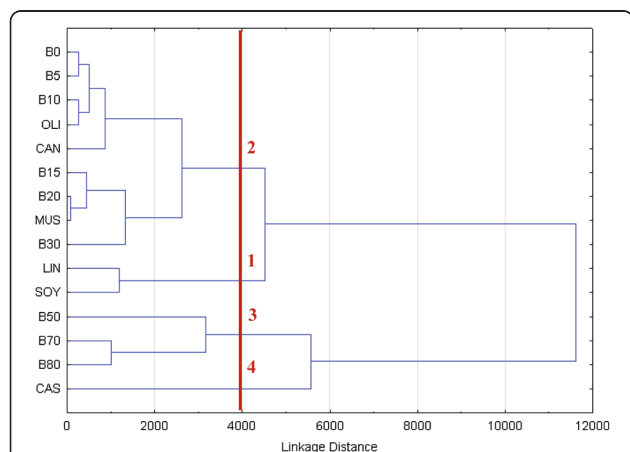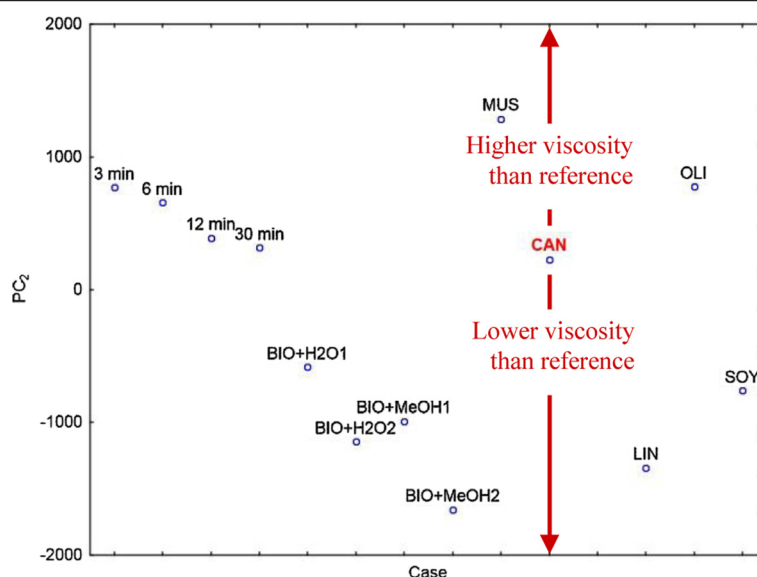
Figure 13 Identification of unwanted residues in biodiesel samples using chemometrics. Transverse relaxation data of the 6 biodiesels; samples collected throughout the monitoring experiment at 3, 6, 12 and 30 min; and mixture samples of rapeseed biodiesel with water or methanol (BIO+H2O1/2 and BIO+MeOH1/2 consist of 3.33% and 6.66% v/v water or methanol in rapeseed biodiesel respectively) are shown in a PC_2 score line plot. The PC_2 scale of the plot was enlarged, in order to focus on the area of interest, therefore the castor biodiesel sample is not shown. The rapeseed biodiesel is marked to easily estimate biodiesel samples with higher or lower viscosities.

the quality of the final product. In addition, the new integrated computational-experimental approach for ^{1}H LF-NMR relaxometry presented, suggests better resolved relaxation time distributions and more accurate solutions.

Materials and methods
Materials
CDCl$_3$ (99.8% + 0.05% v/v TMS) was purchased from D-Chem Ltd., Israel. Glycerol was purchased in a local pharmacy (Ph Eur grade, Floris, Israel). All other chemicals and reagents used in this study were analytical grade. All oils were purchased from local suppliers. Biodiesels were prepared through a base catalyzed reaction using several of the purchased oils. Petrodiesel was purchased at a local gas station.

Fresh olive fruits were harvested from a plot located in the central Negev, Israel. The whole dry olive sample was oven dried at 70°C for 72 h to remove excess moisture. Olive mill pomace was collected from Darawsha olive press (Iksal, Israel).

^{1}H LF-NMR signal acquisition
Relaxation time distribution experiments for peaks assignment of the olive oil and olive stone samples were performed on a DRX23 bench-top pulsed NMR analyzer (Resonance Instruments, Witney, UK) operating at 25°C, equipped with a permanent magnet and a 10 mm probe head operating at 23.4 MHz. Prior to measurement,

samples were equilibrated at 25°C for 1 h. All other ^{1}H LF-NMR measurements were performed on a Maran bench-top pulsed NMR analyzer (Resonance Instruments, Witney, UK) operating at 40°C, equipped with a permanent magnet and different diameter probe heads, operating at 23.4 MHz. Prior to measurement, samples were equilibrated at 40°C for 1 h.

1D relaxometry experiments were performed using a CPMG pulse sequence. This multiple sequence consists of applying a single 90°; pulse followed by multiple consecutive 180° pulses. This allows measuring transverse relaxation, which results from spin-spin interactions.

2D cross-correlation experiments were performed by a T_1-T_2 sequence, where an inversion recovery step $[180°-t_1]$ is inserted in front of the CPMG sequence [16]. Here the T_1 dimension is acquired by repeating the sequence a determined number of steps, where the space t_1 is varied logarithmically between runs. The t_1 period is dominated by longitudinal relaxation, including possible longitudinal cross relaxation processes; while the t_2 period is dominated by transverse relaxation processes [15].

All relaxation time distribution experiments on solid and liquid samples, were analyzed without further preparation. Samples were inserted in glass NMR tubes as whole, without using solvents or further crushing. Parameters in each pulse sequence were tailored according to the type of experiment and material. Following data acquisition the signal was phase rotated and only the main channel was used for the analyses.

Data analysis

Chemometrics

In this work, chemometric data analysis tools included PCA for unsupervised data exploration and PLS for creating multidimensional regression curve fitting [76-78]. Both these methods extract PCs and loadings to maximize the original variance and reduce dimensionality; hence they describe the data in a more condensed form. The PCs are mutually orthogonal and their extraction is such that the first PC holds the maximum variance, the second holds the second-maximum variance, and so on.

HCA was applied for clustering. HCA is an unsupervised clustering technique that examines the interpoint distances between all samples in row space and represents them in a dendrogram. To generate the dendrogram, a common approach is to initially treat each sample as a cluster and join closest clusters together. The process is repeated until only one group remains [77]. The amalgamation rule used was complete linkage and distances between clusters were calculated according to Euclidean distances. Analysis of results was carried out using the distance dendrogram.

All chemometric methods were computed using STATISTICA software (ver. 11.0, StatSoft). PCA and PLS were applied using the NIPALS algorithm on the covariance matrices. Transverse relaxation data was either used as acquired, or pre-processed by dividing the entire signal of each sample by its first (and highest) intensity.

Goodness of fit for the PLS regression model was determined using the validation set. RMSEP was calculated using Eq. (1):

$$RMSEP = \sqrt{\frac{\sum_{i=1}^{n}\left(x_{i,predicted} - x_{i,calculated}\right)^2}{n}} \tag{1}$$

where n is the number of observations.

Monoexponential and continuous distribution fitting of 1D relaxation signals

Monoexponential fitting was performed with the WinFit software package (Oxford Instruments, UK).

Conversion of the relaxation signal into a continuous distribution of relaxation components is performed using Eq. (2), where the probability density $f(T_2)$ is calculated applying ILT, $s(t)$ is the relaxation signal acquired with ^{1}H LF-NMR at time t, T_2 are the time constants, and $E(t)$ is the measurements error:

$$s(t) = \int e^{-t/T_2} f(T_2) dT_2 + E(t). \tag{2}$$

The most common numerical method implemented today for dealing with ill-posed problems of this kind is based on L_2-norm regularization, where Eq. (2) is approximated by a discretized matrix form, and minimized according to the L_2-norm expression:

$$f = argmin\|s - Kf\|_2^2 + \lambda\|f\|_2^2,$$
$$f \geq 0 \tag{3}$$

where K is the discrete Laplace transform, and λ is the L_2 weight. This type of regularization, however, can significantly distort the solution by contributing to the broadening of peaks.

In this work, we applied a novel numerical optimization method developed by our research team for analyzing the ^{1}H LF-NMR relaxometry data. Full description of the algorithm is described in an article recently (2012) submitted to Concepts in Magnetic Resonance A Journal. The new method applies the PDCO solver that can be adjusted to solve the inverse problem with nonnegativity constraints and an L_1 regularization term that stabilizes the solution process without introducing the typical L_2 peak broadening. The underlying principle is that all structured signals have sparse representation in an appropriate coordinate system, and using such a system/dictionary typically results in better solutions with a relatively low level of noise.

The mathematical formulation of our proposed method is the linearly constrained convex optimization problem

$$\min_{f,c,r} \lambda_1\|c\|_1 + \frac{1}{2}\lambda_2\|c\|_2^2 + \frac{1}{2}\|r\|_2^2$$
$$s.t. \; Kf + r = s,$$
$$-f + Bc = 0, \quad f \geq 0, \tag{4}$$

where K is the discrete Laplace transform, f is the unknown spectrum vector, s is the measurements vector, r is the residual vector, and B is a sparsifying dictionary.

L_2 calculations of relaxation time distribution were deconvoluted as a continuous distribution of relaxation times with the WinDXP ILT software package (Distributed ExPonential Analysis, Oxford Instruments, UK).

Continuous distribution fitting of 2D cross correlation relaxometry

2D cross correlation relaxometry signals were analyzed by 2D-ILT as described in [16], using an in-house program written in MATLAB as detailed by Hills et al. [15]. Briefly, the acquired 2D array of CPMG echo trains $s(t_1,t_2)$ is given as

$$s(t_1, t_2) = \iint \left(1 - 2e^{-t_1/T_1}\right) e^{-t_2/T_2} f(T_1, T_2) dT_1 dT_2$$
$$+ E(t_1, t_2), \tag{5}$$

where $s(t_1,t_2)$ is the relaxation signal acquired at t_1 and t_2 times, and the function $f(T_1,T_2)$ corresponds to the probability density of molecules with relaxation times of T_1, T_2.

Extraction

Oil extraction

For non-quantitative oil extraction, oil-containing materials were crushed manually in a mortar and incubated overnight with n-hexane in an orbital shaker at 25°C. The oil and n-hexane solution was then evaporated under a mild vacuum with a rotary evaporator. In cases where large volumes of oil were required (>10 ml), a cold-pressed extruder was used (Komet CA 59G, Monchengladbach, Germany).

Oil extraction for oil content measurements was carried out using a modified procedure according to the AOCS official method [79], using a soxhlet apparatus and n-hexane. Briefly, about 2 g of oil containing materials were manually crushed with a mortar and positioned in the extraction chamber for 24 h. The oil and n-hexane mixture was then evaporated under mild vacuum to obtain pure oil.

Alkali TE

Prior to biodiesel production, oils were heated to 80°C for 1 h to evaporate water, and then allowed to cool down to room temperature. Biodiesels were prepared in a batch laboratory scale TE process with methanol and KOH. Briefly, a potassium hydroxide solution was freshly prepared by mixing methanol (1:6 oil to methanol mol/mol) with KOH (100 g kg^{-1} of the oil). The reaction was carried out for 1 h under reflux at 50°C with constant stirring and then allowed to cool down to room temperature. The mixture was then transferred to a separating funnel and allowed to stand for approximately 1 h. The bottom layer (glycerol, methanol and most of the catalyst) was drained out. The upper layer (FAMEs, some methanol and traces of the catalyst) was cleaned thoroughly by washing 5 times with warm (~50°C) de-ionized water. The solution was then heated to 80°C for 30 min until cleared.

In situ TE of olive mill waste pomace

Prior to in situ TE reaction samples were oven dried at 70°C for 72 h to remove excess moisture. The dry pomace was then ground using a Hsiangtai electric grinder (Taipei Hsien, Taiwan) to provide more surface area for the reaction.

Because of high FFA content (2-13% FFA according to a titration procedure), pomace was first esterified using H_2SO_4. Briefly, 100 g of dry and grounded pomace were reacted under reflux and stirring, with 2 ml H_2SO_4 (0.094 M) and 400 ml methanol. The reaction was carried out for 1 h at 65°C. An alkali TE reaction was then performed as described before. Prior to reaction, the remaining sulfuric acid was neutralized using a KOH in methanol solution (4.8% w/w). Eventually, 200 ml n-hexane was added to extract the biodiesel. The final product was separated into solid and liquid fractions by filtration. The liquid fraction was transferred to a separating funnel and allowed to settle for 30 min. The bottom layer consisting of methanol, residual catalyst and soluble sub-millimeter particles was removed, and the upper layer consisting of the biodiesel produced and n-hexane was washed several times with warm (~50°C) de-ionized water. The biodiesel produced was eventually recovered using a rotary evaporator, and heated to 80°C for 60 min until cleared.

Identification

GC

GC was used for identification and quantification of FAMEs. The FA composition was used to calculate the kinematic viscosity of biodiesels as described by Allen et al. [13] using Eq. (6). μ_i and μ_0 are the kinematic viscosities at 40°C of each FA and biodiesel, respectively; y_i is the mass fraction of each FA. Neat FA viscosities, given as FAMEs, were taken from [75]. The viscosity of arachidic acid (20:0) was assumed to be similar to that of stearic acid (18:0), as suggested by Allen et al. [13].

$$\ln \mu_0 = \sum_{i=1}^{n} y_i \ln \mu_i \qquad (6)$$

GC analyses were conducted on a Varian 3400 apparatus (Palo Alto, CA, USA) equipped with a flame ionization detector and a Stabilwax-DA capillary column (RESTEK, Bellefonte, US; Dimensions: 15 m × 0.32 mm × 0.25 μm).

¹H HR-NMR

^{1}H HR-NMR analyses were conducted on a Bruker DMX-500 NMR spectrometer (Bruker, Germany) operating at 500 MHz. ^{1}H HR-NMR was used to monitor acylglycerol residues in biodiesel. Prior to measurement, samples were dissolved in $CDCl_3$.

The yield (C) of TE reaction was calculated according to Eq. (7), where A_{ME} is the integrated signal at 3.7 ppm corresponding to methyl protons in methyl esters; and A_{CH2} is the integrated signal at 2.3 ppm due to methylene protons adjacent to the ester group in triglycerides [65].

$$C = 100 * \frac{2A_{ME}}{3A_{CH_2}} \qquad (7)$$

Additional files

Additional file 1: Correlation of the slope and T$_2$ of the 9 different oils. Slopes were calculated by fitting the extracted PC_1 and PC_2 of each of the individual oils separately. T_2 was the average value for each of the 4 samples per oil, calculated using monoexponential fitting.

Additional file 2: Correlation of measured *vs.* calculated oil content of the nine different oils through PLS. The correlation was performed on the validation set.

Additional file 3: Relaxation time distribution of different methanol-glycerol mixtures. The methanol to glycerol ratio (M:G) of each mixture is shown on each plot. The relaxation time distribution of methanol (MeOH) and glycerol (Gly) are shown for reference.

Additional file 4: Correlation of the yield calculated from ^{1}H LF-NMR to that of ^{1}H HR-NMR. The yield based on relaxation time distribution was calculated from the oil to biodiesel peaks area. The samples used for the correlation include six samples collected while TE reaction of rapeseed oil was proceeding, following separation and cleaning, and three additional samples prepared using low catalyst concentration (0.05%, 0.1% and 0.15% w/w KOH).

Abbreviations

1D: One dimensional; 2D: Two dimensional; CP: Cross peak; CPMG: Carr, Purcell, Meiboom and Gill; FA: Fatty acid; FFA: Free fatty acid; GC: Gas chromatograph; HCA: Hierarchal cluster analysis; HR-NMR: High resolution nuclear magnetic resonance; ILT: Inverse laplace transform; LF-NMR: Low field nuclear magnetic resonance; PC: Principal component; PCA: Principal component analysis; PDCO: Primal-dual interior method for convex objectives; PLS: Partial least squares; RMSEP: Root mean squared error of prediction; TE: Transesterification.

Competing interests

The authors declare that they have no competing interests.

Authors' contributions

PB designed and performed most of the experiments, analyzed results, contributed in the establishment and validation of the new PDCO algorithm, and drafted the manuscript. AL performed the monitoring of the TE process and calculation of yield using relaxation time distribution experiments. OE performed and optimized the monitoring of the in situ TE process of pomace using relaxation time distribution experiments. OL, YP and MS formulated, designed and established the PDCO algorithm. ZW led and coordinated the overall project, contributed to the development of the experimental design and proofread the manuscript. All authors read and approved the final manuscript.

Author details

[1]The Phyto-Lipid Biotechnology Lab, Departments of Biotechnology, Energy and Environmental Engineering, Ben-Gurion University of the Negev, P.O. Box 653, Beer-Sheva 84105, Israel. [2]Department of Industrial Engineering and Management, Ben-Gurion University of the Negev, P.O. Box 653, Beer-Sheva 84105, Israel. [3]Department of Management Science and Engineering, Stanford University, Stanford, CA, USA.

References

1. Bhardwaj HL: **Utilizing locally-produced canola to manufacture biodiesel**. In *Proceedings of the Sixth National Symposium on Creating Markets for Economic Development of New Crops and New Uses: 14-18 October 2006; San Diego, California*. Edited by Janick J, Whipkey A. Alexandria: ASHS Press; 2007:43–46.
2. Sorda G, Banse M, Kemfert C: **An overview of biofuel policies across the world**. *Energ Policy* 2010, **38**:6977–6988.
3. Gui MM, Lee KT, Bhatia S: **Feasibility of edible oil vs. non-edible oil vs. waste edible oil as biodiesel feedstock**. *Energy* 2008, **33**:1646–1653.
4. Conceicao MM, Candeia RA, Silva FC, Bezerrab AF, Fernandes VJ, Souza AG: **Thermoanalytical characterization of castor oil biodiesel**. *Renew Sust Energ Rev* 2007, **11**:964–975.
5. Berman P, Nizri S, Wiesman Z: **Castor oil biodiesel and its blends as alternative fuel**. *Biomass Bioenerg* 2011, **35**:2861–2866.
6. Openshaw K: **A review of Jatropha curcas: an oil plant of unfulfilled promise**. *Biomass Bioenerg* 2000, **19**:1–15.
7. Hossain ABMS, Salleh A, Boyce AN, Chowdhury P, Naqiuddin M: **Biodiesel fuel production from algae as renewable energy**. *Am J Biochem Biotechnol* 2008, **4**:250–254.
8. Canakci M, Van Gerpen J: **Biodiesel production from oils and fats with high free fatty acids**. *TRANS ASAE* 2001, **44**:1429–1436.
9. Dufreche S, Hernandez R, French T, Sparks D, Zappi M, Alley E: **Extraction of lipids from municipal wastewater plant microorganisms for production of biodiesel**. *J Am Oil Chem Soc* 2007, **84**:181–187.
10. Willson RM, Wiesman Z, Brenner A: **Analyzing alternative bio-waste feedstocks for potential biodiesel production using time domain (TD)-NMR**. *Waste Manage* 2010, **30**:1881–1888.
11. Fernández CM, Ramos MJ, Perez A, Rodriguez JF: **Production of biodiesel from winery waste: extraction, refining, and transesterification of grape seed oil**. *Bioresource Technol* 2010, **101**:7019–7024.
12. Knothe G: **Analyzing biodiesel: standards and other methods**. *J Am Oil Chem Soc* 2006, **83**:823–833.
13. Allen CAW, Watts KC, Ackman RG, Pegg MJ: **Predicting the viscosity of biodiesel fuels from their fatty acid ester composition**. *Fuel* 1999, **78**:1319–1326.
14. Knothe G, Steidley KR: **Kinematic viscosity of biodiesel fuel components and related compounds. Influence of compound structure and comparison to petrodiesel fuel components**. *Fuel* 2005, **84**:1059–1065.
15. Hills B, Benamira S, Marigheto N, Wright K: T_1-T_2 **correlation analysis of complex foods**. *Appl Magn Reson* 2004, **26**:543–560.
16. Song YQ, Venkataramanan L, Hürlimann MD, Flaum M, Frulla P, Straley C: T_1–T_2 **correlation spectra obtained using a fast two dimensional Laplace inversion**. *J Magn Reson* 2002, **154**:261–268.
17. Kroeker RM, Henkelman RM: **Analysis of biological NMR relaxation data with continuous distributions of relaxation times**. *J Magn Reson* 1986, **69**:218–235.
18. Hahn EL: **Spin echoes**. *Phys Rev* 1950, **80**:580–594.
19. Stejskal EO, Tanner JE: **Spin diffusion measurements: SE in the presence of a time-dependent field gradient**. *J Chem Phys* 1965, **42**:288–292.
20. Carr HY, Purcell EM: **Effects of diffusion on free precession in nuclear magnetic resonance experiments**. *Phys Rev* 1954, **94**:630–638.
21. Meiboom S, Gill D: **Modified spin-echo method for measuring nuclear relaxation times**. *Rev Sci Instrum* 1958, **29**:688–691.
22. Abragam A: *The Principles of Nuclear Magnetism*. Clarendon: Oxford University Press; 1961.
23. Gambhir PN: **Application of low-resolution pulsed NMR to the determination of oil and moisture in oilseeds**. *Trends Food Sci Tech* 1992, **3**:191–196.
24. Rubel G: **Simultaneous determination of oil and water contents in different oilseeds by pulsed nuclear magnetic resonance**. *J Am Oil Chem Soc* 1994, **71**:1057–1062.
25. Pedersen HT, Munck L, Engelsen SB: **Low-field ^{1}H nuclear magnetic resonance and chemometrics combined for simultaneous determination of water, oil, and protein contents in oilseeds**. *J Am Oil Chem Soc* 2000, **77**:1069–1077.
26. Gao C, Xiong W, Zhang Y, Yuan W, Wu Q: **Rapid quantitation of lipid in microalgae by time-domain nuclear magnetic resonance**. *J Microbiol Meth* 2008, **75**:437–440.
27. Correa CC, Forato LA, Colnago LA: **High-throughput non-destructive nuclear magnetic resonance method to measure intramuscular fat content in beef**. *Anal Bioanal Chem* 2009, **393**:1357–1360.
28. Bosin WA, Marmor RA: **The determination of the solids content of fats and oils by nuclear magnetic resonance**. *J Am Oil Chem Soc* 1968, **45**:335–337.
29. Jepsen SM, Pedersen HT, Engelsen SB: **Application of chemometrics to low-field ^{1}H NMR relaxation data of intact fish flesh**. *J Sci Food Agr* 1999, **79**:1793–1802.
30. Bertram HC, Andersen HJ, Karlsson AH: **Comparative study of low-field NMR relaxation measurements and two traditional methods in the determination of water holding capacity of pork**. *Meat Sci* 2001, **57**:125–132.
31. Bertram HC, Donstrup S, Karlsson AH, Andersen HJ: **Continuous distribution analysis of T_2 relaxation in meat- an approach in the determination of water-holding capacity**. *Meat Sci* 2002, **60**:279–285.
32. Rutledge DN: **Characterisation of water in agro-food products by time domain-NMR**. *Food Control* 2001, **12**:437–445.

33. Choi SG, Kerr WL: ^{1}H NMR studies of molecular mobility in wheat starch. *Food Res Int* 2003, **36**:341–348.

34. Goetz J, Koehler P: Study of the thermal denaturation of selected proteins of whey and egg by low resolution NMR. *LWT- Food Sci Technol* 2005, **38**:501–512.

35. Lucas T, Le Ray D, Barey P, Mariette F: NMR assessment of ice cream: effect of formulation on liquid and solid fat. *Int Dairy J* 2005, **15**:1225–1233.

36. Prestes RA, Colnago LA, Forato LA, Vizzotto L, Novotny EH, Carrilho E: A rapid and automated low resolution NMR method to analyze oil quality in intact oilseeds. *Anal Chim Acta* 2007, **596**:325–329.

37. Metz H, Mäder K: Benchtop-NMR and MRI – a new analytical tool in drug delivery research. *Int J Pharm* 2008, **364**:170–175.

38. McDonald PJ, Korb JP, Mitchell J, Monteilhet L: Surface relaxation and chemical exchange in hydrating cement pastes: a two-dimensional NMR relaxation study. *Phys Rev E* 2005, **72**:011409.

39. Callaghan PT, Godefroy S, Ryland BN: Diffusion–relaxation correlation in simple pore structures. *J Magn Reson* 2003, **162**:320–327.

40. Godefroy S, Callaghan PT: 2D relaxation/diffusion correlations in porous media. *Magn Reson Imaging* 2003, **21**:381–383.

41. Hürlimann MD, Flaum M, Venkataramanan L, Flaum C, Freedman R, Hirasaki GJ: Diffusion–relaxation distribution functions of sedimentary rocks in different saturation states. *Magn Reson Imaging* 2003, **21**:305–310.

42. Marigheto N, Duarte S, Hills BP: NMR relaxation study of avocado quality. *Appl Magn Reson* 2005, **29**:687–701.

43. Hills BP, Costa A, Marigheto N, Wright K: T_1–T_2 NMR correlation studies of high-pressure processed starch and potato tissue. *Appl Magn Reson* 2005, **28**:13–27.

44. Marigheto N, Luca Venturi, Hills B: Two-dimensional NMR relaxation studies of apple quality. *Postharvest Biol Tech* 2008, **48**:331–340.

45. Furfaro ME, Marigheto N, Moates G, Cross K, Parker ML, Waldron K, Hills B: A multidimensional NMR cross-correlation relaxation study of carrot phloem and xylem: Part I. Peak assignment. *Appl Magn Reson* 2008, **35**:521–535.

46. Hills BP: Applications of low-field NMR to food science. *Ann R NMR S* 2006, **58**:177–230.

47. Nordon A, Macgill CA, Littlejohn D: Process NMR spectrometry. *Analyst* 2001, **126**:260–272.

48. Hopke PK: The evolution of chemometrics. *Anal Chim Acta* 2003, **500**:365–377.

49. Kim YR, Yoo BS, Cornillon P, Lim ST: Effect of sugars and sugar alcohols on freezing behavior of corn starch gel as monitored by time domain ^{1}H NMR spectroscopy. *Carbohyd Polym* 2004, **55**:27–36.

50. Hickey H, MacMillan B, Newling B, Ramesh M, Eijck PV, Balcom B: Magnetic resonance relaxation measurements to determine oil and water content in fried foods. *Food Res Int* 2006, **39**:612–618.

51. Kenar JA: Direct determination of the lipid content in starch–lipid composites by time-domain NMR. *Ind CropProd* 2007, **26**:77–84.

52. Baranowska HM, Sikora M, Kowalski S, Tomasik P: Interactions of potato starch with selected polysaccharide hydrocolloids as measured by low-field NMR. *Food Hydrocolloid* 2008, **22**:336–345.

53. Whittall KP, MacKay AL: Quantitative interpretation of NMR relaxation data. *J Magn Reson* 1989, **84**:134–152.

54. Graham SJ, Stanchev PL, Bronskill MJ: Criteria for analysis of multicomponent tissue T_2 relaxation data. *Magnet Reson Med* 1996, **35**:370–378.

55. Moody JB, Xia Y: Analysis of multi-exponential relaxation data with very short components using linear regularization. *J Magn Reson* 2004, **167**:36–41.

56. Saunders MA, Kim B: *PDCO: Primal-dual interior method for convex objectives.* http://www.stanford.edu/group/SOL/software/pdco.html.

57. Zhang Y, Dube MA, McLean DD, Kates M: Biodiesel production from waste cooking oil: 2. Economic assessment and sensitivity analysis. *Bioresource Technol* 2003, **90**:229–240.

58. ISO 10565: *Simultaneous determination of oil and water contents: Method using pulsed nuclear magnetic resonance spectrometry.* 1998.

59. Berman P, Nizri S, Parmet Y, Wiesman Z: Large-scale screening of intact castor seeds by viscosity using time-domain NMR and chemometrics. *J Am Oil Chem Soc* 2010, **87**:1247–1254.

60. Pattara C, Cappelletti G, Cichelli A: Recovery and use of olive stones: commodity, environmental and economic assessment. *Renew Sust Energ Rev* 2010, **14**:1484–1489.

61. Fedeli E: Lipids in olives. *Prog Chem Fats Other Lipids* 1977, **15**:57–74.

62. Heredia A, Guillén R, Fernández-Bolaños J, Rivas M: Olives stone as a source of fermentable sugars. *Biomass* 1987, **14**:143–148.

63. MacKay AL, Wallace JC, Sasaki K, Taylor IEP: Investigation of the physical structure of the primary plant cell wall by proton magnetic resonance. *Biochemistry* 1988, **27**:1467–1473.

64. Etziony O, Knoll YM, Berman P, Krawczyk C, Yarmolinsky L, Wiesman Z: From organic solid waste to biofuels: in-situ transesterification of olive mill solid waste. In *Proceedings of the 4th International Symposium on Energy from Biomass and Waste, Biodiesel from Biomass: 12-15 November 2012.* Edited by Ragazzi M. Venice, Italy: CISA Publisher; 2012.

65. Meher LC, Vidya Sagar D, Naik SN: Technical aspects of biodiesel production by transesterification-a review. *Renew Sust Energ Rev* 2006, **10**:248–268.

66. Georgogianni KG, Kontominas MG, Pomonis PJ, Avlonitis D, Gergis V: Alkaline conventional and in situ transesterification of cottonseed oil for the production of biodiesel. *Energ Fuel* 2008, **22**:2110–2115.

67. Guillén MD, Ruiz A: [1]H-nuclear magnetic resonance as a fast tool for determining the composition of acyl chains in acylglycerol mixtures. *Eur J Lipid Sci Tech* 2003, **105**:502–507.

68. Skloss TW, Kim AJ, Haw JF: High resolution NMR process analyzer for oxygenates in gasoline. *Anal Chem* 1994, **66**:536–542.

69. McGill CA, Nordon A, Littlejohn D: Comparison of in-line NIR, Raman and UV-visible spectrometries, and at-line NMR spectrometry for the monitoring of an esterification reaction. *Analyst* 2002, **127**:287–292.

70. Buljubasich L, Blümich B, Stapf S: Reaction monitoring of hydrogen peroxide decomposition by NMR relaxometry. *Chem Eng Sci* 2010, **65**:1394–1399.

71. Dalitz F, Cudaj M, Maiwald M, Guthausen G: Process and reaction monitoring by low-field NMR spectroscopy. *Prog Nucl Mag Res Sp* 2012, **60**:52–70.

72. Linck YG, Killner MHM, Danieli E, Blümich B: Mobile low field ^{1}H NMR spectroscopy desktop analysis of biodiesel production. *Appl Magn Reson* 2013, **44**:41–53.

73. Cabeça LF, Marconcini LV, Mambrini GP, Azeredo RBV, Colnago LA: Monitoring the transesterification reaction used in biodiesel production, with a low cost unilateral nuclear magnetic resonance sensor. *Energ Fuel* 2011, **25**:2696–2701.

74. Rashid U, Anwar F: Production of biodiesel through optimized alkaline-catalyzed transesterification of rapeseed oil. *Fuel* 2008, **87**:265–273.

75. Knothe G: Dependence of biodiesel fuel properties on the structure of fatty acid alkyl esters. *Fuel Process Technol* 2005, **86**:1059–1070.

76. Wold S, Berglund A, Kettaneh N: New and old trends in chemometrics. How to deal with the increasing data volumes in R&D&P (research, development and production): with examples from pharmaceutical research and process modeling. *J Chemometr* 2002, **16**:377–386.

77. Alam TM, Alam MK: Chemometric analysis of NMR spectroscopy. *Ann R NMR S* 2005, **54**:41–79.

78. Viereck N, Nørgaard L, Bro R, Engelsen SB: Chemometric analysis of NMR data. In *Modern Magnetic Resonance. Part 3.* Edited by Webb GA. Dordrecht: Springer; 2008:1833–1843.

79. AOCS: *Official methods and recommended practices of the American Oil Chemists' Society (fifth ed.).* Champaign, IL: AOCS Press; 1998.

2.4. **<u>Berman P</u>**, Meiri N, Colnago LA, Moraes TB, Linder C, Levi O, Parmet Y, Saunders M, Wiesman Z: Study of liquid phase molecular packing interactions and morphology of fatty acid methyl esters (biodiesel). *Biotechnol Biofuels* 2015, in press.

Study of liquid phase molecular packing interactions and morphology of fatty acid methyl esters (biodiesel)

Paula Berman[a]
Email: bermansh@gmail.com

Nitzan Meiri[a]
Email: nitzanme@post.bgu.ac.il

Luiz Alberto Colnago[b]
Email: luiz.colnago@embrapa.br

Tiago Bueno Moraes[c]
Email: tiagobuemoraes@gmail.com

Charles Linder[d]
Email: charles.linder@gmail.com

Ofer Levi[e]
Email: levio@bgu.ac.il

Yisrael Parmet[e]
Email: iparmet@bgu.ac.il

Michael Saunders[f]
Email: saunders@stanford.edu

Zeev Wiesman[a,*]
* Corresponding author
Email: wiesman@bgu.ac.il
Tel/fax: 972-8-6477184

[a] The Phyto-Lipid Biotechnology Lab, Departments of Biotechnology, Energy and Environmental Engineering, Ben-Gurion University of the Negev, P.O. Box 653, Beer-Sheva 84105, Israel

[b] Embrapa Instrumentação, Rua 15 de Novembro 1452, São Carlos, SP 13560-970, Brazil

[c] Instituto de Física de São Carlos, Universidade de São Paulo, Av. Trabalhador Sao-Carlense 400, São Carlos-SP, 13566-590, Brazil.

[d] Zuckerberg Center for Water Sciences and Technology and Department of Biotechnology, Ben-Gurion University of the Negev, P.O. Box 653, Beer-Sheva 84105, Israel

[e] Department of Industrial Engineering and Management, Ben-Gurion University of the Negev, P.O. Box 653, Beer-Sheva 84105, Israel

[f] Department of Management Science and Engineering, Stanford University, Stanford, CA

Abstract

Background

^{1}H Low Field Nuclear Magnetic Resonance (LF-NMR) relaxometry has been suggested as a tool to distinguish between different molecular ensembles in complex systems with differential segmental or whole molecular motion and/or different morphologies. In biodiesel applications the molecular structure vs. liquid phase packing morphologies of Fatty Acid Methyl Esters (FAMEs) influences physico-chemical characteristics of the fuel including flow properties, operability during cold weather, blending and more. Still, their liquid morphological structures have been scarcely studied. It was therefore the objective of this work to explore the potential of this technology for characterizing the molecular organization of FAMEs in the liquid phase. This was accomplished by using a combination of supporting advanced technologies.

Results

We show that pure Oleic Acid (OA) and Methyl Oleate (MO) standards exhibited both similarities and differences in the ^{1}H LF-NMR relaxation times (T_2s) and peak areas, for a range of temperatures. Based on X-ray measurements, both molecules were found to possess a liquid crystal-like order, although a larger fluidity was found for MO because as the temperature is increased, MO molecules separate both longitudinally and transversely from one and other. In addition, both molecules exhibited a preferred direction of diffusion based on the apparent hydrodynamic radius. The close molecular packing arrangement and interactions were found to affect the translational and segmental motions of the molecules, as a result of dimerization of the head group in OA as opposed to weaker polar interactions in MO.

Conclusions

A comprehensive model for the liquid crystal-like arrangement of FAMEs in the liquid phase is suggested. The differences in translational and segmental motions of the molecules were rationalized by the differences in the ^{1}H LF-NMR T_2 distributions of OA and MO, which was further supported by ^{13}C High Field (HF)-NMR spectra and ^{1}H HF-NMR relaxation. The proposed assignment allows for material characterization based on parameters that contribute to properties in applications such as biodiesel fuels.

Key words: ^{1}H low field nuclear magnetic resonance relaxometry; Biodiesel physical properties; Methyl oleate; Molecular packing; Oleic acid; Segmental motion.

1. Background

Biodiesel production has increased dramatically over the last decade, raising the need for new rapid and non-destructive analytical tools and technologies. Several [1]H Low Field Nuclear Magnetic Resonance (LF-NMR) applications have been suggested by the authors for the field of biodiesel, including characterization of new alternative biodiesel resources by direct analysis of raw material sources, monitoring of the biodiesel transesterification reaction, and quality evaluation of the final product [1-6]. ^{1}H LF-NMR relaxometry involves the measurement of relaxation constants, T_1 and T_2, as a consequence of interactions between nuclear spins and their surrounding and among nuclear spins [6]. In addition, it was suggested that the application of a novel numerical optimization method for analyzing ^{1}H LF-NMR data [6,7] provides better resolved relaxation time distributions and more accurate solutions when compared with those shown by existing numerical tools. For example, using this optimization method the relaxation time distributions of rapeseed oil and biodiesel samples revealed 4 and 3 peaks respectively, compared to a broad bimodal distribution and a single wide peak distribution for the same samples analyzed using WinDXP software [8].

^{1}H LF-NMR spin-spin (T_2) relaxometry has been suggested as a tool to distinguish between molecular populations in complex systems with differential mobilities and/or microscopic compartmentalization [9-13]. Still, the peaks in the analyzed T_2 distributions of lipids have not been hitherto assigned to the appropriate molecular population arrangements with certainty. Marigheto et al. [14] speculated that the analyzed bimodal T_2 distribution of an avocado oil sample arises from molecules of differing mobility, such as the oleic and palmitic constituents, or from nonequivalent

proton pools of different mobility, such as those on methyl and olefinic groups. Adam-Berret et al. [15] found a similar two-peak distribution for tricaprin in the melt state, and suggested that this may be due to inhomogeneous relaxation rates for the protons along the side chains, or inhomogeneous organization of the Triglycerides (TGs) in the liquid with intermolecular interactions. Of course these hypotheses are interrelated, since different mobilities along the side chains of the TGs in the liquid phase are characteristic of different organizations and vice versa. Callaghan [16] studied the molecular motion of tristearin in the melt and found different T_2s along the chains, which in turn were used to explain the tuning fork molecular configuration.

The liquid morphological structures of lipids, as opposed to crystal structures, have not been significantly studied because their experimental determinations are very difficult and require a combination of different investigation methods. Three models have been previously suggested for the arrangement of TGs in the melt including the smectic, nematic and discotic liquid crystal models, as reviewed by Iwahashi and Kasahara [17]. However, the conclusive structure of liquid TGs still requires further research. Fatty Acids (FAs) are significant building blocks of most lipids, including TGs. Short range order was also found to exist between the aliphatic chains in the liquid state of FAs. This was attributed by Small [18] to a relatively small volume increase occurring during the melting of the crystalline chains to liquids, and was strengthened by the fact that X-ray scattering showed that domains of layered structures, with one dimension roughly equivalent to the lengths of the molecules, are present in the liquid.

The group of Iwahashi has thoroughly studied the self-organization of FAs in the neat liquid state [17,19-25]. They concluded using near-infrared spectroscopy and vapor

pressure osmosis on various FAs, that these exist mostly as dimers, even at high temperature, where the dimers are the units in their intra- or intermolecular movements. These were found to aggregate to form clusters possessing the structure of a quasi-smectic liquid crystal, where the long-chained FA dimers arrange longitudinally and alternately to make an interdigitated structure in the clusters, with the tail of two dimers near the interacting head groups of the adjacent one. This has been determined from measurements of viscosity, density, High Field (HF)-NMR and X-ray diffraction [26].

The physical properties of FAs and their derivatives are largely determined by the length of the hydrocarbon chain and the degree of unsaturation, which affect the different degrees of molecular packing. In the fully saturated compounds, free rotation around each carbon–carbon bond gives the hydrocarbon chain greater flexibility; the most stable conformation is the fully extended form, in which the steric hindrance of neighboring atoms is minimized. These molecules can pack together tightly in nearly crystalline arrays, with atoms all along their lengths in van der Waals contact with the atoms of neighboring molecules. In unsaturated FAs, a cis double bond forces a kink in the hydrocarbon chain. FAs with several such kinks cannot pack together as tightly as one kink or fully saturated FAs, and their intermolecular interactions are therefore weaker. FAs of the same chain length have lower melting points as the degree of unsaturation is increased, as it takes less thermal energy to disorder them [27].

Surprisingly, the liquid structure of Fatty Acid Methyl Esters (FAMEs), which are derivatives of FAs, has caught very little attention in the literature. FAMEs, the basic molecules that constitute biodiesel, can be achieved by transesterification of TGs using methanol in the presence of a catalyst. Their molecular organization in the melt

is of high importance to the field of biodiesel, as it determines physico-chemical properties of the fuel, including flow properties, operability during cold weather, blending and more.

Knothe [28] analyzed the cetane number, heat of combustion, cold flow, oxidative stability, viscosity and lubricity of common FAMEs, and showed that oleic acid methyl ester (methyl oleate) is the best FAME for high quality biodiesel. Furthermore, there are several genetically modified oil seeds available in the market (soybean, sunflower, peanut) with high methyl oleate content (80%).

It was therefore the objective of this work to explore the potential of ^{1}H LF-NMR spin-spin relaxometry technology to study the molecular details and aggregation of FA and their FAME lipid derivatives in the liquid phase, using oleic acid and oleic acid methyl ester as a model biodiesel. This was accomplished by using a combination of supporting advanced technologies, including ^{1}H LF-NMR diffusiometry, X-ray diffraction, ^{13}C and ^{1}H HF-NMR. As will be shown, this new application of ^{1}H LF-NMR is of high importance to the field of biodiesel characterization, and also to other research and applied disciplines.

2. Results

2.1. ^{1}H LF-NMR T_2 distributions

The combined ^{1}H LF-NMR T_2 distributions of Oleic Acid (OA) and Methyl Oleate (MO) at different temperatures are presented in Figures 1A and 1B respectively. Intrinsic T_2 values and relative contributions of each peak are marked on each plot. For example, in Figure 1A at 288 K, intrinsic T_2 values for peaks 1 and 2 are 103 and 251 ms respectively; and relative contributions are 57 and 43% for the same peaks. In

both Figures, T_2 distributions exhibit two distinct peaks at different T_2 values. As suggested before [14,15] for TGs, the two peaks may be the result of two distinct mobility populations of the protons on the chain, or inhomogeneous structural organizations with two different packing densities and intermolecular interaction intensities or types.

Furthermore, pronounced alterations in the T_2 distributions are found. When comparing two distributions for the same temperature, a shift in the T_2 of the peaks of MO is observed towards higher values. Another interesting result is related to the change in the relative contribution of the peaks in the distribution as temperature changes, which is mostly pronounced for MO. A closer look into the effect of temperature on the intrinsic T_2 values and relative areas of each peak can be seen in Figures 2A-2D. A highly linear increase with temperature of intrinsic T_2 values can be observed for all peaks ($R^2 \geq 0.98$, Figure 2A and 2B). This suggests an increase in the mobility of different protons along the chain, or a change in the molecular organization with a change in intermolecular interactions towards the higher mobility peak (or population). Interestingly, the higher mobility peak (T_{22}) is more affected by temperature, as it exhibits larger slopes compared to the low mobility peak (T_{21}).

These differences are induced by small changes in the chemical structure of the lipid materials. Since both molecules (OA and MO) consist of the same tail (same length and position of double bond), the differences in this case are attributed to a methyl ester vs a carboxylic head group, which is responsible for a major intermolecular interaction of the chain with its neighbor.

As described in the introduction, the molecular organization of OA in the liquid has been extensively studied by Iwahashi's team [17 and references therein]. The stability

of the interdigitated structure of OA was mainly attributed to their arrangement in a head-to-head conformation, driven by strong intermolecular hydrogen bonding of the carboxyl groups. In the case of esters, the arrangement of the heads is not obvious and depends on the polarity of the head group. Malkin [29] stated that methyl esters in the solid state behave in a weaker degree like the acids, crystallizing as dimer molecules with the polar groups together. It has also been suggested that a head-to-tail arrangement, where the polar groups in all layers have the same direction, can only be formed in cases of extremely weak polar forces like in ethyl stearate [30]. In a study to determine end-to-end distances of liquid alkanes, Brady et al. [31] substituted one or two ends of the molecules with bromine atom. They found that with a single substitution the chains lined up end-to-end so that the Br's seek maximum contact with each other, and concluded that this was due to stronger interactions between two polar Br than those between Br and a hydrocarbon chain end. This can be considered as analogous to the polar interactions of two ester groups. In a study of the crystal structure of methyl stearate the authors suggested that the molecules form double sheets like the acids, probably due to polar forces between oxygen and carbon atoms [32].

We therefore assume the head-to-head conformation for the MO molecules in the liquid. Based on the crystal structure recently suggested for ethyl acetate [33], we would like to propose the configuration shown in Figure 3. Here the resonance structures of the ester group result in weak interactions between the polarized hydrogen of the methyl carbon and the oxygen of the carbonyl on the opposite MO molecule. This molecular arrangement for MO would maximize the polar interactions. The effect of this weaker interaction on their structure and mobility will be further discussed.

2.2. X-ray measurements

In order to investigate whether short-range order exists for MO, and compare to the already-determined X-ray bands of OA, X-ray measurements were performed. X-ray patterns of liquids consist of one or several broad rings where the position of the maximum $2\theta_{max}$ corresponds with high accuracy to the average intermolecular spacing, d. Iwahashi et al. [21] performed X-Ray Diffraction (XRD) measurements on several types of FAs, and found similar spectra for all the materials, consisting of mainly a large and sharp band around 0.14 nm^{-1}, and a small and broad band around 0.03 nm^{-1}. They suggested that the band around 0.14 nm^{-1} gives a measure of the spacing between adjacent molecules (short range), and the small band at around 0.03 nm^{-1} provided information regarding the long spacing of the plane made by the aligned molecules. In this study, XRD measurements on both materials showed only a single broad peak at around 0.14 nm^{-1}, probably due to instrumentation differences. The 0.03 nm^{-1} peak was therefore measured using Small Angle X-ray Scattering (SAXS) technology.

Figures 4A and 4B show the X-ray spectra for OA and MO at 298 K using XRD and SAXS instruments respectively. As shown, the peak around 0.14 nm^{-1} is sharp for both materials, whereas the peak around 0.03 nm^{-1} is very broad and difficult to resolve, especially for the MO sample. The broadness of the peaks suggests a lower degree of order, especially in the long-range spacing. Short- and long-range spacing, d, derived from the corresponding spectra are summarized in Table 1.

The short- and long-range spacing for the OA material were found to be in excellent agreement with those previously reported [21]. The short-range spacing of both materials was similar, probably due to similarities in the structure of the tails, leading

to close inter-chain interactions. On the other hand, a larger long-range spacing was found for the MO compared to OA, even when considering the distance from melting point (2.383 nm for OA at 298 K versus 2.517 nm for MO at 263 K). The difference in the long-range spacing originates from larger distance between repeating planes. Considering the model proposed in this work for the head-to-head configuration of two opposite MO molecules (Figure 3), it would be fair to suggest that this is the result of the weak CH---O hydrogen bridges leading to larger distance between head groups. To be more specific, MO heads interact through weak polar interactions that form octagons (larger long-spacing), while OA heads interact through hydrogen bonding, which makes hexagons (shorter long-spacing).

The longer spacing between two MO molecules is a clear explanation for its reduced density and lower melting point compared to OA (0.874 g/cm^3 [34] and 253.1 K [35], vs. 0.891 g/cm^3 and 286 K, both taken from [19], for MO and OA respectively with densities reported for 293 K). Both density and melting point parameters suggest a less efficient packing of MO.

To explore the effect of temperature on the short- and long-range spacings, further X-ray measurements were performed (Figures 5A and 5B respectively). Iwahashi et al. [21] found that the long spacing in OA is constant regardless of temperature, whereas the short spacing increases with temperature. Our measurements show a similar increase in the short spacing with temperature for both OA and MO. The long spacing for MO also increased with temperature and showed a moderate, close to linear increase from a temperature close to the melting point until 343 K. These results imply a larger fluidity of MO compared to OA because MO molecules separate both longitudinally and transversely from one and other as temperature is increased. Still,

the appearance of both peaks for MO suggests that a degree of order, though on a smaller scale, is maintained even at high temperatures.

2.3. Self-diffusion coefficients

The molecular structure of the molecules is expected to affect their translational movement. We therefore measured the self-diffusion coefficients, D, of OA and MO at various temperatures (Figure 6). As presented, MO has larger D values compared to OA for all the temperatures, meaning the translational movement of the ester is considerably larger than the acid. Both materials exhibit Arrhenius dependence of the form

Eq. (1)
$$D = D_0 \exp(-\Delta E_{app} / RT)$$

with apparent activation energies, ΔE_{app}, of 27.0 and 19.5 KJ/mol for the OA and MO molecules respectively. ΔE_{app} of OA is in fair agreement with the value reported by Yamamoto et al. [25] for the same molecule, and interestingly also with the value reported for liquid TGs [36]. These results suggest that OA molecular movement within its bulk liquid is considerably reduced compared with MO, and requires an equivalent amount of energy as a TG to initiate diffusion.

Dynamic viscosity measurements at different temperatures were performed on the MO sample (Table 2). These were then used to calculate the apparent hydrodynamic radius, r, from the Stokes-Einstein formula under a slip boundary condition (Eq. (2) [17])

Eq. (2)
$$r = \frac{kT}{4\Pi \eta D}$$

where k is Boltzmann's constant, D is the self-diffusion coefficient and η the dynamic viscosity. The apparent hydrodynamic radius of MO follows a very moderate linear (R^2=0.80) increase with temperature (Table 2). This result agrees with the moderate increase with temperature of the short- and long-range spacings (Figures 5A and 5B respectively). r values of OA were also calculated using the dynamic viscosities shown in [19].

Despite the large difference in ΔE_{app} of OA and MO, their apparent hydrodynamic radius was found to be very close (Table 2).

Iwahashi et al [22] found that nonanoic acids in the liquid state remain as dimers even at 363 K. Based on this finding they concluded that for normal FAs, dimers are the units in their intra- or intermolecular movements. Furthermore, they calculated the hydrodynamic radius of several normal FAs in the range of C8-C18, and found that it decreases very slightly with increasing hydrocarbon chain. This suggested that the rotational (end-over-end) as well as transverse motion of each dimer is severely restricted, and that only a longitudinal translation (translational movement along molecular axes) is allowed.

Since the hydrodynamic radii r of OA and MO are very close, the large difference in D, and consequently ΔE_{app}, can be attributed to their viscosity differences. It is well known that for long hydrocarbons, viscosity increases with number of carbons, due to a higher number of van der Waals interactions with adjacent molecules. Since both molecules have similar tails, it may be rationalized that for the temperature range applied in this study, unlike in the case of OA which occur as dimers, single MO molecules are the units in translational diffusion. Thus in the case of free motion, we would expect a larger difference in hydrodynamic radii r for single versus dimerized

molecules (18 carbons versus 36 carbons). However, as stated before, the motion for long rod-like molecules is restricted to linear molecular movement and therefore similar r values for the OA and MO molecules are to be expected.

2.4. Segmental motion

Spin lattice, T_1, is likely to be correlated to the movement of the carbon atoms, i.e., segmental motion (specifically rotational tumbling and to a lesser extent translational and internal motion) in the molecule. The segmental movements at the end and near the end of the molecule are probably most important for the OA and MO molecules to find the spaces for their translational diffusion [21]. Of course, their close molecular arrangement and intermolecular interactions will work to hinder the segmental motion of some carbons. Segmental motion through the reciprocal of the effective correlation time, $1/\tau_c$, of each carbon can be calculated from T_1, measured by ^{13}C HF-NMR. Figure 7 shows the $1/\tau_c$ values of OA at 298 K and MO at 298, 318, 338 and 358 K. Assignment of ^{13}C chemical shifts to the appropriate peaks was performed according to [37]. The results of $1/\tau_c$ values of OA presented in this work are in excellent agreement with the results presented elsewhere [21].

A very close pattern can be seen when comparing the segmental motion of the different carbons on the OA and MO chains at 298 K. For both molecules, the rotational movement of the double bond carbons is considerably restricted due to stronger intermolecular interactions between the Π electrons of the double bond, and increases towards the end of the chains.

Nevertheless, two main differences are observed, which are both associated with the dissimilarities of head-to-head intermolecular interactions. The first is that all $1/\tau_c$ values of the carbons along the chain of OA are smaller, compared to the $1/\tau_c$ of the

carbons at the same position on MO. This is analogous to the shift of the entire

distribution of MO to higher T_2 values (Figure 1B), and can be attributed to the lower

viscosity of MO. The second involves the rotational movements of the carbons closest

to the head (C2-C4). As suggested before, at a temperature of 298 K, OA molecules

are almost entirely dimerized. This dimerization restricts the rotational movement,

leading to pronounced rigidity compared to the methyl end. The head in MO, on the

other hand, has a higher freedom of movement and is not tightly bonded, since $1/\tau_c$

values decrease from the second carbon towards the double bond.

Nevertheless, there is a pronounced difference in $1/\tau_c$ between the two ends of MO.

Even though no strong hydrogen bonding exists in the case of the ester, the polar

interactions are sufficiently strong to limit the rotation of the head, so that it doesn't

behave like the tail. This strengthens our initial assumption of polar interactions

between the esters head group.

As stated before, translational diffusion is probably initiated by the ends of the

molecules. In the case of OA, dimers of two hydrogen bonded molecules would move

by the flipping of both tails on the dimer. MO molecules, on the other hand, would

find available spaces for translational movement by very vigorous rotation of the tail,

but also wagging of the head.

$1/\tau_c$ values of all carbons in the MO chain increase with temperature, while

maintaining the pattern described before. Interestingly, the $1/\tau_c$ values of all the

carbons on MO at 358 K (apart from C9 and C10) are higher than the $1/\tau_c$ value of

C17 at 298 K. This implies that the entire MO molecule moves around in the same

vigorous manner as the tail does at 298 K. This is not the case for OA, judging by the

values presented in [21]. Owing to the dimerization of the head, even at comparable

high temperatures, the head and adjacent carbons do not reach the same degree of motion as the tail at 298 K.

2.5. ^{1}H and ^{13}C HF-NMR chemical shift analyses

HF-NMR is a useful tool for identifying non-covalent interactions, as chemical shift is a sensitive measure of local chemical environment. Intermolecular interactions can be identified by changes in chemical shift. Therefore, to learn about the intermolecular interactions, and their changes with temperature, we observed the change in chemical shifts of each proton and carbon on OA and MO, acquired using ^{1}H and ^{13}C HF-NMR respectively.

Unless otherwise stated, all chemical shifts moved downfield with increasing temperature. This can be explained by the increase of bonds length with temperature, which requires less energy to cause nuclei inversion. In contrast, the carbon and proton on the carboxyl and hydroxyl groups of the OA respectively, showed a polynomic behavior with increasing temperature, with maxima at approximately 320.5 and 327 K respectively (Figure 8A and 8B for the carbon and proton respectively). Iwahashi et al. [19] found that a discontinuous change takes place in some physical properties of the liquid OA around 328 K, and concluded that the liquid structure or molecular conformation changes into a more highly disordered one. This may serve as an explanation for the up-field increase of chemical shifts above this approximate temperature. Another possible explanation is the possibility that above a given temperature the H bonding interactions between the carboxyl and hydroxyl groups is reduced by the mobility, so that the polar-electrostatic interaction in H-bonding is reduced, inducing an up-field shift. This is similar to the up-field shift

observed on C1 of OA, as a function of pH [38], and on the OH group of octanoic acid as a function of temperature [26].

The ^{1}H and ^{13}C chemical shifts for all other protons and carbons, shows a linear increase with temperature with different slopes. While the slopes for the different protons along the chain are very similar, those for the carbons differ to a great extent depending on their position (Figure 9). It is likely that the carbon with larger $1/\tau_c$, meaning high rotational motion (Figure 7), is less affected by the changes in temperature, and therefore exhibit small slopes. This is true for the carbons in the tail side of both OA and MO molecules. The double bond carbons C9 and C10, and the neighbor carbons, which show smaller $1/\tau_c$ and low mobility, consequently show larger slopes. The C2 and C3 carbons in the head side of the molecules do not follow this behavior. For MO, although these carbons show a moderate increase in mobility with temperature (Figure 7), they show larger slopes than the carbons in the tail side. This apparent anomaly could be explained by the deshielding effect of the carboxyl group with temperature. The effect is induced through the C-C σ bond, and is more effective in the α carbon than the β carbon, so that the slope of C2>C3.

Conversely, in OA, the slope of C2<C3. This can be explained by the polynomic behavior observed for the carboxyl group, which shows an up-field increase in chemical shift with temperature. Similar to MO, this shielding effect propagates trough the C-C σ bonds, and is more intense in carbon α than β, explaining the C2< C3 slope.

2.6. *^{1}H HF-NMR T_1 and T_2*

In order to assign T_2 values of different protons along the chains of OA and MO, the perfect echo sequence [39] was applied on a Bruker AVANCE III 600 MHz NMR spectrometer, at 298, 318 and 338 K. Peaks were assigned according to [40]. All protons exhibited a monoexponential behavior. Figures 10A and 10B show the monoexponential T_2 values for the resolved protons according to the position of the attached carbon. The T_2 values fit very well with the segmental motion presented in Figure 7, with an exception for the double bond protons. For all temperatures, the protons on MO have larger T_2 values compared to the equivalent ones on OA. All the protons show linear increase in T_2 values with temperature. Interestingly, T_2 values of MO show a greater response with temperature, compared to OA. This is possibly comparable to the larger increase with temperature of the higher mobility peak (T_{22}) and relative peak contributions of MO as seen in T_2 distributions (Figures 2A-2D).

^{1}H T_1 values were also measured for OA and MO, on the 600 MHz NMR spectrometer, at 298 K. Table 3 shows the T_1/T_2 ratio of protons according to the position of the attached carbon for the two samples at 298 K. In the case of $2\Pi\nu_0\tau_c<1$, where ν_0 is the Larmor frequency and τ_c is the correlation time, $T_1{\approx}T_2$ with T_2 slightly smaller than T_1. This is the case for non-viscous small molecules that exhibit fast rotation and tumbling. In the case of larger molecules, rotation and tumbling are hindered, and an increase in T_1 along with a decrease in T_2 is to be expected. Based on this designation, MO exhibits liquid-like behavior, while OA shows a more hindered nature, with highest rigidity presented for the head and double bond protons (Table 3).

3. Discussion

The only primary molecular difference between MO and OA is the methyl group on the acid moiety. This significantly affects the morphological structure of the material above its melting point. A question that should be raised at this point is whether MO in the liquid at the temperature range of this study has a molecular arrangement resembling that of OA. A molecular arrangement in this case would resemble to some extent that of a liquid crystal (as suggested for OA [19]), meaning molecules within this arrangement diffuse much like those in a liquid, while maintaining some degree of orientational and sometimes positional order as a function of the specific morphology. To be more exact, this would mean that at least one molecular axis tends to point along a preferred direction as the molecules undergo diffusion [41].

Following this classification, it is suggested that both OA and MO possess a liquid crystal-like order, according to the apparent hydrodynamic radius, r, since for both molecules the rotational, as well as transverse, motion is to some extent restricted, and only a longitudinal translation is allowed. Still, the dimerization due to hydrogen bonding of the head groups in OA leads to a greater molecular rigidity compared to MO, and to a more efficient packing. Considering the head-to-head model interaction suggested in this paper, it is also reasonable to assume the quasi-smectic liquid crystal-like structure for MO, where heads are aligned next to tails in an interdigitated structure, similarly to the case of OA [19]. Evidence can be seen from the long-spacing (Table 1) of lateral planes, which is roughly equivalent to the length of a single MO molecule. In the case of adjacent heads the long-spacing is expected to be approximately double the one reported. However, the broader small angle peak acquired for MO (Figure 4B) suggests a less ordered structure in this respect.

It is also important to consider that the self-organization of these long rod-like molecules is temperature dependent, and may vary to a great extent as temperature increases further away from the melting point. Phase transition temperatures can give an estimation of intermolecular interactions and the degree of molecular order. Higher melting points are related to more efficient packing in the solid. Boiling is the temperature required to break all intermolecular interactions present in the liquid. Crystallization is affected by the degree of order present in the liquid, in a way that more ordered molecules will crystalize at higher temperatures. The crystallization, melting and boiling points of OA and MO according to the literature are shown in Table 4 (for OA the lower melting point for the α polymorph is referenced). The higher crystallization, melting and boiling points of OA are an indication of the higher degree of intermolecular interactions and molecular packing arrangements compared to MO, both in the solid and in the liquid. Based on their chemical structure, this is clearly the effect of hydrogen bonding of the head groups in OA, versus weaker polar interactions for MO.

Interestingly, a significantly larger temperature hysteresis between crystallization and melting points exists for MO compared to OA (20.6 versus 8.3 K, respectively calculated from Table 4). This suggests a smaller degree of order in MO, requiring substantially reduced temperature to crystallize, since crystallization requires good molecular packing to reach the adequate entropy level.

Lastly, the task of assigning the molecular basis of the two peaks in the T_2 distributions remains (Figures 1A and 1B). Based on the acquired information, we would now like to refer to the original suggestions for the two peaks and offer more informed explanations.

a.   The two peaks are the result of inhomogeneous organizations with two different packing densities and intermolecular interaction intensities or types.

Badmaev et al. [44] suggested a cluster model by which any liquid presents a micro-inhomogeneous medium, consisting of two dynamic components: ordered areas (clusters) and an inhomogeneous disorder matrix. Hernqvist [45] also proposed a dynamic model for liquid tristearin that consists of a lamellar liquid crystalline phase, where the size and orientation of the units vary with diffusion rates of the molecules and therefore with changes in temperature. This can be described as transiently structured liquid with centers of organized structures forming and dissolving continuously and thus forming an equilibrium structure.

Following the cluster model, a reasonable assignment for the T_2 distributions of OA and MO would be that the first peak (T_{21}) consists of the molecules in the liquid crystal clusters and the second peak (T_{22}) would be the result of the more liquid-like molecules. The molecular structure described before, would therefore be responsible for the organization within the liquid crystal clusters, whereas the other liquid molecules in the amorphous morphology volumes would diffuse randomly throughout the sample volume with the molecular axes in rapid rotary like movement. This kind of microstructural organization can be the result of structural memory coming from the solid structure, and can very well explain the two peaks.

Following this model, T_{21} would stand for average T_2 value for all protons inside the liquid crystal cluster, and T_{22} the average T_2 value for the free more mobile ones. Since a very small difference exists between the two groups, T_{21} and T_{22} have close values at each temperature, although due to a more ordered nature and closer packing, T_{21} is smaller. As temperature increases, molecules from the cluster break up and

transfer to the disordered matrix, as can be seen for the change in the relative contributions of the peaks. This pattern is more observed in the case of MO, in the range of temperatures tested in this study. As suggested before, due to dimerization of the heads in OA, it has a denser arrangement and requires higher activation energy to initiate diffusion. As a result, the exchange of molecules between the two groups is considerably slower than that of MO, and the peak loss of T_{21} in OA is significantly less than in MO as the temperature is increased.

A very interesting phenomenon that supports this model was observed in T_2 distributions, whose possible explanation may be monitoring of the exchange of molecules between amorphous and liquid crystal environments until stabilization. This can be seen for MO heated from 193 K to 288 K, the temperature of measurement (Figure 11). Measurements were taken at five increasing times (t1-t5 according to the order of measurement) until final stabilization was achieved at t4. As shown, the relative contribution of the peaks changes in favor of the second peak as time progresses, until reaching a steady state.

Pulse NMR has long been suggested as a tool for measuring solid fat content in partially crystallized fats. In the food industry, solid fat content values measured at different temperatures can be used to help predict important attributes such as mouth-feel and hardness. In this application the signals of both the solid (crystallized) fat and liquid oil are acquired. Possibly, with the current method, it is also conceivable to measure the ratio between the more rigid (clusters) and looser parts of the liquid. NMR and especially LF-NMR relaxometry would therefore be an excellent tool for monitoring changes in weak morphologies and/or interactions. This may be due to the low energy required to excite spin systems. The low frequency relaxation process in

liquids concerns low energy processes, and can be explained by interaction of clusters.

b. *The two peaks are the result of two distinct mobility populations of the protons on the chain.*

Since temperature influences the self-organization of OA and MO, as suggested before, comparison of distributions would be made relative to the temperature of melting of each compound. Therefore, the comparison would be performed by subtracting the melting point of each compound (~288 and 253 K for OA and MO, respectively) from the temperature of measurement. Following this rule, the MO distribution acquired at 288 K should be compared with the OA distribution acquired at 318 K, and so on. It can be seen (Figures 1A and 1B) that T_{22} is almost similar for the two materials (most pronounced for high temperatures), whereas T_{21} of the OA is shorter than that of MO. This can indicate of two populations: T_{22} is very close for both materials and can be assigned as the less restricted parts of the molecules; T_{21}, on the other hand, is the more rigid part of the molecules, where OA is more restricted than MO (due to smaller values). Rigidity will lead to differences in intermolecular interactions, such that the more rigid parts have a close neighbor to interact with, leading to lower T_2. The relative contribution of the peaks changes with temperature towards the less rigid peak. This is more pronounced for MO, since its head is freer to move compared to OA, as shown by the segmental motion and T_2 values measured on a 600 MHz ^{1}H HF-NMR spectrometer (Figure 7 and Figures 10A and 10B respectively). Peaks assignment would therefore be as follows:

For OA, at intermediate temperature, the hydrogens close to the head, from C2 to C10 (18 hydrogens) are less mobile (T_{21} group) than the hydrogens from OH and from the

tail, C11 to C18 (18 Hydrogens, T_{22} group). The 1:1 ratio between these two groups is observed at 308 K. At higher temperatures, part of the head (C2 - C10 hydrogens) becomes with mobility similar to the tail. At lower temperature part of the tail hydrogens is in the head signal.

The assignment for MO is similar. At low temperatures, the C11 to C18 and OCH_3 (20 hydrogens) are grouped in T_{22} and C2 to C10 (16 hydrogens) in T_{21}. This is the ratio at 288 K. At higher temperatures, the T_2 of part of the hydrogens from the head group "jump" from the short to long T_2. At 338 K, apparently, only the two olefinic hydrogens are part of T_{21} (6/94%).

In order to rule out the possibility that the large change in relative contributions of the peaks of MO, in response to an increase of temperature, is due to a loss of structural organization at temperatures far above the melting point, additional measurements were carried out at 258, 268 and 278 K (Figure 12, this is an extension of Figure 1B). Two peaks were once again observed for all temperatures, with similar trends of increasing T_2 values and relative contributions with increasing temperatures, meaning the change in T_2 values of the peaks and distribution between populations is constant from the melting point and above. This strengthens our assumption that the different response to temperature of OA and MO is due to differences in their chemical composition (head interactions). Following the comparison rule proposed before, the T_2 distributions near melting should be compared (288 and 258 K for OA and MO molecules respectively). Based on the peaks assignment suggested before, it appears that at 258 K 75% of MO is rigid, though still more mobile than OA (both T_{21} and T_{22} have larger values than for OA).

Both theories for the assignment of peaks in the T_2 distributions can be sustained by logical reasoning. However, the supporting data presented, especially ^{13}C and ^{1}H HF-NMR measurements, suggests that the two peaks are the result of two distinct mobility populations of the protons on the chain. An additional possible experiment to get a more conclusive choice between the models could be the use of partial deuterated OA and MO. For example, deuterating the carbons in the tail end (C11 to C18). In case that the T_2 distribution remains unchanged, it would support the first model. However, a large reduction in the relative contribution and T_2 value of the second peak would support the second model. Additional possible experiments would also involve measurement of several other standard FAs and FAMEs materials of various chain lengths and degrees of unsaturation. Our research group has already initiated a thorough research design comprising these experiments. However these are beyond the scheme of the current work and will be discussed in a separate publication.

The goal of this work was to explore the potential of ^{1}H LF-NMR relaxomtery for characterizing the molecular organization of lipids in the liquid phase. Although the T_2 distributions acquired may well explain the cluster model of a microstructure arrangement and exchange of molecules between domains, the supporting measurements performed suggest otherwise. Still, bearing in mind that the mobility of the molecules is the direct outcome of their morphological structure, the differences in the molecular arrangement of OA and MO can be proposed by monitoring the differences in T_2 distributions and peaks area in response to a gradient of temperatures. This can be observed from the similarities in T_2 distributions in relation to melting point. In this way, the large change in relative contribution of the peaks for MO suggests of a less dense packing compared to OA. Ultimately, the dimerization of

the head in OA compared to weaker polar interactions of the head can be clearly deduced from the increased intrinsic T_2 values of MO.

Compared to other spectroscopic methods used in this study, ^{1}H LF-NMR was found to be highly susceptible to low energy, weak intermolecular interactions and aggregation of molecules. This technology is therefore suggested as a potentially important tool for the field of biodiesel. Several disadvantages have been suggested for the use of biodiesel in unmodified diesel engines including, cold weather operability and flow properties. In addition, a major problem exists with oxidative stability and the stability of biodiesel-petrodiesel blends, especially during prolonged storage. These physico-chemical properties are the direct outcome of the mobility and molecular structure of the fuel in the liquid. A possible application could be to test different additives to reduce dipolar interaction between MO heads. A small amount of additive could increase mobility and reduce viscosity, which would be easily observed by ^{1}H LF NMR. The same could be applied to test the effect of biodiesels prepared from different feedstocks, meaning different FA profiles, and/or biodiesel-petrodiesel blends, and their differences in mobilities and packing. By reducing the temperature going from the liquid down to the crystallization point, this technology may also be applied to test the initiation of crystallization and to monitor its progress. ^{1}H LF-NMR can also be used for monitoring oxidation of biodiesels. An indication for this application we found in the course of our experiments on a sample of methyl linolenate. An additional peak at lower than usual T_2 values was observed following prolonged storage.

4. Conclusions

We have shown that OA and MO have both similarities and differences as seen in the ^{1}H LF-NMR relaxation times and relative contributions according to temperature. These were attributed to a degree of liquid crystal-like order of both molecules that is temperature dependent, and that affects their ability to interact with close neighbors. Two suggestions have been made for the peaks: two distinct mobility populations of the protons on the chain; or a microstructural organization of the liquid with ordered areas and inhomogeneous disorder matrix. These properties allow for the material characterization based on parameters that contribute to important material properties in applications such as biodiesel fuels. This new application is of high potential to the field of biodiesel, and to other research and applied disciplines wherein relative weak interaction forces play an important part in physico-chemical characteristics.

5. Materials and methods

5.1. Materials

High purity ($\geq$99%) OA and MO lipid standards were purchased from Sigma-Aldrich. Standards were used as received without further purification. Both standards were kept at 253 K between measurements, and heated from this temperature to the required temperature of measurement.

5.2. ^{1}H LF-NMR relaxometry and diffusiometry

All ^{1}H LF-NMR measurements were performed on a 20 MHz minispec bench-top pulsed NMR analyzer (Bruker Analytic GmbH, Rheinstetten, Germany), equipped with a permanent magnet and a 10-mm temperature controlled probe head. Measurements were first performed in the temperature range of 288 – 348 ± 0.03 K in 5 K steps. Prior to measurement, samples were heated for minimum 1 h and then

allowed to equilibrate inside the instrument for 5 min. All measurements were performed on liquid standards (above melting point). For each temperature and sample the following parameters were optimized: receiver gain, magnetic field offset, detection angles, P90, P180 and homogeneity.

For MO, comparison of the data acquired at several temperatures starting from 193 or 253 K was performed, and similar distributions were found for the same temperature. However, the time to achieve stable results from 193 K was very long (several hours, especially for the higher temperatures). Therefore, MO was kept at 253 K between measurements, and heated from this temperature to the required temperature of measurement.

Determination of spin-spin relaxation (T_2) was performed using a CPMG (Carr, Purcell, Meiboom and Gill [46,47]) pulse sequence. τ of 0.4 and 1.125 s and recycle delay of 4 and 6 s were used for the OA and MO samples respectively. Additional CPMG measurements of MO were performed at close to melting temperatures (258 – 278 ± 0.03 K in 10 K steps). Acquisition at low temperatures for MO was performed with τ of 0.4 – 0.5 s and recycle delay of 5 s. For all the analyses, 32 scans were accumulated and 8000 echoes were acquired. Data was acquired in magnitude mode due to better repeatability and stability of results, and further analyzed using the PDCO optimization algorithm with $\alpha_2=0.5$, as described in [7]. CONTIN (software application for inverse Laplace transformation of LF-NMR relaxometry data available in minispec) was also used for analyzing the acquired CPMG data, in order to compare distributions with PDCO. The mathematical formulation of CONTIN is described in [48]. Both methods exhibited very similar T_2 distributions, although better repeatability and stability was found with PDCO analyses.

The self-diffusion coefficient, D, was determined by the Pulsed-Field Gradient Spin Echo (PFGSE) method [49]. The PFGSE sequence was used with 16 scans, τ of 7.5 ms and a recycle delay of 6 s. Typical gradient parameters were Δ of 7.5 ms, δ of 0.5 ms, time between the 90° pulse to the first gradient pulse of 1 ms and g of 1.6 T/m. A water sample (1.25 g/L $CuSO_4$) was used for calibration. D values of water were taken from [50]. Each reported value is the average of a minimum of 10 measurements.

5.3. High field ^{1}H and ^{13}C-NMR chemical shift, spin-spin and spin-lattice relaxation time

The high field ^{1}H and ^{13}C-NMR measurements were performed on a BRUKER AVANCE III operating at 600 MHz for ^{1}H nuclei and 150 MHz for ^{13}C. Prior to measurement, samples were heated for minimum 10 min and added in a 5 mm NMR tube. For lock signal, a closed 1 mm capillary tube, filled with D_2O, was added to the sample. The non-spinning samples were allowed to equilibrate inside the instrument for 15 min after reaching the set temperature. Before each measurement, shimming was optimized using automated and manual procedures. The chemical shifts, in parts per millions (ppm), were obtained without reference signal. The ^{1}H and ^{13}C NMR spectra were obtained using 4 and 8 scans and recycle delay of 30 s and 120 s, respectively.

The ^{1}H and ^{13}C longitudinal relaxation time, T_1, were measured using the inversion recovery method [51]. The ^{1}H transverse relaxation time, T_2, was measured using a modified (perfect echo) CPMG pulse sequence (PROJECT - Periodic Refocusing of J Evolution by Coherence Transfer) that resulted in spectra without J modulation [39].

The calculations of T_1 and T_2 were carried out with the subroutines included in the TOPSPIN 3.2 software package.

^{13}C HF-NMR spin-lattice relaxation of a protonated carbon is overwhelmingly dominated by dipole-dipole interactions with the attached protons [21]. T_1 is therefore related to the number of directly bonded hydrogen, N, and the effective correlation time, τ_c, for the rotational movement of the carbon atoms in the object molecule. Thus, T_1 is approximately given in terms of N and $1/\tau_c$

Eq. (3)
$$T_1 = \frac{r_{CH}^6}{N\hbar^2 \gamma_C^2 \gamma_H^2}\left(\frac{1}{\tau_C}\right)$$

where $\hbar$ is Planck's constant and γ_C and γ_H are the gyromagnetic ratios of ^{13}C and ^{1}H, respectively. Here, r_{CH} is the C-H distance, usually about 0.109 nm, and the reciprocal of the effective correlation time, $1/\tau_c$, represents the magnitude of the segmental rotation for the carbon atom at a different position.

5.4. X-ray methods

In this study, XRD and SAXS techniques were used for measuring the short and long range spacing between adjacent molecules respectively.

XRD data was collected on Panalytical Empyrean Powder Diffractometer equipped with position sensitive (PSD) X'Celerator detector using Cu K$_\alpha$ radiation (λ=0.154 nm) and operated at 40 kV and 30 mA. The usual Bragg-Brentano $\theta/2\theta$ geometry was employed. $\theta/2\theta$ scans were run during 15 min in a 2θ range of 2 – 35° with step equal to ~0.0167°. Measurements were performed at a range of 298 – 338 K in 10 K steps.

SAXS measurements were performed on a SAXSLAB GANESHA 300-XL (Skovlunde, Denmark) instrument. Cu K$_\alpha$ (λ=0.154 nm) radiation was generated by Genix 3D Cu-source (operated at 47 mV and 0.55 mA) with integrated Monochromator, 3 pinholes collimation and two-dimensional Pilatus 300K detector. The distance between the sample and detector was 350 mm. q range was between 0.0012 to 0.067 nm^{-1}. OA was measured at 298 K, for comparison with the literature, and MO was measured at several temperatures including, 263 K, 298 – 318 K in 10 K steps and 338 K.

5.5. Dynamic viscosity

Dynamic viscosity measurements of MO were performed on a Rheometer AR 2000 (TA Instruments), on a double gap peltier cylinder system in steady state flow mode, in the temperature range of 288 – 358 K. For each temperature, 10 points were acquired in the range shear rate 10 – 300 s^{-1}, and the average was reported.

6. List of abbreviations

CPMG: Carr, Purcell, Meiboom and Gill; FA: Fatty Acid; FAME: Fatty Acid Methyl Ester; HF-NMR: High Field Nuclear Magnetic Resonance; LF-NMR: Low Field Nuclear Magnetic Resonance; MO: Methyl Oleate; OA: Oleic Acid; PFGSE: Pulsed-Field Gradient Spin Echo; SAXS: Small Angle X-ray Scattering; TG: Triglyceride; XRD: X-Ray Diffraction.

7. Competing interests

The authors declare that they have no competing interests.

8. Authors' contributions

This work is part of the doctoral thesis of PB and she is the main author. PB designed most of the experiments, analyzed results, contributed in the establishment and validation of the new PDCO algorithm and drafted the manuscript. PB and NM performed the ^{1}H LF-NMR measurements and analysis of results. LAC and TBM performed the ^{1}H HF-NMR measurements and analysis of results. OL, YP and MS formulated, designed and established the PDCO algorithm. ZW, LAC and CL contributed to the development of the experimental design and proofread the manuscript. ZW led and coordinated the overall project. All authors read and approved the final manuscript.

9. Acknowledgements

10. References

1. Colnago LA, Engelsberg M, Souza AA, Barbosa LL: **High-throughput, non-destructive determination of oil content in intact seeds by continuous wave-free precession NMR.** *Anal Chem* 2007, **79:**1271–1274.

2. Prestes RA, Colnago LA, Forato LA, Vizzotto L, Novotny EH, Carrilho E: **A rapid and automated low resolution NMR method to analyze oil quality in intact oilseeds.** *Anal Chim Acta* 2007, **596:**325–329.

3. Berman P, Nizri S, Parmet Y, Wiesman Z: **Large-scale screening of intact castor seeds by viscosity using time domain NMR and chemometrics.** *J Am Oil Chem Soc* 2010, **87:**1247–1254.

4. Willson RM, Wiesman Z, Brenner A: **Analyzing alternative bio-waste feedstocks for potential biodiesel production using time domain (TD)-NMR.** *Waste Manage* 2010, **30:**1881–1888.

5. Cabeça LF, Marconcini LV, Mambrini GP, Azeredo RBV, Colnago LA: **Monitoring the transesterification reaction used in biodiesel production, with a low cost unilateral nuclear magnetic resonance sensor.** *Energ Fuel* 2011, **25:**2696–2701.

6. Berman P, Leshem A, Etziony O, Levi O, Parmet Y, Saunders M, Wiesman Z: **Novel ^{1}H low field (LF)-NMR applications for the field of biodiesel.** *Biotechnol Biofuels* 2013, **6:**55.

7. Berman P, Levi O, Parmet Y, Saunders M, Wiesman Z: **Laplace inversion of LR-NMR relaxometry data using sparse representation methods.** *Concept Magn Reson A* 2013, **42:**72–88.

8. **WinDXP Toolbox.** Software release version 1.8, 2006. Distributed EXPonential Analysis. Witney, UK: Oxford Instruments.

9. Silva RC, Carneiro GF, Barbosa LL, Lacerda V, Freitas JC, Castro EV: **Studies on crude oil-water biphasic mixtures by low-field NMR.** *Magn Reson Chem* 2012, **50:**85–88.

10. Barros CN, Arêas EP, Figueiredo EN, Arêas JA: **Low-resolution ^{1}H spin–spin relaxation of n-decane/water emulsions stabilized by β-casein.** *Colloid Surface B* 2006, **48:**119–127.

11. Bertram HC, Lars W, Jacob HN, Henrik JA: **Direct measurement of phase transitions in milk fat during cooling of cream—a low-field NMR approach.** *Int Dairy J* 2005, **15:**1056–1063.

12. Chatakanonda P, Chinachoti P, Sriroth K, Piyachomkwan K, Chotineeranat S, Tang HR, Hills B: **The influence of time and conditions of harvest on the functional behaviour of cassava starch—a proton NMR relaxation study.** *Carbohyd Polym* 2003, **53:**233–240.

13. Hills BP, Le Floc'h G: **NMR studies of non-freezing water in cellular plant tissue.** *Food Chem* 1994, **51:**331–336.

14. Marigheto N, Duarte S, Hills B: **NMR relaxation study of avocado quality.** *Appl Magn Reson* 2005, **29:**687–701.

15. Adam-Berret M, Boulard M, Riaublanc M, Mariette F: **Evolution of fat crystal network microstructure followed by NMR.** *J Agr Food Chem* 2011, **59:**1767–1773.

16. Callaghan PT: **The use of ^{13}C spin relaxation to investigate molecular motion in liquid tristearin.** *Chem Phys Lipids* 1977, **19:**56–73.

17. Iwahashi M, Kasahara Y: **Dynamic molecular movements and aggregation structures of lipids in a liquid state.** *Curr Opin Colloid Inter Sci* 2011, **16:**359–366.

18. Small DM: **Lateral chain packing in lipids and membranes.** *J Lipid Res* 1984, **25:**1490–1500.

19. Iwahashi M, Yamaguchi Y, Kato T, Horiuchi T, Sakurai I, Suzuki M: **Temperature dependence of molecular conformation and liquid structure of cis-9-octadecenoic acid.** *J Phys Chem* 1991, **95:**445–451.

20. Iwahashi M, Suzuki M, Czarnecki MA, Liu Y, Ozaki Y: **Near-IR molar absorption coefficient for the OH-stretching mode of cis-9-octadecenoic acid and dissociation of the acid dimers in the pure liquid state.** *J Chem Soc Faraday Trans* 1995, **91:**697–701.

21. Iwahashi M, Kasahara Y, Matsuzawa H, Yagi K, Nomura H, Terauchi H, Ozaki Y, Suzuki M: **Self-diffusion, dynamical molecular conformation and liquid structures of n-saturated and unsaturated fatty acids.** *J Phys Chem B* 2000, **104:**6186–6194.

22. Iwahashi M, Kasahara Y, Minami H, Matsuzawa H, Suzuki M, Ozaki Y: **Molecular behaviors of n-fatty acids in liquid state.** *J Oleo Sci* 2002, **51:**157–164.

23. Iwahashi M, Takebayashi S, Umehara A, Kasahara Y, Minami H, Matsuzawa H: **Dynamical dimer structure and liquid structure of fatty acids in their binary liquid mixture: dodecanoic and 3-phenylpropionic acids system.** *Chem Phys Lipids* 2004, **129:**195–208.

24. Iwahashi M, Umehara A, Wakisaka K, Kasahara Y, Minami H, Matsuzawa H, Shinzawa H, Ozaki Y, Suzuki M: **Effect of cholesterol and other additives on viscosity, self-diffusion coefficient, and intramolecular movements of oleic acid.** *J Phys Chem B* 2007, **111:**740–747.

25. Yamamoto S, Matsuda H, Kasahara Y, Iwahashi M, Takagi T, Baba T, Kanamori T: **Dynamic molecular behavior of semi-fluorinated oleic, elaidic and stearic acids in the liquid state.** *J Oleo Sci* 2011, **61:**649–657.

26. Matsuzawa H, Tsuda M, Minami H, Iwahashi M: **Dynamic molecular behavior and cluster structure of octanoic acid in its liquid and CCl$_4$ solution.** *Food Nutr Sci* 2013, **4:**25–32.

27. Nelson DL, Cox MM: *Lehninger Principles of Biochemistry.* 5th ed. New York: WH Freeman; 2009.

28. Knothe G: **"Designer" biodiesel: optimizing fatty ester composition to improve fuel properties.** *Energ Fuel* 2008, **22:**1358–1364.

29. Malkin T: **Alternation in properties of long chain carbon compounds.** *Nature* 1931, **127:**126–127.

30. Larsson K: **Molecular arrangement in glycerides.** *Fette, Seifen, Anstrichmittel* 1972, **74:**136–142.

31. Brady GW, Wasserman E, Wellendorf J: **Structure studies in liquid alkanes including direct determination of end-to-end distances.** *J Chem Phys* 1967, **47:**855–856.

32. Aleby STIG, von Sydow E: **The crystal structure of methyl stearate.** *Acta Crystallogr* 1960, **13:**487–492.

33. Boese D, Kirchner M, Echeverria GA, Boese R: **Ethyl acetate: x-ray, solvent and computed structure.** *Chem Phys Chem* 2013, **14:**799–804.

34. Ramírez-Verduzco LF, Rodríguez-Rodríguez JE, Jaramillo-Jacob ADR: **Predicting cetane number, kinematic viscosity, density and higher heating value of biodiesel from its fatty acid methyl ester composition.** *Fuel* 2012, **91:**102–11.

35. Knothe G, Dunn RO: **A comprehensive evaluation of the melting points of fatty acids and esters determined by differential scanning calorimetry.** *J Am Oil Chem Soc* 2009, **86:**843–856.

36. Callaghan PT, Jolley KW: **Translational motion in the liquid phases of tristearin, triolein and trilinolein.** *Chem Phys Lipids* 1980, **27:**49–56.

37. Gunstone FD, Pollard MR, Scrimgeour CM, Vedanayagam HS: **Fatty acids. Part 50. [13]C nuclear magnetic resonance studies of olefinic fatty acids and esters.** *Chem Phys Lipids* 1977, **18:**115–129.

38. Forato LA, Yushmanov VE, Colnago LA: **Interaction of two prolamins with 1-^{13}C oleic acid by ^{13}C NMR.** *Biochemistry* 2004, **43:**7121–7126.

39. Aguilar JA, Nilsson M, Bodenhausen G, Morris GA: **Spin echo NMR spectra without J modulation.** *Chem Commun* 2012, **48:**811–813.

40. Gunstone FD: *The lipid handbook.* 2nd ed. Gunstone FD, Harwood JL, Padley FB, editors. London: Chapman & Hall; 1995.

41. Collings PJ, Hird M: *Introduction to liquid crystals: chemistry and physics.* Taylor & Francis Inc; 1997.

42. Dunn RO: **Crystallization behavior of fatty acid methyl esters.** *J Am Oil Chem Soc* 2008, **85:**961–972.

43. Cermak SC, Evangelista RL, Kenar JA: Distillation of natural fatty acids and their chemical derivatives. Distillation - Advances from Modeling to Applications. Zereshki D, editor. ISBN: 978-953-51-0428-5; 2012. [http://www.intechopen.com/books/distillation-advancesfrom-modeling-to-applications/distillation-of-natural-fatty-acids-and-their-chemical-derivatives]

44. Badmaev BB, Dembelova TS, Damdinov BB: **The investigation of shear elasticity of liquids at low-frequent shear influence.** *J Mol Liq* 2006, **127:**163–167.

45. Hernqvist L: **On the structure of triglycerides in the liquid state and fat crystallization.** *Fette, Seifen, Anstrichmittel* 1984, **86:**297–300.

46. Carr HY, Purcell EM: **Effects of diffusion on free precession in nuclear magnetic resonance experiments.** *Phys Rev* 1954, **94:**630–638.

47. Meiboom S, Gill D: **Modified spin-echo method for measuring nuclear relaxation times.** *Rev Sci Instrum* 1958, **29:**688–691.

48. Provencher SW: **A constrained regularization method for inverting data represented by linear algebraic or integral equations.** *Comput Phys Commun* 1982, **27:**213–227.

49. Stejskal EO, Tanner JE: **Spin diffusion measurements: spin echoes in the presence of a time-dependent field gradient.** *J Chem Phys* 1964, **42:**288–292.

50. Holz M, Heil SR, Sacco A: **Temperature-dependent self-diffusion coefficients of water and six selected molecular liquids for calibration in accurate ^{1}H NMR PFG measurements.** *Phys Chem Chem Phys* 2000, **2:**4740–4742.

51. Abragam A: *The Principles of Nuclear Magnetism.* Clarendon: Oxford University Press; 1961.

Figures Legend:

Figure 1. Combined ^{1}H Low Field (LF)-NMR T_2 distributions of (A) OA and (B) MO at different temperatures. The relative contributions of each peak, in relation to other peaks and intrinsic T_2 values are shown on each plot. For the same temperature, the peaks in MO have larger T_2 values compared to OA. As temperature increases, a shift in the T_2 of the peaks is observed towards higher values and the relative concentration of the peaks changes, especially for MO.

Figure 2. Variation with temperature of intrinsic T_2 values and relative contributions of OA and MO peaks. Comparison of intrinsic T_2 values of (**A**) OA and (**B**) MO; and relative contributions of (**C**) short (T_{21}) and (**D**) long (T_{22}) peaks of OA and MO.

Figure 3. Proposed configuration for the ester groups of two opposite MO molecules interacting with each other. The resonance structures of the ester group result in weak interactions between the polarized hydrogen of the methyl carbon and the oxygen of the carbonyl on the opposite MO molecule. This molecular arrangement for MO would maximize the polar interactions.

Figure 4. X-ray spectra of OA and MO measured using (A) XRD and (B) SAXS at 298 K. The peak at around 0.14 nm^{-1} ($2\theta \approx 19.8°$) is sharp for both materials, whereas the peak at around 0.03 nm^{-1} ($2\theta = 4.2°$) is very broad and difficult to resolve, especially for the MO sample. SAXS: Small Angle X-ray Scattering; XRD: X-Ray Diffraction.

Figure 5. Response of (A) short- and (B) long-range spacings, d, with temperature using X-ray measurements. A similar increase in the short spacing with temperature for both OA and MO was observed. The long spacing for MO also increased with temperature and showed a moderate, close to linear increase from a temperature close to the melting point until 343 K.

Figure 6. Self-diffusion coefficient, D, of OA and MO at various temperatures. MO exhibits larger D values compared to OA for all the temperatures, meaning the translational movement of the ester is considerably larger than the acid.

Figure 7. Segmental motion of OA and MO at different temperatures. Segmental motion through the reciprocal of the effective correlation time, $1/\tau_c$, of each carbon can be calculated from T_1, measured by ^{13}C High Field (HF)-NMR. OA was measured at 298 K, and MO at 298, 318, 338 and 358 K. The structure of OA along with designation of carbon numbers is shown for reference.

Figure 8. High Field (HF)-NMR chemical shift, ν, of the OA head (A) ^{13}C and (B) ^{1}H at different temperatures. The carbon and proton on the carboxyl and hydroxyl groups respectively of OA, showed a polynomic behavior with increasing temperature, with maxima at approximately 320.5 and 327 K respectively.

Figure 9. The slopes for the ^{13}C High Field (HF)-NMR chemical shift, ν, as a function of temperature for each carbon. The slopes were calculated using linear regression of the change in ^{13}C chemical shifts with temperature. Apart from C2, OA and MO have very similar slopes. On the other hand, the slopes differ to a great extent depending on their position.

Figure 10. Monoexponential T_2 values of the resolved protons according to the position of the attached carbons. Measurements of (**A**) OA and (**B**) MO were performed at 298, 318 and 228 K using ^{1}H High Field (HF)-NMR spectrometer.

Figure 11. Monitoring of the exchange of molecules between populations (possibly amorphous and liquid crystal environments) until stabilization. Combined ^{1}H Low Field (LF)-NMR T_2 distributions of MO heated from 193 to 288 K, the temperature of measurement, at five increasing times (t1-t5 according to the order of measurement). The first measurement (t1) was performed following 1 h of stabilization at 288 K. The relative contribution of each peak, in relation to other peaks and intrinsic T_2 values, are shown on each plot. The relative contribution of the peaks changes in favor of the second peak as time progresses, until reaching a steady state.

Figure 12. Combined ^{1}H Low Field (LF)-NMR T_2 distributions of MO at low temperatures (just above melting point). This Figure is an extension of Figure 1B. The relative contribution of each peak, in relation to other peaks and intrinsic T_2

values, are shown on each plot. The change in T_2 values of the peaks and distribution

between populations is constant from the melting point and above.

Tables:

Table 1 Short- and long-range spacing, d, of OA and MO at 298 K.

	d_{OA} [nm]	d_{MO} [nm]
Short spacing (XRD)	0.459	0.460
Long spacing (SAXS)	2.383	2.531
		2.517^{a}

[a]Long spacing measured at 263 K.

d_{OA} and d_{MO} are the short- and long-range spacings of OA and MO respectively.

SAXS: Small Angle X-ray Scattering; XRD: X-Ray Diffraction.

Table 2 Dynamic viscosity, η of MO, and apparent hydrodynamic radius, r, of

MO and OA according to temperature.

T [K]	η_{MO} [mPa s]	r_{MO} [nm]	r_{OA}^{a} [nm]
288	6.97	0.339	
293	6.03	0.332	0.315
298	5.27	0.336	
303	4.66	0.339	0.337
308	4.14	0.340	
313	3.71	0.341	0.330
318	3.34		
323	3.03	0.344	0.337
328	2.76		
333	2.52	0.345	0.345
338	2.32		
343	2.15	0.348	0.364
348	1.99		
353	1.85		
358	1.72		

η_{MO} is the dynamic viscosity of MO; r_{MO} and r_{OA} are the apparent hydrodynamic radii of MO and OA respectively.

Table 3 ^{1}H T_1/T_2 ratio of OA and MO measured using High Field (HF)-NMR spectrometer at 298 K.
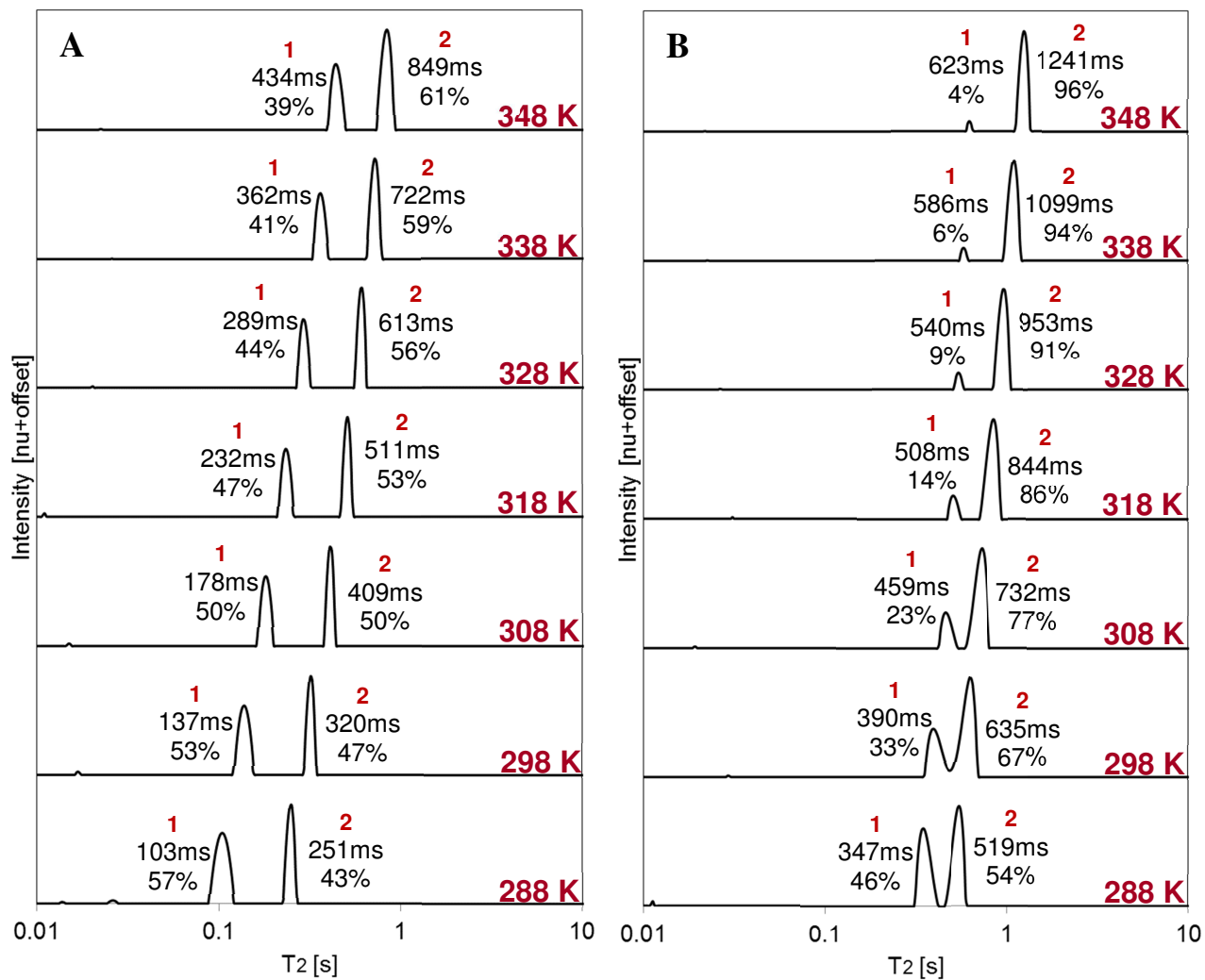
	^{1}H T_1/T_2	
	OA	MO
C2	8.50	2.54
C3	7.59	2.65
C8/C11	4.48	2.23
C9/C10	5.87	2.71
C18	3.95	2.66

Table 4 Comparison of phase transition points of OA and MO.

	Crystallization point [K]	Melting point [K]	Boiling point[a] [K]
OA	277.7 [14]	286.0[b] [14]	496.0 [43]
MO	232.5 [42]	253.1 [35]	474.0 [43]

a Measured at 1.333 kPa.

b The melting point for the α polymorph is referenced.

Figure 1

Figure 2

110

Figure 3

112

Figure 5

113

Figure 6

Figure 7

115

Figure 8

116

Figure 9

Figure 10

Figure 11

Intensity [nu+offset]

1	2	
283ms	461ms	**278K**
53%	47%	

1	2	
232ms	401ms	**268K**
65%	35%	

1	2	
189ms	355ms	**258K**
75%	25%	

0.01   0.1   1   10

T_2 [s]

120

Figure 12
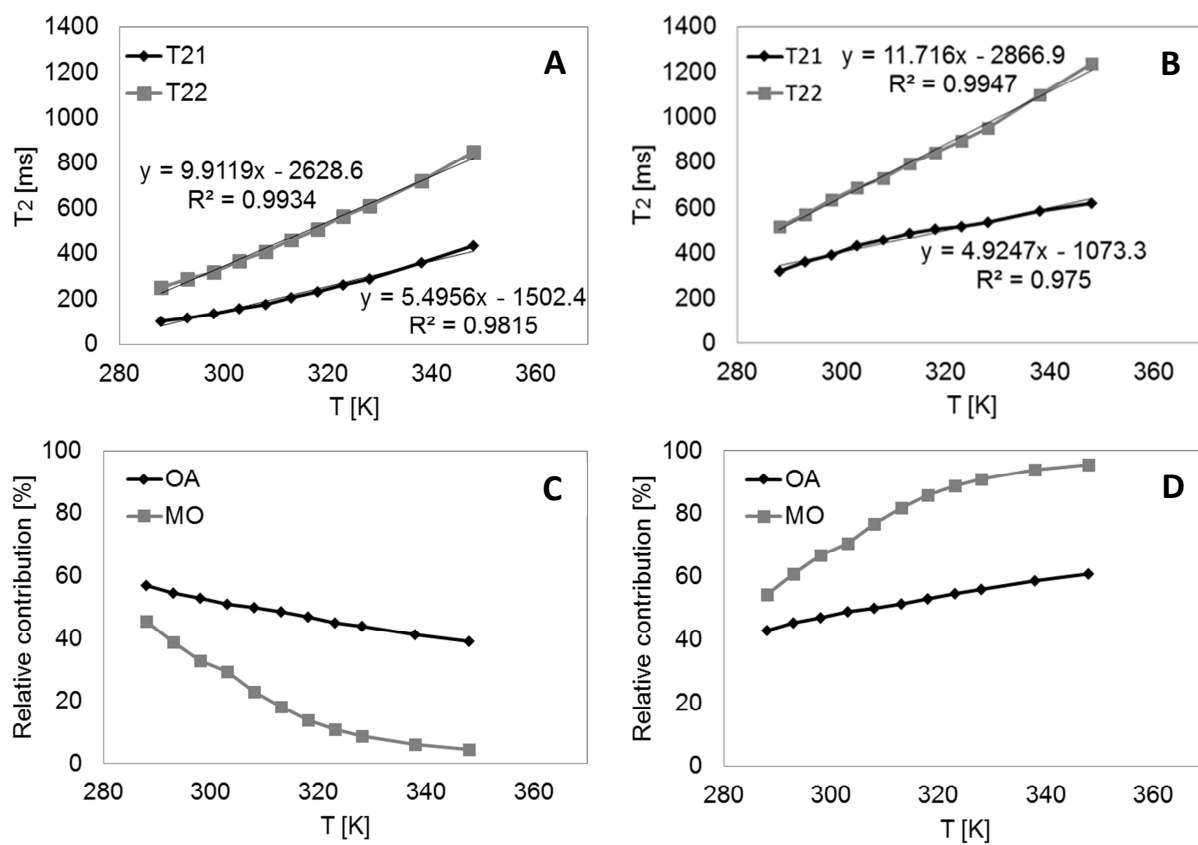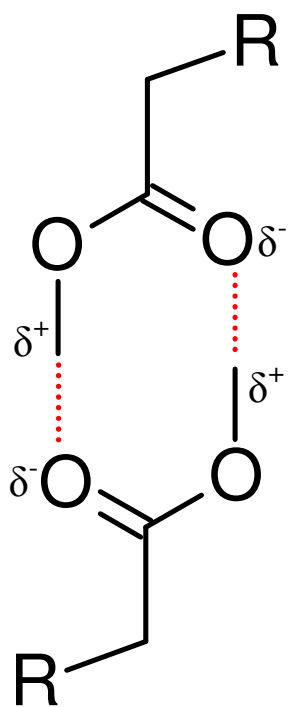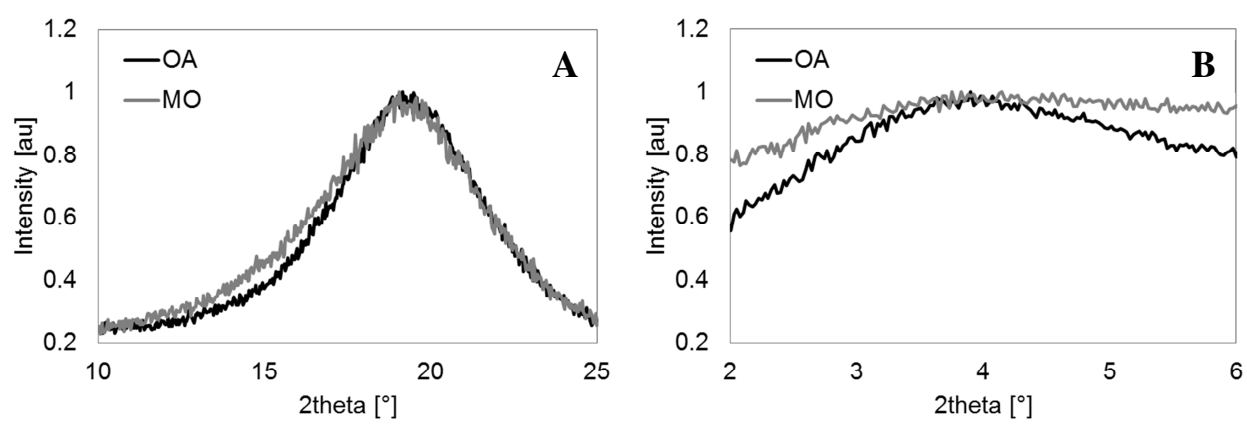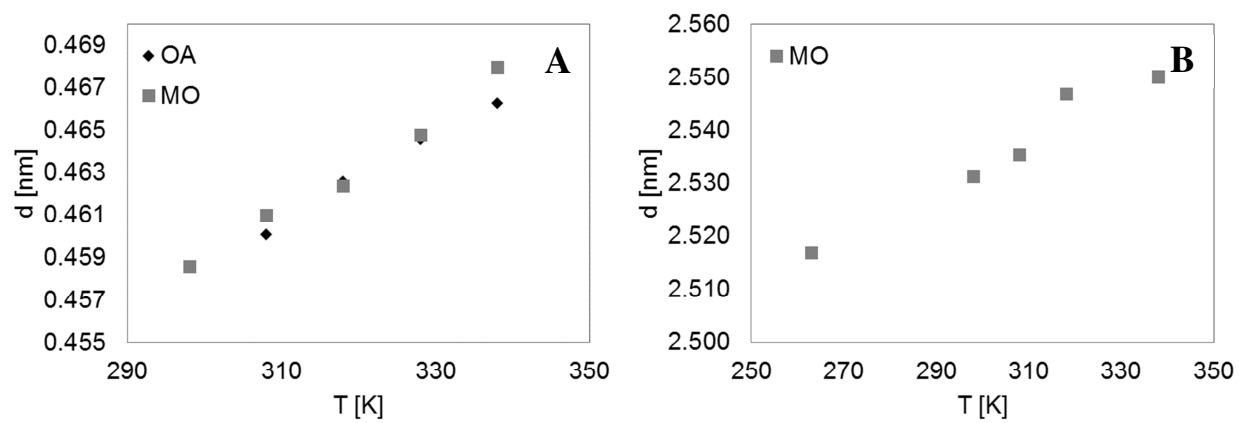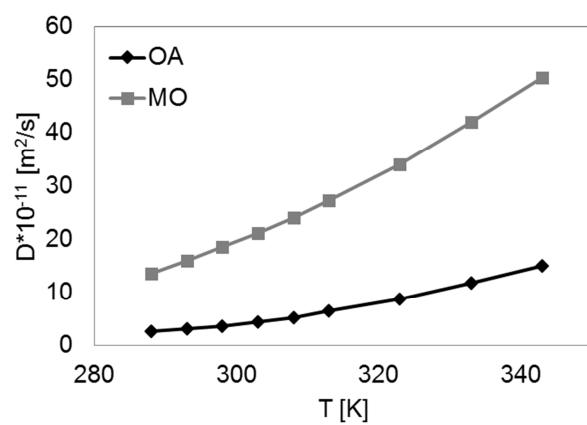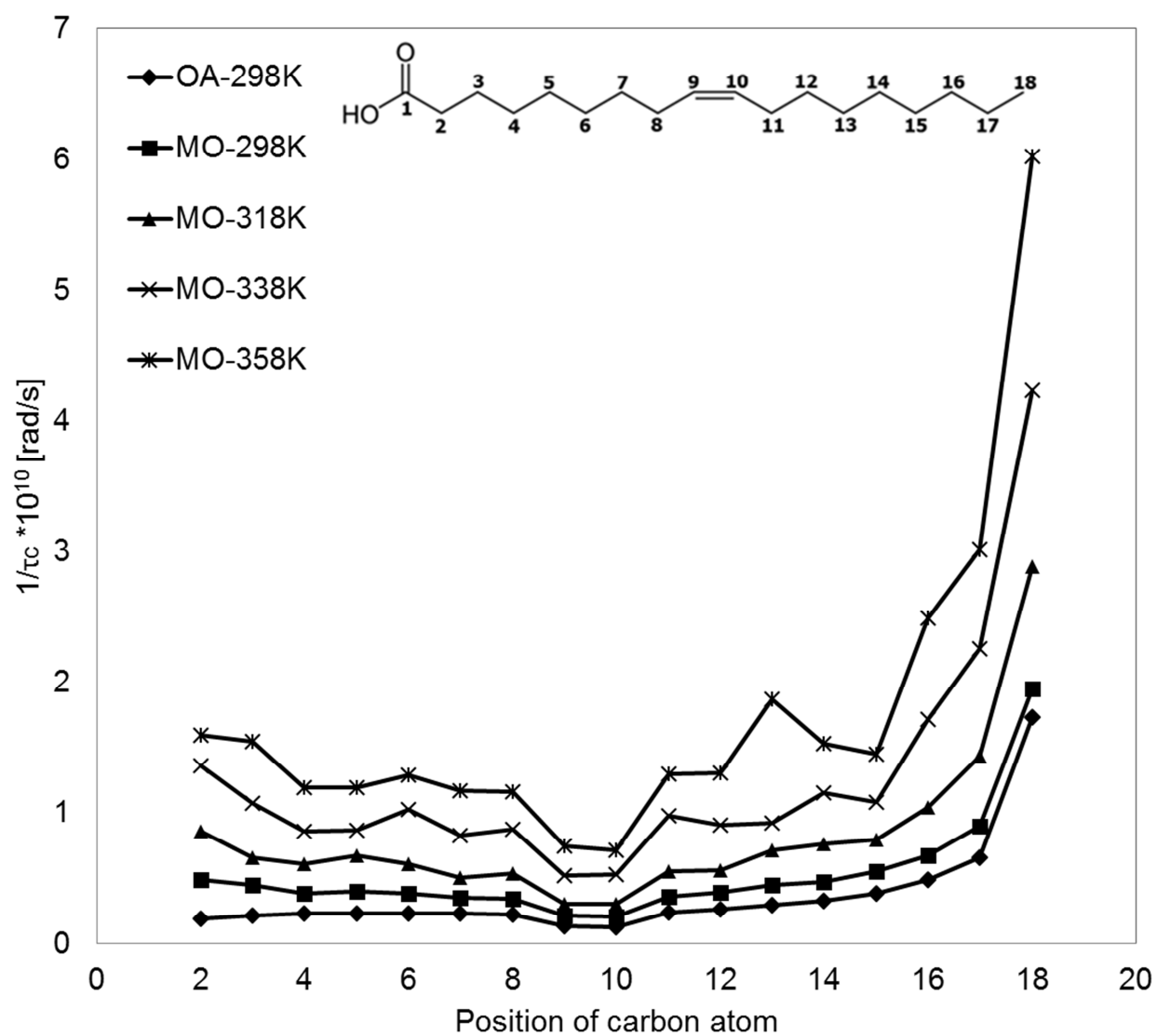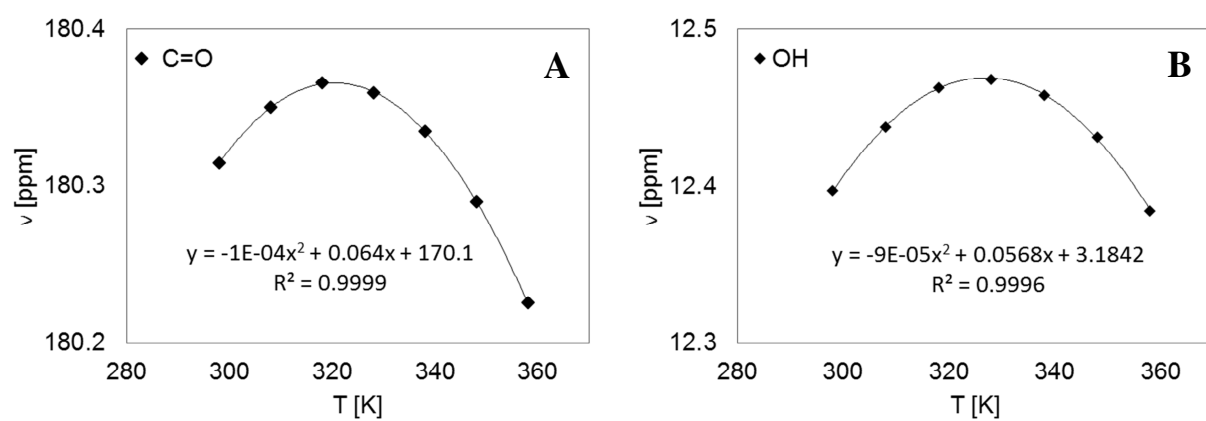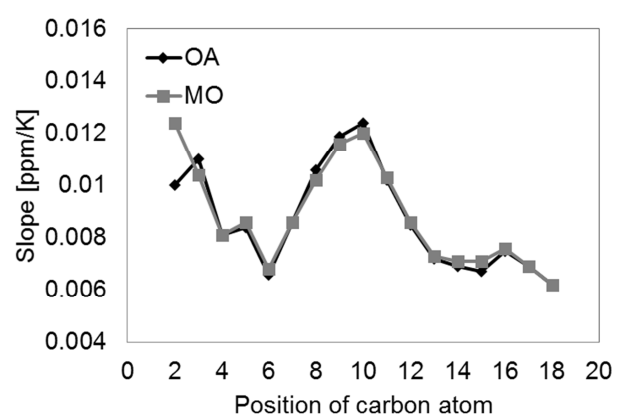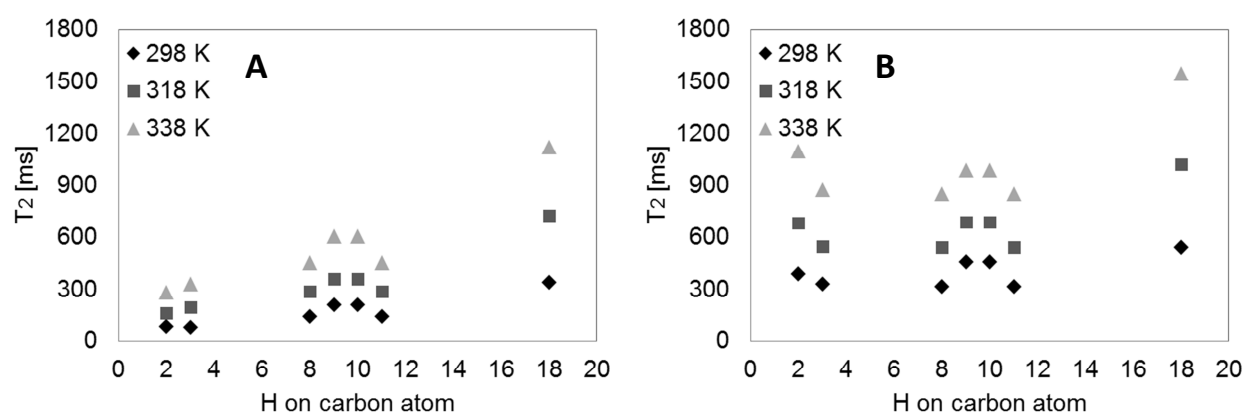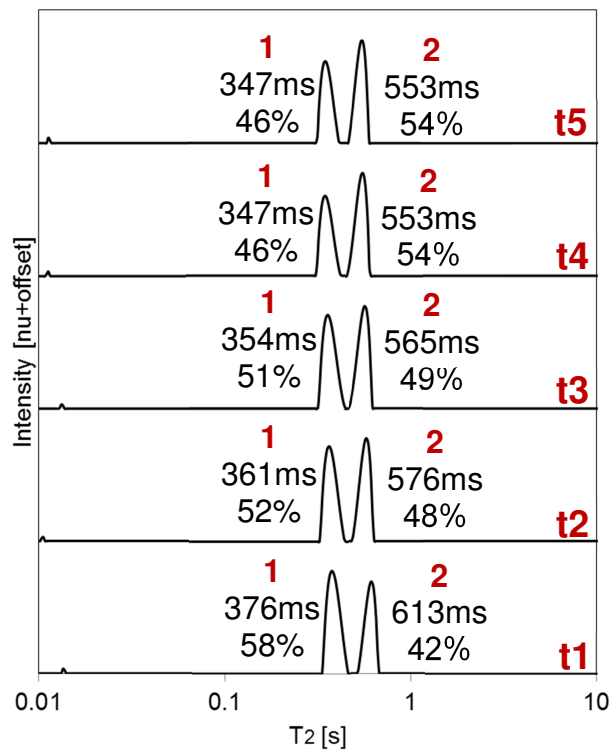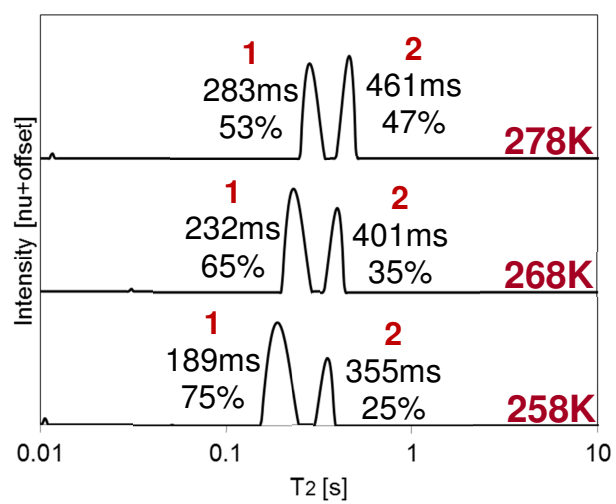
2.5. Meiri N, **Berman P**, Colnago LA, Moraes TB, Linder C and Wiesman Z: Liquid phase characterization of molecular interactions in polyunsaturated and n-fatty acid methyl esters by [1]H Low field nuclear magnetic resonance, submitted to *Biotechnol Biofuels* journal.

Biotechnology for Biofuels

Liquid phase characterization of molecular interactions in polyunsaturated and n-fatty acid methyl esters by 1H Low field nuclear magnetic resonance

--Manuscript Draft--

Manuscript Number:	
Full Title:	Liquid phase characterization of molecular interactions in polyunsaturated and n-fatty acid methyl esters by 1H Low field nuclear magnetic resonance
Article Type:	Research
Abstract:	Background To identify and develop the best renewable and low carbon footprint biodiesel substitutes for petroleum diesel, the properties of different biodiesel candidates should be studied and characterized with respect to molecular structures versus biodiesel liquid property relationships. In our previous paper, 1H Low Field Nuclear Magnetic Resonance (LF-NMR) relaxometry was investigated as a tool for studying the liquid phase molecular packing interactions and morphology of Fatty Acid Methyl Esters (FAMEs). The technological potential was demonstrated with oleic acid and methyl oleate standards having similar alkyl chains but different head groups. In the present work, molecular organization versus segmental and translational movements of FAMEs in their pure liquid phase, with different alkyl chain lengths (10-20 carbons) and degrees of unsaturation (0-3 double bonds), were studied with 1H LF-NMR relaxometry and X-ray, 1H LF-NMR diffusiometry, and 13C High Field NMR. Results Based on density values and X-ray measurements, it was proposed that FAMEs possess a liquid crystal-like order above their melting point, consisting of random liquid crystal aggregates with void spaces between them, whose morphological properties depend on chain length and degree of unsaturation. FAMEs were also found to exhibit different degrees of rotational and translational motions, which were rationalized by chain organization within the clusters, and the degree and type of molecular interactions and temperature effects. At equivalent fixed temperature differences from melting point, saturated FAME molecules were found to have similar translational motion regardless of chain length, expressed by viscosity, self-diffusion coefficients, and spin-spin (T2) 1H LF-NMR. T2 distributions suggest increased alkyl chain rigidity and reduced temperature response of the peaks' relative contribution with increasing unsaturation is a direct result of the alkyl chain's morphological packing and molecular interactions. Conclusions Both the peaks' assignments for T2 distributions of FAMEs and the model for their liquid crystal-like morphology in the liquid phase were confirmed. The study of morphological structures within liquids and their response to temperature changes by 1H LF-NMR has a high value in the field of biodiesel and other research and applied disciplines in numerous physicochemical- and organizational-based properties, processes, and mechanisms of alkyl chains, molecular interactions, and morphologies. Keywords: 1H low field nuclear magnetic resonance relaxometry; Biodiesel physical properties; Fatty acid methyl esters; Melting point; Molecular packing; Segmental motion; Translational motion.
Corresponding Author:	Zeev Wiesman ISRAEL
Corresponding Author Secondary Information:	
Corresponding Author's Institution:	
Corresponding Author's Secondary Institution:	
First Author:	Nitzan Meiri
First Author Secondary Information:	

Order of Authors:	Nitzan Meiri	
	Paula Berman	123
	Luiz Alberto Colnago	
	Tiago Bueno Moraes	
	Zeev Wiesman	
Order of Authors Secondary Information:		

Liquid phase characterization of molecular interactions in polyunsaturated and

n-fatty acid methyl esters by [1]H Low field nuclear magnetic resonance

Nitzan Meiri[a]
Email: nitzanme@post.bgu.ac.il

Paula Berman[a]
Email: bermansh@gmail.com

Luiz Alberto Colnago[b]
Email: luiz.colnago@embrapa.br

Tiago Bueno Moraes[c]
Email: tiagobuemoraes@gmail.com

Charles Linder[d]
Email: charles.linder@gmail.com

Zeev Wiesman[a,*]
[*] Corresponding author
Email: wiesman@bgu.ac.il
Tel/fax: 972-8-6477184

[a] The Phyto-Lipid Biotechnology Lab, Departments of Biotechnology, Energy and

Environmental Engineering, Ben-Gurion University of the Negev, P.O. Box 653,

Beer-Sheva 84105, Israel

[b] Embrapa Instrumentação, Rua 15 de Novembro 1452, São Carlos, SP 13560-970,

Brazil

[c] Instituto de Física de São Carlos, Universidade de São Paulo, Av. Trabalhador Sao-

Carlense 400, São Carlos-SP, 13566-590, Brazil.

[d] Zuckerberg Center for Water Sciences and Technology and Department of

Biotechnology, Ben-Gurion University of the Negev, P.O. Box 653, Beer-Sheva

84105, Israel

124

Abstract

Background

To identify and develop the best renewable and low carbon footprint biodiesel substitutes for petroleum diesel, the properties of different biodiesel candidates should be studied and characterized with respect to molecular structures versus biodiesel liquid property relationships. In our previous paper, [1]H Low Field Nuclear Magnetic Resonance (LF-NMR) relaxometry was investigated as a tool for studying the liquid phase molecular packing interactions and morphology of Fatty Acid Methyl Esters (FAMEs). The technological potential was demonstrated with oleic acid and methyl oleate standards having similar alkyl chains but different head groups. In the present work, molecular organization versus segmental and translational movements of FAMEs in their pure liquid phase, with different alkyl chain lengths (10-20 carbons) and degrees of unsaturation (0-3 double bonds), were studied with ^{1}H LF-NMR relaxometry and X-ray, ^{1}H LF-NMR diffusiometry, and ^{13}C High Field NMR.

Results

Based on density values and X-ray measurements, it was proposed that FAMEs possess a liquid crystal-like order above their melting point, consisting of random liquid crystal aggregates with void spaces between them, whose morphological properties depend on chain length and degree of unsaturation. FAMEs were also found to exhibit different degrees of rotational and translational motions, which were rationalized by chain organization within the clusters, and the degree and type of molecular interactions and temperature effects. At equivalent fixed temperature differences from melting point, saturated FAME molecules were found to have similar translational motion regardless of chain length, expressed by viscosity, self-diffusion coefficients, and spin-spin (T_2) ^{1}H LF-NMR. T_2 distributions suggest

125

increased alkyl chain rigidity and reduced temperature response of the peaks' relative contribution with increasing unsaturation is a direct result of the alkyl chain's morphological packing and molecular interactions.

Conclusions

Both the peaks' assignments for T_2 distributions of FAMEs and the model for their liquid crystal-like morphology in the liquid phase were confirmed. The study of morphological structures within liquids and their response to temperature changes by ^{1}H LF-NMR has a high value in the field of biodiesel and other research and applied disciplines in numerous physicochemical- and organizational-based properties, processes, and mechanisms of alkyl chains, molecular interactions, and morphologies.

Keywords: [1]H low field nuclear magnetic resonance relaxometry; Biodiesel physical properties; Fatty acid methyl esters; Melting point; Molecular packing; Segmental motion; Translational motion.

Background

Diesel fuel has a vital function in the transportation sector, yet its combustion emits greenhouse gases and it is a finite resource; a cost effective renewable substitute should have equivalent fuel efficiency, small net carbon emission, and be readily available worldwide. A potentially attractive alternative to fossil fuel is the use of plant oils – biodiesel [1]. Biodiesel is defined as mono-alkyl esters of long chain fatty acids (FAs), offering a viable alternative to petroleum-based diesel fuel. Biodiesel is non-toxic, degrades four times faster than diesel, and its blending with diesel fuel increases engine efficiency. It also doesn't produce greenhouse effects and is safer in storage due to its high flash point [2]. For these and other reasons, biodiesel production has gradually grown in recent years, raising the need for new rapid and cost effective analytical tools and technologies for developmental characterization and quality control. [1]H low field nuclear magnetic resonance (LF-NMR) holds good potential in the fuel industry with many applications including determination of physical, chemical, structural, and dynamic properties.

In our previous work [3], the molecular packing of methyl oleate (18:1) in its liquid phase was studied. The results from X-ray, LF-NMR diffusiometry, and high field (HF)-NMR measurements were rationalized for the first time by a given liquid phase packing model of fatty acid methyl esters (FAMEs; biodiesel). The developed model for 18:1 proposed that liquid FAMEs have short range order, where molecules arrange in a head-to-head conformation due to polar interactions, and their aggregate morphology retains a quasi-smectic liquid order. The two molecule chains arrange longitudinally, and alternately to make an interdigitated structure, where in the same lateral plane, the ester groups of one molecule and the terminal methyl groups of the neighboring molecule are aligned side by side, similar to FAs [4,5]. The translational

127

movement of FAMEs on the other hand, was found to differ from that of FAs, which are mostly dimerized due to head group hydrogen bonding. While the FA dimer is the basic unit of inter- and intra-molecular movements [4,5], FAME molecules diffuse as monomers.

Biodiesel is a mixture of different FAMEs, with 18:1 as one of the main components, and each component affects the biodiesel properties as a function of its relative concentration. Therefore, to fully characterize biodiesel properties it is necessary to further investigate different FAMEs that vary in chain lengths and number of double bonds.

Very little research has been performed on the liquid phase molecular organization of FAMEs. In general, the physical properties of FAs and their biodiesel derivatives are largely determined by the length of the hydrocarbon chain, the degree of unsaturation, and the effect of molecular packing. In the fully saturated compounds, the hydrocarbon chain is highly flexible with free rotation around each carbon–carbon bond. The most stable conformation is the completely stretched arrangement, wherein the steric hindrance of neighboring atoms is minimized. This conformation allows tight packing in nearly crystalline arrays, stabilized by van der Waals force interactions between the atoms of neighboring molecules. In unsaturated hydrocarbons, chain bending occurs due to *cis* double bonds. The intermolecular interactions of molecules with alkyl chains having several *cis*-bond bends are weaker than molecules with only one *cis*, because of molecular packing with lower packing density compared to one *cis* bond or a fully saturated hydrocarbon. These loosely ordered arrays of unsaturated molecules have lower melting points than

128

monounsaturated molecules of the same chain length, because less thermal energy is needed for overcoming molecular interactions [6].

Matsuzawa et al. [7] studied different molecular packing densities, and suggested that the existence of aggregate clusters most likely determines the liquid properties of FAs such as density and fluidity. It is feasible to assume that this is similar for FAMEs; hence the liquid morphological structure of these materials will affect the physicochemical properties of the biodiesel including viscosity, density, fluid dynamics, and low temperature operability. These properties are of great importance to the field of biodiesel and each is based on different liquid characteristics. For example, viscosity, defined as a liquid's resistance to flow, is a function of the intermolecular forces of attraction within a liquid. Density, on the other hand, defined as the mass per unit volume of a material, depends on how tightly the molecules are packed together. The former rely on interactions between one molecule to its neighbor, while the latter depends on the conformation of a molecule and its packing density properties.

It has been shown that ^{1}H LF-NMR spin-spin (T_2) relaxometry can be applied to differentiate between morphological populations in complex systems [8-12]. Still, there isn't a certainty about the origin of triacylglycerol peaks in ^{1}H LF-NMR relaxation time distributions. It has been suggested that the bimodal T_2 distribution of liquid tricaprin is due to inhomogeneous relaxation rates for the protons along the side chains, or inhomogeneous organization of the triacylglycerols in the liquid with intermolecular interactions [13]. In our previous work [3], these hypotheses were considered regarding oleic acid (18:1 acid) and 18:1, two similar alkyl chain

129

molecules with different head groups, and it was suggested that the two peaks are the result of two distinct mobility populations of the protons on the chain.

In the present study, in order to characterize FAME aggregate structures and how they influence viscosity, liquid density, and temperature effects we focused on further exploring the assignment of the bimodal peaks in ^{1}H LF-NMR T_2 distributions for different FAME molecules, with similar head groups but different alkyl chain lengths (10 to 20 carbons) and degrees of unsaturation (0, 1, 2, and 3 double bonds). Our objective was to study the relationship between molecular organization versus segmental and translational movements of different FAMEs in their pure liquid phase using ^{1}H LF-NMR relaxometry and supporting advanced technologies, including X-ray diffraction, ^{1}H LF-NMR diffusiometry, and ^{13}C HF-NMR.

Results and discussion

^{1}H LF-NMR T_2 distributions of FAMEs at 313 K

Biodiesel is a complex mixture of FAMEs with different lengths, degrees of unsaturation, and composition. It is therefore important to understand the molecular organization versus segmental and translational movements of the separate FAMEs, in order to explain their behavior in the biodiesel blend. The FAMEs evaluated in this study and their literature data of melting temperatures (denoted as T_m) are summarized in Table 1. Throughout this manuscript, FAMEs are identified by their structures.

The combined ^{1}H LF-NMR T_2 distributions of some saturated and unsaturated FAMEs at 313 K are presented in Figure 1. T_2 distributions are arranged by increasing chain length and degree of unsaturation. Intrinsic T_2 values and % relative

contribution (RC) of the peaks are marked on each plot. All T_2 distributions exhibit

two distinct peaks at different T_2 values and RC. These will be denoted as P_1 and P_2

with increasing T_2 values ($T_{2,1}$ and RC_1 will therefore stand for intrinsic T_2 value and

RC of P_1). FAME 18:3 was found to be very prone to oxidation. Almost immediately

following the first measurements an additional peak at low T_2 values appeared that

increased over time (Additional file 1). This same event occurred with different fresh

samples and at different temperatures. In this study, therefore, fresh samples were

used whenever the oxidation peak exceeded an RC of 5%, and only the two main

peaks, not related to oxidation, are discussed.

As shown, each FAME exhibits a slightly different T_2 distribution, which can be

explained by the differences in chemical structures. For the saturated esters, with

increasing chain length RC_1 increases in relation to RC_2 (0, 4, 15, 33, and 48% RC_1

for 10 to 18 carbons) and both $T_{2,1}$ and $T_{2,2}$ values decrease. For the unsaturated esters,

with increasing number of double bonds, again RC_1 increases in relation to RC_2 (18,

46, and 65% RC_1 for 1 to 3 double bonds, respectively) whereas T_2 values of both

peaks increase.

Following the peak assignments we previously suggested [3]; it is proposed that

FAMEs have reduced mobility with increasing chain length and saturation, and intra-

molecularly more rigid parts with increasing chain length and degree of unsaturation.

Interestingly, for the 18 carbon esters, when comparing the fully saturated to

monounsaturated, RC_1 decreases to a greater extent (48 versus 18% RC_1 for 18:0 and

18:1, respectively). This may suggest different molecular organizations and/or type of

interactions for the saturated versus unsaturated FAMEs, since the morphology of the

131

alkyl chains, intermolecular interactions, and absolute temperature of measurement contribute to the ^{1}H LF-NMR T_2 distributions of FAMEs.

In our previous work, we compared T_2 distributions of 18:1 and 18:1 acid relative to the temperature of melting of each compound, and several similarities were suggested for the peaks of each standard, which strengthened their assignment to two distinct mobility populations of the protons on the chain. Adam Berret et al. [13] suggested that liquid triglycerides with three similar fully saturated alkyl chains have comparable behavior for the same difference from their melting temperature, and that the effect of chain length was attenuated with this representation. A similar observation was suggested for different chain length liquid alkanes [18]. This similar behavior is the result of comparable structures and type of interactions between alkyl chains.

Prior to melting, the atoms in a solid have restricted molecular motion and are confined to vibrating about their mean positions within the lattice/morphology structure of the solid. By increasing the temperature of the solid matter, the amplitude of the molecular vibrations increases, until at a certain temperature, intermolecular bonds within the solid break, allowing for bond rotation, and the molecules become free to rotate and translate within the liquid volume. The temperature of transition for a specific substance is the melting point. This is determined by the strength of a crystal lattice, which in turn is controlled primarily by three factors: intermolecular forces, molecular symmetry and packing, and the conformational degrees of freedom of a molecule [19].

Following this approach, in order to gain a deeper understanding of the molecular organization, and rotational and translational motions of saturated FAMEs in the

liquid phase, additional measurements in this work include comparisons according to melting temperatures of each FAME material. Unsaturated FAMEs, on the other hand, have different intermolecular interactions, molecular freedom, and packing, leading to more complicated molecular structures, and rotational and translational motions, which cannot be standardized comprehensively by melting point. These will therefore be compared at absolute temperatures of measurement.

X-ray measurements

In our previous work [3] we suggested a model for the liquid crystal-like arrangement of pure 18:1 molecules in the liquid phase, where two molecules arrange in a head-to-head conformation due to polar interactions, and head groups are aligned next to tails in an interdigitated structure, similarly to the case of 18:1 acid (Figure 2). In order to explore the molecular arrangement of the saturated FAMEs in this present study, the long- and short-range spacings were determined using small angle X-ray scattering (SAXS) and X-ray diffraction (XRD), respectively, close to their melting points at T_m+15 K (Table 2).

The X-ray diffraction spectra acquired resemble those of 18:1 acid and 18:1, as previously reported [3]. Two bands at around 0.14 and 0.03 nm^{-1} were observed, which give a measure of the spacing between adjacent molecules (short-range spacing), and long-range spacing of the plane made by head groups of the aligned molecules, respectively. Due to technical specifications of the XRD instrument, short-range spacing measurements were only available above ambient temperature; therefore measurements of short (10 and 12 carbons) saturated FAMEs, whose T_m+15 K are below 298 K were performed at 298 K. SAXS showed no peaks for 10:0 at T_m+15 K. It was thus measured at T_m+5 K.

All the FAMEs measured exhibited similar short-range spacing. As anticipated, for the saturated FAMEs, longer long-range spacings were found with increasing chain length. The long-range spacing for 10:0, however, was expected to be approximately half that of 20:0. According to Table 2 this was not the case. This same occurrence was previously presented for the long-range spacing of 8:0 acid [7], and was explained as 8:0 acid molecules being only partly interdigitated compared to 18:0 acid molecules, which are completely interdigitated. We believe that the same arrangement applies also for the FAMEs in hand, since even though the head group is different, the structure of the tails is similar.

Above melting temperature, and in accordance with our previous work on 18:1 [3], the results are explained in that the studied FAMEs possess a liquid crystal-like structure, consisting of randomly aggregated liquid clusters with void spaces between them. This kind of microstructural organization can be the result of structural memory coming from the solid structure of FAMEs molecules, where polar interactions exist between heads and molecules arrange in an interdigitated structure. Evidence for this microstructural arrangement can be viewed by differences in density (Table 3). The reported data was compiled from the studies by Pratas et al. [20,21].

Knothe and Steidley [22] have suggested that the density of saturated and monounsaturated FAMEs decreases linearly with increasing temperature. Also, for saturated FAMEs at the same absolute temperature, density slightly decreases with increasing chain length, whereas for unsaturated molecules, density increases with increasing number of double bonds. These density measurements suggest, contrary to our expectation from molecular translational studies, that 18:3 molecules are the most closely packed, while saturated FAMEs are the most loosely packed. Iwahashi and

134

Kasahara [23] found similar behavior for saturated and mono-unsaturated FAs, and have explained this discrepancy by the form of cluster aggregation. They suggested that saturated molecules aggregate tightly to make rigid clusters. These clusters form a liquid morphology with many void spaces between the aggregate clusters leading to an overall lower liquid density and, consequently, a large apparent molar volume. Unsaturated molecules, on the other hand, form similar clusters that appear softer, and can aggregate closer together to form smaller and fewer void spaces between the clusters, leading to increased density and molar volume.

The same holds for the FAMEs in this study. Apparently, chain length can have the same effect on density, where the shorter the chain the softer the cluster leading to increased packing density of the cluster and liquid density. Interestingly, the decrease in density with increasing chain length is not uniform. For the saturated compounds at 313 K, density decreases by 2.1, 1.7, 1.4, 1.0 kg/m^3 for 10 to 18 carbons, respectively. This is true also for other temperatures according to Knothe and Steidley [22], and may be explained by the degree of interdigitation of rods inside the clusters as previously discussed.

Self-diffusion coefficients

The effect of the chemical structure of FAMEs on their translational movement is shown in Figure 3A and B for measurement at a single temperature that was above the melt points for all the FAMEs, and for normalized temperature differences according to the T_m of each FAME, respectively. Interestingly, these results show conflicting trends that can be traced back to the change in morphology and translational motion above the melting point. The self-diffusion coefficient, D, is related to a fluid's viscosity from the Stokes-Einstein equation. From the physicochemical point of view,

135

viscosity is related to the resistance of a molecule to move/slide relative to another molecule. Therefore, viscosity must be closely correlated with the structural parameters of the fluid particles [24].

In Figure 3A (the same temperature for all FAMEs), the shorter the chain of the fully saturated FAME, the faster it diffuses. This can be explained by fewer intermolecular bonds and by the partly interdigitated structure of the shorter FAMEs. For the same chain length, the more double bonds, the larger the D. These results correlate very well with the T_2 relaxation distributions presented in Figure 1. It is well known that kinematic viscosity increases with chain length and with increasing degree of saturation [15]. The effect of unsaturation has been attributed to interference of the double bonds with the molecules' ordered structure by adding kinks to the chain. Ramirez-Verduzco et al. [25] suggested that coil-like *cis*-configuration hinders the interactive approach of the sp^2 atoms with the double bond of neighboring molecules. This means that the translational movement of the unsaturated FAMEs increases with the number of double bonds.

When comparing the translational motion of the FAMEs at similar distances from their melting point (Figure 3B) different trends are observed. Apparently all saturated FAMEs, regardless of chain length, exhibit almost similar translational movement. This can be rationalized by their similar structures and interactions, resulting in similar aggregate morphologies. The increase in melting points with chain length (Table 1) is accounted for by the increase in the number of van der Waals interactions. Therefore, at similar distances from melting point, the differences in translational motion are attenuated by the relative quantities of thermal energy. In addition, saturated FAMEs exhibit highest translational movement, followed by the

136

monounsaturated FAMEs (16:1, 18:1), and then the di- (18:2) and tri-unsaturated (18:3) ones. As suggested before, when comparing FAMEs with different degrees of unsaturation, several additional variables need to be considered that can explain the opposite trend in D, including temperature, type and number of interactions, and aggregate morphologies for different alkyl chain configurations.

Segmental motion

In our previous work [3], the differences in the ^{1}H LF-NMR T_2 distributions of 18:1 acid and 18:1 FAME were supported by ^{13}C HF-NMR relaxation, suggesting that the two peaks in the T_2 distributions are the result of two distinct mobility populations of the protons on the chain. To further explore this assumption, the $1/\tau_c$ values of some saturated and unsaturated FAMEs were measured at T_m+15 K and 298 K, respectively (Figure 4A and B). Spin lattice, T_1, is likely to be correlated to the movement of the carbon atoms, i.e., segmental motion (specifically, rotational tumbling and to a lesser extent translational and internal motion) in the molecule. Assignment of ^{13}C chemical shifts to the appropriate peaks was performed according to the literature [26]. As previously suggested, the tail in all FAMEs moves more vigorously than the interior chain. In addition, the head has greater freedom of movement and is not tightly bonded, since $1/\tau_c$ values decrease from the second carbon towards the center of the chain.

According to Figure 4A, the longer the chain length, the more rigid carbons there are in the interior part of the FAME molecule chain. These results fit very well with the data presented in the literature [27] for the segmental motion of 9:0 acid and 18:0 acid. This can be rationalized by an increase in van der Waals interactions with increasing chain length, as suggested also by the molecular organization as viewed

137

from the X-ray results (partial versus full interdigitated structure for short- and long-chain FAMEs, respectively). The lower $1/\tau_c$ values for all carbons in 10:0 compared to 16:0 and 18:0 can be attributed to the large difference in the absolute temperature of measurement of the three (273 K for 10:0 versus 318 K and 328 K for 16:0 and 18:0, respectively).

For the unsaturated FAMEs at an absolute temperature of 298 K, the rotational movement of the tail increases with number of double bonds. This correlates with the self-diffusion coefficient of unsaturated FAMEs at absolute temperatures (Figure 3A), since as suggested in the literature, the segmental movements at the end and near the end of the molecule are probably most important for the FAME molecules to find the spaces for their translational diffusion [3,28]. Segmental motion mainly of the tail is facilitated due to the bending of the molecule, which leads to reduced van der Waals interactions and higher degree of freedom. The motion of the double bond carbons, on the other hand, is considerably restricted (Figure 4B). Pi et al. [29] stated that the movement and bending of alkyl chain of 18:2 acid from C9 to C13 is more regulated compared with that in the alkyl chain of 18:1 acid due to the presence of an additional C=C bond. The decrease in segmental motion at the double bond position can therefore be attributed to the larger energy barrier to bond rotation as a result of the double bonds, and stronger intermolecular interactions between the π electrons. This implies increased rigidity with an increased number of double bonds as previously suggested according to the relative contribution of the peaks in T_2 distributions (Figure 1).

^{1}H LF-NMR T_2 distributions at different temperatures

138

The combined ^{1}H LF-NMR T_2 distributions of saturated and unsaturated FAMEs are presented in Figures 5A-E and 6A-C with increasing chain length and degree of unsaturation, respectively. For the saturated FAMEs measurements are compared at similar temperature distances from their T_m, whereas the results for the unsaturated FAMEs are shown at absolute temperatures of measurement. Intrinsic T_2 values and % RC of each peak are marked on each plot.

In accordance with our previous work [3], for the saturated FAMEs, as temperature increases $T_{2,1}$ and $T_{2,2}$ shift to higher values and RC_1 decreases in favor of RC_2. For the saturated FAMEs, the effect of presenting results at specific distances from melting point versus one absolute temperature can be seen by comparing T_2 distributions in Figure 5A-E, at any one of the temperature distances, to Figure 1. According to this normalization, certain constancy can be observed in $T_{2,1}$ and $T_{2,2}$, especially for 10:0 and 12:0, and for 14:0–18:0. RC_1, on the other hand, increases with chain length in relation to RC_2, as stated for the absolute single temperature comparison (Figure 1). This increase can be explained by the addition of rigid parts of the molecule and number of van der Waals interactions, as manifested from the segmental motion (Figure 4A).

It was established in the past that mono-exponential T_2 values of FAMEs correlate with their viscosity for the same temperature [30,31]. Table 4 presents the mono-exponential T_2s for the saturated FAMEs and dynamic viscosities, η, according to [20], at T_m+5 K and at 313 K for reference. Mono-exponential T_2s at 313 K were calculated from the relaxation data used for the analyses presented in Figure 1. As shown, saturated FAMEs exhibit very similar translational motion at similar distances from melting point compared to absolute temperatures, according to the dynamic

139

viscosity values and mono-exponential T_2s, even though their melting points differ to a great extent (Table 1). These results are comparable with the self-diffusion coefficients presented in Figure 3A and B for absolute and normalized temperatures, respectively. In addition, the mono-exponential T_2s at T_m+5K in Table 4 resemble each other to a greater degree than $T_{2,1}$ and $T_{2,2}$ in Figure 5 for the same temperatures (for 10:0 to 18:0 a T_2 range of 589-617 versus 644-761 ms for mono-exponential T_2 and $T_{2,2}$, respectively). This suggests that the overall translational motion of saturated FAMEs is not affected solely by the mobility of the different parts of the molecules, and that the RCs of the peaks indicate other molecular parameters (e.g., molecular interactions) that also play an important part.

The unsaturated FAMEs (Figure 6A-C) also display an increase in $T_{2,1}$ and $T_{2,2}$ with temperature. The RCs of the peaks, on the other hand, exhibit different trends with temperature and number of double bonds. In general for the unsaturated FAMEs, RC_2 increases with temperature in relation to RC_1; however, this response is attenuated with increasing number of double bonds. For the temperature range 258-308 K, RC_2 increases in the ranges 24-77%, 42-53%, and 33-35% for 1-3 double bonds, respectively. The change in RC of the peaks with increasing temperature and unsaturation may reflect the number and type of weak intermolecular interactions.

In this study our characterization of different FAME molecules by ^{1}H LF-NMR relaxometry, diffusion, ^{13}C HF-NMR, and X-Ray methods gives a clear indication of their molecular morphology and intermolecular interactions. For the saturated molecules, the longer the chain length the higher the melting point, since their chain configuration is linear and molecules can pack closely together, with maximum interactions due to an increasing number of van der Waals contacts, as manifested by

140

increasing RC_1. For the same chain length and increasing number of double bonds, melting temperatures decrease. Unsaturated molecules of *cis* configuration cannot pack as close due to bending of the chain at the double bond position, minimizing secondary interactions. As seen from their melting temperatures, they require much less energy for disordering the crystal structure and breaking intermolecular interactions to achieve molecular motion above the melt point.

When going from the fully saturated to the mono-unsaturated 18-carbon molecule, a reduction in RC_1 occurs in the ^{1}H LF-NMR T_2 distributions (Figure 1). This can be explained as a sharp decrease in the number of van der Waals interactions due to bending of the 18:1 chain, as previously discussed. When increasing the number of double bonds, increase in π-π interactions takes place as revealed by an increase in RC_1 as shown when going from 18:1$\rightarrow$18:2$\rightarrow$18:3. This can also explain the decrease with unsaturation of the RC_1 response to increasing temperature, since it is well known that less energy (temperature) is required to break van der Waals interactions compared to π-π interactions.

These results strengthen the peak assignment suggested for the ^{1}H LF-NMR T_2 distributions of FAMEs, where the two peaks are the result of two distinct mobility populations of the protons on the chain affected by the molecular structure and weak intermolecular interactions. In a previous paper [32] we presented the ^{1}H LF-NMR T_2 distribution of a rapeseed biodiesel sample measured at 313 K. In that study, the biodiesel sample exhibited three peaks with intrinsic T_2 values of 338, 671, and 1141 ms. Given that the main constituents in this biodiesel at decreasing ratios are 18:1, 18:2, 18:3, 16:0, and 18:0, the peaks can be assigned as the average contribution according to the three regions designated a, b, and c in Additional file 2. An

interesting study would be to explore the change in ^{1}H LF-NMR RC of the peaks in

biodiesels from different sources and at different temperatures, to study dynamic

processes, melting mechanisms, and structural organizations of alkyl chains, with

important applications in the development of biodiesel fuels.

Conclusions

Both the peaks' assignments for ^{1}H LF-NMR T_2 distributions of FAMEs and the

model for their liquid crystal-like structure/morphology in the liquid phase, used to

rationalize the assignment, were confirmed in the present work. This morphology

along with the number and type of interactions and temperature effects generated

differences in translational and rotational movements of the molecules, which were

monitored using the presented ^{1}H LF-NMR methodology. The study of morphological

structures within liquids and their response to temperature changes by ^{1}H LF-NMR is

a powerful tool. This new application of ^{1}H LF-NMR is of potentially great interest to

the field of biodiesel, and to other research and applied disciplines with the potential

of studying numerous physicochemical- and organizational-based properties,

processes, and mechanisms of alkyl chains.

Materials and Methods

Materials

Pure samples (≥99%) of methyl ester standards (Table 1) were purchased from Sigma

Aldrich and used without further purification. These FAMEs exhibit a wide range of

melting points and consequently are in different states for the same absolute

temperature [33]. Some of the measurements were therefore compared according to a

given temperature distance from melting point ($T=T_m+d$, where T is the actual

142

temperature of measurement, T_m is the melting point, and d the temperature distance

from T_m). The melting temperatures used for the materials in this study are within ±2

K from the melting temperatures reported in the literature (Table 1).

^{1}H LF-NMR relaxometry and diffusiometry

Measurements were carried out on a 20 MHz minispec bench-top pulsed NMR

analyzer (Bruker Analytic GmbH, Germany), equipped with a permanent magnet and

a 10-mm temperature controlled probe head. Prior to measurement, samples were

heated from 193 K for a minimum 3 h and then allowed to equilibrate inside the

instrument for 5 min. All measurements were performed on liquid standards (above

melting point). Receiver gain was optimized for each temperature and sample.

Determination of spin-spin relaxation time constant (T_2) was performed using a

CPMG pulse sequence [34,35]. τ and recycle delay were between 0.4 and 1.5 s and 4

and 8 s, respectively. For all the analyses 32 scans were accumulated and 8000 echoes

were acquired. Data was acquired in magnitude mode due to better repeatability and

stability of results, and further analyzed using the PDCO inverse Laplace transform

optimization algorithm with $a_2=0.5$ as described in the literature [36].

Mono-exponential fitting of the acquired CPMG raw data was performed by SPSS

software (version 15.0, SPSS Inc.) using Eq. (1):

Eq. (1) $$s(t) = we^{-t/T_2}$$

where s(t) is the acquired signal at t time, w is the pre-exponential weighting factor,

and T_2 is the mono-exponential relaxation time constant for transverse relaxation.

The self-diffusion coefficient, D, was determined by the pulsed-field gradient spin echo (PFGSE) method [37]. The pulse sequence was used with 16 scans, τ of 7.5 ms, and a recycle delay of 6 s. Typical gradient parameters were Δ of 7.5 ms, δ of 0.5 ms, time between the 90° pulse to the first gradient pulse of 1 ms and G of 1.6 T/m. A double distilled water sample was used for calibration. D values of water were taken from [38]. Each reported value is the average of a minimum of 10 measurements.

High field (HF) ^{13}C-NMR relaxometry

Measurements were performed on a BRUKER AVANCE III operating at 150 MHz for ^{13}C. Prior to measurement, samples were heated for minimum 10 min and added to a 5 mm NMR tube. For lock signal, a closed 1 mm capillary tube, filled with D_2O, was added to the sample. The non-spinning samples were allowed to equilibrate inside the instrument for 15 min after reaching the set temperature. Before each measurement, shimming was optimized using automated and manual procedures. The chemical shifts, in parts per millions (ppm), were obtained without reference signal. The spectra were obtained using 8 scans and recycle delay of 120 s.

The longitudinal relaxation times, T_1, were measured using the INVREC method [39]. The calculations of T_1 were carried out with the subroutine included in the TOPSPIN 3.2 software package.

^{13}C HF-NMR spin-lattice relaxation of a protonated carbon is overwhelmingly dominated by dipole-dipole interactions with the attached protons [28]. T_1 is therefore related to the number of directly bonded hydrogen, N, and the effective correlation time, τ_c, for the rotational movement of the carbon atoms in the object molecule. Thus, T_1 is approximately given in terms of N and $1/\tau_c$:

144

$$\text{Eq. (2)} \qquad\qquad T_1 = \frac{r_{CH}^6}{N\hbar^2\gamma_C^2\gamma_H^2} \cdot \frac{1}{\tau_C}$$

where ħ is Planck's constant and γ_C and γ_H are the gyromagnetic ratios of ^{13}C and ^{1}H, respectively. Here, r_{CH} is the C-H distance, usually about 0.109 nm, and the reciprocal of the effective correlation time, $1/\tau_c$, represents the magnitude of the segmental rotation for the carbon atom at a different position.

X-ray methods

XRD and SAXS techniques were used for measuring the short- and long-range spacing between adjacent molecules, respectively.

XRD data was collected on Panalytical Empyrean Powder Diffractometer equipped with position sensitive (PSD) X'Celerator detector using Cu K_α radiation (λ=0.154 nm) and operated at 40 kV and 30 mA. The usual Bragg-Brentano $\theta/2\theta$ geometry was employed. $\theta/2\theta$ scans were run during 15 min in a 2θ range of 2-35° with step equal to ~0.0167°.

SAXS measurements were performed on a SAXSLAB GANESHA 300-XL (Skovlunde, Denmark) instrument. Cu K_α (λ=0.154 nm) radiation was generated by Genix 3D Cu-source (operated at 47 mV and 0.55 mA) with integrated Monochromator, 3 pinholes collimation, and two-dimensional Pilatus 300K detector. The distance between the sample and detector was 350 mm. q range was between 0.0012 and 0.067 nm^{-1}.

List of abbreviations

FA: fatty acid; FAME: fatty acid methyl ester; HF-NMR: high field nuclear magnetic resonance; LF-NMR: low field nuclear magnetic resonance; PFGSE: pulsed-field

gradient spin echo; RC: relative contribution; SAXS: small angle X-ray scattering;

XRD: X-ray diffraction.

Competing interests

The authors declare that they have no competing interests.

Authors' contributions

NM performed the ^{1}H LF-NMR measurements and analyzed all the results. PB

drafted the manuscript and contributed to the analysis of results. LAC and TBM

performed the HF-NMR measurements. NM, PB, LAC, CL and ZW contributed to

the development of the experimental design and proofread the manuscript. ZW led

and coordinated the overall project. All authors read and approved the final

manuscript.

Acknowledgements

References

146

1. Meher L, Vidya Sagar D, Naik S. Technical aspects of biodiesel production by transesterification—a review. Renew Sust Energ Rev. 2006;10(3)**:**248-68.

2. Murugesan A, Umarani C, Subramanian R, Nedunchezhian N. Bio-diesel as an alternative fuel for diesel engines—A review. Renew Sust Energ Rev. 2009;13(3)**:**653-62.

3. Berman P, Meiri N, Colnago LA, Moraes TB, Linder C, Levi O, Parmet Y, Saunders M, Wiesman Z. Study of liquid phase molecular packing interactions and morphology of fatty acid methyl esters (biodiesel) by ^{1}H low field nuclear magnetic resonance relaxometry. Biotechnol Biofuels. in press.

4. Iwahashi M, Yamaguchi Y, Kato T, Horiuchi T, Sakurai I, Suzuki M. Temperature dependence of molecular conformation and liquid structure of *cis*-9-octadecenoic acid. J Phys Chem. 1991;95(1)**:**445-51.

5. Iwahashi M, Suzuki M, Czarnecki MA, Liu Y, Ozaki Y. Near-IR molar absorption coefficient for the OH-stretching mode of *cis*-9-octadecenoic acid and dissociation of the acid dimers in the pure liquid state. J Chem Soc Faraday T. 1995;91(4)**:**697-701.

6. Nelson DL, Lehninger AL, Cox MM. Lehninger principles of biochemistry. 4th ed. New York: W.H. Freeman; 2004.

7. Matsuzawa H, Tsuda M, Minami H, Iwahashi M. Dynamic Molecular Behavior and Cluster Structure of Octanoic Acid in Its Liquid and CCl4 Solution. Food Nutr Sci. 2013;4:25.

8. Barros CN, Arêas EP, Figueiredo EN, Arêas JA. Low-resolution ^{1}H spin–spin relaxation of *n*-decane/water emulsions stabilized by β-casein. Colloid Surf B. 2006;48(2)**:**119-27.

9. Silva RC, Carneiro GF, Barbosa LL, Lacerda V, Freitas JC, Castro EV. Studies on crude oil-water biphasic mixtures by low-field NMR. Magn Reson Chem. 2012;50(2)**:**85-8.

10. Bertram HC, Wiking L, Nielsen JH, Andersen HJ. Direct measurement of phase transitions in milk fat during cooling of cream—a low-field NMR approach. Int Dairy J. 2005;15(10)**:**1056-63.

11. Chatakanonda P, Chinachoti P, Sriroth K, Piyachomkwan K, Chotineeranat S, Tang H, Hills B. The influence of time and conditions of harvest on the functional behaviour of cassava starch—a proton NMR relaxation study. Carbohydr Polym. 2003;53(3)**:**233-40.

12. Hills B, Le Floc'h G. NMR studies of non-freezing water in cellular plant tissue. Food Chem. 1994;51(3)**:**331-6.

13. Adam-Berret M, Boulard M, Riaublanc A, Mariette F. Evolution of fat crystal network microstructure followed by NMR. J Agric Food Chem. 2011;59(5)**:**1767-73.

14. Knothe G, Dunn RO. A comprehensive evaluation of the melting points of fatty acids and esters determined by differential scanning calorimetry. J Am Oil Chem Soc. 2009;86(9)**:**843-56.

15. Knothe G. Dependence of biodiesel fuel properties on the structure of fatty acid alkyl esters. Fuel Process Technol. 2005;86(10)**:**1059-70.

16. Lide DR. Handbook of Chemistry and Physics. 88th ed. Boca Raton, FL: CRC Press; 2007.

17. Gunstone FD, Harwood JL, Dijkstra AJ, editors. The Lipid Handbook. 3rd ed. Boca Raton: CRC Press; 2007.

18. Ovchinnikov YK, Antipov EM, Markova GS, Bakeev NF. Comparative investigation of short-range order in unbranched alkanes and polyethylene. Makromolekul Chem. 1976;177(5)**:**1567-81.

19. Katritzky AR, Jain R, Lomaka A, Petrukhin R, Maran U, Karelson M. Perspective on the relationship between melting points and chemical structure. Cryst Growth Des. 2001;1(4)**:**261-5.

20. Pratas MJ, Freitas S, Oliveira MB, Monteiro SC, Lima AS, Coutinho JA. Densities and viscosities of fatty acid methyl and ethyl esters. J Chem Eng Data. 2010;55(9)**:**3983-90.

21. Pratas MJ, Freitas S, Oliveira MB, Monteiro SC, Lima ÁS, Coutinho JA. Densities and viscosities of minority fatty acid methyl and ethyl esters present in biodiesel. J Chem Eng Data 2011;56(5)**:**2175-80.

22. Knothe G, Steidley KR. A comprehensive evaluation of the density of neat fatty acids and esters. J Am Oil Chem Soc. 2014;91(10)**:**1711-22.

23. Iwahashi M, Kasahara Y. Dynamic molecular movements and aggregation structures of lipids in a liquid state. Curr Opin Colloid In. 2011;16(5)**:**359-366.

24. Demirbas A. Relationships derived from physical properties of vegetable oil and biodiesel fuels. Fuel. 2008;87(8)**:**1743-8.

25. Ramírez-Verduzco LF, Rodríguez-Rodríguez JE, Jaramillo-Jacob AdR. Predicting cetane number, kinematic viscosity, density and higher heating value of biodiesel from its fatty acid methyl ester composition. Fuel. 2012;91(1)**:**102-11.

26. Gunstone F, Pollard M, Scrimgeour C, Gilman N, Holland B. Fatty acids. Part 48. ^{13}C nuclear magnetic resonance studies of acetylenic fatty acids. Chem Phys Lipids. 1976;17(1)**:**1-13.

27. Iwahashi M, Kasahara Y, Minami H, Matsuzawa H, Suzuki M, Ozaki Y. Molecular Behaviors of n-Fatty Acids in Liquid State. J Oleo Sci 2002;51(3)**:**157-64.

28. Iwahashi M, Kasahara Y, Matsuzawa H, Yagi K, Nomura K, Terauchi H, Ozaki Y, Suzuki M. Self-diffusion, dynamical molecular conformation, and liquid structures of n-saturated and unsaturated fatty acids. J Phys Chem B. 2000;104(26)**:**6186-94.

29. Pi F, Shinzawa H, Czarnecki MA, Iwahashi M, Suzuki M, Ozaki Y. Self-assembling of oleic acid (*cis*-9-octadecenoic acid) and linoleic acid (*cis*-9, *cis*-12-octadecadienoic acid) in ethanol studied by time-dependent attenuated total reflectance (ATR) infrared (IR) and two-dimensional (2D) correlation spectroscopy. J Mol Struct. 2010;974(1)**:**40-5.

30. Prestes RA, Colnago LA, Forato LA, Vizzotto L, Novotny EH, Carrilho E. A rapid and automated low resolution NMR method to analyze oil quality in intact oilseeds. Anal Chim Acta. 2007;596(2)**:**325-9.

31. Berman P, Nizri S, Parmet Y, Wiesman Z. Large-scale screening of intact castor seeds by viscosity using time-domain NMR and chemometrics. J Am Oil Chem Soc. 2010;87(11)**:**1247-54.

150

32. Berman P, Leshem A, Etziony O, Levi O, Parmet Y, Saunders M, Wiesman Z. Novel 1H low field nuclear magnetic resonance applications for the field of biodiesel. Biotechnol Biofuels. 2013;6(1)**:**55-6834-6-55.

33. Marangoni A. Fat crystal networks. Boca Raton, FL: CRC Press; 2005.

34. Carr HY, Purcell EM. Effects of diffusion on free precession in nuclear magnetic resonance experiments. Phys Rev. 1954;94(3)**:**630.

35. Meiboom S, Gill D. Modified spin-echo method for measuring nuclear relaxation times. Rev Sci Instrum. 1958;29(8)**:**688-91.

36. Berman P, Levi O, Parmet Y, Saunders M, Wiesman Z. Laplace inversion of low-resolution NMR relaxometry data using sparse representation methods. Concepts Magn Reson 2013;42(3)**:**72-88.

37. Stejskal E, Tanner J. Spin diffusion measurements: spin echoes in the presence of a time-dependent field gradient. J Chem Phys 1965;42(1)**:**288-92.

38. Holz M, Heil SR, Sacco A. Temperature-dependent self-diffusion coefficients of water and six selected molecular liquids for calibration in accurate 1H NMR PFG measurements. Phys Chem Chem Phys. 2000;2(20)**:**4740-2.

39. Abragam A, Hebel L. The principles of nuclear magnetism. Am J Phys 1961;29(12)**:**860-1.

Figure legends

Figure 1. Combined ^{1}H LF-NMR T_2 distributions of FAMEs at 313 K. Plots are arranged by increasing chain length (bottom to top) and increasing degrees of unsaturation. The relative contributions of each peak in relation to the other peak and intrinsic T_2 values are shown on each plot. FAMEs are referred by their structures.

Figure 2. Molecular arrangement representation of 18:1 FAME molecules in the liquid. 18:1 FAME molecules arrange very similarly to 18:1 acid in an interdigitate structure where heads interact through polar interactions in a head-to-head conformation. The two molecule chains arrange longitudinally and alternately to make an interdigitated structure, where in the same lateral plane, the ester groups of one molecule and the terminal methyl groups of the neighboring molecule are aligned side by side. This model was suggested in our previous paper [3].

Figure 3. Self-diffusion coefficients, D, of FAMEs in response to temperature. D measurements are compared at (A) absolute temperature and (B) temperature distances from each sample's melting point (T_m) for all FAMEs. FAMEs are referred to by their structures. For the absolute temperatures (A), diffusion increases with decreasing chain length and for the same chain length increasing number of double bonds. For the normalized temperatures (B), saturated FAMEs exhibit highest and almost similar translational movement, followed by the monounsaturated FAMEs (16:1, 18:1), the di- (18:2) and tri-unsaturated (18:3) ones. The conflicting trends can be traced back to the change in morphology and translational motion above the melting point.

Figure 4. Segmental motion of some FAMEs. Segmental motion through the reciprocal of the effective correlation time, $1/\tau_c$, of the carbon atoms at different

152

positions of (A) saturated FAMEs (10:0, 16:0, and 18:0) at T_m (melting point) +15 K

and (B) unsaturated FAMEs (18:1, 18:2, and 18:3) at 298 K. FAMEs are referred to

by their structures. The structures of 18:0 and 18:1 in (A) and (B), respectively, along

with designation of carbon numbers are shown for reference.

Figure 5. **Combined ^{1}H LF-NMR T_2 distributions of saturated FAMEs at**

different temperatures. Comparison between the T_2 distributions of the saturated

(A) 10:0, (B) 12:0, (C) 14:0, (D) 16:0, and (E) 18:0 FAMEs at different temperature

distances from their melting points (T_m). FAMEs are referred to by their structures.

The relative contributions of each peak in relation to the other peak and intrinsic T_2

values are shown on each plot.

Figure 6. Combined ^{1}H LF-NMR T_2 distributions of unsaturated FAMEs at

different temperatures. Comparison between the T_2 distributions of the unsaturated

(A) 18:1, (B) 18:2, and (C) 18:3 FAMEs at different temperatures. FAMEs are

referred to by their structures. The relative contributions of each peak in relation to

the other peak and intrinsic T_2 values are shown on each plot.

Additional files

Additional file 1.pdf. Combined ^{1}H LF-NMR T_2 distributions of 18:3 at

increasing degrees of oxidation. Measurements were performed at 293 K. Plots are

denoted A, B, C by increasing time of natural oxidation. The Relative Contribution

(RC) of the additional peak was found to increase over time, as marked on each plot,

while the ratio between RC_1 and RC_2 (RC of P_1 and P_2, respectively) was kept

unchanged.

Additional file 2.pdf. Combined ^{1}H LF-NMR T$_2$ distributions of a rapeseed biodiesel sample and its main FAMEs at 313 K. Plots are arranged by increasing chain length (bottom to top) and increasing degrees of unsaturation. Peaks are assigned to three regions (a, b, c) according to intrinsic T$_2$s. FAMEs are referred to by their structures.

Table 1. Summary of the FAMEs evaluated in this study and literature data of melting temperatures (T_ms).

IUPAC name	Common name	Structure	T_m [K]
Methyl decanoate	Methyl caprate	10:0	259.5 [14]
Methyl dodecanoate	Methyl laurate	12:0	278.0 [15]
Methyl tetradecanoate	Methyl myristate	14:0	292.0 [16]
Methyl hexadecanoate	Methyl palmitate	16:0	303.0 [16]
Methyl octadecanoate	Methyl stearate	18:0	312.1 [16]
Methyl eicosanoate	Methyl arachidate	20:0	318.8 [17]
Methyl Z-9-hexadecenoate	Methyl palmitoleate	16:1	238.9 [14]
Methyl Z-9-octadecenoate	Methyl oleate	18:1	253.0 [15]
Methyl Z,Z-9,12-octadecadienoate	Methyl linoleate	18:2	238.0 [15]
Methyl Z,Z,Z-9,12,15-octadecatrienoate	Methyl linolenate	18:3	227.5 [15]

T_m: Melting temperature.

Table 2. Short- and long-range spacing of saturated FAMEs measured at T_m+15 K.

FAME structure	Short spacing [nm]	Long spacing [nm]
10:0	0.459[a]	1.70[b]
12:0	0.461[a]	2.08
14:0	0.459	2.27
16:0	0.462	2.53
18:0	0.455	2.64
20:0	0.457	2.83

[a]Measurements performed at ambient temperature.

[b]Measurement performed at T_m+5 K.

T_m: Melting temperature.

Table 3. Densities, ρ, of some FAMEs measured at 313 K (compiled from the literature).

FAME structure	ρ [kg/m^3]
10:0	856.0 [20]
12:0	853.9 [20]
14:0	852.2 [20]
16:0	850.8 [20]
18:0	849.8 [20]
16:1	853.8 [21]
18:1	859.5 [20]
18:2	871.5 [20]
18:3	887.0 [20]

ρ: Density.

Table 4. Mono-exponential T_2 and dynamic viscosity, η, of saturated FAMEs at T_m+5 K and 313 K.

FAME structure	T_m+5 K		313 K	
	T_2 [ms]	η^a [mPa·s]	T_2 [ms]	η^a [mPa·s]
10:0	589	na	1206	1.48
12:0	601	4.07	974	2.08
14:0	606	3.98	774	2.84
16:0	612	4.21	662	3.75
18:0	617	4.43	560	4.99

[a]Dynamic viscosity values were taken from [20].

na: data not available.

T_m: Melting temperature; T_2: Spin-spin relaxation time; η: Dynamic viscosity.
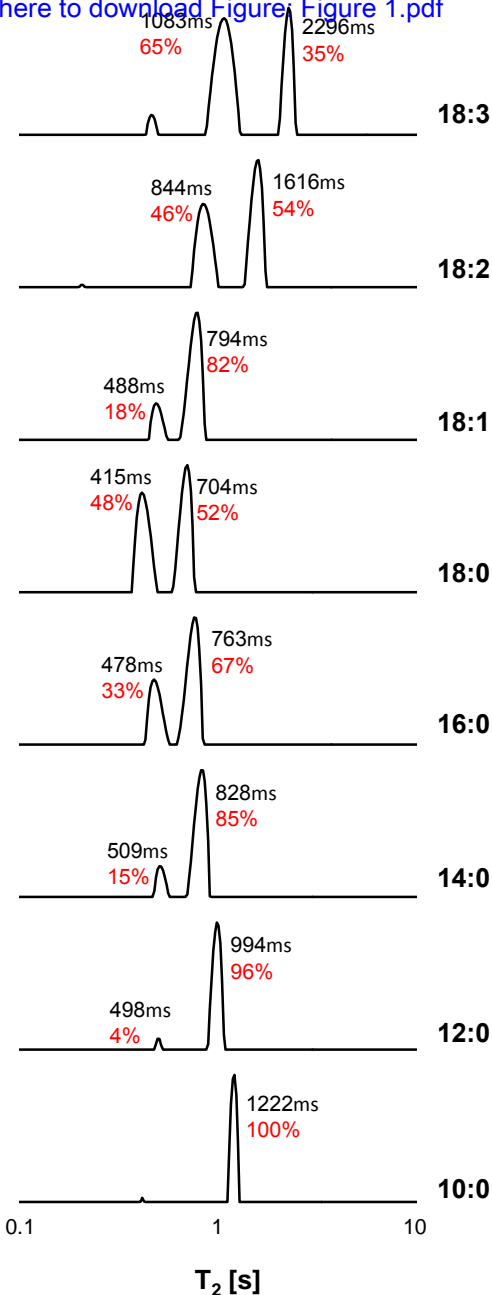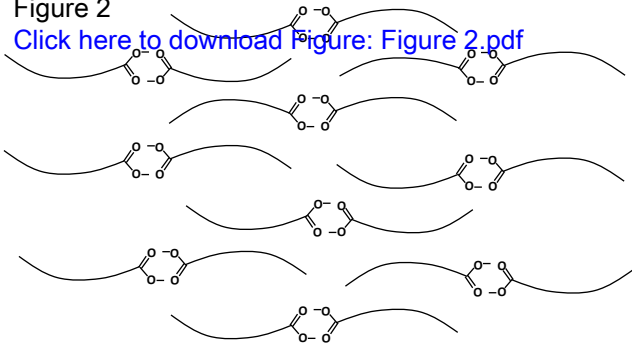
Figure 1

Figure 2

Figure 3
Click here to download Figure: Figure 3.pdf
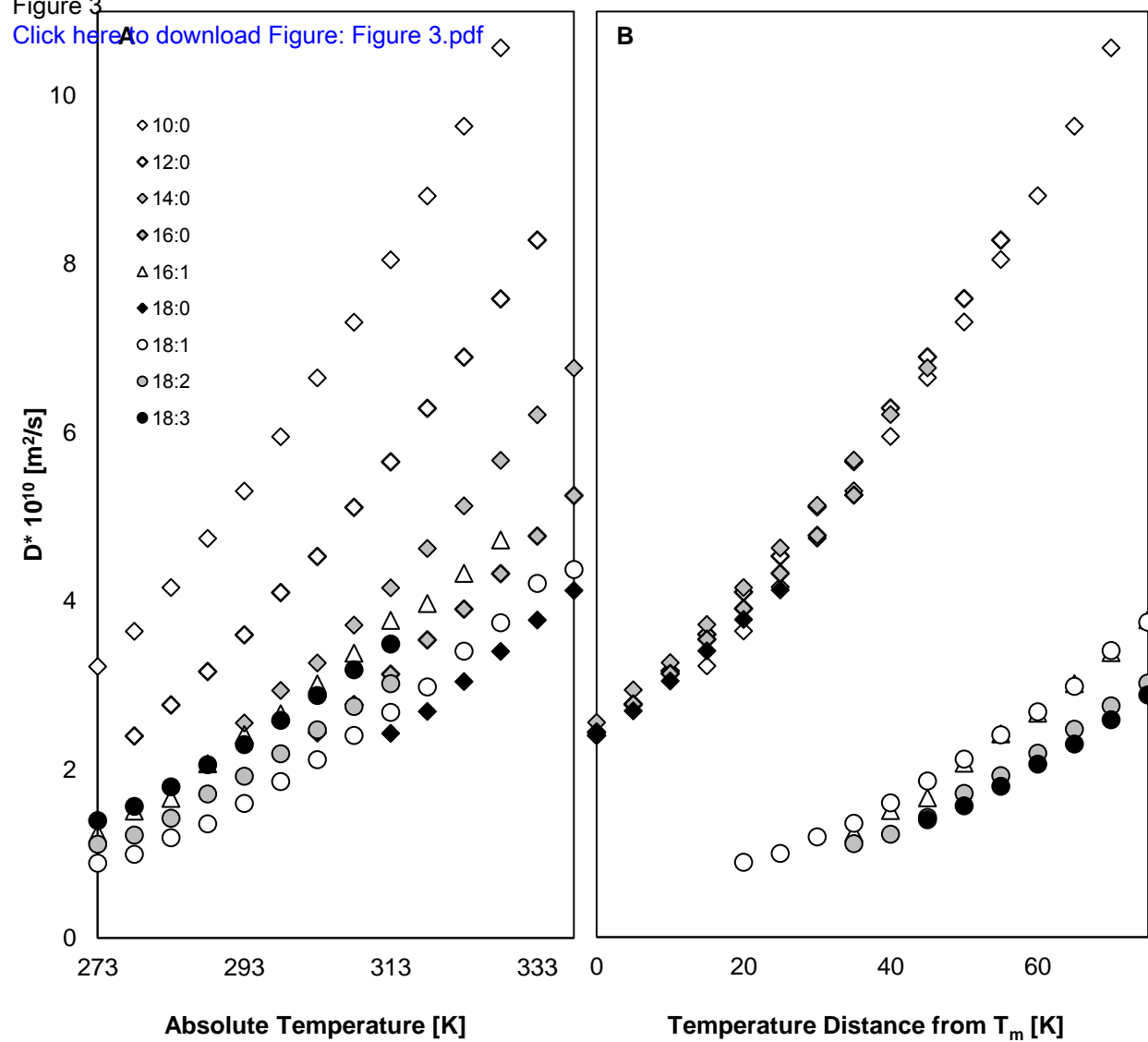
Figure 3

Figure 4
Click here to download Figure: Figure 4.pdf

Figure 4
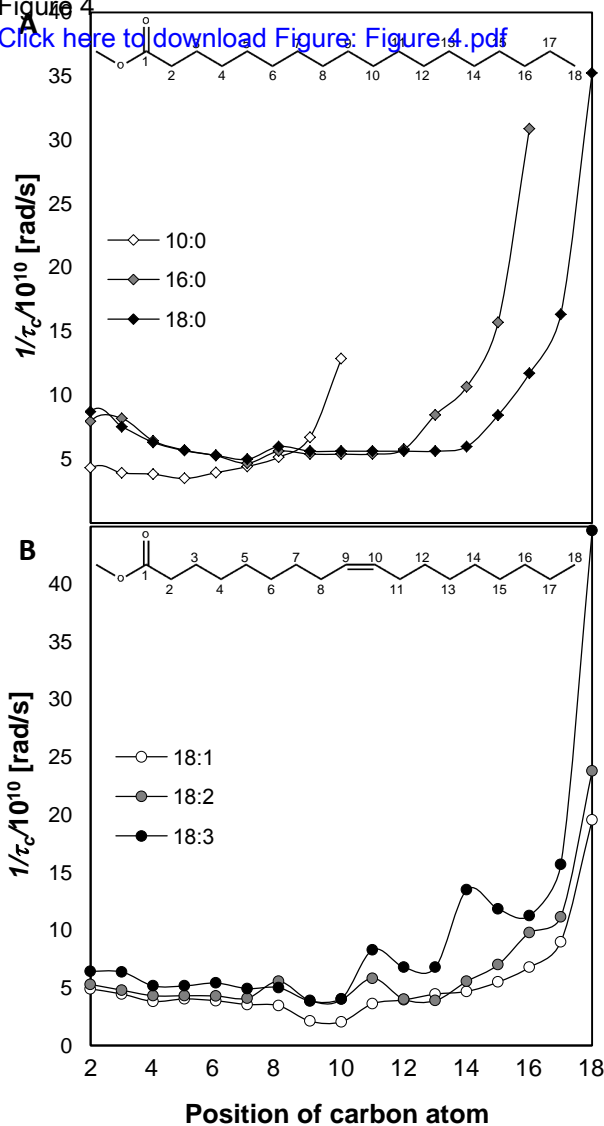
Figure 5
Click here to download Figure: Figure 5.pdf

Figure 5

Figure 6
Click here to download Figure: Figure 6.pdf

Figure 6

Supplumentary material 1

Supplumentary material 2
Click here to download Supplementary Material: Additional file 2.pdf

Rapeseed biodiesel

18:3

18:2

18:1

18:0

16:0

Normalized Intensity [nu+offset]

T_2 [s]

0.1   1   10
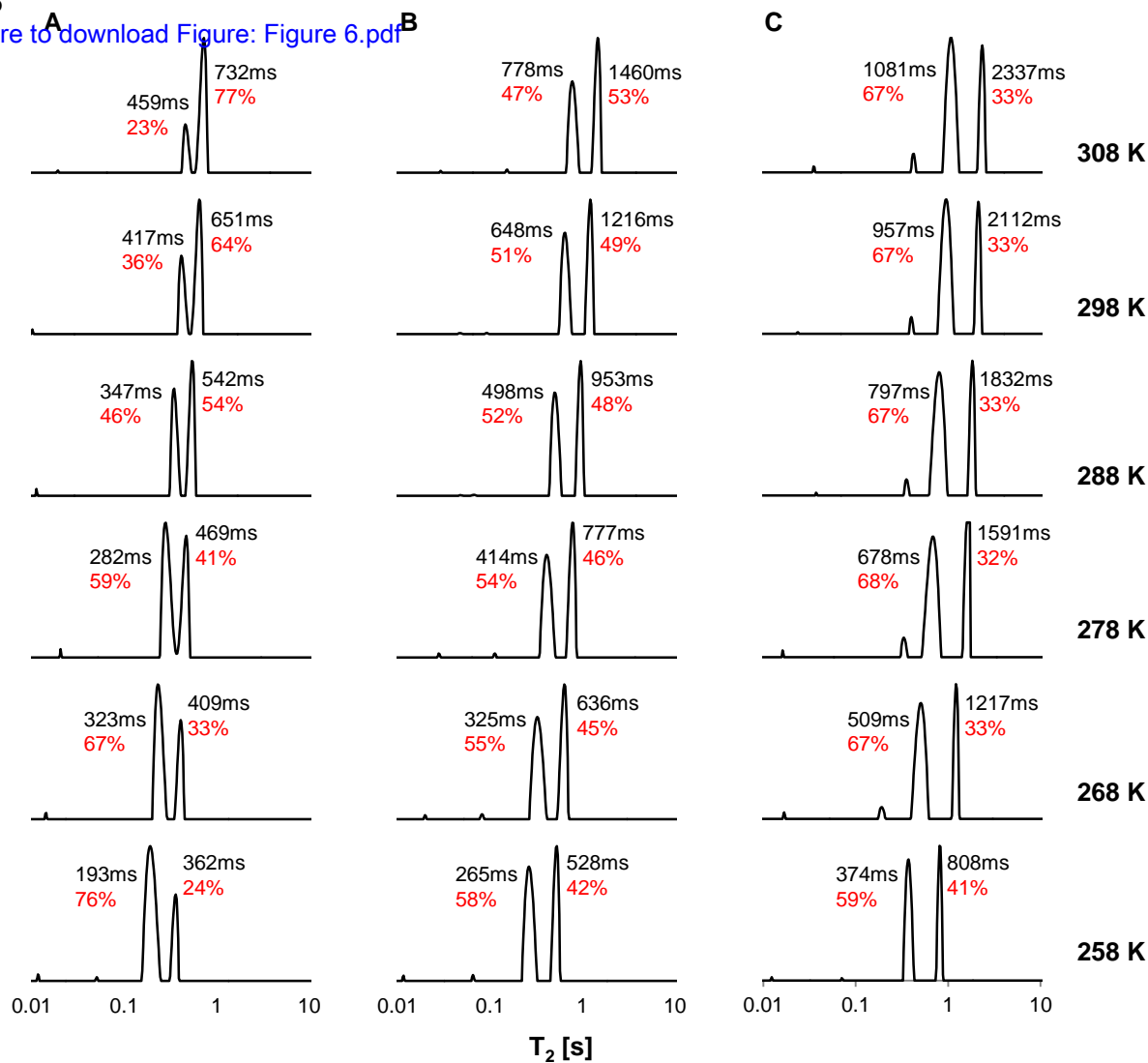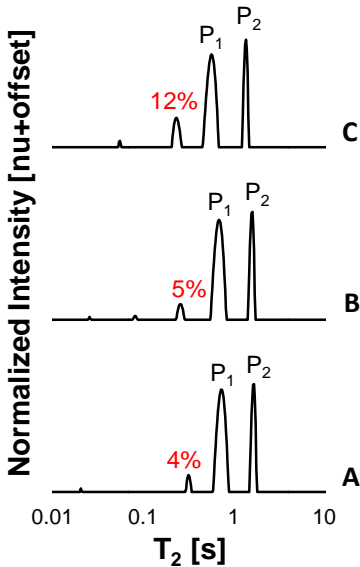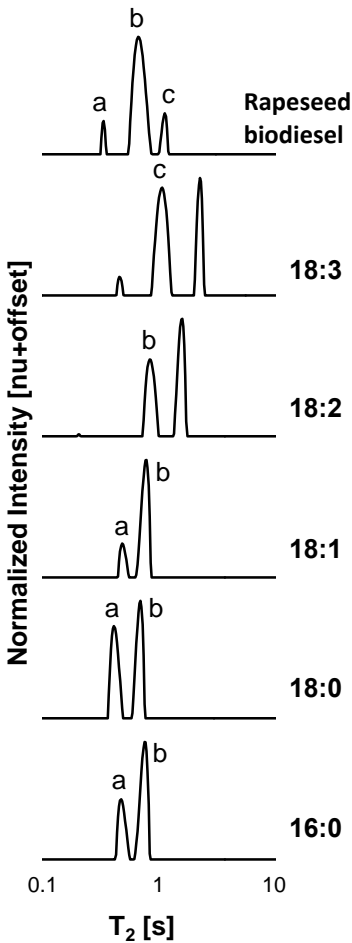
CHAPTER 3

Discussion

Biodiesel production has increased dramatically over the last decade; however, several technical challenges still remain for improving its sustainability as a biofuel, including (a) researching for advanced, high prospect, second generation biodiesel feedstocks; (b) development of alternative transesterification conversion routes for transformation of complex, poor quality feedstocks; (c) coping with diverse biodiesel physical properties owing to an assortment in feedstock quality and fatty acid compositions; and more. In this work, comprehensive applied ^{1}H LF-NMR tools were developed for addressing several of these technical challenges. These relate to the whole process of biodiesel production: from feedstock to the end biodiesel product.

3.1. Development of an improved data analysis tool for Laplace inversion of ^{1}H LF-NMR relaxation signals using advanced sparse representation methods

As a first stage, we developed an improved ILT algorithm (PDCO) for analyzing ^{1}H LF-NMR relaxometry data, to enhance the existing potential of characterization of materials from biological origin such as lipids. In the first publication [I] we detail its mathematical formulation, calibration, and validation of results, which consisted of the following stages:

a. Establishment of the mathematical formulation of the new optimization problem using PDCO.

b. Calibration of the regularization parameters using simulations.

c. Validation of PDCO solutions using calibrated coefficients by comparison to:

- The noise-free signal

- Common L_2 solution using WinDXP

- Common L_2 solution using PDCO (α_1=0)

d. Resolution and stability analyses of PDCO solutions compared to the others.

Since the ILT is a notorious and common ill-conditioned inversion problem, whose direct inversion is unstable in the presence of noise or artifacts, choosing appropriate regularization coefficients was therefore crucial for the establishment of an accurate and stable solution. This was accomplished using simulated data computed with an in-house Matlab function library. According to simulations, universal, robust regularization coefficients were determined that provide accurate and stable solutions for a broad range of signal types and SNR levels.

One simple example that emphasizes the advantage of applying the PDCO tool is shown for oil, biodiesel, and 1:1 volumetric biodiesel-oil mixture samples (Figure 3.1 (a)-(c), respectively). Due to overlapping between the oil and biodiesel peaks, and widening of peaks imparted by the algorithm, the WinDXP (common) solution for the mixture is difficult to resolve. The PDCO solution, on the other hand, shows clear separated peaks.
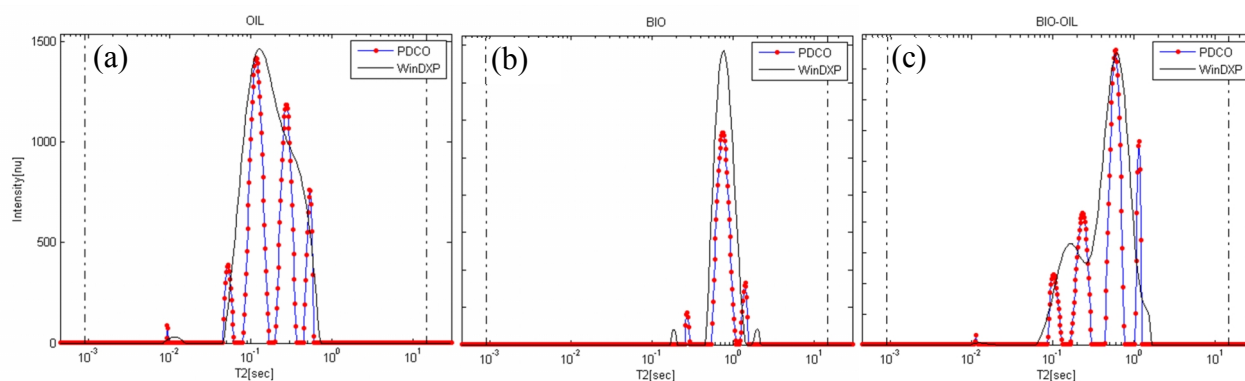

Figure 3.1. Comparison of WinDXP and PDCO solutions on a real ^{1}H LF-NMR dataset acquired from rapeseed (a) oil, (b) biodiesel, and (c) 1:1 biodiesel-oil mixture samples.

Two other authors have presented broad-peak distributions, like the ones presented here for the WinDXP solutions of pure avocado [53] and palm [70] oil samples. These were also analyzed using WinDXP. In contrast, the PDCO solutions have four distinct, moderately resolved peaks. As for this data, the original solution is unknown; these results raise the question of improved resolution versus the risk of introducing false peaks. In the course of this work and in accordance with the literature, several arguments were raised that needed to be addressed in order to increase confidence in the solutions:

1st Argument: *The PDCO algorithm works excellently for narrow-peak signals but fails to resolve broad distributions.*

- Providing that the broad-peak signal is the true signal, no peak-splitting is to be expected in the solution according to the broad peaks simulations.

2nd Argument: *The narrow peaks signals of PDCO are in fact a result of under-regularization.*

- In the case of under-regularizing, unstable solutions are to be expected in the form of spurious peaks that are due to random noise. As shown, all four repetitions of the PDCO solutions, per and between numbers of scans were found to be highly repeatable and stable.

3rd Argument: *It is not physically feasible to resolve such close peaks.*

- From a physical point of view, and in accordance with the resolution analysis, the minimum separation between peaks in the oil sample can in theory be accurately resolved for SNR > 1000 (intrinsic T_2 values at 46 ms, 114 ms, 277 ms, and 542 ms).

Based on these arguments, it is our belief that the PDCO formulation provides better resolved relaxation time distributions and more accurate solutions. Eventually, application of this algorithm enabled monitoring the process of biodiesel production through a TE reaction, and evaluating the quality of the biodiesel product, as discussed in the third publication [III]; none of which were possible using the common WinDXP solution. Still, assignment of the different peaks in the relaxation time distributions is required. This is not an obvious task, as several authors also struggled with this question for the wider bimodal distribution [53,68,70], and did not provide a conclusive solution. We addressed this question in the fourth and fifth publications [IV,V].

3.2. Design of novel ¹H LF-NMR applications for the characterization of new alternative biodiesel resources in their whole conformation, monitoring of the biodiesel TE reaction, and quality evaluation of the final product, using advanced data analysis tools

The potential of ^{1}H LF-NMR technology for the field of biodiesel was shown through a series of comprehensive applications, as described in the second and third publications [II,III]. This research consisted of applying different data analysis methods to correlate the information acquired with ^{1}H LF-NMR on different materials to standard chromatographic and spectroscopic methods.

3.2.1. Selection of alternative biodiesel feedstocks

Oil content and physical properties related to FA composition are important parameters in the successful commercialization of a new feedstock. The advantage of ^{1}H LF-NMR technology for selection of alternative biodiesel feedstocks is the ability to analyze feedstocks in their whole conformation. This can be performed substantially faster in a single step without extracting and/or reacting the oil components. In this study two ^{1}H LF-NMR tools were suggested for the screening of alternative biodiesel feedstocks:

- Chemometric tools for large scale screening of oilseeds using a fast CPMG pulse sequence followed by PCA and/or PLS for unsupervised exploration or multivariate regression, respectively. In the second publication [II], a PCA model was developed for exploration within many different genotypes of castor seeds for a specific one with reduced viscosity. In the third publication [III], PCA and PLS models were suggested for simultaneous evaluation of oil content and biodiesel physical properties of different types of oilseeds (having different FA compositions). These tools suggest high potential for screening within and between different types of oilseeds, and are especially advantageous when large batches are involved, or an unknown type of oilseed is measured. In the case where composite materials consist of oil and additional constituents including fibers, compartmentalized water, and others, chemometric tools were less suitable.

- Relaxation time distribution (1D) and cross correlation (2D) methods by ILT were suggested for selection of alternative biodiesel feedstocks according to chemical composition [III]. These tools were applied to olives as a test case. T_2 distribution analysis and cross-correlation methods allow the identification of components in composite materials. These can be used to identify separately oil, fibers, compartmentalized water and more, to search for new biodiesel feedstocks. The

application of these methods in combination with simple linear and/or multivariate regression methods, can lead to the construction of intelligent and robust calibration curves and prediction models. In this work data analysis was performed using WinDXP in order to compare the analyses with the 2D ILT tool, which is based on L_2 regularization. In our first publication [I] we suggest that the PDCO algorithm could also be applied for establishment of an improved 2D ILT tool, which is known to distort peaks [70]. It is our belief that application of improved ILT tools would further improve the resolution capabilities leading to more accurate analyses. This remains for further research.

3.2.2. Monitoring of the biodiesel TE reaction

The TE process is affected by the mode of reaction condition, molar ratio of alcohol to oil, type of alcohol, type and amount of catalysts, reaction time and temperature, and purity of reactants [17]. Therefore, monitoring the progression of the TE reaction and calculation of its yield are of paramount importance for optimizing the conditions of the TE reaction and predicting the quality of the biodiesel produced. In the third publication [III] we suggest three applications that use ^{1}H LF-NMR relaxometry: at-line and off-line monitoring of a simple alkali TE reaction, and monitoring of an *in situ* TE reaction of olive pomace.

For monitoring of the alkali reaction, identification of different constituents in liquid mixtures is desired. As shown, the WinDXP ILT analyses yielded broad distributions for the mixture samples, and therefore could not be used, either qualitatively or quantitatively. Application of the newly developed PDCO algorithm, on the other hand, yielded a tool where monitoring of the TE reaction was qualitatively performed at-line, until reaching equilibrium, and yield quantification was carried out off-line, following phase separation and cleaning of the upper layer.

Monitoring of the *in situ* TE reaction of olive pomace was performed using the WinDXP ILT toolbox, by analyzing the solid pomace and biodiesel products at each step of the reaction (acid esterification, alkali TE, and n-hexane extraction). Following the peak assignments previously proposed [III], the main peaks in the T_2 distributions of the solid pomace were the fiber and oil constituents, and in the liquid product were the biodiesel and residues of unreacted acylglycerol. As the reaction progressed, it

was shown that the relative content of the oil peaks were reduced in the reacted solid pomace samples, until achieving low oil content pomace; whereas the quality of the biodiesel product increased. In this work, monitoring of the *in situ* biodiesel TE process was performed qualitatively. However, development of calibration curves or the use of internal standards can reveal important quantitative information, including oil content, conversion yield, quantity of biodiesel produced, and more. These applications were further developed by our team for optimization of the *in situ* TE process of olive pomace and summarized in [72].

3.2.3. Quality assessment of the biodiesel product

In the third publication [III] we show that the yield of the TE reaction can be calculated from the oil to biodiesel peaks area by ^{1}H LF-NMR T_2 distributions. This gives an approximation of residual acylglycerol content in the biodiesel, which is a qualitative indication of whether it meets international standards. Another qualitative aspect is the biodiesel FA composition, which affects several physical properties of the fuel. In this work we proposed a tool that allows the assignment into viscosity groups of samples whose viscosity is unknown, simply by acquiring their transverse ^{1}H LF-NMR signals and analyzing them using chemometric tools. These methods can also be applied to find biodiesel samples that have residues of unreacted acylglycerol and/or methanol, and poorly separated and cleaned glycerol and water, provided a high quality biodiesel of the same source is used for comparison. All the aforementioned residues influence the viscosity of the sample, and accordingly affect the acquired transverse relaxation signal.

3.3. Assignment of the peaks of lipid standard materials analyzed by the new ILT algorithm to the appropriate molecular population arrangements

In the fourth and fifth publications [IV,V] we aimed at assigning the peaks of FAME standard materials to the appropriate components. Here simple FA and FAME standards were used instead of TAGs in order to simplify the experimental design.

Two possible explanations for the broad bimodal distribution of oil acquired by ^{1}H LF-NMR were suggested in the literature: (a) inhomogeneous relaxation rates for the protons along the side chains, or (b) inhomogeneous organization of the TAGs in the liquid with intermolecular interactions [68]. In order to address these questions for the

materials in hand, we first explored the organization of OA and MO in the liquid [IV]. The self-organization of OA and other FAs in the liquid has been extensively studied by the group of Iwahashi [73 and references therein]. FAMEs, on the other hand, have caught very little attention. Based on supporting methods and the available information, we suggested the model in Figure 3.2 for the arrangement of MO in the liquid, where molecules arrange in a head-to-head conformation due to polar interactions, and heads are aligned next to tails in an interdigitated structure, similarly to OA.
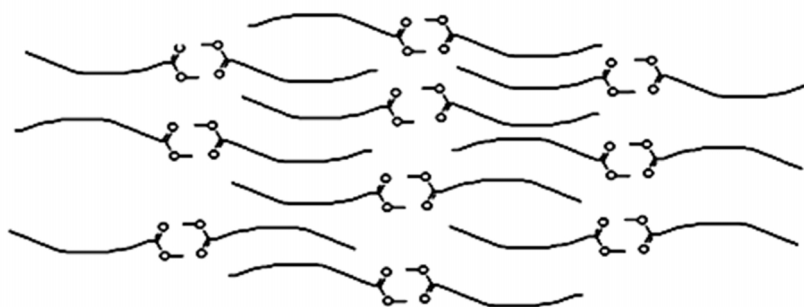

Figure 3.2. Molecular arrangement representation of MO molecules in the liquid. MO molecules arrange very similarly to OA in an interdigitated structure where heads interact through polar interactions in a head-to-head conformation.

Both theories for the assignment of peaks in the T_2 distributions of FAMEs were found to possibly explain the acquired data by logical reasoning. However, the supporting data presented in the fourth publication [IV], especially ^{13}C and ^{1}H HF-NMR measurements, suggests that the two peaks are the result of two distinct mobility populations of the protons on the chain. Still, bearing in mind that the mobility of the molecules is the direct outcome of their morphological structure, the differences in the molecular arrangement of OA and MO can be proposed by monitoring the differences in T_2 distributions and peaks area in response to a gradient of temperatures. This can be observed from the similarities in T_2 distributions in relation to melting point. In this way, the large change in relative contribution of the peaks for MO suggests of a less dense packing compared to OA. Ultimately, the dimerization of the head in OA compared to weaker polar interactions of the head can be clearly deduced from the increased intrinsic T_2 values of MO.

These findings were further supported in the fifth publication [V]. T_2 measurements additionally suggested that FAMEs have reduced mobility with increasing chain length and saturation and intra-molecularly more rigid parts with increasing chain length and degree of unsaturation. This was explained as for the saturated FAMEs, the longer the chain length the higher the melting point, since their chain configuration is linear and molecules can pack closely together, with maximum interactions due to an increasing number of van der Waals contacts, as manifested by increasing relative contribution of the less mobile peak (Peak 1) in T_2 distributions (Fig. 3.3). For the same chain length and increasing number of double bonds, melting temperatures decrease. Unsaturated molecules of *cis* configuration cannot pack as close due to bending of the chain at the double bond position, minimizing secondary interactions. As seen from their melting temperatures, they require much less energy for disordering the crystal structure and breaking intermolecular interactions to achieve molecular motion above the melt point.

A sharp decrease in the number of van der Waals interactions was found when going from the fully saturated to the mono-unsaturated 18 carbon molecule. When increasing the number of double bonds, increase in π-π interactions takes place as revealed by an increase in the relative contribution of Peak 1, as shown when going from 18:1→18:2→18:3 (Figure 3.3). This can also explain the decrease with unsaturation of this peak's response to increasing temperature, since it is well known that less thermal energy is required to break van der Waals interactions compared to π-π interactions. This arrangement along with the degree and type of interactions and temperature effects generated differences in translational and rotational movements of the molecules, which were monitored using the presented methodology.
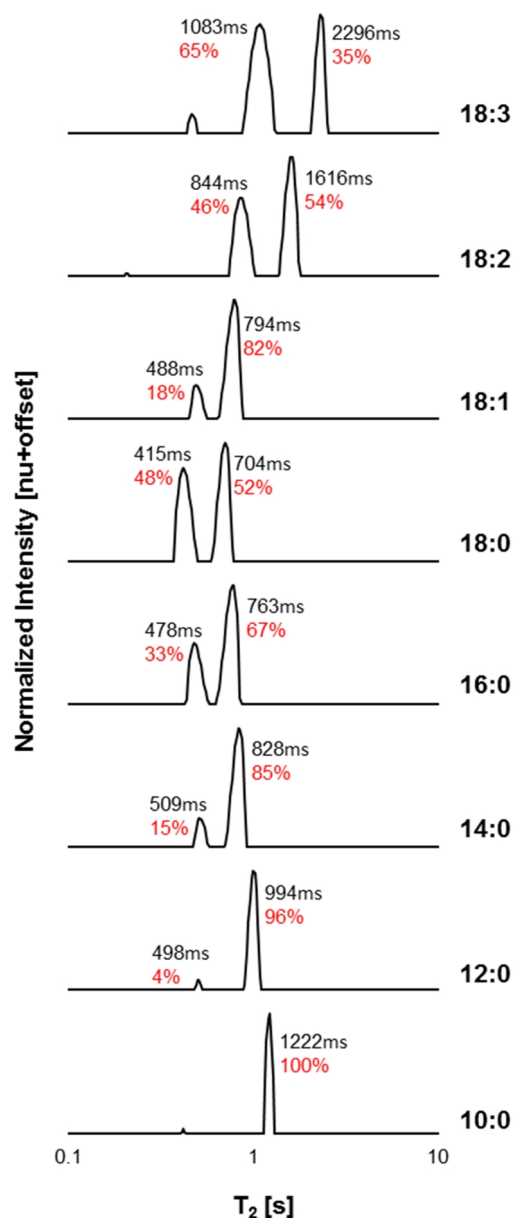
Figure 3.3. Combined ^{1}H LF-NMR T$_2$ distributions of FAMEs at 313 K. Plots are arranged by increasing chain length (bottom to top) and increasing degrees of unsaturation. The relative contributions of each peak, in relation to the other peak and intrinsic T$_2$ values are shown on each plot. FAMEs are referred to by their structures.

In the third publication [III] we presented the ^{1}H LF-NMR T$_2$ distribution of a rapeseed biodiesel sample measured at 313 K. In that study, the biodiesel sample exhibited three peaks with intrinsic T$_2$ values of 338, 671, and 1141 ms. Given that the main constituents in this biodiesel at decreasing ratios are 18:1, 18:2, 18:3, 16:0, and 18:0, the peaks can be assigned according to the three regions designated in

Figure 3.4, as the average contribution of distinct mobility populations of the protons on the chain affected by the molecular structure and weak intermolecular interactions.
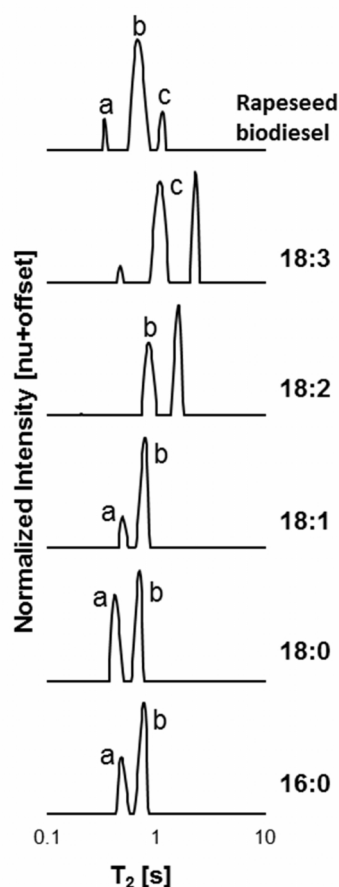

Figure 3.3. Combined ^{1}H LF-NMR T$_2$ distributions of a rapeseed biodiesel sample and its main FAMEs at 313 K. Plots are arranged by increasing chain length (bottom to top) and increasing degrees of unsaturation. Peaks are assigned to three regions (a, b, c) according to intrinsic T$_2$s. FAMEs are referred to by their structures.

Even though the aim of the fourth and fifth publications [IV,V] was to assign the peaks of FAMEs standard materials analyzed by the new ILT algorithm, to the appropriate components, this new application of ^{1}H LF-NMR shows a high prospect to the field of biodiesel, and to other research and applied disciplines with the potential of studying numerous physicochemical- and organizational-based properties, processes, and mechanisms of alkyl chains.

CHAPTER 4

Concluding remarks and future perspectives

In this work, diverse areas of research including biotechnology, lipidomics, physics, engineering, signal processing, and modeling were applied to address an environmental necessity. As a result, several novel tools and methodologies were developed and theoretical aspects were discussed to address some of the technical challenges facing the biodiesel field.

The novelty of this work lies in the developed tools and suggested methodologies. Development of an improved ILT tool for analyzing ^{1}H LF-NMR relaxometry data using sparse representation methods, led to improved resolution of analyses. As a result, a promising new tool was suggested for resolving close peaks, leading to numerous new ^{1}H LF-NMR applications. More notably, a new application for studying the molecular organization of FAMEs and other lipid materials was developed.

This work has also dealt with novel theoretical aspects. Using the developed ^{1}H LF-NMR tools and other supporting methods, we were able to suggest a comprehensive model for the molecular self-organization of FAMEs in the liquid. This has not been comprehensively discussed before in the literature, and may have important implications for physico-chemical characteristics of the fuel.

The potential for future applications using the developed tools is significant for the field of biodiesel, but also to other research and applied disciplines. The new ILT PDCO algorithm for data analysis of ^{1}H LF-NMR is a powerful new tool that can shed light on new constituents and increase resolution of analyses for the numerous applications and researches published in the literature. Using the methodologies presented in this dissertation, we suggest the possibility of further studying dynamic processes, melting mechanisms, and structural organizations of alkyl chains, with important applications in the development of biodiesel fuels.

Further application of the described methodology for the development of an improved 2D ILT algorithm for analyzing cross-correlation ^{1}H LF-NMR data, may also lead to improved analyses as for the 1D case.

References

List of publications in this dissertation

I. **<u>Berman P</u>**, Levi O, Parmet Y, Saunders M, Wiesman Z: Laplace inversion of LR-NMR relaxometry data using sparse representation methods. Concept Magn Reson A 2013, **42:**72–88.

II. **<u>Berman P</u>**, Nizri S, Parmet Y, Wiesman Z: Large-scale screening of intact castor seeds by viscosity using time-domain NMR and chemometrics. J Am Oil Chem Soc 2010, **87:**1247–1254.

III. **<u>Berman P</u>**, Leshem A, Etziony O, Levi O, Parmet Y, Saunders M, Wiesman Z: Novel ^{1}H low field (LF)-NMR applications for the field of biodiesel. Biotechnol Biofuels 2013, **6:**55.

IV. **<u>Berman P</u>**, Meiri N, Colnago LA, Moraes TB, Linder C, Levi O, Parmet Y, Saunders M, Wiesman Z: Study of liquid phase molecular packing interactions and morphology of fatty acid methyl esters (biodiesel) by ^{1}H low field nuclear magnetic resonance relaxometry. Biotechnol Biofuels 2015, in press.

V. Meiri N, **<u>Berman P</u>**, Colnago LA, Moraes TB, Linder C and Wiesman Z: Liquid phase characterization of molecular interactions in polyunsaturated and n-fatty acid methyl esters by ^{1}H Low field nuclear magnetic resonance, submitted to *Biotechnol Biofuels* journal.

General list of publications

1. O'Keefe SF: Nomenclature and classification of lipids. In: *Food Lipids: Chemistry, Nutrition, and Biotechnology*. 3rd edition. Part 1: Chemistry and properties, Edited by Akoh CC, Min DB. Taylor and Francis Group; 2008:3–37. 2008

2. Gunstone F: Fatty acids – Nomenclature, structure, isolation and structure determination, biosynthesis and chemical synthesis. In: *Fatty Acid and Lipid Chemistry*. 1st edition. Chapman and Hall; 1996:1–34.

3. Jaworski J, Cahoony EB: Industrial oils from transgenic plants. Curr Opin Plant Biol 2003, **6:**178–184.

4. Knothe G: Dependence of biodiesel fuel properties on the structure of fatty acid alkyl esters. Fuel Process Technol 2005, **86:**1059–1070.

5. Kinast JA: Production of biodiesel from multiple feedstocks and properties of biodiesel/diesel blends. Final report; NREL: Golden, CO, 2003.

6. Gui MM, Lee KT, Bhatia S: Feasibility of edible oil vs. non-edible oil vs. waste edible oil as biodiesel feedstock. Energy 2008, **33:**1646–1653.

7. Zhang Y, Dube MA, McLean DD, Kates M: Biodiesel production from waste cooking oil: 2. Economic assessment and sensitivity analysis. Bioresource Technol 2003, **90:**229–240.

8. Conceicao MM, Candeia RA, Silva FC, Bezerrab AF, Fernandes VJ, Souza AG: Thermoanalytical characterization of castor oil biodiesel. Renew Sust Energ Rev 2007, **11:**964–975.

9. Berman P, Nizri S, Wiesman Z: Castor oil biodiesel and its blends as alternative fuel. Biomass Bioenerg 2011, **35:**2861–2866.

10. Openshaw K: A review of Jatropha curcas: an oil plant of unfulfilled promise. Biomass Bioenerg 2000, **19:**1–15.

11. Hossain ABMS, Salleh A, Boyce AN, Chowdhury P, Naqiuddin M: Biodiesel fuel production from algae as renewable energy. Am J Biochem Biotechnol 2008, **4:**250–254.

12. Canakci M, Van Gerpen J: Biodiesel production from oils and fats with high free fatty acids. Trans ASAE 2001, **44:**1429–1436.

13. Dufreche S, Hernandez R, French T, Sparks D, Zappi M, Alley E: Extraction of lipids from municipal wastewater plant microorganisms for production of biodiesel. J Am Oil Chem Soc 2007, **84:**181–187.

14. Willson RM, Wiesman Z, Brenner A: Analyzing alternative bio-waste feedstocks for potential biodiesel production using time domain (TD)-NMR. Waste Manage 2010, **30:**1881–1888.

15. Fernández CM, Ramos MJ, Perez A, Rodriguez JF: Production of biodiesel from winery waste: extraction, refining, and transesterification of grape seed oil. Bioresource Technol 2010, **101:**7019–7024.

16. Canoira L, Alcantara R, Garcia-Martinez MJ, Carrasco J: Biodiesel from Jojoba oil-wax: Transesterification with methanol and properties as a fuel. Biomass Bioenerg 2006, **30:**76–81.

17. Meher LC, Vidya Sagar D, Naik SN: Technical aspects of biodiesel production by transesterification—a review. Renew Sustain Energy Rev 2006, **10:**248–268.

18. Moreau RA, Scott KM, Haas MJ: The identification and quantification of steryl glucosides in precipitates from commercial biodiesel. J Am Oil Chem Soc 2008, **85:**761–770.

19. Lu H, Liu Y, Zhou H, Yang Y, Chen M, Liang B: Production of biodiesel from *Jatropha curcas* L. oil. Comput Chem Eng 2009, **33**:1091–1096.

20. Ma F, Hanna MA: Biodiesel production: a review. Bioresource Technol 1999, **70:**1–15.

21. Vyas AP, Verma JL, Subrahmanyam N: A review on FAME production processes. Fuel 2010, **89:**1–9.

22. Knothe G: Analyzing biodiesel: standards and other methods. J Am Oil Chem Soc 2006, **83**:823–833.

23. Allen CAW, Watts KC, Ackman RG, Pegg MJ: Predicting the viscosity of biodiesel fuels from their fatty acid ester composition. Fuel 1999, **78:**1319–1326.

24. Knothe G, Steidley KR: Kinematic viscosity of biodiesel fuel components and related compounds. Influence of compound structure and comparison to petrodiesel fuel components. Fuel 2005, **84:**1059–1065.

25. Nelson DL, Cox MM: Lehninger Principles of Biochemistry. 5th ed. New York: WH Freeman; 2009.

26. Matsuzawa H, Tsuda M, Minami H, Iwahashi M: Dynamic molecular behavior and cluster structure of octanoic acid in its liquid and CCl_4 solution. Food Nutr Sci 2013, **4:**25–32.

27. Abragam A: The Principles of Nuclear Magnetism. Clarendon: Oxford University Press; 1961.

28. Song YQ, Venkataramanan L, Hürlimann MD, Flaum M, Frulla P, Straley C: T_1–T_2 correlation spectra obtained using a fast two dimensional Laplace inversion. J Magn Reson 2002, **154:**261–268.

29. Kroeker RM, Henkelman RM: Analysis of biological NMR relaxation data with continuous distributions of relaxation times. J Magn Reson 1986, **69:**218–235.

30. Hahn EL: Spin echoes. Phys Rev 1950, **80:**580–594.

31. Stejskal EO, Tanner JE: Spin diffusion measurements: SE in the presence of a time-dependent field gradient. J Chem Phys 1965, **42:**288–292.

32. Carr HY, Purcell EM: Effects of diffusion on free precession in nuclear magnetic resonance experiments. Phys Rev 1954, **94:**630–638.

33. Meiboom S, Gill D: Modified spin-echo method for measuring nuclear relaxation times. Rev Sci Instrum 1958, **29:**688–691.

34. Gambhir PN: Application of low-resolution pulsed NMR to the determination of oil and moisture in oilseeds. Trends Food Sci Tech 1992, **3:**191–196.

35. Rubel G: Simultaneous determination of oil and water contents in different oilseeds by pulsed nuclear magnetic resonance. J Am Oil Chem Soc 1994, **71:**1057–1062.

36. Pedersen HT, Munck L, Engelsen SB: Low-field ^{1}H nuclear magnetic resonance and chemometrics combined for simultaneous determination of water, oil, and protein contents in oilseeds. J Am Oil Chem Soc 2000, **77:**1069–1077.

37. Gao C, Xiong W, Zhang Y, Yuan W, Wu Q: Rapid quantitation of lipid in microalgae by time-domain nuclear magnetic resonance. J Microbiol Meth 2008, **75:**437–440.

38. Correa CC, Forato LA, Colnago LA: High-throughput non-destructive nuclear magnetic resonance method to measure intramuscular fat content in beef. Anal Bioanal Chem 2009, **393:**1357–1360.

39. Bosin WA, Marmor RA: The determination of the solids content of fats and oils by nuclear magnetic resonance. J Am Oil Chem Soc 1968, **45:**335–337.

40. Jepsen SM, Pedersen HT, Engelsen SB: Application of chemometrics to low-field ^{1}H NMR relaxation data of intact fish flesh. J Sci Food Agr 1999, **79:**1793–1802.

41. Bertram HC, Andersen HJ, Karlsson AH: Comparative study of low-field NMR relaxation measurements and two traditional methods in the determination of water holding capacity of pork. Meat Sci 2001, **57:**125–132.

42. Bertram HC, Donstrup S, Karlsson AH, Andersen HJ: Continuous distribution analysis of T_2 relaxation in meat- an approach in the determination of water-holding capacity. Meat Sci 2002, **60:**279–285.

43. Rutledge DN: Characterisation of water in agro-food products by time domain-NMR. Food Control 2001, **12:**437–445.

44. Choi SG, Kerr WL: ^{1}H NMR studies of molecular mobility in wheat starch. Food Res Int 2003, **36:**341–348.

45. Goetz J, Koehler P: Study of the thermal denaturation of selected proteins of whey and egg by low resolution NMR. LWT- Food Sci Technol 2005, **38:**501–512.

46. Lucas T, Le Ray D, Barey P, Mariette F: NMR assessment of ice cream: effect of formulation on liquid and solid fat. Int Dairy J 2005, **15:**1225–1233.

47. Prestes RA, Colnago LA, Forato LA, Vizzotto L, Novotny EH, Carrilho E: A rapid and automated low resolution NMR method to analyze oil quality in intact oilseeds. Anal Chim Acta 2007, **596:**325–329.

48. Metz H, Mäder K: Benchtop-NMR and MRI – a new analytical tool in drug delivery research. Int J Pharm 2008, **364:**170–175.

49. McDonald PJ, Korb JP, Mitchell J, Monteilhet L: Surface relaxation and chemical exchange in hydrating cement pastes: a two-dimensional NMR relaxation study. Phys Rev E 2005, **72:**011409.

50. Callaghan PT, Godefroy S, Ryland BN: Diffusion–relaxation correlation in simple pore structures. J Magn Reson 2003, **162:**320–327.

51. Godefroy S, Callaghan PT: 2D relaxation/diffusion correlations in porous media. Magn Reson Imaging 2003, **21:**381–383.

52. Hürlimann MD, Flaum M, Venkataramanan L, Flaum C, Freedman R, Hirasaki GJ: Diffusion–relaxation distribution functions of sedimentary rocks in different saturation states. Magn Reson Imaging 2003, **21:**305–310.

53. Marigheto N, Duarte S, Hills BP: NMR relaxation study of avocado quality. Appl Magn Reson 2005, **29:**687–701.

54. Hills BP, Costa A, Marigheto N, Wright K: T_1–T_2 NMR correlation studies of high-pressure processed starch and potato tissue. Appl Magn Reson 2005, **28:**13–27.

55. Marigheto N, Luca Venturi, Hills B: Two-dimensional NMR relaxation studies of apple quality. Postharvest Biol Tech 2008, **48:**331–340.

56. Furfaro ME, Marigheto N, Moates G, Cross K, Parker ML, Waldron K, Hills B: A multidimensional NMR cross-correlation relaxation study of carrot phloem and xylem: Part I. Peak assignment. Appl Magn Reson 2008, **35:**521–535.

57. Hills BP: Applications of low-field NMR to food science. Ann R NMR S 2006, **58:**177–230.

58. Nordon A, Macgill CA, Littlejohn D: Process NMR spectrometry. Analyst 2001, **126:**260–272.

59. Hopke PK: The evolution of chemometrics. Anal Chim Acta 2003, **500:**365–377.

60. Alam TM, Alam MK: Chemometric analysis of NMR spectroscopy. Annu Rep NMR Spectro 2005, **54:**41–79.

61. Kim YR, Yoo BS, Cornillon P, Lim ST: Effect of sugars and sugar alcohols on freezing behavior of corn starch gel as monitored by time domain ^{1}H NMR spectroscopy. Carbohyd Polym 2004, **55:**27–36.

62. Hickey H, MacMillan B, Newling B, Ramesh M, Eijck PV, Balcom B: Magnetic resonance relaxation measurements to determine oil and water content in fried foods. Food Res Int 2006, **39:**612–618.

63. Kenar JA: Direct determination of the lipid content in starch–lipid composites by time-domain NMR. Ind CropProd 2007, **26:**77–84.

64. Baranowska HM, Sikora M, Kowalski S, Tomasik P: Interactions of potato starch with selected polysaccharide hydrocolloids as measured by low-field NMR. Food Hydrocolloid 2008, **22:**336–345.

65. Whittall KP, MacKay AL: Quantitative interpretation of NMR relaxation data. J Magn Reson 1989, **84:**134–152.

66. Graham SJ, Stanchev PL, Bronskill MJ: Criteria for analysis of multicomponent tissue T_2 relaxation data. Magnet Reson Med 1996, **35:**370–378.

67. Moody JB, Xia Y: Analysis of multi-exponential relaxation data with very short components using linear regularization. J Magn Reson 2004, **167:**36–41.

68. Adam-Berret M, Boulard M, Riaublanc M, Mariette F: Evolution of fat crystal network microstructure followed by NMR. J Agr Food Chem 2011, **59:**1767–1773.

69. Callaghan PT: The use of ^{13}C spin relaxation to investigate molecular motion in liquid tristearin. Chem Phys Lipids 1977, **19:**56–73.

70. Assifaoui A, Champion D, Chiotelli E, Verel A: Characterization of water mobility in biscuit dough using a low-field ^{1}H NMR technique. Carbohydr Polym 2006, **64:**197–204.

71. Venturi L, Woodward N, Hibberd D, Marigheto N, Gravelle A, Ferrante G, Hills BP: Multidimensional cross-correlation relaxometry of aqueous protein systems. Appl Magn Reson 2008, **33:**213–234.

72. Etziony O: From organic solid waste to biofuels: *in-situ* transesterification of olive pomace. Unpublished master's thesis, Ben Gurion University of the Negev, Beer Sheva, Israel; 2013.

73. Iwahashi M, Kasahara Y: Dynamic molecular movements and aggregation structures of lipids in a liquid state. Curr Opin Colloid In 2011, **16:**359–366.

תקציר

ביודיזל הינו תחליף מקובל לדיזל שמקורו בדלק פוסילי (מאובנים). ייצור הביודיזל בעולם האמיר בצורה דרמטית במהלך העשור האחרון, אולם, מספר אתגרים טכנולוגיים עדיין קיימים לשיפור הקיימות שלו כדלק ביולוגי, כולל (א) חיפוש אחר דור שני מתקדם של מקורות לביודיזל; (ב) פיתוח של שיטות טרנסאסטריפיקציה אלטרנטיביות להמרת חומרי מוצא מורכבים ובעלי איכות ירודה לביודיזל; (ג) התמודדות עם תכונות פיזיקליות מגוונות של תוצר הביודיזל כתוצאה משימוש במגוון מקורות בעלי איכות ופרופיל חומצות שומן מגוונים; ועוד. אתגרים אלו העלו צורך בפיתוח שיטות ובטכנולוגיות אנליטיות מהירות ולא הרסניות. מרבית השיטות האנליטיות המקובלות היום אינן יכולות לנתח חומרים מורכבים בצורתם הטהורה, ודורשים מיצוי וניקוי מקדימים של החומרים הרצויים, ע"י שימוש בממסים לא ידידותיים לסביבה ואנליזות מסובכות. תהודה מגנטית גרעינית (תמ"ג) בשדה נמוך ידועה ככלי לאבחנה בין אוכלוסיות במערכות מורכבות, בעלות מוביליות שונה ו/או התארגנויות בתי מבנים. עם זאת, נדרש עדיין פיתוח של כלים ושיטות לאיסוף וניתוח נתונים, להתמודדות עם האתגרים הטכנולוגיים הספציפיים לתחום הביודיזל.

בדיסרטציה זו אנו מתארים פיתוח של אלגוריתם משופר להיפוך לפלס של נתוני רלקסציה של תמ"ג בשדה נמוך ע"י שימוש בשיטות עיבוד אותות לייצוג דליל. שיטה זו הניבה התפלגויות קבועי רלקסציה בעלות יכולות הפרדה משופרות והובילה לפתרונות מדויקים יותר, ביחס לאלו של התוכנה המסחרית המקובלת. ע"י שימוש באלגוריתם החדש ובשיטות כמומטריות, פותחו מספר יישומי תמ"ג אשר מתייחסים למגוון מן האתגרים הטכנולוגיים הניצבים בפני המרת חומר המוצא לתוצר הביודיזל הסופי. מתוכם יישומי תמ"ג לאפיון מקורות אלטרנטיביים חדשים לביודיזל בתצורתם הטהורה, ניטור תהליך טרנסאסטריפיקציה, ובחינת איכות תוצר הביודיזל הסופי. בשלב האחרון, הצענו הסבר כוללני למשמעות הפיקים בהתפלגויות קבועי רלקסציה של חומצות שומן מתיל אסטר בפאזה הנוזלית, ע"י לימוד המבנה המולקולרי מול תנועה סגמנטלית (תנועה שונה של חלקים שונים במולקולה) ותנועה בראונית (תנועה במרחב).

הפוטנציאל להמשך מימוש יישומים עתידיים ע"י שימוש בשיטות שפותחו הינו חשוב לתחום הביודיזל, אך גם לדיסציפלינות מחקריות ויישומיות אחרות. אלגוריתם ההיפוך לפלס לעיבוד נתוני רלקסציה של תמ"ג בשדה נמוך, הוא כלי חדש ורב עוצמה אשר יכול לזהות מרכיבים חדשים ולהגביר את יכולת ההפרדה שלהם, ולספק מידע שטרם נחקר. ע"י שימוש בשיטות העבודה המוצגות בדיסרטציה זו, אנו מציעים אפשרות להמשך מחקר מעמיק של תהליכים דינמיים, מנגנוני המסה, וסידור מבני של קבוצות אלקיל, עם יישומים חשובים לפיתוח של דלקי ביודיזל.

הצהרת תלמיד המחקר עם הגשת עבודת הדוקטור לשיפוט

אני החתום מטה מצהיר/ה בזאת : (אנא סמן) :

X חיברתי את חיבורי בעצמי, להוציא עזרת ההדרכה שקיבלתי מאת מנחה/ים.

X החומר המדעי הנכלל בעבודה זו הינו פרי מחקרי <u>מתקופת היותי תלמיד/ת</u>
<u>מחקר</u>.

____ בעבודה נכלל חומר מחקרי שהוא פרי שיתוף עם אחרים, למעט עזרה טכנית
הנהוגה בעבודה ניסיונית. לפי כך מצורפת בזאת הצהרה על תרומתי ותרומת
שותפי   למחקר, שאושרה על ידם ומוגשת בהסכמתם.

תאריך <u>27.1.2015</u>   שם התלמיד/ה   <u>פאולה ברמן</u>   חתימה   _____

העבודה נעשתה בהדרכת

פרופ׳ זאב ויסמן
מהמחלקה להנדסת ביוטכנולוגיה

פרופ׳ יעל אידן
מהמחלקה להנדסת תעשייה וניהול

ביחידה להנדסה סביבתית

הפקולטה להנדסה

פיתוח של כלים חכמים מבוססי תהודה מגנטית גרעינית בשדה נמוך לתחום הביודיזל

מחקר לשם מילוי חלקי של הדרישות לקבלת תואר "דוקטור לפילוסופיה"

מאת

פאולה   ברמן

הוגש לסינאט אוניברסיטת בן גוריון בנגב

אישור המנחים:

פרופ׳ זאב ויסמן: _____ *Z. WIESMAN*

פרופ׳ יעל אידן: _____ *Yael Edan*

אישור דיקן בית הספר ללימודי מחקר מתקדמים ע"ש קרייטמן _____

ז׳ בתמוז   27.1.2015

באר שבע

פיתוח של כלים חכמים מבוססי תהודה מגנטית גרעינית בשדה נמוך לתחום הביודיזל

מחקר לשם מילוי חלקי של הדרישות לקבלת תואר "דוקטור לפילוסופיה"

מאת

פאולה   ברמן

הוגש לסינאט אוניברסיטת בן גוריון בנגב

ז' בתמוז   **27.1.2015**

באר שבע